Interorbital spin exchange in a state-dependent optical lattice

Luis Riegger

München 2019

Interorbital spin exchange in a state-dependent optical lattice

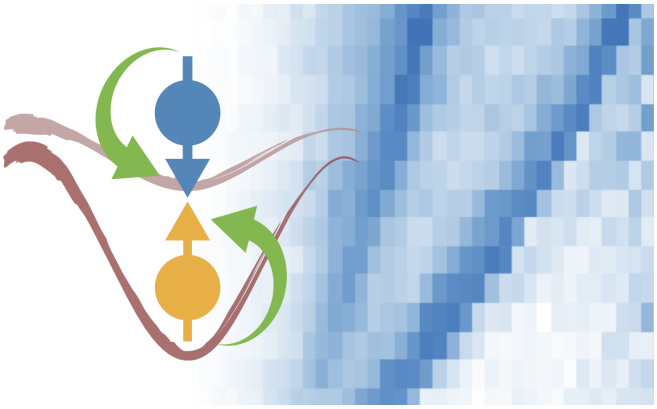

Dissertation an der Fakultät für Physik
Ludwig-Maximilians-Universität München

vorgelegt von

Luis Riegger

aus Karlsruhe

München, den 10. Februar 2019

Tag der mündlichen Prüfung: 1. April 2019

Erstgutachter: Prof. Immanuel Bloch

Zweitgutachter: Prof. Ulrich Schollwöck

Weitere Prüfungskommissionsmitglieder: Prof. Jonathan Finley, Prof. Wolfgang Zinth

Zusammenfassung

Diese Arbeit beschreibt die Realisierung eines zustandsabhängigen optischen Gitters für Ytterbium-Quantengase mit zwei elektronischen Orbitalen sowie die Beobachtung einer einstellbaren interorbitalen Spinaustauschkopplung zwischen mobilen und lokalisierten magnetischen Momenten. Ultrakalte Gase erdalkaliartiger Atome wie Ytterbium in derartigen optischen Gittern eignen sich als vielfältige Modellsysteme zur Simulation von Phänomenen und Aggregatzuständen aus der Festkörperphysik, welche durch einen orbitalen Freiheitsgrad bestimmt sind. Beispiele hierfür sind die Physik schwerer Fermionen, Kondo-Spinabschirmung sowie der kolossale magnetoresistive Effekt in Kondo-artigen Modellen.

Fermionische Ytterbiumatome im elektronischen Grundzustand und im metastabilen, angeregten Uhrenzustand weisen eine unterschiedliche Beweglichkeit im optischen Gitter auf, analog zu Elektronen in verschiedenen Festkörperorbitalen. Eine starke Entkopplung des Kernspins vom elektronischen Drehimpuls führt zu einer SU(N)-Symmetrie der interorbitalen Wechselwirkungen und bedingt hiermit die Entstehung einer natürlichen Spinaustauschkopplung mittels zweier unabhängiger Streukanäle. Wir präsentieren die Umsetzung unseres orbitalen optischen Gittersystems, welche auf den unterschiedlichen Polarisierbarkeiten der Uhrenzustände beruht und allgemeingültig für alle erdalkaliartigen Atome ist. Das optische Gitter erhält die SU(N)-Symmetrie der Wechselwirkungen weitgehend und die starke Lokalisierung der elektronisch angeregten Atome beschränkt verlustreiche Kollisionsprozesse. Mit der kontrollierten Herstellung von Mischungen in verschiedenen Kernspins und Orbitalen, welche den Spinaustauschwechselwirkungen unterliegen, unternehmen wir einen ersten Schritt zur Realisierung des Kondo-Gittermodells mit ultrakalten Atomen. Mit Hilfe optischer Spektroskopie zwischen der beiden Uhrenzuständen charakterisieren wir die starken interorbitalen Wechselwirkungen in Gegenwart des Gitterpotentials. In Fall niedriger Gitterfüllfaktoren führt die Kombination der starken interorbitalen Wechselwirkungen und der Mobilität der Grundzustandsatome zu einer effektiven Spinaustauschkopplung, analog zu der im Kondo-Modell. Wir beobachten den Austauschprozess anhand der Magnetisierungsdynamik, welche durch ein anfängliches Spin-Ungleichgewicht zwischen den Orbitalen induziert wird. Weiterhin zeigen wir, dass die Austauschkopplung mittels der Gittertiefe resonant gesteuert werden kann. Der zu Grunde liegende Mechanismus basiert auf der Kopplung an gebundene Zustände des Spin-Singulett-Streukanals.

Abstract

This thesis reports on the creation of a state-dependent optical lattice for two-orbital ytterbium quantum gases and the observation of a tunable interorbital spin-exchange coupling between itinerant and localized magnetic moments. Ultracold gases of earth-alkaline-like atoms, such as ytterbium, in state-dependent optical lattices have recently been suggested for the simulation of a large variety of paradigmatic orbital models and phenomena. These include Kondo- and Anderson-type models featuring heavy-fermion physics, Kondo spin screening, or colossal magnetoresistance. In analogy to electrons in distinct orbitals of solid-state systems, fermionic ytterbium atoms in the electronic ground state and the metastable exited clock state exhibit different mobility in the optical lattice. A strong decoupling of the nuclear spin and the electronic angular momentum results in SU(N)-symmetric interactions and the emergence of a natural spin-exchange coupling through two interorbital scattering channels.

We present and characterize our orbital lattice implementation which relies on different ac polarizabilities of the clock states and is general for all earth-alkaline-like atoms. It is expected to preserve the SU(N) symmetry of the interactions and the strong localization of the excited-state atoms limits lossy collisions. By preparing mixtures of nuclear spins and electronic orbitals, subject to spin-exchange interactions, we take a first step towards the realization of the Kondo lattice model with ultracold atoms. Through optical spectroscopy between the two clock states, we characterize the strong interorbital interactions in the presence of the lattice potential. In a setting with low lattice filling factors, the interorbital on-site interactions in conjunction with the mobility of the ground-state atoms lead to an effective spin-exchange coupling, analogous to the one in the well-known Kondo Hamiltonian. The associated exchange process is observed through magnetization dynamics resulting from initial spin imbalances between different orbitals. We find that the exchange coupling can be controlled resonantly via the external confinement. This is enabled through coupling to center-of-mass excited bound states of the spin-singlet scattering channel.

Contents

Introduction

Free electrons are characterized by their elementary electric charge and their intrinsic angular momentum, the spin. In contrast, electrons in solid materials typically carry a third key property: the orbital which characterizes their localization on an atomic site. The interplay of these three degrees of freedom and the Coulomb interaction between the electrons leads to a wealth of quantum many-body phenomena. Strong correlations can develop which underly the emergence of magnetism, metal-insulator transitions and high-temperature superconductivity.

In certain materials, the orbital degree of freedom and its strong coupling with the spin and lattice dynamics plays a decisive role. A prominent example is the Kondo effect which occurs in electronic solid-state systems featuring localized magnetic moments. It describes the strong singlet spin screening of these localized moments by the conduction electrons. The discovery of the Kondo effect was in the context of the well-known low-temperature resistivity anomaly in dilute magnetic alloys [1–3]. Extensive theoretical and experimental studies have led to a good understanding of the underlying Kondo impurity model, dominated by antiferromagnetic (AFM) spin-exchange coupling [4].

In more recent years, a new family of strongly correlated materials, so-called heavy-fermion (HF) compounds have become a focus of interest. This was fueled mainly by the discovery of unconventional superconductivity in these compounds [5–7]. They contain a dense matrix of rare-earth or actinide ions, acting as localized magnetic moments immersed in a quantum sea of itinerant conduction electrons [8–12]. The strongly enhanced quasiparticle mass in these materials is attributed to a lattice version of the Kondo effect, again leading to the formation of Kondo singlets [13–16]. Quantum fluctuations of the electronic and magnetic degrees of freedom are strongly coupled, and the emergence of non-Fermi liquid behavior close to a quantum critical point between HF and magnetic phases is of particular interest [8, 11, 16, 17].

Other “orbital materials” that recently have attracted a lot of interest are manganite and other transition-metal oxides with perovskite structure. So-called colossal magnetoresistance is observed upon the application of external magnetic fields, mediated by a ferromagnetic (FM) Hund’s coupling between spin and orbital degrees of freedom [18–21].

Reaching a deeper understanding of the orbital phenomena in these materials is both a challenge and a goal in modern condensed matter physics. It could lead to the development of new classes of materials featuring unconventional high-temperature superconductivity, colossal magnetoresistance or multiferroic properties for spintronics [14, 22].

Beyond question, significant advances in condensed matter theory have been triggered by the study of strongly correlated, multi-orbital systems. In particular, the non-perturbative nature of the Kondo effect and the failure of simple mean-field approximations necessitated the

development of fundamentally new techniques, including analytic and numerical renormalization group methods, Bethe ansatz, large-N expansions and dynamical mean-field theory [4, 23] (and references therein). Yet, many open questions remain, particularly regarding the non-Fermi liquid effects around the quantum critical point in HF compounds [17]. Moreover, current theoretical efforts to understand the physics of out-of-equilibrium systems with spin-orbital coupling have been motivated by recent transport measurements in mesoscopic quantum dot systems and spectroscopic studies of the electromagnetic response of correlated materials [24–29]. The formation dynamics of the Kondo singlet screening cloud has been studied for varying Kondo coupling anisotropies [30–34], extending previous studies of the equilibrium properties [32].

In order to describe the observations in these strongly correlated electronic systems on a microscopic level, seemingly simple model Hamiltonians have been formulated. Hubbard models constitute a prominent example used for the description of crystalline materials. They capture the transport properties of metals as well as the magnetic phenomena arising from strong interactions between the electrons [35]. Despite their formal simplicity, featuring only nearest-neighbor tunnel mobility and on-site interactions, Hubbard models serve as a prototype model for many strongly correlated phases observed in condensed matter systems. Notably, the doped Mott insulating phase of the Fermi-Hubbard model is assumed to capture high-temperature superconducting properties [36].

Coupling to additional orbital degrees of freedom can easily be included in these Hubbard-type models, which enables the description of localized magnetic moments. In particular, the periodic Anderson model [2] and the Kondo lattice model (KLM) [13] have been found to provide a good description of the orbital physics in intermetallic compounds, capturing the competition between magnetic order and HF properties [14]. A FM version of the KLM has been shown to host colossal magnetoresistance [20, 21], and the Kugel-Khomskii model is used to describe spin-orbital interactions of Mott insulating states in manganites or other transition-metal oxides with perovskite structure [18, 19, 37].

A direct validation of these microscopic models in condensed matter systems is often hindered by experimental inaccessibility or their intrinsic complexity, and depending on the parameter regime, a theoretical treatment can be very demanding or impossible. In the last two decades, ultracold gases of neutral atoms have proven themselves as a viable and powerful tool for the simulation of such models, and thus, of solid state materials [38, 39]. Despite their relatively low densities, advanced laser cooling technologies can be used to reach temperatures in the nanokelvin range, where both bosonic and fermionic gases enter a quantum degenerate regime. Experimental techniques are available that offer a great degree of control over the state preparation and detection. For example, the interaction strength can be widely tuned via Feshbach resonances for many atomic species [40]. In that way, strongly correlated states of matter have been realized and systematically probed, as demonstrated by the realization of the crossover between the Bardeen-Cooper-Schrieffer state and a molecular Bose-Einstein condensate in Fermi gases [41].

Ultracold atoms in optical lattices provide an excellent platform for realizing bosonic and fermionic Hubbard models in varying geometries and dimensionalities [42–44]. In contrast to

solid state systems, the lattice depth, and thereby the mobility and transport properties, as well as the on-site interactions can easily and dynamically be varied. Notably, the interaction-driven Mott insulating phase has been realized in a single-band Hubbard model [45, 46]. Access to the band structure, quasimomentum distribution and even spin correlations can be gained from the density distributions after expansion from the trap [47, 48]. Moreover, direct in-situ observation reveals the density distribution in the trap [49], and with the advent of quantum gas microscopes, detection and manipulation of charge and spin on a single-site level has been made possible [44, 50–52]. In fermionic systems, low-temperature phases of the single-band FHM have been accessed, exhibiting magnetic spin correlations, and even long-range AFM order [44] (and references therein). Controlled spin imbalances can be prepared to investigate the effect of impurity doping on the magnetic order [53].

Most quantum simulation experiments with ultracold atoms have employed alkali metals. In contrast, alkaline-earth(-like) atoms (AEA) possess two valence electrons. As a consequence, a more complex, Helium-type level structure emerges where the metastable state $^3\mathrm{P}_0$ in the electronic spin-triplet manifold is connected to the ground state $^1\mathrm{S}_0$ via an ultranarrow optical transition. This so-called clock transition has made AEA ideal for the realization of highly accurate and stable atomic clocks [54–57].

Ytterbium and strontium are the most commonly used AEA species and quantum degenerate atomic gases of most fermionic and bosonic isotopes have been realized. In the context of quantum simulation, their (meta-)stable clock states can serve as an additional orbital degree of freedom, along with an independent spin degree of freedom that is provided by the nuclear spin of the fermionic isotopes. Due to the closed outer shell in both clock states, with zero total electronic angular momentum, the hyperfine coupling vanishes and the orbital degree of freedom is highly decoupled from the nuclear spin I. In fact, the low-energy intra- and interorbital interactions obey an SU($N = 2I + 1$) symmetry [58]. For ^{173}Yb ($I = 5/2$) and ^{87}Sr ($I = 9/2$), an enhanced SU($N > 2$) symmetry compared to electronic condensed matter systems emerges, which has been verified experimentally [59–61].

At the level of single-orbital physics, this SU(N) symmetric nature of the interactions provides access to high-symmetry analogs of electronic spin-1/2 models and the emergence of novel, exotic phases of matter, such as valence bond and Abelian chiral spin liquid states, has been predicted [62–66]. Recent experimental manifestations of the enhanced symmetry are in the creation of a large-N spin liquid in one-dimensional systems [67], the realization of SU(6)-symmetric Mott insulators [68, 69], and the observation of AFM correlations in SU(4) samples in an optical dimerized cubic lattice [70], all realized with ^{173}Yb.

The earliest proposals which involved both the orbital degree of freedom as well as the SU(N) symmetry in the spin sector have studied fermionic AEA as a promising platform for quantum computation [64, 71–75], as well as for the implementation of artificial gauge fields [76]. The increased SU(N) symmetry could even enable the realization of non-Abelian gauge potentials and spin-orbit Hamiltonians with a close connection to the gauge interactions in quantum chromodynamics [77, 78].

Coming back to the simulation of multi-orbital lattice models, the two clock states of AEA can be exploited to mimic electrons in distinct orbitals of solid materials. Degenerate fermionic

gases of AEA with their orbital and nuclear-spin degree of freedom have recently been proposed as model systems for the simulation of both orbital magnetism as well as Kondo physics, including heavy-fermion states [58, 66, 79–81]. Two-orbital SU(N)-symmetric Hamiltonians can be modelled that capture the interplay between spin, charge and orbital degree of freedom. In particular, Kondo impurity and lattice models with both FM and AFM coupling should be accessible [34, 58, 79–84]. These rely on two main ingredients: the strong localization of one orbital and the presence of spin-exchanging interactions between the localized and mobile magnetic moments. Compared to previous proposals for alkali atoms [85–87], both can be realized simultaneously and naturally with fermionic AEA.

The spin-exchange interactions arise directly from the interplay of two available interorbital scattering channels, associated with spin-singlet and triplet superposition states [58]. By monitoring the equilibration dynamics of a spin imbalance between the population in different orbitals, as well as by spectroscopic techniques, the interorbital interactions have been quantified in previous experiments. A natural FM exchange coupling was measured for ^{173}Yb and ^{87}Sr [59–61], in contrast to an AFM coupling in ^{171}Yb [88]. For ^{173}Yb, the exchange coupling was found to be exceptionally large due to the large s-wave scattering length in the spin-singlet scattering channel [59, 60]. Beyond that, the associated shallow bound state leads to the emergence of a magnetically tunable interorbital Feshbach resonance which has recently been observed at accessible magnetic fields [89–91]. The orbital state-dependent mobility of the magnetic moments is straightforward to accomplish using AEA in optical lattices with electronic state-dependent ac Stark shifts [73, 74, 92]. The orbital degree is then encoded in the clock states which belong to different electronic manifolds. This represents a significant advantage over approaches with alkali atoms which rely on the use of different atomic species [86, 93] or excited bands of an optical lattice [85, 94] – lacking a direct spin-exchange coupling or suffering from reduced stability in higher lattice bands, respectively.

This thesis

The main subject of this thesis is the experimental implementation of an orbital state-dependent optical lattice (SDL) for ytterbium and the study of the interorbital interactions of fermionic ^{173}Yb in this setup. The atomic ground state $^1S_0$ and the metastable excited clock state $^3P_0$ take the role of the mobile and localized lattice orbitals, and different nuclear spin components act as a pseudo-spin. We demonstrate how a static and monochromatic optical lattice potential can be devised to realize the necessary state-dependent confinement for the realization of Kondo models. The spin-independent nature of the atom-light coupling preserves the SU(N) symmetry of the interactions and direct collisional losses between the excited-state atoms [59, 95, 96] are avoided by their strong localization.

Coherent optical control of the clock transition enables control of the population in the localized orbital $^3P_0$ in a spin-resolved way. Starting with degenerate two-spin mixtures of ^{173}Yb, we characterize the interorbital interactions in the SDL by means of clock-line interaction spectroscopy. A model for the two-channel on-site interactions in the setting of mixed confinement for the two orbitals is introduced. We find that the low-energy spectrum is strongly influenced

by a molecular bound state of spin-singlet nature. By monitoring the out-of-equilibrium spin relaxation dynamics of localized magnetic moments interacting with mobile "bath" atoms on separate lattice sites, we can directly access the strength of the spin-exchange coupling in the SDL. We demonstrate how the effective Kondo-type coupling strength can be tuned resonantly with the external confinement via coupling to spin-singlet bound states. This first realization of interorbital spin-exchanging interactions with orbital state-dependent mobility in a gas of ultracold fermions lays the groundwork for using AEA as a testbed for orbital lattice models.

Outline of this thesis

This thesis is structured as follows.

In Chapter 1, we review the atomic properties of ytterbium. The consequences of its AEA level structure are discussed with regard to atom-light and Zeeman coupling, as well as its interatomic interactions. We focus on the optical and magnetic properties of the two clock states. In particular, their differential dipole polarizability is predicted over a large range of wavelengths which enables the realization of orbital state-dependent and independent optical potentials. Furthermore, known properties of the intra- and interorbital interactions are reviewed, illustrating the origin of the spin-exchanging interactions in fermionic ytterbium.

Chapter 2 discusses the implementation of our orbital SDL. The orbital state-dependent band structure is discussed on a single-particle level and we introduce the notion of mixed on-site confinement in the tight-binding approximation. The wavelength-dependent differential polarizability, leading to the localization of the excited clock state orbital, is quantified via clock line spectroscopy and parametric heating techniques. We characterize the atomic lifetime limits in the SDL setup, imposed by collisional losses between atoms in the excited clock state. Finally, we review existing proposals and ideas on the simulation of multiorbital lattice models using fermionic AEA in a SDL. It is shown how the two-orbital SU(N) Fermi-Hubbard model is naturally realized and how it connects to the SU(N) generalized version of the KLM. The accessibility of interesting many-body phases in different experimental parameter regimes is discussed.

In Chapter 3, an overview over the experimental apparatus and techniques is presented. The laser beam geometry of the optical trapping potentials, defining the confinement for the ytterbium atoms is illustrated. We introduce the available techniques for state manipulation and detection, including the coherent control of the electronic orbital via coupling to the clock transition and nuclear-spin-resolved imaging.

In Chapter 4, a model for the on-site interactions in the mixed confinement of the SDL is introduced. It considers the two interorbital scattering channels associated with the spin singlet and triplet states as well as the coupling introduced by finite magnetic fields. Considering a regularized contact potential allows us to treat the strong interactions in the singlet channel including a set of shallow bound states induced by the confinement. The low-energy eigenstates are probed spectroscopically using the clock transition and we identify a strong confinement dependence caused by coupling between the lowest on-site trap states and center-of-mass excitations of the bound singlet.

Chapter 5 presents the experimental observation of out-of-equilibrium magnetization dynamics in two-orbital spin mixtures. We directly observe the spin-exchange dynamics in the SDL and find that the process is well described by an effective exchange coupling arising from the state-dependent mobility and the two repulsive on-site interaction channels. Notably, we observe a resonant tunability of the exchange rate via the external confinement. The tuning mechanism is explained by finite coupling to on-site singlet bound states, holding the potential to invert the sign of the Kondo coupling in an effective low-energy model.

In Chapter 6, we characterize the collective mobility in the SDL, with the potential realization of heavy fermion phases and the associated mass enhancement in mind. The effective mass is probed via center-of-mass dipole oscillations of fermionic and bosonic samples in an additional harmonic confinement. In particular, we investigate the energy dependence and the effect of the finite Fermi pressure on the oscillation dynamics. Finally, we artificially introduce a controllable hybridization of the lattice orbitals by means of adiabatic clock "light dressing", in analogy to the exchange coupling in the KLM.

Publications

The main experiments and results obtained during the work on this thesis are presented in the following publications:

- L. Riegger, N. Darkwah Oppong, M. Höfer, D. R. Fernandes, I. Bloch and S. Fölling. *Localized magnetic moments with tunable spin exchange in a gas of ultracold fermions*. Phys. Rev. Lett. 120, 143601 (2018)

- C. Hofrichter, L. Riegger, F. Scazza, M. Höfer, D. R. Fernandes, I. Bloch, and S. Fölling. *Direct probing of the Mott crossover in the SU(N) Fermi-Hubbard model*. Phys. Rev. X 6, 021030 (2016)

- M. Höfer, L. Riegger, F. Scazza, C. Hofrichter, D. R. Fernandes, M. M. Parish, J. Levinsen, I. Bloch and S. Fölling. *Observation of an orbital interaction-induced Feshbach resonance in* ^{173}Yb. Phys. Rev. Lett. 115, 265302 (2015)

The following article has also been published in the course of this PhD:

- L. Riegger, G. Orso, and F. Heidrich-Meisner. *Interaction quantum quenches in the one-dimensional Fermi-Hubbard model with spin imbalance.* Phys. Rev. A 91, 043623 (2015)

Further details on our experimental setup and previous measurement results can be found in Refs. [97–99].

CHAPTER 1

Ytterbium – a two-orbital atom

Ytterbium an alkaline-earth-like atom (AEA). The designation is justified by the nature of its electron shell, featuring a set of complete internal shells, as well as two valence electrons in an outer s-shell. This structure is found only for group-two elements, namely the alkaline-earth metals Be, Mg, Ca, Sr, Ba and Ra, as well as transition metals from the d-block (Zn, Cd, Hg) and f-block (Yb, No) of the periodic table. AEA possess a peculiar level structure, similar to the one of Helium, where the electronic states can be separated into a spin singlet and triplet manifold. Optical dipole transitions between the manifolds are inhibited which entails the presence of metastable states and ultranarrow transitions. Moreover, the total electronic angular momentum of the lowest electronic states, the clock states, vanishes, leading to a decoupling from the nuclear spin. For fermionic AEA, this does not only imply a strongly reduced sensitivity to external magnetic fields, but it also causes the emergence of SU(N) symmetric interactions.

These properties radically distinguish them from alkali atoms with one valence electron and have led to a large variety of experimental applications and theoretical interest. This includes the realization of highly precise and accurate optical atomic clocks [57]. In the context of quantum simulation with ultracold neutral atoms, the decoupling of the electronic angular momentum from the nuclear spin can be exploited to realize strongly correlated states of matter involving orbital magnetism and Kondo-type spin-exchange coupling [58, 80, 81]. The ground state $^1S_0$ and metastable excited clock state $^3P_0$ then act as the orbital degree of freedom, along with the spin degree of freedom provided by the nuclear spin I of fermionic isotopes (see Fig. 1.1). Two interaction channels between the clock states lead to the emergence

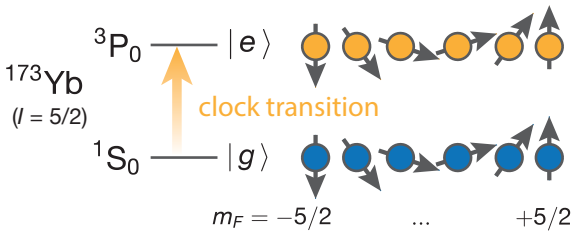

Figure 1.1 – An electronic and spin degree of freedom can be used simultaneously in fermionic alkaline-earth-like atoms, illustrated for ^{173}Yb: the ultranarrow optical clock transition couples the clock states $^1S_0$ and $^3P_0$. Both electronic orbitals feature multiple nuclear spin states ($N = 6$ for a nuclear spin $F = I + J = 5/2$), decoupled from the electronic angular momentum.

of a natural exchange interaction between the orbitals.

In this Chapter, we review the essential atomic properties of ytterbium concerning the realization of such orbital lattice models. We discuss off-resonant atom-light coupling which enables the realization of orbital state-dependent lattices, based on the differential dipole polarizability of the clock states. Taking known optical transition properties into account, we estimate the polarizability of the lowest-lying electronic states over a large wavelength range and compare to existing theory. Coherent light coupling in AEA is discussed, with a focus on the clock transition which is relevant both for state preparation and detection of orbital mixtures. In this context, we also investigate the effect of Zeeman and hyperfine coupling which strongly influences the atom-light coupling strength and causes spectroscopic shifts.

Furthermore, a review of the low-energy scattering properties of AEA is presented. The emergence of the extended SU(N) symmetry and the interorbital spin-exchange interactions are discussed.

1.1 Atomic properties, level structure and transitions

Ytterbium, as a lanthanide with atomic number $Z = 70$, is a rare-earth element with an electronic structure (Xe)$4f^{14}6s^2(^1\mathrm{S}_0)$ in the ground state. Conveniently, many stable isotopes exists. The bosonic isotopes are ^{168}Yb, ^{170}Yb, ^{172}Yb,^{174}Yb and ^{176}Yb; the fermionic isotopes are ^{173}Yb and ^{171}Yb. Thanks to a relatively large natural abundance of all isotopes, enrichment processes are rendered unnecessary for the production of ultracold atomic gases. Also, multi-isotope mixtures can easily be created [100]. The experiments described in Chapters 4 to 6 of this thesis employ fermionic ^{173}Yb, as well as bosonic ^{174}Yb in Chapter 6. With regard to future applications of ^{171}Yb, exhibiting an inverted sign of the interorbital exchange interactions [88], we specifically compare to the properties of this isotope in the next sections. The bosonic isotopes all carry an even number of protons and neutrons in a so-called even-even nucleus with $I = 0$. In contrast, the nucleus of the fermionic isotopes ^{173}Yb ($I = 5/2$) and ^{171}Yb ($I = 1/2$) is characterized by a half integer nuclear spin.

The electronic properties of AEA are largely determined by the two valence electrons in the outer s-shell. Most higher-lying eigenstates are in the so-called intermediate coupling regime, influenced by spin-orbit coupling and electrostatic interactions [101]. However, in good approximation, the electronic levels can be labeled by the Russell-Saunders (RS) symbols, suggesting bare, LS coupling eigenstates $^{2S+1}\mathrm{L}^0_J$, where the orbital angular momentum L, the electronic spin S and the total electronic angular momentum J are good quantum numbers [102]. To lowest order, the optical transition strengths between the states are then determined by the standard dipole selection rules. State-mixing induced by different coupling mechanisms can cause a violation of the selection rules leading to small but finite transition strengths. Possible coupling mechanisms are discussed in Section 1.2.

As depicted in Fig. 1.2, the level spectrum is split into an electronic spin-singlet and triplet manifold, characterized by their total electronic spin $S = 0$ or $S = 1$. The atomic ground state $^1\mathrm{S}_0$ is a $6s^2$ spin-singlet configuration with angular momentum $J = 0$.

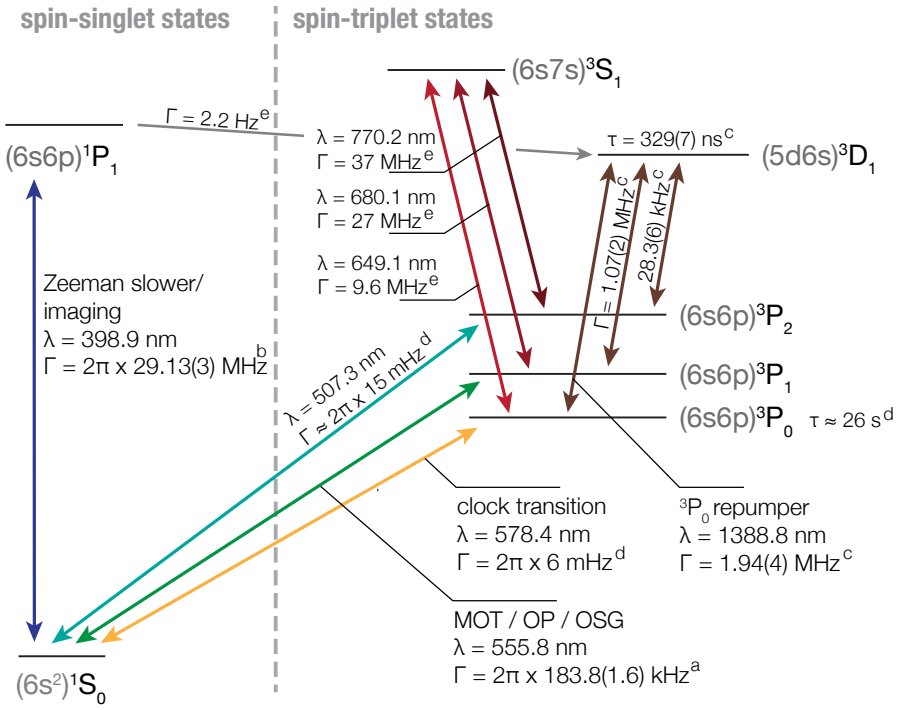

Figure 1.2 – Partial term diagram for ^{173}Yb atomic levels and transitions relevant to this work. Optical transitions are denoted with arrows and associated wavelengths λ and decay rates Γ. Atomic levels are labeled with their associated bare LS eigenstates $^{2S+1}L_J$ and lifetime τ. The hyperfine structure is not shown. The values are taken from references indicated by the superscripts [a][103], [b][104], [c][105], [d][106] and [e][107].

The blue imaging and cooling transition Within an electronic spin manifold, strong dipole-allowed transitions can be found. A prominent example is the broad 398.9 nm transition $^1S_0 \rightarrow (6s6p)^1P_1$ with a natural linewidth of $\Gamma_{\text{blue}} = 2\pi \times 29.13\,\text{MHz}$, obtained from photoassociation spectroscopy [104]. The transition frequency is $\nu^{174}_{\text{blue}} = 751.526\,533\,49(33)\,\text{THz}$ [108] for ^{174}Yb. Experimentally determined hyperfine and isotope shifts for the fermionic isotopes can be found in the references provided in Fig. 1.2. The transition is nearly closed and the large linewidth and photon scattering rate make it suitable for both Zeeman slowing and absorption imaging of the ground-state atoms.

In contrast, the electrons of the three lowest-lying excited states $^3P_0$, $^3P_1$, $^3P_2$ are in a $6s6p$ spin-triplet configuration. The transitions connecting these states to the ground state $^1S_0$ are typically designated as intercombination lines. Generally, these transitions between the spin manifolds are forbidden by the dipole selection rule $\Delta S = 0$, and therefore relatively weak.

The green intercombination line Featuring a natural linewidth of $\Gamma = 184\,\text{kHz}$, the strongest intercombination line is $^1S_0 \rightarrow {}^3P_1$, with a centroid of the transition frequency at $\nu^{173}_{\text{green}} = 539.385\,606(10)\,\text{THz}$ (555.8 nm) for ^{173}Yb [103]. Because this transition is closed and of intermediate strength, it is well-suited as the cooling transition in the magneto-optical trapping (MOT) stage of our setup, providing relatively small Doppler temperatures while maintaining

a reasonable capture velocity [59]. Note that for the fermionic isotopes with $I > 0$, a hyperfine and magnetic substructure emerges for the states with $J \neq 0$ which strongly influences the atom-light and Zeeman coupling. This is discussed in detail in Section 1.2. As a result, light coupling to the $^1S_0 \rightarrow {}^3P_1$ transition can be used in the preparation of nuclear spin state (m_F) mixtures via optical pumping (OP), or for an m_F-selective optical Stern Gerlach (OSG) technique (see Chapter 3).

The clock transition Because the metastable excited state $^3P_0$ has zero angular momentum $J = 0$, like the ground-state, the transition $^1S_0 \rightarrow {}^3P_0$ violates an additional dipole selection rule, namely $\Delta J \not\rightarrow J = 0$. Therefore it is denoted as doubly forbidden and its extremely small linewidth on the 10-milihertz scale is only enabled for fermionic isotopes through hyperfine coupling with $^1P_1$ and $^3P_1$. For the bosonic isotopes a finite atom-light coupling strength can only be induced by "quenching" the transition via a strong external magnetic field, that leads to Zeeman cross coupling with other states of the triplet manifold. A detailed discussion of the properties of the metastable clock state and the clock transition to the ground state is provided in Section 1.4. Coherent, nuclear-spin-resolved manipulation of the clock transition, and thereby the population of $^3P_0$, can be achieved using a narrow-linewidth laser at finite magnetic fields (see Section 3.5.2).

Further transitions which are relevant to this work lie within the spin-triplet manifold and connect the $6s6p$ states with the higher-lying states $(6s7s)^3S_1$ and $(5d6s)^3D_1$. In particular, our implementation of a state-dependent optical lattice for the two clock states relies on a laser frequency close to the transition $^3P_0 \rightarrow {}^3S_1$, inducing a significant light shift for the $^3P_0$ atoms (see Chapter 2). Resonant coupling to the transition $^3P_0 \rightarrow {}^3D_1$ is employed for repumping metastable $^3P_0$ atoms to the ground state where they can be imaged (see Section 3.5.3).

1.2 Zeeman and hyperfine coupling

In this section, we want to discuss the effect of Zeeman, hyperfine and other coupling mechanisms on the lowest-energy states of ytterbium. Above, we have labeled the atomic levels of ytterbium by their RS symbols, denoting LS coupling eigenstates $^{2S+1}L_J^0$. However, in AEA, like ytterbium or strontium, this is assumption is broken by several coupling mechanisms. The bare RS states are mixed my spin-orbit coupling and electrostatic interaction between the two electrons. Also, one needs to consider inter-state Zeeman coupling in the case of external magnetic fields, and for fermionic isotopes with $I > 0$, there is additional hyperfine mixing of the lowest-lying states. First, this leads to a violation of certain dipole selection rules and, consequently, a finite linewidth of the intercombination and clock transition. Second, the state mixing leads to a modification of the Zeeman shift. This particularly affects the clock states $^1S_0$ and $^3P_0$ with angular momentum of $J = 0$. Their magnetic coupling is mainly governed by the nuclear spin I and therefore strongly reduced compared to states with $J > 0$. In particular, for the bosonic isotope with $I = 0$, the linear Zeeman effect is entirely suppressed. This would imply the same magnetic sensitivity for both clock states with $J = 0$ and $F = I$. Yet, the state

mixing mechanisms induce finite differential magnetic shifts between the clock states, even for the bosonic isotope.

1.2.1 Coupling in (nsnp) two-electron systems

To understand the effect of the different coupling mechanisms, we follow the approach by Lurio et al. [101] for the simultaneous treatment of Zeeman, hyperfine and spin-orbit coupling between the states of an (nsnl) state manifold in a two-electron system. Their approach is based on the relativistic Breit-Wills model for the hyperfine interactions [109, 110] and neglects configuration interaction that can become important in heavy many-electron systems. Yet, it has been successfully employed in the case of ^{87}Sr [111] and other species [112, 113] to derive quantitatively correct values for the differential Zeeman splitting of the clock states as well as an estimated $^3\mathrm{P}_0$ lifetime compatible with an ab-initio calculation including the configuration interaction [106]. A numerical diagonalization of the total Hamiltonian including spin-orbit coupling, hyperfine and Zeeman interactions allows us to determine the eigenspectrum for the lowest-lying excited states for large range of magnetic fields.

Intermediate coupling

In the case of ytterbium, we consider the excited states of the (6s6p) manifold, $^1\mathrm{P}_1$, $^3\mathrm{P}_0$, $^3\mathrm{P}_1$ and $^3\mathrm{P}_2$. In the absence of hyperfine and Zeeman coupling, the states of highest and lowest angular momentum J are uncoupled and remain the bare RS states: $|^3\mathrm{P}_0\rangle = |^3\mathrm{P}_0^0\rangle$ and $|^3\mathrm{P}_2\rangle = |^3\mathrm{P}_2^0\rangle$. The states with $J = 1$ however are subject to finite spin-orbit coupling and electrostatic interaction and are transformed into [101, 111]

$$\begin{pmatrix} |^3\mathrm{P}_1\rangle \\ |^1\mathrm{P}_1\rangle \end{pmatrix} = U \begin{pmatrix} |^3\mathrm{P}_1^0\rangle \\ |^1\mathrm{P}_1^0\rangle \end{pmatrix} \quad \text{with} \quad U = \begin{pmatrix} \alpha & \beta \\ -\beta & \alpha \end{pmatrix}. \tag{1.1}$$

This is called the regime of intermediate coupling and one can switch between the two basis sets using the unitary transform U that contains the mixing angles β and $\alpha = \sqrt{1-\beta^2}$.

It turns out that the mixing angles can be determined experimentally, assuming the lifetime of the bare RS state $^3\mathrm{P}_1^0$ is indeed zero and the measured finite decay rate $\Gamma_{^3\mathrm{P}_1}$ of $^3\mathrm{P}_1$ is entirely caused by the spin-orbit coupling with $^1\mathrm{P}_1$. Then, using Eq. (1.33), which relates the decay rate to the transition frequency and the reduced dipole matrix element, for both bare RS states leads to [101, 111]

$$\frac{\beta^2}{\alpha^2} = \frac{\Gamma_{^3\mathrm{P}_1}}{\Gamma_{^1\mathrm{P}_1}} \frac{\nu^3(^1\mathrm{P}_1 - {}^1\mathrm{S}_0)}{\nu^3(^3\mathrm{P}_1 - {}^1\mathrm{S}_0)}. \tag{1.2}$$

For ytterbium and the experimentally determined transition linewidths and frequencies (see Fig. 1.2), we obtain a mixing angle[1]

$$\beta = -0.1295(6) \quad (\alpha = 0.99157(8)), \tag{1.3}$$

[1]The sign of β can be inferred from the derivation of the intermediate coupling coefficients in [109]. The uncertainty is inherited from the uncertainties in the transition linewidths.

nearly an order of magnitude larger than in ^{87}Sr [111]. A matrix representation of the transformation in the bare RS state basis is shown in Fig. 1.3(b).

Zeeman coupling

The total Zeeman Hamiltonian $H_Z = \mu_0 g_S \mathbf{S}\cdot\mathbf{B} + \mu_0 g_L \mathbf{L}\cdot\mathbf{B} - \mu_0 g_I \mathbf{I}\cdot\mathbf{B}$ couples the electronic spin **S** and angular momentum **L** as well as the nuclear spin **I** with the external magnetic field. The electronic Landé factors are the universal values $g_S \approx 2.00232$ [114] and $g_L = 1$. The nuclear Landé factor is given by the ratio of the nuclear magnetic moment μ_I and the Bohr magneton μ_0:

$$g_I = \frac{\mu_I}{\mu_0 I}\,. \tag{1.4}$$

μ_I is typically of the order of the nuclear magneton $\mu_N \approx \mu_0/1836.15$ [114] and therefore strongly reduced compared to the electronic moments. For the two fermionic ytterbium isotopes, it has been determined by means of m_F-resolved optical pumping experiments[2] [118, 120]:

$$\begin{aligned}\mu_I(^{173}\mathrm{Yb}) &= -0.67989(3)\mu_N\,,\\ \mu_I(^{171}\mathrm{Yb}) &= +0.49367(1)\mu_N\,.\end{aligned} \tag{1.5}$$

In the basis of bare RS states, Lurio et al. [101] provide the full expression for the Zeeman Hamiltonian within an (nsnl) manifold ($l = p = 1$ in our case):

$$\begin{aligned}\langle S'LJ'F'm_F'|H_z^0|SLJFm_F\rangle =& \delta_{SS'}\delta_{m_F m_F'}(-1)^{F'-m_F'}\begin{pmatrix} F' & 1 & F\\ -m_F & 0 & m_F\end{pmatrix}\sqrt{(2F'+1)(2F+1)}\\ &\times\left[\delta_{JJ'}(-1)^{I+J+F+1}\begin{Bmatrix} I & F' & J\\ F & I & 1\end{Bmatrix}\langle I|H_z^n|I\rangle\right.\\ &\left.+(-1)^{I+J+F'+1}\begin{Bmatrix} J' & F' & I\\ F & J & 1\end{Bmatrix}\langle J'|H_z^e|J\rangle\right]\end{aligned} \tag{1.6}$$

[2] The given values include the correction for diamagnetic shielding by the electron cloud. Another value for the nuclear moment, that is frequently cited, is $\mu_I(^{173}\mathrm{Yb}) = -0.67755(3)\mu_N$, measured by Olschewski and Otten [115] in a "precursor" experiment, and listed in [116, 117]. In contrast to the more recent study [118], it does not take light shift corrections into account.

In an independent NMR measurement, Gossard et al. obtain $\mu_I(^{173}\mathrm{Yb}) = 0.68002(3)\mu_N$ [119], consistent with Eq. (1.5) and also listed in [120]. Note that we use the values from the collection by Stone [120], which corrects the original values from the optical pumping [118] and NMR [119] experiments with updated fundamental constants and atomic reference data.

with the nuclear and electronic reduced matrix elements[3]

$$\begin{aligned}\langle I|H_z^n|I\rangle &= -g_I\sqrt{I(I+1)(2I+1)}\mu_0 B\\ \langle J'|H_z^e|J\rangle &= \sqrt{(2J+1)(2J'+1)}\mu_0 B\left[g_L(-1)^{L+S+J'+1}\begin{Bmatrix}L & J' & S\\ J & L & 1\end{Bmatrix}\sqrt{l(l+1)(2l+1)}\right.\\ &\quad\left.+g_S(-1)^{L+S+J+1}\begin{Bmatrix}S & J' & L\\ J & S & 1\end{Bmatrix}\sqrt{S(S+1)(2S+1)}\right].\end{aligned} \tag{1.7}$$

Here, $(\cdot)$ and $\{\cdot\}$ indicate Wigner-3j and Wigner-6j symbols, respectively. A matrix representation of the bare Zeeman Hamiltonian for ^{173}Yb is shown in Fig. 1.3(a).

Low-field Zeeman shifts On the diagonal of H_z^0, one recovers the linear Zeeman shift term

$$\Delta_z^{(1)} = g_F m_F \mu_0 B \tag{1.8}$$

with the standard definition of the Landé factors

$$\begin{aligned}g_F &= g_J\frac{F(F+1)+J(J+1)-I(I+1)}{2F(F+1)} - g_I\frac{F(F+1)+I(I+1)-J(J+1)}{2F(F+1)} \quad \text{and}\\ g_J &= g_L\frac{J(J+1)+L(L+1)-S(J+1)}{2J(J+1)} + g_S\frac{J(J+1)+S(S+1)-L(L+1)}{2J(J+1)}.\end{aligned} \tag{1.9}$$

To account for finite spin-orbit coupling, we can transform the bare Zeeman Hamiltonian to the intermediate coupling regime via $H_z = U^\dagger H U$ with U from Eq. (1.1) [see Fig. 1.3(c)]. One finds that Eq. (1.8) still holds, except that the orbital Landé factors g_J for the two $J=1$ states are modified by the state mixing to [101]:

$$\begin{aligned}g_J'\left(^3\mathrm{P}_1\right) &= \alpha^2 g_J\left(^3\mathrm{P}_1^0\right) + \beta^2 g_J\left(^1\mathrm{P}_1^0\right)\\ g_J'\left(^1\mathrm{P}_1\right) &= \alpha^2 g_J\left(^1\mathrm{P}_1^0\right) + \beta^2 g_J\left(^3\mathrm{P}_1^0\right).\end{aligned} \tag{1.10}$$

The experimentally determined mixing angles in Eq. (1.2) for ytterbium result in a modification of the linear Zeeman shift on the percent level. The resulting linear shift is a good approximation for the states $^3\mathrm{P}_1$ and $^1\mathrm{P}_1$ if the Zeeman energy is much smaller than the hyperfine splitting and if hyperfine and Zeeman cross-coupling between the (6s6p) states are neglected. We have evaluated the linear Zeeman shift $\Delta_z^{(1)}$ for a collection of experimentally relevant states in Figs. A.2 to A.5.

Ground-state Zeeman shift The ground state with $J=0$ and $g_J=0$ is not subject to interstate coupling and Eq. (1.8) is actually an exact expression for the Zeeman shift for near-arbitrary magnetic fields. From the measured μ_I in Eq. (1.5), we infer the following nuclear Landé factors for the fermionic isotopes:

$$\begin{aligned}g_F^g(^{173}\mathrm{Yb}) &= -g_I(^{173}\mathrm{Yb}) = +207.30(1)\,h\,\mathrm{Hz/G}\mu_0,\\ g_F^g(^{171}\mathrm{Yb}) &= -g_I(^{171}\mathrm{Yb}) = -752.61(2)\,h\,\mathrm{Hz/G}\mu_0.\end{aligned} \tag{1.11}$$

[3] Note the inverted sign for the nuclear reduced matrix element compared to [101] to account for the selected μ_I sign convention, consistent with [111].

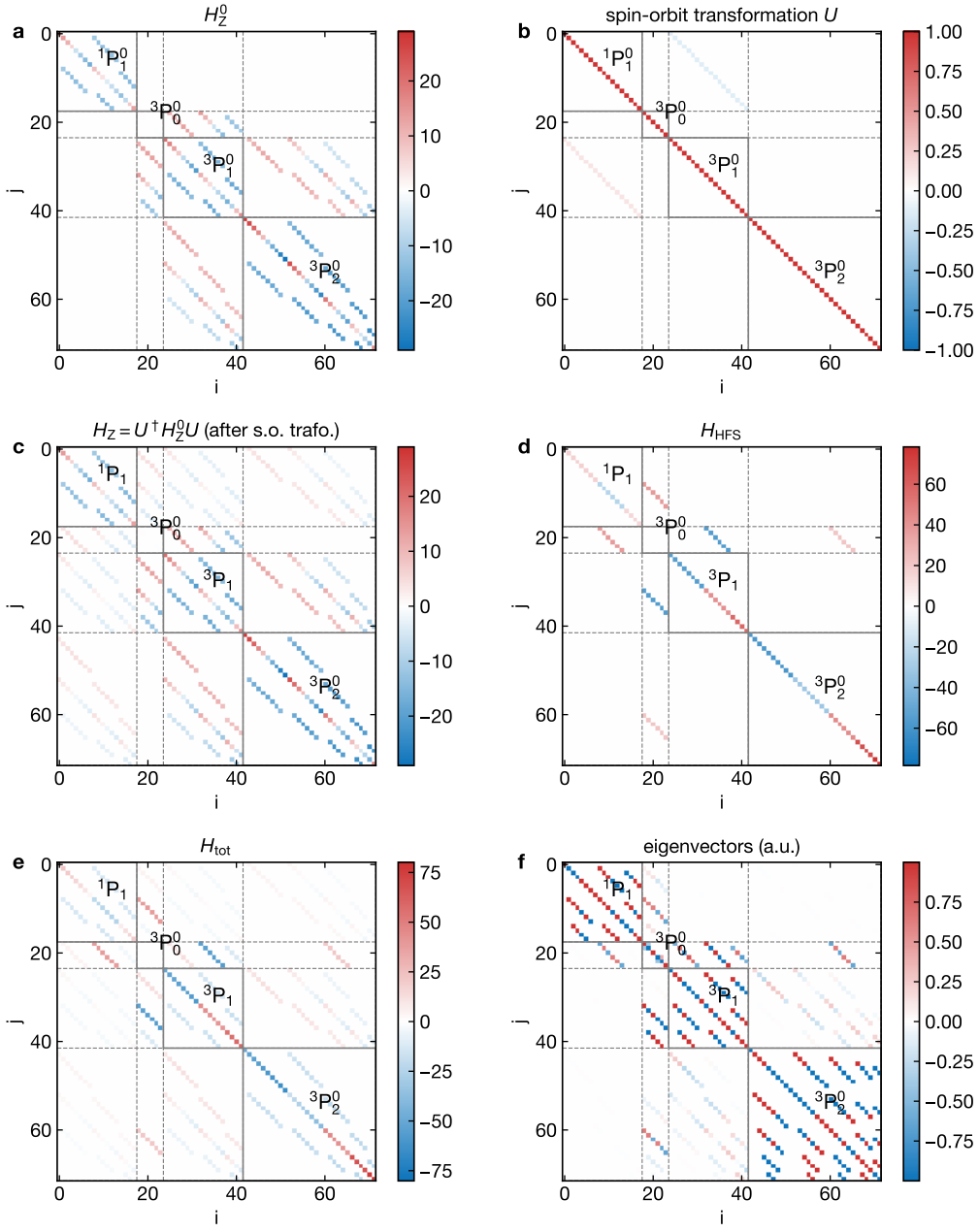

Figure 1.3 – Hyperfine and Zeeman Hamiltonians including spin-orbit, hyperfine and Zeeman cross coupling in the (6s6p) state manifold of ^{173}Yb (see Section 1.2). The Hamiltonians are in the basis of the bare RS states (superscript zero) or in the intermediate coupling basis (no superscript). They are sorted by descending F and by descending m_F for every F. The matrix elements are in a.u. and for better contrast, we plot the square root of the amplitude. (a) Zeeman Hamiltonian ($B = 200\,\mathrm{G}$) in the bare RS basis. (b) Transformation U from bare RS basis into the intermediate coupling regime (mixing angle $\beta = -0.1295(6)$). (c) Zeeman Hamiltonian after basis transformation $H_z = U^\dagger H_z^0 U$. (d) Hyperfine coupling H_{HFS} up to quadrupole order within the (6s6p) states, and cross couplings set to $\alpha_0 = 1.432 \times 10^{-4}$, $\beta_0 = \alpha_0/100$, $\gamma_0 = \alpha_0/100$. (e) Total coupling Hamiltonian $H_{\mathrm{tot}} = H_z + H_{\mathrm{HFS}}$. (f) Eigenvectors of H_{tot} (a.u.).

In Figure 1.11, the Zeeman shift of the ground state is compared to the one of the clock state $^3P_0$ in ^{173}Yb which is of similar magnitude, carrying only a small differential shift (see Section 1.4). The weak magnetic sensitivity of the $J = 0$ clock states limits the application of many state preparation and detection techniques that are available for alkali atoms in the ground state and which are relying on strong Zeeman splitting or magnetic field gradients. However, it is beneficial for the realization of optical clock experiments, reducing the necessary amount of magnetic field stabilization [57].

Zeeman cross coupling The Zeeman Hamiltonian in Eq. (1.6) for bare RS states is diagonal in the magnetic quantum number m_F and the spin S. Consequently, magnetic fields can only couple states within the spin-triplet manifold. In particular, one finds a non-vanishing coupling between the clock state $^3P_0$ and $^3P_1^0$, as well as between $^3P_2$ and $^3P_1^0$ [see Fig. 1.3(a)]. It is responsible for the small quadratic Zeeman shift of the clock state, independent of the atomic isotope (see Section 1.4).

Again, we have to account for spin-orbit and electrostatic coupling between $^1P_1^0$ and $^3P_1^0$ by applying the transformation $H_z = U^\dagger H U$ [see Fig. 1.3(c)]. The state mixing leads to the intermediate-strength E1 decay channel of $^3P_1$ to the ground state, inherited from $^1P_1$, the so-called intercombination line. Effectively, the state mixing then also induces a small Zeeman coupling of the clock state with $^1P_1$ contributing to an enhanced strength of the clock transition at finite magnetic fields (see Section 1.4).

Hyperfine coupling

For bosonic isotopes of AEA, the inter-state coupling is entirely determined by spin-orbit and Zeeman coupling. Fermionic isotopes additionally possess a nuclear spin $I > 0$ and finite nuclear magnetic moment which can couple to the electron angular momentum J. This leads to a hyperfine structure on the GHz scale as well as hyperfine cross coupling between the states of a two-electron (nsnl) state manifold.

Up to quadrupole order, the hyperfine interaction Hamiltonian is given by [121]

$$H_{\mathrm{HFS}} = A\frac{\mathbf{I}\cdot\mathbf{J}}{\hbar^2} + B\frac{\frac{3}{\hbar^2}(\mathbf{I}\cdot\mathbf{J})^2 + \frac{3}{2\hbar}(\mathbf{I}\cdot\mathbf{J}) - I(I+1)J(J+1)}{2I(2I-1)J(2J-1)}, \tag{1.12}$$

where A specifies the strength of the magnetic-dipole coupling and B of the electric-dipole coupling. This follows from a multipole expansion of the relativistic hyperfine interaction Hamiltonian in the field potentials [101, 110]. The octopole term or higher coupling terms vanish for $I, J \leq 1$ and therefore for all states of ^{173}Yb that we use in the experiment. For ^{171}Yb, only the dipole term remains, since the quadrupole term is zero for $I, J \leq 1/2$.

The hyperfine coupling Hamiltonian is diagonal in the quantum numbers F and m_F associated with the total angular momentum $\mathbf{F} = \mathbf{I} + \mathbf{J}$. Considering only first order coupling of the electron magnetic moment with the nucleus, we obtain the diagonal elements of the hyperfine Hamiltonian:

$$\Delta_{\mathrm{HFS}} = A\frac{K}{2} + B\frac{\frac{3}{2}K(K+1) - 2I(I+1)J(J+1)}{2I(2I-1)2J(2J-1)} \tag{1.13}$$

with $K = F(F+1)-I(I+1)-J(J+1)$. This is a good approximation for the hyperfine structure (HFS) energy shift. The dipole and quadrupole coupling constants A and B can be determined spectroscopically and a collection of known values for experimentally relevant states in ^{173}Yb and ^{171}Yb is provided in Table A.1. The evaluated hyperfine shifts for all available F are indicated in Figs. A.2 to A.5.

Hyperfine cross coupling As with the Zeeman coupling, there can be finite (second-order) hyperfine coupling between the states of the two-electron (6s6p) manifold in ytterbium, mixing states of equal F and m_F (see Fig. 1.3(d) and Eq. (A.1) for the definition of the off-diagonal matrix elements). The consequences of the hyperfine cross-coupling are most dramatic for the clock state $^3\mathrm{P}_0$. To first order, it leads to a state mixing of the clock state with the intermediate coupling representations of $^1\mathrm{P}_1$ and $^3\mathrm{P}_1$, and with $^3\mathrm{P}_2^0$ [111, 122]:

$$|^3\mathrm{P}_0\rangle = |^3\mathrm{P}_0^0\rangle + \alpha_0|^3\mathrm{P}_1\rangle + \beta_0|^1\mathrm{P}_1\rangle + \gamma_0|^3\mathrm{P}_2\rangle \tag{1.14}$$

Once more, the state mixing with $J = 1$ states contributes to an enhanced Zeeman shift and decay rate of the clock state. As demonstrated in [101, 111, 112, 122], we can approximately relate the hyperfine coupling constants α_0, β_0 and γ_0 to experimentally measured hyperfine splittings in the singlet and triplet manifold using the Breit-Wills theory for the two-electron wave functions (see Appendix A). For ^{173}Yb, we find that, the dipole coupling α_0 with $^3\mathrm{P}_1$ is nearly two orders of magnitude larger than β_0 and γ_0, very similar to Strontium [111].

This allows us to extract a rather precise value of the $^3\mathrm{P}_1$ mixing angle $\alpha_0 \approx 1.45 \times 10^{-4}$ as well as a corse estimate of $\beta_0 \approx -6.4 \times 10^{-6}$ from the experimentally determined linear differential Zeeman shift of the clock transition and the theoretically predicted lifetime, via Eq. (1.47) and Eq. (1.45) in Section 1.4.

All couplings combined

To predict energy shifts for the (6s6p) states over a large range of magnetic fields, we diagonalize the total coupling Hamiltonian, that is, the sum $H_{\mathrm{tot}} = H_{\mathrm{HFS}} + U^\dagger H_Z^0 U$ of the hyperfine and Zeeman Hamiltonian in the intermediate coupling basis [see Fig. 1.3(e-f)]. The coupling constants α, β, α_0, A and B take the values specified above, whereas β_0 and γ_0 are expected to be strongly suppressed and set to zero.

The resulting spectrum for the $J > 0$ state $^3\mathrm{P}_1$ is shown in Fig. 1.4, for magnetic fields up to 500 G. The eigenenergies display the typical Breit-Rabi like behavior where the low-field linear Zeeman shift is governed by the hyperfine states which transform into fine-structure eigenstates at high fields. We also calculate the magnetic field and hyperfine splitting (Figs. A.2 to A.5) for $^1\mathrm{P}_1$ and $^3\mathrm{P}_2$, for (5d6s)$^3\mathrm{D}_1$ used in the repumping transition, and for (6s7s)$^3\mathrm{S}_1$ which provides the largest contribution to the ac polarizability of the clock state $^3\mathrm{P}_0$ in our state-dependent lattice at 670 nm (see Section 1.3.4).

For the states in the (6s6p) manifold, the included inter-state coupling leads to modifications of the energy shifts on the percent level. These need to be taken into account when a

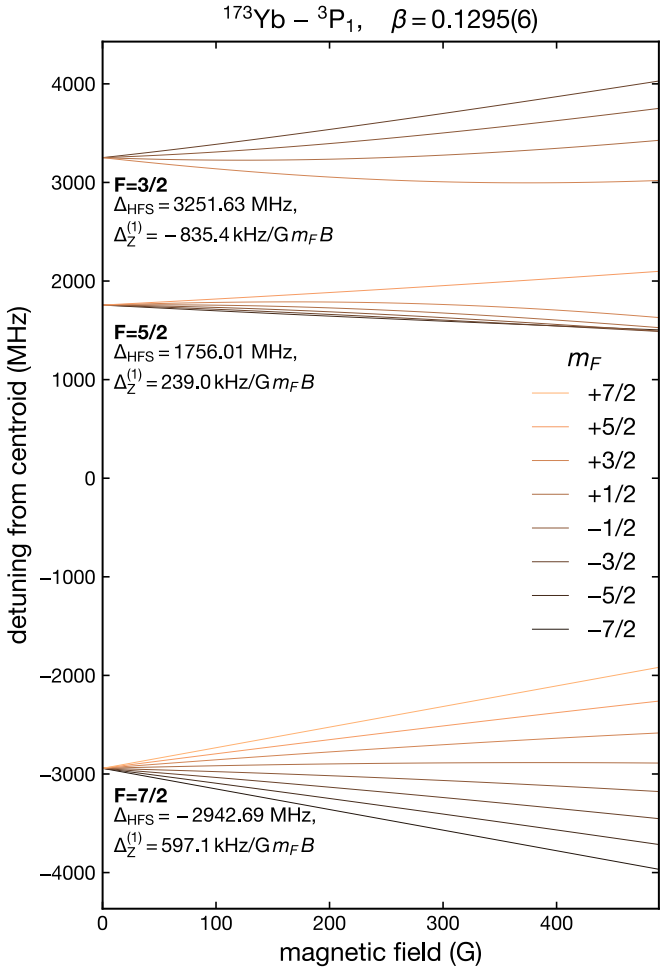

Figure 1.4 – Hyperfine structure and magnetic sensitivity of ^{173}Yb (6s6p)^{3}P$_1$. All frequency shifts are relative to the ^{1}S$_0 \rightarrow {}^3$P$_1$ transition centroid. Underlying hyperfine coupling constants are from [103]. Eigenspectrum from diagonalization of full coupling Hamiltonian for (6s6p) manifold with experimentally determined mixing angle $\beta = -0.1295(6)$ (see Section 1.2). The low-field linear Zeeman shift $\Delta_Z^{(1)}$ is calculated from Eq. (1.8).

quantitatively correct theoretical description is required, like for the calibration of the experimental magnetic field using the intercombination transition ^{1}S$_0 \rightarrow {}^3$P$_1$ in Section 3.2.1. Also, the Zeeman and hyperfine cross-couplings cause a qualitatively different behavior for the clock state ^{3}P$_0$ when compared to the uncoupled system or to the ground state, as explained in section Section 1.4.

1.3 Ytterbium coupling with light

The coupling between external light fields and atoms is one of the most important concepts for trapping neutral atoms and manipulating their internal degrees of freedom [123]. This is especially true for AEA where the two stable clock states do not possess orbital angular momentum

and therefore only exhibit very weak dependence on external magnetic fields (Section 1.2).

One can distinguish between two different regimes of atom-light interaction, the resonant or near-resonant and the far-detuned case. For example, we use near-resonant light for clock-line spectroscopy and spin-resolved absorption imaging. Far-off-resonant light is employed for creating optical traps for the degenerate Fermi gas, in particular, the orbital state-dependent lattice potential. An extensive treatment of the physics of atom light interactions is given in [121] and we follow the notation there. In the following section, we review the relevant concepts in view of the aforementioned applications. We derive expressions for the light-induced dipole shifts and scattering rates, taking into account the hyperfine structure of the transitions in fermionic ytterbium. We estimate not only the scalar, but also vectorial and tensorial light shifts for a broad range of wavelengths from a manifold of contributing atomic transitions. This allows us to make suitable wavelength selections for state-dependent dipole potentials that are selective either on the nuclear-spin Zeeman state or the electronic orbital.

1.3.1 Atom-light coupling

For our applications, the atom-light interactions can be treated on a semiclassical level where multiple quantized atomic levels are considered but the light is treated as a classical electric field. Assuming the dipole approximation where the wavelength λ is much larger than the size of the atom, the propagation direction of the light does not need to be considered and the electric field at the position of the atom can be written as

$$\mathbf{E}(t) = \mathbf{E}_0 \cos(\omega t + \phi) = \mathbf{E}^{(+)} e^{-i\omega t} + \mathbf{E}^{(-)} e^{+i\omega t} = 2\,\Re(\mathbf{E}^{(+)} e^{-i\omega t}) \tag{1.15}$$

with $\mathbf{E}_0$ along the light polarization vector and where $\mathbf{E}^{(\pm)} = \mathbf{E}_0 e^{\mp i\phi}/2$ are the conjugate components of the field in complex notation with positive (negative) frequency ω ($-\omega$).

1.3.2 Dipole potentials and radiative forces

When the incident light field frequency ω is far detuned from an atomic transition frequency ω_0, the atom-light interactions are dominated by a second-order, dispersive effect, the *ac Stark shift* or dynamic light shift. This is the case when the light detuning $\Delta = \omega - \omega_0$ becomes large compared to the transition rate $\Gamma = 2\pi\gamma$, with γ the natural linewidth for a closed transition. The external, oscillating light field induces an oscillating dipole moment $\mathbf{d}(t) = \mathbf{d}^{(+)} e^{-i\omega t} + \mathbf{d}^{(-)} e^{+i\omega t}$ in the atom which in turn interacts with the electric field via [121]

$$V_{\mathrm{ac}}(t) = -\mathbf{d}(t) \cdot \mathbf{E}(t)/2\,. \tag{1.16}$$

The dynamic polarizability $\alpha(\omega)$ around an atomic transition is frequency dependent and describes the strength of the induced dipole for a given external field through $\mathbf{d}^{(+)} = \alpha(\omega)\mathbf{E}^{(+)}$.

The ac Stark shift can then be written as

$$V_{\mathrm{ac}}(t) = -\left[\alpha(\omega)\mathbf{E}^{(+)} e^{-i\omega t} + \alpha^*(\omega)\mathbf{E}^{(-)} e^{+i\omega t}\right]\left[\mathbf{E}^{(+)} e^{-i\omega t} + \mathbf{E}^{(-)} e^{+i\omega t}\right]/2 \tag{1.17}$$

In calculating the time-averaged interaction energy $V_{\mathrm{ac}} = \langle V_{\mathrm{ac}}(t) \rangle$ as a function of laser intensity $I = 2\epsilon_0 c |E^{(+)}|^2 = \epsilon_0 c |E|^2/2$, we neglect the physically irrelevant terms oscillating at twice the optical frequency and obtain

$$V_{\mathrm{ac}} = -\Re[\alpha(\omega)]\,|E^{(+)}|^2 = -\frac{1}{2\epsilon_0 c}\Re[\alpha(\omega)]\,I\,. \tag{1.18}$$

Thus, the generated light shift for an atomic state is proportional to the real part of the dynamic polarizability and the light intensity.

Dipole forces

If the light intensity, and thereby the light shift, is varied spatially, one can create a conservative force proportional to the gradient of the intensity:

$$\mathbf{F}(\mathbf{r}) = \nabla V_{\mathrm{ac}}(\mathbf{r}) = \frac{1}{2\epsilon_0 c}\Re[\alpha(\omega)]\,\nabla I\,. \tag{1.19}$$

This force can restore a particle position to points of maximum or minimum intensity, depending on the sign of the polarizability α (see Fig. 1.5). It provides the trapping mechanism for optical dipole traps and lattices [123].

Light scattering

In addition to the conservative dipole force, there is a dissipative part of the dipole atom-light interaction that is tied to dipole oscillations out of phase with the incident light. This leads to a light power [123]

$$P_{\mathrm{sc}} = \langle \dot{\mathbf{d}}(t)\mathbf{E}(t) \rangle = \frac{\omega}{\epsilon_0 c}\,\Im\left[\alpha(\omega)\right] I \tag{1.20}$$

being absorbed by the atom and spontaneously reemitted into the light field. Considering an incoming stream of photons with energy $\hbar\omega$, the resulting scattering rate is given by

$$\Gamma_{\mathrm{sc}} = \frac{P_{\mathrm{sc}}}{\hbar\omega} = \frac{1}{\hbar\epsilon_0 c}\,\Im\left[\alpha(\omega)\right] I\,. \tag{1.21}$$

Compared to the dipole force in Eq. (1.19), the radiation pressure is still proportional to the light intensity but scales with the imaginary part of the polarizability.

Through scattering of photons, the atom can pick up quantized recoil momenta $p_{\mathrm{rec}} = \hbar k$ and associated recoil energy

$$E_{\mathrm{rec}} = \frac{\hbar^2 k^2}{2m} \tag{1.22}$$

with $k = 2\pi/\lambda$ the light field wavenumber and m the mass of the atom. For weak confinements, this can lead to a gain in kinetic energy and heating. When the incident light field frequency ω is close to an atomic transition frequency ω_0, the light atom interactions are dominated by this resonant scattering of photons. Optical traps that are based on radiation pressure can capture thermal atoms. In the context of ultracold gases experiments, such traps are mainly used for magneto-optical trapping and Zeeman slowing. The photon recoils and light-assisted collisions typically limit the final achievable temperature in these traps to the μK regime [123].

1.3.3 Dipole polarizability

While Eqs. (1.18) and (1.21) for the light shift and scattering rate in terms of the polarizability are general for any detuning and saturation of an atomic transition, the dynamic polarizability $\alpha(\omega)$ of an atomic state depends on the specific electronic state structure.

Far-detuned dipole potentials

If the light frequency ω is close to a atomic transition of frequency ω_{fi} between states $|i\rangle$ and $|f\rangle$, the generated light shifts and scattering properties for the connected states are dominated by this transition. Effectively, the system can then be described as a simplified two-level system. Furthermore, typical optical dipole traps and lattices operate in the limit of large detuning compared to the linewidth ($\Delta_{\mathrm{fi}} = \omega - \omega_{fi} \gg \Gamma_{\mathrm{fi}}$) and low saturation of the transition. The real and imaginary part of the polarizability of state $|i\rangle$ are then given by [121, 123]

$$\begin{aligned} \Re[\alpha_{fi}(\omega)] &= \frac{2\omega_{fi}}{\hbar(\omega_{fi}^2 - \omega^2)} |\langle i|\hat{\epsilon}\cdot\mathbf{d}|f\rangle|^2 \\ \Im[\alpha_{fi}(\omega)] &= \frac{2\omega_{fi}^2\omega^3}{3\pi c^3\hbar^2\epsilon_0(\omega_{fi}^2 - \omega^2)^2} |\langle i|\hat{\epsilon}\cdot\mathbf{d}|f\rangle|^4 \end{aligned} \tag{1.23}$$

where $\langle i|\hat{\epsilon}\cdot\mathbf{d}|f\rangle$ is the dipole matrix element connecting the initial and final state through light of polarization $\hat{\epsilon}$. In practice, the dipole matrix element is often easiest inferred from an experimentally determined transition strength Γ_{fi} by means of [121]

$$\Gamma_{fi} = \frac{\omega_{fi}^3}{3\pi\epsilon_0\hbar c^3} |\langle i|\hat{\epsilon}\cdot\mathbf{d}|f\rangle|^2 . \tag{1.24}$$

Finally, evaluating the light shift in Eq. (1.18) and the scattering rate in Eq. (1.21) as a function of detuning and transition strength leads to the well-known expressions

$$\begin{aligned} V_{\mathrm{ac}}^{fi} &= -\frac{3\pi c^2}{2\omega_{fi}^3}\left(\frac{\Gamma_{fi}}{\Delta_{fi}} + \frac{\Gamma_{fi}}{\omega_{fi}+\omega}\right) I \quad \text{and} \\ \Gamma_{\mathrm{sc}}^{fi} &= \frac{3\pi c^2}{2\hbar\omega_{fi}^3}\left(\frac{\omega}{\omega_{fi}}\right)^3\left(\frac{\Gamma_{fi}}{\Delta_{fi}} + \frac{\Gamma_{fi}}{\omega_{fi}+\omega}\right)^2 I . \end{aligned} \tag{1.25}$$

For detunings $\Delta_{fi} \ll \omega_{fi}$ (rotating-wave approximation), only the terms $V_{\mathrm{ac}} \propto 1/\Delta_{fi}$ and $\Gamma_{\mathrm{sc}} \propto 1/\Delta_{fi}^2$ remain. Consequently, red-detuned light with $\Delta_{fi} < 0$ will lead to an attractive potential for the energetically lower-lying state while the energetically higher-lying state sees the inverse, repulsive potential, and vice versa for blue detuned light with $\Delta_{fi} > 0$.

The simple scaling relation between dipole and radiative force

$$\frac{V_{\mathrm{ac}}}{\Gamma_{\mathrm{sc}}} = \hbar\frac{\Delta}{\Gamma} \tag{1.26}$$

is the main principle underlying the experimental operation of far-detuned trapping potentials. Although the absorptive part of the dipole interaction always causes residual photon scattering,

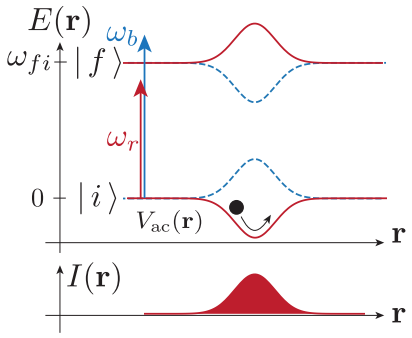

Figure 1.5 – Schematic of spatially dependent light shifts in a two-level system. Red-detuned (blue-detuned) light ω_r (ω_b) induces attractive (repulsive) potential for the lower lying state and vice versa for the excited state. The intensity distribution $I(\mathbf{r})$ has a Gaussian profile and traps the $|i\rangle$ state in the intensity maximum for red-detuned light.

the relative strength of the conservative dipole force increases with the detuning. So, at least for a two-level atom, the ultimate performance of a dipole trap is only limited by the available laser power.

Multi-level systems

In "real" atomic systems, the two-level picture can be a good approximation in the vicinity of a strong dipole-allowed resonance. However, to obtain the polarizability for an arbitrary laser wavelength and state $|i\rangle$, optical transitions to all final states $|f\rangle$ with a significant coupling strength have to be considered. This is especially important for many-electron systems like AEA with a large number of available transitions and a resolvable hyperfine substructure of the transitions for near-resonant detunings. In the following, we will focus on the light shift, and the real part of α only. In general, the estimation of scattering rates in a multi-level atom requires the use of rate or master equations to account for optical pumping between different levels of the magnetic substructure. Also, one needs to account for interference between the fields radiated on the different transitions [121, 124].

As a result of second-order time-independent perturbation theory in the atom field interaction, the resulting energy shift of a state $|i\rangle$ is just a sum over the ac Stark shift contributions from all available transitions $V_{\mathrm{ac}} = \sum_{f\neq i} V_{\mathrm{ac}}^{fi}$. This state sum can be incorporated into the total polarizability of a multi-level system as $\alpha(\omega) = \sum_{f\neq i} \alpha_{fi}(\omega)$ [121].

Obviously, for a given atomic state and wavelength, individual light shift contributions can have different sign and cancel each other. This can lead to a reduced or even vanishing total light shift for one electronic state compared to another state that lies in a different transition manifold. This is the central idea behind our implementation of a monochromatic orbital state-dependent lattice, as explained in Section 2.

Hyperfine structure and angular-momentum degeneracy

In order to treat the angular momentum degeneracy and the non-spherical nature of the m_F sublevels in the hyperfine structure, the scalar polarizability $\alpha(\omega)$ needs to be generalized to a tensor $\alpha_{\mu\nu}(\omega)$. The light polarization is still included in the field vector $E_\mu^{(+)}$ while the anisotropy of the atomic angular momentum states is captured in the tensor $\alpha_{\mu\nu}$. This tensor can couple field and atom anisotropically such that the induced dipole vector becomes

$$d_\mu^{(+)} = \alpha_{\mu\nu}(\omega) E_\nu^{(+)}$$

and the light shift can be calculated as [121]

$$V_{\mathrm{ac}} = -d_\mu^{(+)} E_\mu^{(-)}/2 - d_\mu^{(-)} E_\mu^{(+)}/2 = -\Re[\alpha_{\mu\nu}] E_\mu^{(-)} E_\nu^{(+)} \tag{1.27}$$

with the real part of the polarizability tensor

$$\Re[\alpha_{\mu\nu}(\omega)] = \sum_{f\neq i} \frac{2\omega_{fi}}{\hbar(\omega_{fi}^2 - \omega^2)} \langle i|d_\mu|f\rangle\langle f|d_\nu|i\rangle\,. \tag{1.28}$$

In the case of hyperfine states, we put $|i\rangle = |F\, m_F\rangle$ and $|f\rangle = |F'\, m_F'\rangle$ and the index f runs over the F' and m_F' quantum numbers. We choose the magnetic quantization axis along the z axis ($\hat{z}$). Finally, one can split the rank-2 polarizability tensor into its irreducible scalar, vector and tensor components and carry out the summation[4] in Eq. (1.27) for the total light shift to arrive at:

$$\begin{aligned} V_{\mathrm{ac}}(F, m_F, \omega) = &-\alpha^{(0)}(F,\omega)\,|E^{(+)}|^2 \\ &-\alpha^{(1)}(F,\omega)\,(i\mathbf{E}^{(-)}\times\mathbf{E}^{(+)})_z\,\frac{m_F}{F} \\ &-\alpha^{(2)}(F,\omega)\,\frac{(3|E_z^{(+)}|^2 - |E^{(+)}|^2)}{2}\,\frac{3m_F^2 - F(F+1)}{F(2F-1)} \end{aligned} \tag{1.29}$$

where the scalar, vector and tensor polarizabilities are defined independent of m_F as [121]:

$$\begin{aligned} \alpha^{(0)}(F,\omega) &= \sum_{F'} \frac{2}{3}\frac{\omega_{F'F}}{\hbar(\omega_{F'F}^2 - \omega^2)} \left|\langle F|\mathbf{d}|F'\rangle\right|^2 \\ \alpha^{(1)}(F,\omega) &= \sum_{F'} (-1)^{F'+F+1}\sqrt{\frac{6F(2F+1)}{F+1}} \begin{Bmatrix} 1 & 1 & 1 \\ F & F & F' \end{Bmatrix} \frac{\omega_{F'F}}{\hbar(\omega_{F'F}^2 - \omega^2)} \left|\langle F|\mathbf{d}|F'\rangle\right|^2 \\ \alpha^{(2)}(F,\omega) &= \sum_{F'} (-1)^{F'+F}\sqrt{\frac{40F(2F+1)(2F-1)}{3(F+1)(2F+3)}} \begin{Bmatrix} 1 & 1 & 2 \\ F & F & F' \end{Bmatrix} \frac{\omega_{F'F}}{\hbar(\omega_{F'F}^2 - \omega^2)} \left|\langle F|\mathbf{d}|F'\rangle\right|^2 . \end{aligned} \tag{1.30}$$

Here, $\langle F|\mathbf{d}|F'\rangle$ are the reduced matrix elements and $\omega_{F'F}$ are the transition frequencies between $|F\rangle$ and $|F'\rangle$.

[4] For a step-by-step derivation and formal justification of the polarizability tensor, see [121].

Scalar, vector and tensor shifts in the experiment Instead of using complex field amplitudes in Eq. (1.29), we can formulate the total light shift in terms of laser polarization and intensity. This clarifies, which components of the polarizability become relevant in the experiment. Assuming a laser beam of intensity $I = 2\epsilon_0 c|E^{(+)}|^2$ propagating along the unit vector $\hat{k}$, a degree of circular polarization[5] q ($q = \pm 1$ for right (left) circular and $q = 0$ for linear polarized light) and a polarization vector $\hat{\epsilon}$, then

$$\begin{aligned} V_{\mathrm{ac}}(F, m_F, \omega) = -\frac{I}{2\epsilon_0 c}\Big[&\alpha^{(0)}(F,\omega) \\ &+ \alpha^{(1)}(F,\omega)\, q\, (\hat{k}\cdot\hat{z})\, \frac{m_F}{F} \\ &+ \alpha^{(2)}(F,\omega)\, \frac{3|\hat{\epsilon}_z|^2 - 1}{2}\, \frac{3m_F^2 - F(F+1)}{F(2F-1)}\Big]. \end{aligned} \tag{1.31}$$

All the components of the light shift are proportional to the laser light intensity and can act as conservative forces on the atom. However, the scalar light shift only depends on the orbital and angular momentum quantum numbers, while the vector and tensor light shifts also depend on the nuclear Zeeman state m_F. The vector light shift only occurs for circularly polarized light along the quantization axis (σ^+ and σ^- light) and is proportional to m_F. This generates an energy shift equivalent to a linear Zeeman shift, generating an effective magnetic field. The tensor shift, depends on the absolute value of m_F only, and can be mapped to a dc electric field. It becomes maximal for a linear polarization vector oriented along the quantization axis. A thorough discussion of the dynamical ac Stark shift in the presence of multiple laser beams and arbitrary polarization in the context of atomic clock physics with AEA is given in [124].

1.3.4 Ytterbium light shifts from transition data

In our experiments, we make use of the scalar as well as the vector and tensor components of the light shift. The non-scalar components can be useful for creating m_F-dependent optical potentials and gradients. For example, for the spin-resolved detection of ground-state atoms, we employ an optical Stern-Gerlach (OSG) technique on the ${}^1\mathrm{S}_0 \rightarrow {}^3\mathrm{P}_1$ transition, using an m_F-dependent potential gradient (see Section 3.6.2). In our optical lattices, the trapping potential mainly originates from the scalar polarizability. This avoids resolving the m_F substructure, such that spin dynamics in the clock states are not disturbed by the trapping potential. In particular, this preserves the SU(N) symmetry of interacting Hamiltonians implemented with fermionic ytterbium.

In the following, we want to estimate the dynamical ac Stark shift for the three lowest-lying states of ^{173}Yb, namely the ground state ${}^1\mathrm{S}_0$, the metastable clock state ${}^3\mathrm{P}_0$, and ${}^3\mathrm{P}_1$. To evaluate the total light shift in Eq. (1.29), we need to know all available transition frequencies and the associated transition strength, given by the dipole matrix elements $\langle F|\mathbf{d}|F'\rangle$ between the hyperfine states $|F\rangle$ and $|F'\rangle$.

[5] The degree of circular polarization q for a beam along $\hat{z}$ is defined as in [124] for an arbitrary, normalized polarization (Stones) vector $\hat{\epsilon} = e^{i\phi}(\hat{x} - \eta\, i\hat{y})/\sqrt{1+\eta^2}$ as $q = 2\eta/(1+\eta^2)$ and the degree of linear polarization as $l = \sqrt{1-q^2}$.

For an accurate prediction of the polarizability of the low-lying states of AEA, relativistic many-body perturbation theory (MBPT) and configuration interaction methods (CI) can be employed to construct an effective Hamiltonian for the two valence electrons and solve for the eigenenergies and dipole matrix elements [125–128]. In [125], the ab initio calculation is further refined with experimental transition data to match the measured magic wavelength $\lambda_m = 759.35(2)\,\mathrm{nm}$ [129] of ^{174}Yb and thereby also improve the prediction of other magic wavelengths.

However, for a large range of wavelengths, most of the relevant transitions from the states $^1\mathrm{S}_0$, $^3\mathrm{P}_0$ and $^3\mathrm{P}_1$ go into states that are well approximated by LS coupling eigenstates. Thus, we can get a reasonable approximation for the polarizabilities by only using measured state energies and transition or spontaneous decay rates Γ between presumed fine-structure eigenstates $|J\rangle \equiv |LSJ\rangle$: Since the dipole operator couples only to the electron position, we can decompose the hyperfine reduced matrix element $\langle F|\mathbf{d}|F'\rangle \equiv \langle JIF|\mathbf{d}|J'IF'\rangle$ into its electronic and nuclear component [121]

$$\langle F|\mathbf{d}|F'\rangle = \langle J|\mathbf{d}|J'\rangle(-1)^{F'+J+I+1}\sqrt{(2J+1)(2F'+1)}\begin{Bmatrix} J & J' & 1 \\ F' & F & I \end{Bmatrix}. \tag{1.32}$$

Now, the unknown electronic reduced matrix element $\langle J_g|\mathbf{d}|J_e\rangle$ can be related to a measured spontaneous decay rate $\Gamma_{J_eJ_g}$ from the higher-lying fine-structure state[6] $|J_e\rangle$ to $|J_g\rangle$ and the according transition frequency ω_{ge} via [121]

$$\Gamma_{J_eJ_g} = \frac{\omega^3_{J_eJ_g}}{3\pi\epsilon_0\hbar c^3}\frac{2J_g+1}{2J_e+1}|\langle J_g|\mathbf{d}|J_e\rangle|^2. \tag{1.33}$$

Obviously, the larger the decay rate of the transition, the stronger the reduced dipole matrix element, and the larger the contribution to the polarizability of the atom at wavelengths far away from the transition. In Table B.1, we give a collection of significant transitions starting from the states $^1\mathrm{S}_0$, $^3\mathrm{P}_0$, $^3\mathrm{P}_1$ in the visible to near-IR wavelength range. The given decay rates Γ are inferred from measured state life times τ and theoretically estimated branching ratio β into the desired state (see Appendix B.1).

Clock state light shifts

For the realization of orbital state-dependent and -independent optical potentials, a precise knowledge of the ac Stark shifts for the two ytterbium clock states is required (see Chapter 2). The clock states belong to different electronic spin manifolds, namely the spin singlet ($S = 0$) and triplet ($S = 1$) manifold. Therefore, they are subject to a different set of optical dipole transitions, always connecting states of different parity.

In the visible to near-IR range of wavelengths that we use for optical trapping, the dominant transitions for the ground state atoms are mostly to the excited odd-parity $^1\mathrm{P}_1$ states in the singlet manifold and the $(6s6p)^3\mathrm{P}_1$ state in the triplet manifold. Also, one must consider

[6] Note that the order of states in the reduced matrix elements is important and $|\langle J'|\mathbf{d}|J\rangle|^2 = \frac{2J+1}{2J'+1}|\langle J|\mathbf{d}|J'\rangle|^2$ (analogously for F) [121].

coupling to the odd-parity state $(\mathrm{Xe})4f^{13}5d6s^2(7/2,5/2)_{J=1}$ with an electronic core excitation from the $4f$ subshell, energetically close to the $(6s6p)^1P_1$ state [125].

In contrast, the metastable clock state $^3P_0$ is influenced by transitions to even-parity states in the triplet manifold. In the visible to near-IR range, the main contributions are from the 1389 nm transition to $(6s5d)^3D_1$ and the 649 nm transition to $(6s7s)^3S_1$.

The total ac Stark shift for the two clock states calculated from the transition collection in Table B.1 and Eq. (1.31) is shown in Figure 1.6 for a large range of wavelengths.

Scalar light shift In Figure 1.6(a), the dominant scalar contribution to the light shift, from our LS coupling calculation, is compared to the ab initio calculations by Dzuba et al. [125, 128]. For the ground state, we find very good agreement with the data from [125] for wavelengths above the 556 nm transition to $^3P_1$, that is, for the wavelengths used in our trapping potentials. However, for $^3P_0$, our estimates show a systematic positive offset to the CI+MBPT predictions. Generally, for smaller wavelengths the density of transitions increases. This limits the expected accuracy of the theoretical CI+MBPT predictions and of our LS coupling estimate due to increased Coulomb mixing with core-excited states [125]. Wavelengths that are sufficiently far from poles in the polarizability and in the photon scattering rate can be used for optical trapping. The scalar light shift for the two clock states scales in a qualitatively different way with the wavelength and we can identify several distinct wavelengths with special trapping properties. This is also the underlying mechanism for the orbital state-dependent lattice at 670 nm, where $^3P_0$ atoms experience a deeper potential compared to the $^1S_0$ atoms (see Section 2.2).

Vector and tensor shifts In Figures 1.6(b–e), we show the estimated (maximum) vector and tensor light shift, normalized to the scalar shift, for σ and π light, respectively. In contrast to the bosonic ^{174}Yb with $F = 0$, the fermionic isotope ^{173}Yb with $F = 5/2$ in the clock states experiences finite vector and tensor shifts. Yet, if the light detuning is large compared to the hyperfine splitting of the transitions, these shifts are heavily suppressed for electronically scalar states ($J = 0$), due to cancellations in the sum over the hyperfine substructure in Eq. (1.30) [57, 111]. For the wavelengths and polarizations used in our trapping potentials (see Fig. 3.5), they do not exceed a relative strength of 10^{-6} compared to the scalar light shift, neither for $^1S_0$ nor for $^3P_0$. In practice, minimization of the vector and tensor shift can be accomplished by an appropriate choice of polarization and beam geometry. In the context of modern 3D lattice clock experiments, the vector shift is avoided by using purely linear polarized light and the tensor shift can be adjusted to cancel the scalar shift by detuning from the magic lattice wavelength limiting the systematic clock shifts to the 10^{-18} level [56].

Nuclear Zeeman state-dependent optical potentials When the light detuning is chosen close to the hyperfine structure of a transition, and the laser linewidth allows to resolve these shifts, the vector and tensor shifts can become the dominant contributions to the overall ac Stark shift, even for the "scalar" clock states. For example, this is exploited in our technique for nuclear-spin-resolved detection of the ground state atoms, where different m_F components

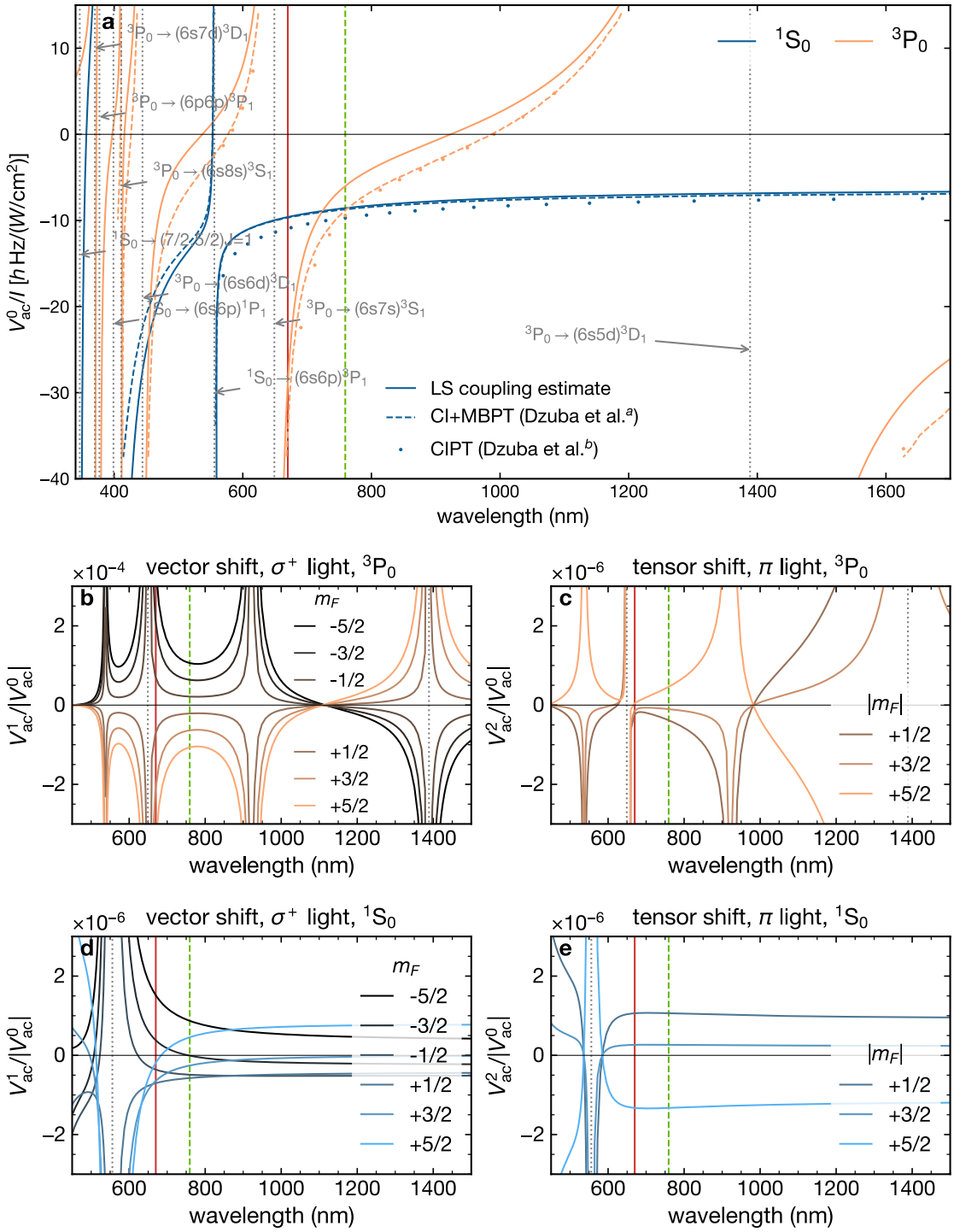

Figure 1.6 – Scalar, vector and tensor light shift of the clock states $^1S_0$ (blue) and $^3P_0$ (orange). (a) Scalar light shift V^0_{ac} in units of laser intensity from the LS coupling estimate (solid lines) and from ab-initio CI+MBPT calculations [a][125] (dashed lines) and [b][128] (circles). The position of the relevant optical transitions from Table B.1 are marked by dotted lines. (b–c) Strongly suppressed vector (tensor) shift V^1_{ac} (V^2_{ac}) of $^3P_0$ for fully σ^+ (π) polarized light from LS coupling estimate, normalized to magnitude of scalar light shift. (d–e) Same for $^1S_0$. Experimentally determined magic wavelength 759.35(2) nm [129] and state-dependent lattice wavelength of 670 nm are marked by green dotted and red solid lines.

experience different forces from an optical potential gradient close to the 556 nm $^1S_0 \rightarrow {}^3P_1$ transition (see Section 3.6.2). The total light shifts for $^1S_0(m_F)$ in the vicinity of this transition are shown in Figure 1.7 for σ^+ and π polarized light. The three poles can be associated with

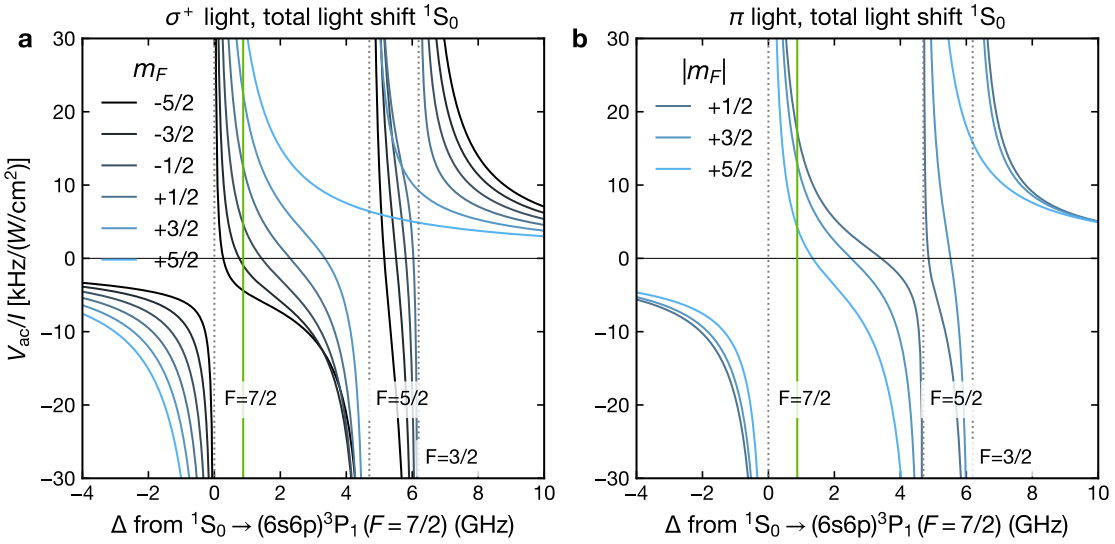

Figure 1.7 – Total ac Stark shift ΔV_{ac} estimate of the $^1S_0$ state induced by (a) σ^+-polarized or (b) π-polarized light of intensity I. The light detuning Δ is relative to the $^1S_0 \rightarrow {}^3P_1$(F=7/2) transition. The detuning of $\sim$0.9 GHz used for the optical Stern-Gerlach laser beam in our experiment is indicated by the green solid line.

the three hyperfine states (F=3/2, 5/2, 7/2) of $^3P_1$. The vector light shift induced by σ^+ polarized light is different for all m_F. The tensor light shift only splits different absolute values $|m_F|$. Note that the magnitude of the total light shift in the hyperfine splitting range surpasses the scalar shift in Fig. 1.6 by roughly a factor of 10^3.

Using spatially homogeneous potentials of 556 nm light, one can thus realize an artificial magnetic field for the ground-state atoms. Compared to real magnetic fields produced by electric coils, these optical potentials have the advantage of fast switching and modulation time scales enabling the realization of fast quench experiments and Floquet-type Hamiltonians. For example, a nuclear state-dependent potential to tune the differential Zeeman shift between the clock states has been proposed for the Floquet engineering of a Kondo model with tunable anisotropy [34]. The proposal suggests using wavelengths close to the 1389 nm (repumper) transition connecting $^3P_0$ to $^3D_1$. An estimate of the m_F-dependent light shifts in the hyperfine splitting range around this transition is given in Fig. B.1.

Light shifts for $^3P_1$

Using the transition data listed in Table B.1, we also estimate the polarizability for the state $^3P_1$. Being a non-scalar $J = 1$ state, it is connected to the ground state through the singly dipole forbidden intercombination line $^1S_0 \rightarrow {}^3P_1$. In our experiment, this transition is used resonantly for optical pumping of $^1S_0$ atoms into different m_F components in the presence of a deep 1064 nm optical dipole trap. It is also used to resonantly push out selected m_F states of a

degenerate Fermi gas from weakly confining dipole traps or optical lattices after evaporation. The resonant pumping or push light pulses happen on time scales of up to several 100 ms during which the atoms spend half of the time in the excited state $^3P_1$ and experience the associated light shift as an additional trapping potential.

In Figure 1.8, we show the scalar polarizability obtained from the *LS* coupling estimate and compare it to a recent CI+MBPT calculation [128]. Close to the 556 nm intercombination transition, the atoms in $^3P_1$ obviously experience the opposite light shift compared to the ground-state atoms. For higher wavelengths, the main contributions come from the transitions to $(6s7s)^3S_1$, $(6s5d)^3D_2$ and $(6s5d)^3D_1$, leading to a scalar polarizability that resembles the one of $^3P_0$ for a large visible to near IR wavelength range. We note that at the wavelength of 1064 nm of our crossed optical dipole trap, the scalar light shift for $^3P_1$ is close to a zero crossing and the atoms experience a reduced effective trapping potential during the optical pumping. In contrast to the clock states, the state $^3P_1$ with $J = 1$ has non-negligible vector and tensor polarizabilities which leads to a strong dependence of the trap depth on m_F (see Figure 1.8(b-c) for $F = 7/2$ and Figure B.3 for the other hyperfine levels).

1.3.5 Relative optical transition strengths

The optical transitions we use in the experiment have vastly different linewidths. The broad transition $^1S_0 \rightarrow {}^1P_1$ in the electronic singlet manifold of ^{173}Yb is fully allowed by dipole selection rules and has a linewidth in the MHz range. The intercombination line $^1S_0 \rightarrow {}^3P_1$ is singly forbidden by the spin-conservation selection rule and only inherits a small transition strength through spin-orbit coupling of $^3P_1$ with $^1P_1$. The transition from the ground state to the clock state $^3P_0$ is doubly forbidden by additionally breaking the J angular momentum selection rule and its finite linewidth is only due to hyperfine coupling with the aforementioned states.

As a consequence of the inherited line structure from $^1P_1$, the three transitions all exhibit the same relative dipole coupling strength between different m_F states of a hyperfine manifold and for a given field polarization. In Eq. (1.32) and (1.33), we have obtained expressions for the reduced matrix element between hyperfine and fine-structure coupling eigenstates. This allows us to predict the dipole transition strength between hyperfine levels from a measured decay rate in the fine structure. However, the reduced dipole element neglects the magnetic substructure of the hyperfine states[7]. The full dipole matrix element between two states $|F\, m_F\rangle$ and $|F'\, m_F'\rangle$, according to the Wigner-Eckart theorem, can be decomposed into a reduced matrix element and an associated Clebsch-Gordan coefficient carrying the angular momentum dependence of the transition [121]:

$$\begin{aligned}\langle F\, m_F|\mathbf{d}|F'\, m_F'\rangle &= \langle F|\mathbf{d}|F'\rangle(-1)^{F'-F+m_F'-m_F}\sqrt{\frac{2F+1}{2F'+1}}\left\langle F'\, m_F'|F\, m_F; 1\, -q\right\rangle \\ &= \langle F|\mathbf{d}|F'\rangle(-1)^{F'-m_F-1}\sqrt{2F+1}\begin{pmatrix} F & 1 & F' \\ m_F & q & -m_F'\end{pmatrix}.\end{aligned} \tag{1.34}$$

[7] In the polarizability calculation above, the magnetic substructure of the hyperfine states has been taken care of explicitly by decomposing the polarizability tensor into its irreducible components.

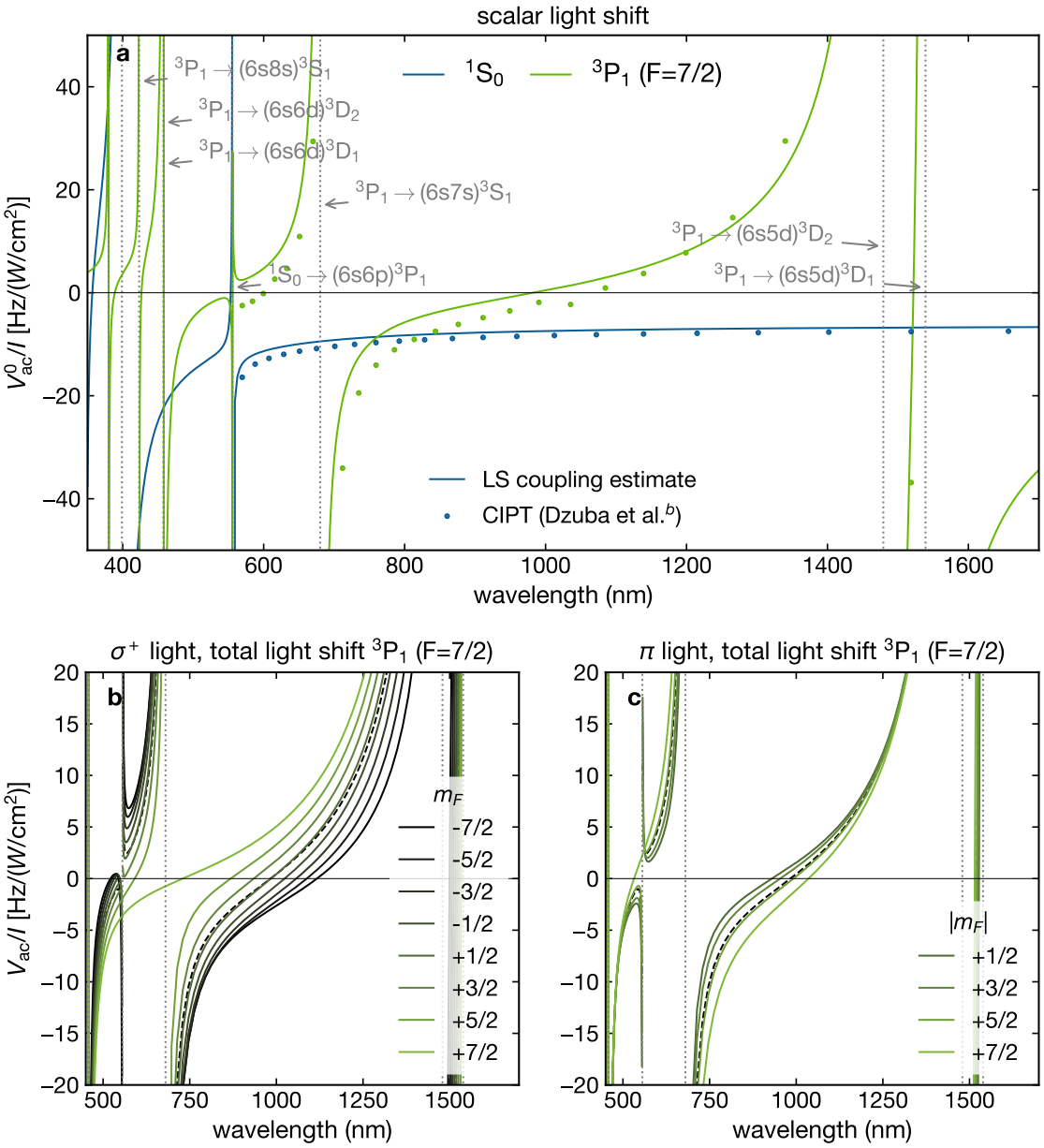

Figure 1.8 – Light shifts of $^3P_1$ (F=7/2) (green) and $^1S_0$ (blue). (a) Scalar light shift V_{ac}^0 in units of laser intensity from the LS coupling estimate (solid lines) and from an ab-initio CI+MBPT calculation [b][128] (circles). The position of the relevant optical transitions from Table B.1 are marked by dotted lines. (b–c) Total light shift V_{ac} including vector and tensor shift of $^3P_0$ from LS coupling estimate for fully (b) σ^+ and (c) π polarized light. The vector light shift included in (b) becomes comparable to the scalar shift for the displayed wavelengths. For different hyperfine states, see Figure B.3.

The Clebsch-Gordan coefficient[8] $\left\langle F'\, m_F' | F\, m_F; 1\, -q \right\rangle$ includes the degree of circular light polarization q introduced in Eq. (1.31) with $q = \pm 1$ for σ^+ (σ^-) and $q = 0$ for π-polarized light. Further using Eq. (1.32), the hyperfine reduced matrix element can be decomposed into the fine-structure reduced matrix element and an additional angular momentum coupling part, yielding $\langle F\, m_F | \mathbf{d} | F'\, m_F' \rangle = \langle J | \mathbf{d} | J' \rangle\, C_{ss'}$ with

$$C_{ss'} = (-1)^{J+I-m_F} \sqrt{(2F+1)(2F'+1)(2J+1)} \begin{Bmatrix} J & J' & 1 \\ F' & F & I \end{Bmatrix} \begin{pmatrix} F & 1 & F' \\ m_F & q & -m_F' \end{pmatrix}, \tag{1.35}$$

the relative transition strength between different magnetic hyperfine states.

Figure 1.9 shows these relative transition strengths between the m_F levels of different hyperfine states for the transitions from $^1\mathrm{S}_0$ to $^1\mathrm{P}_1$, $^3\mathrm{P}_1$ and $^3\mathrm{P}_0$. Not only do they obey the selection rule $m_F' = m_F + q$ for coupling with the light angular momentum but they also vary within a hyperfine transition manifold. When resonantly addressing these transitions, the appropriate Clebsch-Gordan coefficients must be considered in the evaluation of the dipole coupling. For example, the Rabi frequency of the coherent state preparation of the clock state is proportional to $C_{ss'}$. An additional magnetic field can serve to provide a differential Zeeman shift between the two electronic states (see Figure 1.9). If the splitting becomes larger than the transition linewidth, the transitions between different m_F can be selectively addressed.

1.3.6 Coherent coupling

By studying the coupling of far-detuned light with a multi-level atomic system, we have obtained expressions for the dynamic light shift over a large wavelength range. Now, we want to introduce the concept of saturated, coherent coupling of a two-level atomic system with resonant and near-resonant light, adopting the well-known dressed-state picture [121, 130, 131]. In our experiments, coherent control of an optical transition is particularly relevant in the context of clock line spectroscopy and coherent preparation of superposition states of $^1\mathrm{S}_0$ and $^3\mathrm{P}_0$. Also, the dressed state picture is relevant for understanding the results in Chapter 6, where an effective interorbital exchange coupling in a state-dependent lattice is realized by means of a Rabi coupling on the clock transition.

Let's consider a two-level system of states $|g\rangle$ and $|e\rangle$ that is addressed by a monochromatic light field $\mathbf{E}$ of intensity $I = (\epsilon_0 c/2)|E|^2$ with detuning Δ from the transition frequency ω_{eg}. Within the rotating-wave approximation and neglecting the finite lifetime of the excited state, one finds that the Hamiltonian describing the coupled atom-light system is given by [121, 131]

$$H_{al} = \hbar \begin{bmatrix} 0 & \Omega_0/2 \\ \Omega_0/2 & -\Delta \end{bmatrix} \tag{1.36}$$

in the basis of the bare atomic eigenstates $|g\rangle$ and $|e\rangle$. The resonant Rabi frequency Ω_0 quantifies the strength of the resonant ($\Delta = 0$) coupling between the bare eigenstates and is deter-

[8] We have also given an alternative form using the Wigner-3j symbol.

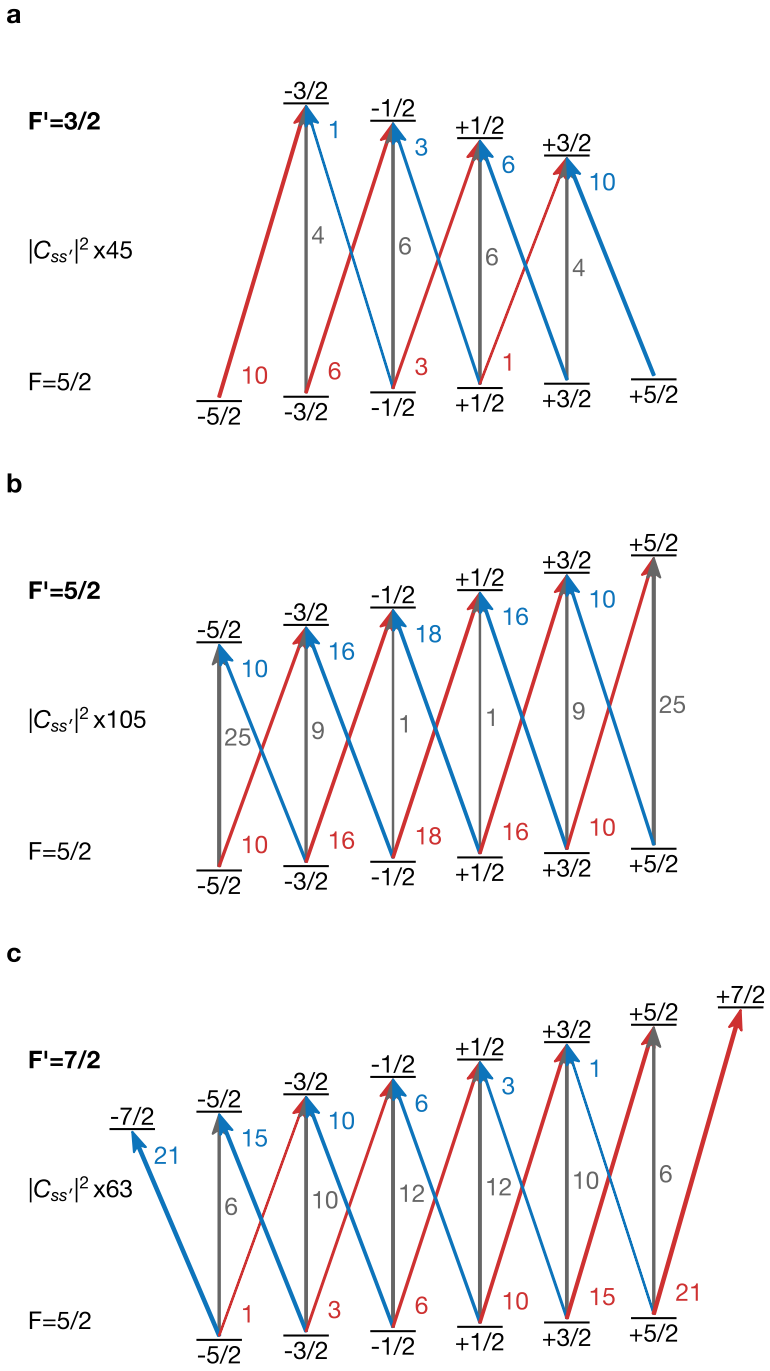

Figure 1.9 – Dependence of the dipole coupling strength on the hyperfine and magnetic substructure for an optical transition from ${}^1\mathrm{S}_0(F = 5/2)$ to ${}^1\mathrm{P}_1(F')$. The relative transition strengths $C_{ss'}$ (Clebsch-Gordan coefficients) are identical for transitions to ${}^3\mathrm{P}_0$ and ${}^3\mathrm{P}_1$ since their finite dipole coupling is caused only by spin-orbit and hyperfine coupling with ${}^1\mathrm{P}_1$. The same structure is obtained for ${}^3\mathrm{P}_0 \rightarrow {}^3\mathrm{S}_1$ and ${}^3\mathrm{P}_0 \rightarrow {}^3\mathrm{D}_1$. Possible transitions are indicated by arrows connecting different m_F sates, driven by σ^+, σ^- or π polarized light. A possible breaking of the degeneracy by a differential linear Zeeman shift is illustrated with the m_F-dependent level shifts (not to scale).

mined by the dipole matrix element $\mathbf{d}_{eg} = \langle g|\mathbf{d}|e\rangle$ and the light intensity I:

$$\hbar\Omega_0 = -\mathbf{d}_{\mathrm{eg}} \cdot \mathbf{E} = -\langle g|\mathbf{d}\cdot\hat{\epsilon}|e\rangle \sqrt{\frac{2I}{\epsilon_0 c}}\,. \tag{1.37}$$

For a transition between two hyperfine states in ytterbium, the dipole matrix element can be obtained from Eq. (1.34).

The atom-light coupled eigenstates of the system are called the *dressed states*

$$|+\rangle = \sin(\theta)|g\rangle + \cos(\theta)|e\rangle \quad \text{and} \quad |-\rangle = \cos(\theta)|g\rangle - \sin(\theta)|e\rangle\,. \tag{1.38}$$

and describe the combined system of the atom coupled with the light field, with a mixing angle (Stückelberg angle) of $\theta = \arctan(-\Omega_0/\Delta)/2$. The associated eigenenergies are

$$E_\pm = \frac{\hbar}{2}\left(\pm\Omega - \Delta\right), \tag{1.39}$$

using the expression

$$\Omega = \sqrt{\Omega_0^2 + \Delta^2} \tag{1.40}$$

for the generalized Rabi frequency.

When a system is prepared in $|g\rangle$ or $|e\rangle$ and resonant light is suddenly switched on, the out-of-equilibrium system is projected onto the new dressed-state eigenbasis and will oscillate between $|g\rangle$ and $|e\rangle$ with frequency Ω_0. For finite detuning, the oscillation frequency is increased to Ω, and the modulation depth, i.e., the excitation fraction P_e from $|g\rangle$ to $|e\rangle$, decreases to Ω_0^2/Ω^2.

Using light pulses of controlled length Δt and phase one can create arbitrary superpositions between the bare atomic states. In particular, resonant π pulses with $\Delta t = \pi/\Omega_0$ can transfer a state population from $|g\rangle$ to $|e\rangle$ and inversely. In our experiment, this is used in the context of fast, coherent clock line spectroscopy and for the preparation and detection of many-body states with orbital excitations. When the detuning of a π pulse is scanned around the resonance while maintaining the pulse length, a "Rabi line shape"

$$P_e(\Delta) = \frac{\pi}{2}\,\mathrm{sinc}^2\left(\frac{\pi}{2}\frac{\sqrt{\Omega_0^2+\Delta^2}}{\Omega_0}\right) \tag{1.41}$$

emerges where the width of the central peak scales linearly with the resonant Rabi frequency and with the square root of the intensity. Power broadening the width of the clock transition line shape can help in compensating the differential light shifts in the orbital state-dependent lattice (see 3.5.2).

Alternatively, if the light intensity or detuning are ramped on slowly enough, the system always follows the evolving eigenspectrum. Then, one can transfer atoms adiabatically from the bare atomic states into the dressed states (see Chapter 6) or even from $|g\rangle$ to $|e\rangle$ and back, in a so called adiabatic rapid passage (see Sec. 3.5.2).

1.3.7 Decoherence and saturation

The discussion above is only valid in the limit of very short times compared to the excited-state lifetime of the two-level system or the coherence time of the laser. In other words, the Rabi frequency needs to be larger than the linewidth of the transition ($\Omega \gg \Gamma$) and the laser linewidth. This is a very good approximation for the clock transition addressed by our small-linewidth laser. Moderate light intensities are enough to reach Rabi frequencies exceeding both the laser linewidth and the natural transition linewidth by orders of magnitude.

When this approximation is not valid, decoherence from spontaneous decay or limited laser linewidth need to be accounted for in semi-classical rate equations, the so-called optical Bloch equations, or in an appropriate master equation [121]. One consequence is that the Rabi oscillations are damped, and for times $t \gg 1/\Gamma$ the excited-state population (essentially the line shape of the transition) converges to a steady-state value of [121]

$$P_e = \frac{1}{2}\frac{s}{1+s} \tag{1.42}$$

with the saturation parameter

$$s = \frac{2\Omega^2}{\Gamma^2}\frac{1}{1+(2\Delta/\Gamma)^2}\,. \tag{1.43}$$

The saturation effect quantifies the nonlinear response of the atom to strong fields. In terms of laser intensity, one typically defines the saturation intensity I_{sat} such that $I/I_{\mathrm{sat}} = 2\Omega^2/\Gamma^2$, and for a two-level system [121]:

$$I_{\mathrm{sat}} = \frac{\hbar\omega_{eg}\Gamma}{2\pi\sigma_0}\,, \tag{1.44}$$

with $\sigma_0 = 3\lambda^2/2\pi$ the resonant photon scattering cross section.

In the limit of small laser intensity $I \ll I_{\mathrm{sat}}$ ($s \ll 1$), Eq. (1.42) and the photon scattering rate $\Gamma_{\mathrm{sc}} = \Gamma P_e$ take the form of a simple Lorentzian with Γ the FWHM. However, when the optical transition is strongly saturated ($s \gg 1$), the scattering rate is bounded by $\Gamma/2$ and $P_e = 1/2$ which leads to so-called power broadening of the transition.

In our experiment, this mechanism is exploited in the saturated absorption imaging technique on the ${}^1\mathrm{S}_0 \rightarrow {}^1\mathrm{P}_1$ transition. In order to ensure the transparency of dense atomic samples, the imaging beam intensity is increased into the saturated regime where the scattering cross section of the atoms is reduced (see Section 3.6.1).

1.4 The metastable orbital and the clock transition

Ytterbium, as an AEA, possesses the typical separation of the lowest-lying eigenstates into electronic spin triplet and spin singlet states (see Fig. 1.2). Along with this separation goes the existence of the metastable excited state $|e\rangle \equiv (6s6p)|^3\mathrm{P}_0\rangle$ with angular momentum $J = 0$ in the triplet manifold. The only lower-lying state is the true ground state $|g\rangle \equiv |^1\mathrm{S}_0\rangle$ which is part of the spin-singlet manifold and also has $J = 0$.

By dipole selection rules, the transition of $^3P_0$ to $^1S_0$ is doubly forbidden. This is the reason for the very narrow linewidth of the so-called clock transition and makes ytterbium, and similarly strontium, ideal candidates for optical clock experiments [95]. Precise measurements of the fermionic clock frequency have yielded

- $\nu_{\text{clock}}^{174} = 518.294\,025\,309\,217\,8(9)$ THz for ^{174}Yb [132],
- $\nu_{\text{clock}}^{173} = 518.294\,576\,845\,268\,(10)$ THz for ^{173}Yb [133] and
- $\nu_{\text{clock}}^{171} = 518.295\,836\,590\,863\,59\,(31)$ THz for ^{171}Yb [134].

Using core-excited states as alternative clock states has recently been proposed [128]. These transitions have a strong dependence on the fine-structure constants and the gravitational potential and could allow to study physics beyond the Standard Model via studying the non-linearity of King's plot.

In combination with a narrow-linewidth laser, spectroscopy of the $^1S_0 \rightarrow {}^3P_0$ clock transition allows us to probe the eigenspectrum of our atomic samples with good spectral resolution, including interacting many-body systems (see Section 4.3). For the fermionic isotopes, there is a small but finite linear differential Zeeman shift between the two clock states which even allows for nuclear-spin-selective spectroscopy and state preparation.

Moreover, a direct consequence of the near-vanishing dipole matrix element between the clock states is the long lifetime of the excited state $^3P_0$, exceeding most other relevant timescales in our experiments. We then have two stable electronic orbitals $|g\rangle$ and $|e\rangle$ with identical nuclear magnetic spin structure at our disposal (see Fig. 1.1). This makes it straightforward to implement a monochromatic state-dependent lattice potentials for the two "species" (see Chapter 2). The differential Zeeman shift between the metastable states is an essential ingredient for the recently discovered orbital Feshbach resonance [90, 91] in ^{173}Yb, providing the mixing mechanism for the two interorbital interaction channels.

In the following, we will review the mechanisms that induce a finite lifetime of $^3P_0$ in the fermionic and bosonic isotopes of ytterbium as well as the origin and magnitude of the differential magnetic Zeeman shift between the clock states.

Coupling to the clock states

As demonstrated in Section 1.2, the two valence electrons are in a $6s^2$ configuration for $^1S_0$, whereas the excited state $^3P_0$ is in a $6s6p$ configuration and is subject to hyperfine and Zeeman coupling with other states of this manifold. The bare RS state $^3P_0^0$ undergoes state mixing with $^3P_1$ and $^1P_1$ which enables an E1 decay channel to the ground state [111].

Hyperfine quenching While all isotopes experience Zeeman coupling at finite magnetic field, only the fermionic isotopes undergo hyperfine coupling and inherit a zero-field lifetime of [112]

$$\tau(^3P_0, B=0) = \left(\frac{\nu(^3P_1 - {}^1S_0)}{\nu(^3P_0 - {}^1S_0)}\right)^3 \left(\frac{\beta}{\alpha_0\beta + \beta_0\alpha}\right)^2 \tau(^3P_1). \tag{1.45}$$

The hyperfine and intermediate coupling and the associated mixing angles have been defined in Section 1.2.1 and Eq. (1.14). Note that although the hyperfine mixing α_0 with $^3\mathrm{P}_1$ is around two orders of magnitude larger than the mixing coefficient β_0 with $^1\mathrm{P}_1$, both couplings contribute significantly to the final lifetime. Lifetimes of 26 s ($\Gamma = 2\pi \times 6.1$ mHz) for ^{173}Yb and 23 s ($\Gamma = 2\pi \times 6.9$ mHz) for ^{171}Yb have been predicted from ab initio relativistic many-body atomic structure calculations, with an estimated uncertainty on the few-percent level [106].

Since both clock states are $J = 0$ states, they carry the same magnetic substructure. It is inherited by spin-orbit and hyperfine coupling from the transition $^1\mathrm{S}_0 \rightarrow {}^1\mathrm{P}_1$ and is shown in Fig. 1.9 for ^{173}Yb and $F = 5/2$. Choosing the appropriate light polarization and laser frequency, transitions between the different nuclear-spin states and orbitals can be driven coherently using a narrow-linewidth laser (Section 1.3.6). Experimentally, the strength of the clock transition can then be determined by measuring the frequency of coherent Rabi oscillations[9] in a non-interacting sample of spin-polarized atoms in an optical lattice (Section 4.3). The Rabi frequency is dependent on the nuclear-spin configuration and can be related to the dipole matrix element via Eq. (1.37). In the case of ^{173}Yb, a Rabi frequency consistent with the theoretical prediction within 10% has been obtained [97].

Zeeman quenching The bosonic isotopes with $I = 0$, including ^{174}Yb, are not subject to hyperfine coupling and therefore the clock state has a vanishing decay rate and Rabi coupling to the ground state. However, one can effectively "quench" the transitions by applying large external magnetic fields, as has been proposed by Taichenachev et al. [135] and demonstrated experimentally in [129]. The B-field dependent Rabi coupling $\Omega(B)$ to the clock state results from a small admixture ξ of $|^3\mathrm{P}_1\rangle$ to the bare clock state $|^3\mathrm{P}_0^0\rangle$ through Zeeman coupling. The off-diagonal matrix elements of the Zeeman Hamiltonian in Eq. (1.6) lead to a coupling $\hbar\Omega_Z = \langle {}^3\mathrm{P}_0|H_z|{}^3\mathrm{P}_1\rangle$ and a mixing angle $\xi = \Omega_Z/\Delta({}^3\mathrm{P}_1 - {}^3\mathrm{P}_0)$ to first order. A light field can then couple to the quenched clock transition with the overall Rabi frequency

$$\Omega(B) = \xi\,\Omega_L = \Omega_L\Omega_Z(B)/\Delta({}^3\mathrm{P}_1 - {}^3\mathrm{P}_0) = \alpha\,B\sqrt{I_0} \tag{1.46}$$

where $\Omega_L = \langle {}^1\mathrm{S}_0|\mathbf{d}\cdot\mathbf{E}|{}^3\mathrm{P}_1\rangle/\hbar$ is the regular Rabi coupling to the intercombination line with light intensity I_0. The Rabi coupling for ^{174}Yb has been evaluated to $\alpha = 0.966$ Hz/(G$\sqrt{\mathrm{W/cm^2}}$) [129, 135], leading, e.g., to a considerable coupling of around 60 Hz for an accessible external field of 100 G and 1 W/cm^2 clock laser intensity.

For fermionic isotopes, the Zeeman quenching of the clock transition also plays a role for large magnetic fields and exists as a separate coupling mechanism besides the hyperfine quenching. Using the formalism in Section 1.2.1, we can simultaneously treat the hyperfine an Zeeman coupling to evaluate the associated mixing angles for the clock state of ^{173}Yb. Taking into account the Zeeman degeneracies and appropriate selection rules for the light

[9] The clock transition Rabi coupling can be connected to the Rabi coupling with $^3\mathrm{P}_1$, yielding $\Omega({}^3\mathrm{P}_0, B = 0) = \frac{\alpha_0\beta+\beta_0\alpha}{\beta}\Omega({}^3\mathrm{P}_1)$. In principle, another straightforward approach would be to measure the lifetime of excited-state atoms in a deep 3D optical lattice. In practice however, the natural clock state lifetime can be difficult to disentangle from the decay rate induced by repumping to the ground state via two-photon transitions, driven by the 760 nm optical lattice light.

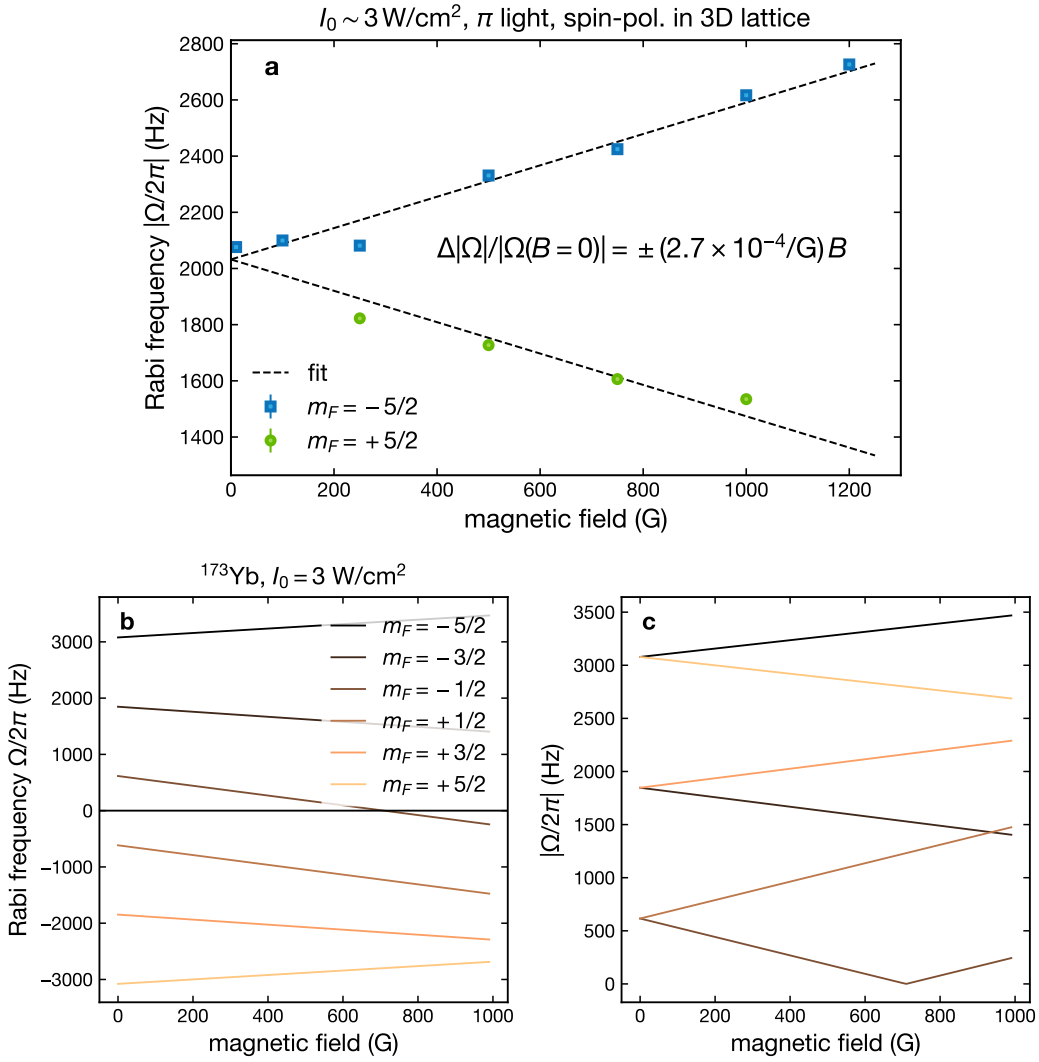

Figure 1.10 – Magnetic field quenching of the clock transition. (a) Experimentally measured absolute Rabi frequencies for spin-polarized ^{173}Yb atoms addressed on the clock transition $^1S_0 \rightarrow {}^3P_0$ (π polarization, intensity $I_0 \approx 3\,\mathrm{mW/cm^2}$) in a deep 3D magic-wavelength lattice. The two nuclear spin components $m_F = -5/2$ (squares) and $m_F = +5/2$ (circles) experience different Rabi coupling strength for finite external magnetic fields. The dashed line is a linear fit with inverse slope for the two m_F. (b) Theoretically expected $\Omega(B)$ (including sign) and (c) absolute value $|\Omega|$ from the 6s6p Zeeman and hyperfine coupling model in Section 1.2.1.

coupling Hamiltonian, Eq. (1.34), we evaluate the Rabi coupling to different m_F components of $^3\mathrm{P}_0$ at finite magnetic fields [see Fig. 1.10 (b–c)]. It turns out that for π transitions, the Rabi frequencies Ω from the hyperfine coupling ($B = 0$) have opposite sign for opposing m_F, whereas the Zeeman induced frequency component has the same sign for both m_F. Looking at the absolute value $|\Omega|$, the Rabi coupling to $m_F = +5/2$ is enhanced linearly with increasing magnetic field, whereas the opposite, decreasing slope is found for $m_F = +5/2$.

We have verified this behavior experimentally by performing clock line spectroscopy on separate, spin-polarized fermionic samples in a deep 3D optical lattice [see Fig. 1.10(a)]. The linear Zeeman quenching of the Rabi rate with inverse slope for the two magnetic components $m_F = \mp 5/2$ is reproduced and we extract a slope of $\Delta|\Omega|/|\Omega(B=0)| = \pm(2.7 \times 10^{-4}/\mathrm{G})B$. Note, that different slopes are found theoretically for the other m_F components and that the total Rabi coupling for the $m_F = -1/2$ state can be nulled for magnetic fields below 1000 G.

Differential clock-line shift

Although the magnetic sensitivity for both clock states with $J = 0$ is strongly reduced, there is a finite differential Zeeman shift between the two, arising from the same coupling mechanisms that causes the finite strength of the clock transition (Fig. 1.11). There are two types of differential Zeeman shifts for AEA, a linear m_F-dependent and an m_F-independent quadratic part. The linear shift is an important parameter for the interorbital interactions, even causing a magnetic Feshbach-resonance at experimentally accessible magnetic fields [90, 91] and it ultimately enters in the uncertainty of the experimentally determined interorbital scattering lengths. The differential Zeeman shift can also be an interesting tuning knob in the context of two-orbital many-body systems, leading to an effective chemical potential difference for different m_F states. Large differential shifts can inhibit exothermic spin-exchanging dynamics between nuclear spin product states [59] and small, time-dependent Zeeman shifts can potentially be used to explore anisotropic Kondo models [34].

Linear shift The linear shift depends on the m_F quantum number is induced through hyperfine coupling. From the Zeeman and hyperfine coupling model in Section 1.2.1, one obtains the perturbative result for the differential Landé factor [111, 112]:

$$\begin{aligned}\delta g &\approx -2(\alpha\alpha_0 - \beta\beta_0)\frac{\langle {}^3\mathrm{P}_0^0, m_F|H_Z^0|{}^3\mathrm{P}_1, F = I, m_F\rangle}{\mu_0 m_F B} \\ &= -\sqrt{\frac{8}{3I(I+1)}}(\alpha\alpha_0 - \beta\beta_0)(g_S - g_L)\end{aligned} \tag{1.47}$$

neglecting terms of order α_0^2, β_0^2, γ_0^2 and higher. The differential Landé factor δg is added to the nuclear Landé factor g_I [Eq. (1.4)] for the $^3\mathrm{P}_0$ atoms and the linear differential Zeeman

shift $\delta(B)$ between $|e\rangle$ and $|g\rangle$ atoms in m_F' and m_F becomes

$$\begin{aligned}\delta(B) &\equiv \Delta_Z^{(1)}(|e\rangle) - \Delta_Z^{(1)}(|g\rangle) \\ &= \left[\underbrace{(-\delta g - g_I)}_{\equiv g_e} m_F' - \underbrace{(-g_I)}_{\equiv g_g} m_F\right] \mu_0 B\end{aligned} \tag{1.48}$$

which reduces to $\delta(B) = -\delta g\, m_F \mu_0 B$ for $m_F = m_F'$.

We have determined the linear differential Zeeman shift by means of a spectroscopic differential measurement technique, described in Section 3.2.2. The measurement scheme is independent of the absolute value of the magnetic field and the quadratic Zeeman shift and only relies on the knowledge of the nuclear magnetic moment μ_I, which is the dominant contribution to the provided uncertainty. For ^{173}Yb, we have measured the differential Landé factor[10]

$$\delta g = -110.81(37)\, h\,\mathrm{Hz/G}\mu_0\,. \tag{1.49}$$

This differential shift, together with the theoretically predicted lifetime of the clock state, is used to determine the hyperfine mixing angles $\alpha_0, \beta_0, \gamma_0$ indicated in Fig. 1.11.

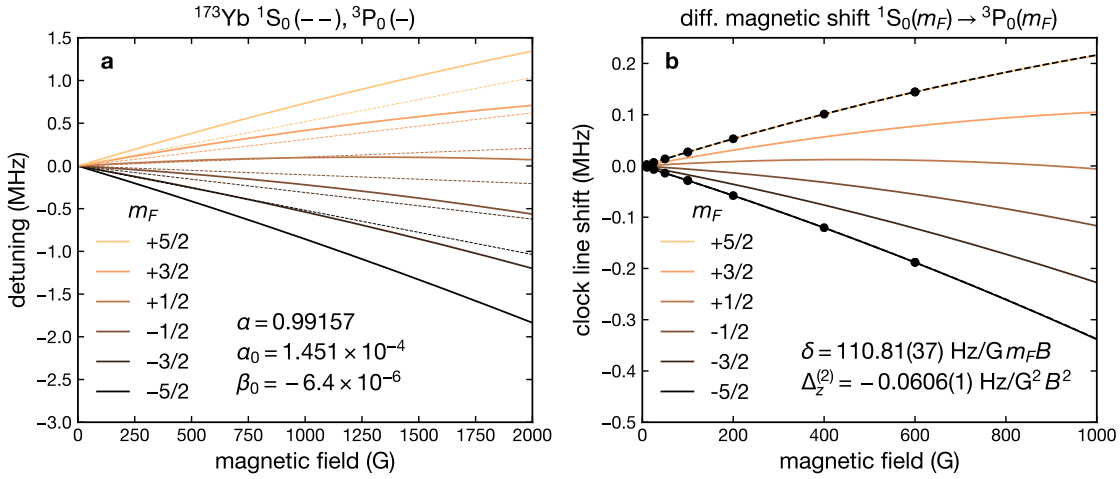

Figure 1.11 – (a) Total Zeeman shift of the ^{173}Yb clock states for all m_F from the (nsnp) coupling calculation in 1.2.1. The hyperfine coupling coefficients are extracted from a model fit of the measured δg and the theoretically expected ^{3}P$_0$ lifetime. (b) Differential magnetic shift of the clock transition ^{1}S$_0 \rightarrow {}^3$P$_0$ for π transitions between equal m_F. Comparison of the nsnp model data (solid lines) with the spectroscopy data (circles). A fit to the measurement data (dashed line) using the independently determined δg yields the quadratic shift $\Delta_Z^{(2)}$.

Quadratic shift The quadratic shift $\Delta_Z^{(2)}$ is due to Zeeman coupling of ^{3}P$_0$ with ^{3}P$_1$, present for both bosonic and fermionic isotopes and expected to be (largely) identical for all isotopes,

[10] It is comparable to the measured differential shifts in other AEA and isotopes: −108.4(4) h Hz/μ_0G for ^{87}Sr [111] and −191(7) h Hz/μ_0G for ^{171}Yb [136]. Consistent theoretical estimates using CI+MBPT methods are given in [137].

that is, also m_F independent[11] [111]. From the (nsnp) coupling model in Section 1.2, one obtains the perturbative result

$$\Delta_Z^{(2)} \approx -\alpha^2 \frac{\sum_{F'} |\langle {}^3\mathrm{P}_0^0, m_F | H_Z^0 | {}^3\mathrm{P}_1, F', m_F \rangle|^2}{\nu({}^3\mathrm{P}_1 - {}^3\mathrm{P}_0)} = -\alpha^2 \frac{2(g_S - g_L)^2 \mu_0^2}{3\,\nu({}^3\mathrm{P}_1 - {}^3\mathrm{P}_0)} B^2 \tag{1.50}$$

ignoring terms of order α_0, β_0, β^2 and higher [111]. We have verified that this approximation matches with the diagonalization of the full coupling Hamiltonian for ^{173}Yb on the 10^{-4} level for magnetic fields up to 1000 G.

Experimentally, we can extract the quadratic shift (and the magnetic field calibration) from clock spectroscopy at varying magnetic fields and for different m_F states by exploiting the known, independently measured linear differential shift. We find[12]

$$\Delta_Z^{(2)} = -0.0606(1)\mathrm{Hz/G}^2\,. \tag{1.51}$$

The total Zeeman shift for the ground and excited state as well as the total differential shifts are shown in Fig. 1.11(a). The calculated differential Zeeman shift is shown along with the measured spectroscopy data in Fig. 1.11(b).

1.5 Interaction properties

The suitability of ultracold atoms for the simulation of strongly correlated states of matter relies on the presence of interatomic interactions. The experimental results presented later in this thesis have their origin in the special nature of the interorbital interactions between the two clock states ($|g\rangle$ and $|e\rangle$) of ytterbium. In the following, we review the theoretical description of the low-energy scattering between AEA. We focus on the emergence of an extended SU(N) symmetry in the collisions between fermionic isotopes, as well as the spin-orbital exchange interaction that arises naturally from the presence of two interorbital scattering channels.

1.5.1 Low-energy scattering

In general, a full theoretical description of a two-body scattering process between two atoms is a non-trivial task. At high scattering energies and small interparticle distances, the wave functions can become distorted and the microscopic nature of the scattering potential needs to be taken into account. However, for the quantum degenerate samples typically prepared in ultracold atom experiments, strong simplifications can be made in the description of the scattering process. A detailed review on interatomic scattering, including the physics of Feshbach resonances, is provided in [40]. In most cases, ultracold atomic gases are very dilute, with an interparticle spacing that is large compared to the range of the scattering potential, the van

[11] For the fermionic isotopes, Boyd et al. predict an m_F^2 dependent shift that is suppressed on the 10^6 level [111].

[12] This is in reasonable agreement with $\Delta_Z^{(2)} = -0.06112(1)\mathrm{Hz/G}^2$ from the (nsnp) coupling calculation and consistent with the theoretically predicted value 0.062 Hz/G^2 [135] and previously measured values 0.066(4) Hz/G^2 [129] and 0.0612(10) Hz/G^2 [132] using ^{174}Yb.

der Waals length. Then, it is mostly sufficient to only consider binary elastic collisions. The interaction potential $V(\mathbf{r})$ depends on the interparticle separation $\mathbf{r}$ and in ultracold atomic gases, it typically is spherically symmetric. By expanding $V(r)$ into spherical harmonics and Legendre polynomials, it is straight-forward to show that in the low-energy limit (momentum $k \to 0$), the scattering amplitude

$$f = -\frac{1}{a^{-1} + ik} \tag{1.52}$$

is isotropic and depends only on a single parameter, the s-wave scattering length a. If required, finite energy dependence can be introduced to lowest order via the additional effective range parameter r_{eff} and the replacement $a^{-1} \mapsto a^{-1} - \frac{1}{2} r_{\text{eff}} k^2$ [40] (see Section 4.2). Knowledge of the actual radial dependence of $V(r)$ is therefore not required and in most cases, a is best determined experimentally. The Pauli exclusion principle also plays an essential role in the interactions: The spatial wavefunction describing the s-wave scattering is spherically symmetric. Thus, in contrast to identical bosons, two identical fermions cannot interact via s-wave collisions but only via odd partial waves, e.g., higher-energy p-wave collisions.

In the end, a simplified scattering potential can be introduced that contains only the scattering length a as a model parameter. It is found that the true finite-range potential can be replaced by the zero-range Fermi-Huang pseudopotential [138]

$$V(\mathbf{r}) = \frac{4\pi\hbar^2 a}{m} \delta_{\text{reg}}(\mathbf{r}), \tag{1.53}$$

yielding an identical scattering amplitude [Eq. (1.52)], with m the atomic mass. A regularized delta potential $\delta_{\text{reg}}(\mathbf{r}) = \delta(\mathbf{r}) \frac{\partial}{\partial r} r$ instead of a bare delta function increases the domain of the potential and can be required for the description of strong interactions. In particular, it supports a spectrum of bound molecular states in the presence of an external confinement [139]. Regularized contact interactions will be used in Chapter 4 for an accurate description of the strong interorbital on-site interaction in the optical lattice. In second quantization, the interaction Hamiltonian for multiple fermions can be written as [140]

$$\begin{aligned} H_{\text{int}} &= \frac{1}{2} \sum_{\sigma,\sigma'} \int \int \mathrm{d}^3 r \, \mathrm{d}^3 r' \, \hat{\psi}^\dagger_\sigma(\mathbf{r}) \hat{\psi}^\dagger_{\sigma'}(\mathbf{r}) \, V(\mathbf{r} - \mathbf{r}') \, \hat{\psi}_{\sigma'}(\mathbf{r}') \hat{\psi}_\sigma(\mathbf{r}') \\ &= \frac{4\pi\hbar^2 a}{m} \frac{1}{2} \sum_{\sigma,\sigma'} \int \mathrm{d}^3 r \, \hat{\psi}^\dagger_\sigma(\mathbf{r}) \hat{\psi}^\dagger_{\sigma'}(\mathbf{r}) \hat{\psi}_{\sigma'}(\mathbf{r}) \hat{\psi}_\sigma(\mathbf{r}) . \end{aligned} \tag{1.54}$$

σ, σ' denote possible internal degrees of freedom, e.g., the nuclear spin projection m_F, or the electronic orbital $|g\rangle$, $|e\rangle$. The fermionic creation (annihilation) operators for atomic wavefunctions at a position $\mathbf{r}$, in the internal state σ, are given as $\hat{\psi}^\dagger_\sigma$ ($\hat{\psi}_\sigma$). The fermionic anticommutation relations $\{\hat{\psi}, \hat{\psi}^\dagger\} = \delta_{\sigma\sigma'} \delta(\mathbf{r} - \mathbf{r}')$ ensure that fermions in identical internal states do not scatter. Inserting the set of localized Wannier functions into this expression, yields the familiar expression of the Hubbard on-site interactions in a lattice, Eq. (2.20).

Isotope	^{173}Yb	^{171}Yb	^{174}Yb
$a_{gg}(a_0)$	$199.4(2.1)^a$	$-2.8(3.6)^a$	$104.9(1.5)^a$
$a_{eg}^{+}(a_0)$	$1878(37)^b$	$225(13)^e$	n/a
$a_{eg}^{-}(a_0)$	$219.7(2.2)^b$	$355(6)^e$	n/a
$a_{ee}(a_0)$	$306(10)^d$	n/a	n/a
$\beta_{eg}^{\star}(\mathrm{cm}^3/\mathrm{s})$	$2.2(3)\times10^{-13\ b}$	$3(2)\times10^{-11\ c}$	n/a
$\beta_{eg}^{-}(\mathrm{cm}^3/\mathrm{s})$	$<3.0(1)\times10^{-15\ d}$	n/a	n/a
$\beta_{ee}(\mathrm{cm}^3/\mathrm{s})$	$2.2(6)\times10^{-11\ d}$	$5(3)\times10^{-11\ c}$	n/a

Table 1.1 – Collection of known *s*-wave scattering lengths a (units of Bohr radius a_0) and two-particle loss rate coefficients β for intra and interorbital scattering in ^{173}Yb, ^{171}Yb and ^{173}Yb. The values are from the measurements indicated by the superscripts ^{a} [100], ^{b} [99], ^{c} [141], ^{d} [59] and ^{e} [88]. For ^{173}Yb, β_{eg}^{-} for the orbital singlet state has been obtained in a 3D lattice experiment at an ambient field of 7 G, and $\beta_{eg}^{\star}$ gives an effective loss rate for a bulk system at the position of the Feshbach resonance.

1.5.2 Inelastic scattering

In addition to the elastic s-wave scattering discussed above, inelastic collisions can become relevant under certain conditions. Considering only two-body collisions, inelastic processes can occur when relaxation processes of internal degrees of freedom are available. Then, the internal energy is converted into kinetic energy of the atom pair, causing heating. If the kinetic energy surpasses the trap depth, particles can be lost from the trap. In our experiment, this is particularly relevant for collisions involving $|e\rangle$ atoms which carry electronic excitation energies.

A two-particle loss processes between atoms in different internal states σ and σ' can be captured by a rate equation [142, 143]

$$\dot{n}_\sigma(t) = -\beta_{\sigma\sigma'} n_\sigma(t) n_{\sigma'}(t) \tag{1.55}$$

with an associated two-body loss rate coefficient $\beta_{\sigma\sigma'}$. Here, n_σ and $n_{\sigma'}$ are real-space densities of the two state populations. Experimentally determined loss rate coefficients for the isotopes ^{173}Yb, ^{174}Yb and ^{171}Yb are summarized in Table 1.1. Note that the wavefunction symmetry is also relevant for the inelastic collisions. Thus, at low temperatures, only distinguishable fermions undergo lossy collisions. In Section 2.7, we study collision-induced losses between $|e\rangle$ atoms in different nuclear spin states, trapped in optical lattices of varying depth.

More loss processes become possible when additional particles are involved in a scattering process. For example, three-body recombination could underly the atoms loss observed along the spin-exchange dynamics of two-orbital mixtures in Chapter 5. Inelastic collisions with the high-vacuum background gas are strongly suppressed by the low vacuum pressure and quantified in Section 2.6.

1.5.3 Large-spin systems and SU(N)-symmetric interactions

Due to the quantum mechanical exchange interactions, the scattering potential between spinful fermions can depend on the total spin configuration of the atom pair [40, 144]. For example, this leads to the splitting of spin-singlet and triplet interaction potential in electronic spin-1/2 systems [40]. For fermionic systems of larger spin, like spinor gases or AEA, the treatment of the interactions needs to be generalized [58, 145]. The role of the spin is then typically taken by the total atomic angular momentum $F \geq 1/2$ and its projection m_F, labeling the eigenspectrum of the hyperfine interactions. In the special case of AEA in the two clock states with $J = 0$, the total atomic angular momentum $F = I$ is entirely determined by the nuclear spin $I \geq 1/2$. As we will see, this decoupling of nuclear and electronic angular momentum leads to an extended SU(N) symmetry of the interactions. For a comprehensive discussion of the symmetry properties involved in the scattering of AEA atoms, we refer to [58, 97].

Large-spin scattering

In general, F and m_F are good quantum numbers for free spin-F fermions, subject to SU(2) rotational symmetry of the spin. In collisions involving alkali atoms, at short interparticle distances, the hyperfine interactions become comparable to the exchange interaction and the SU(2) symmetry of the individual atom spin is broken. However, in the case of s-wave collisions, the combined angular momentum F_p of the atom pair and its projection m_{F_p} are still maintained. This is assured by the rotational invariance of the scattering potential: The total angular momentum must be conserved in the collision, and since the orbital angular momentum is zero for s-wave collisions, the internal spin part F_p must also be conserved. This additional SU(2) symmetry exists independently for every possible $F_p = 0, 2, ..., 2F - 1$, with F_p even to preserve the correct quantum statistics [144, 145]. Overall, the system is described by a SU(2)$^{N/2}$ symmetry, with $N \equiv 2F + 1$ and $N/2$ the number of available F_p. Every F_p is associated with a separate scattering channel with an independent scattering length a_{F_p}, leading to a generalized pseudo-potential interaction Hamiltonian [145]

$$V(\mathbf{r}) = \frac{4\pi\hbar^2}{m}\delta_{\text{reg}}(\mathbf{r})\sum_{F_p} a_{F_p}\mathcal{P}_{F_p}\,. \tag{1.56}$$

Here, $\mathcal{P}_{F_p}$ is the projector onto states with pair angular momentum F_p.

In practice, considering scattering between fermions in the same F but different m_F, the interference of multiple scattering channels leads to the population of different m_F states while preserving the pair projections m_{F_p} [see Fig. 1.12(a)]. Notably, coherent spin-oscillations have been observed in large-spin ($F = 9/2$) fermionic spinor gases of ^{40}K in optical lattices, exploring the entire manifold of m_F states [146–149].

The emergence of SU(N) symmetry in AEA

This is in stark contrast to the very strong suppression of spin-changing collisions in the clock states of AEA, including ytterbium, and can be explained by the emergence of an increased

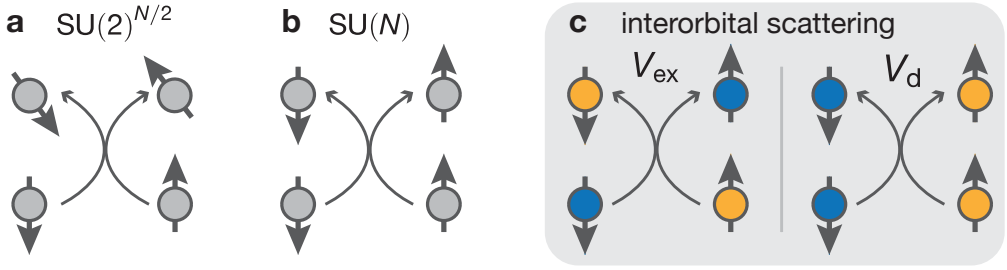

Figure 1.12 – Low-energy scattering of spinful fermions: (a) A spin-changing collision process between high-spin alkali atoms obeying an SU(2)$^{N/2}$ symmetry; with $N = 2F + 1$ and $F > 1/2$ the total atomic angular momentum. The pair angular momentum and projection F_p and m_{F_p} are preserved. (b) Enhanced SU(N) symmetry in AEA, preserving the individual F and m_F of the scattering partners. (c) Interorbital scattering between ^{1}S$_0$ and ^{3}P$_0$ atoms: an interorbital exchange (V_{ex}) and a direct interaction (V_d) process are available.

SU(N) symmetry of the interactions [58]. In AEA, the orbital angular momentum J of the ground state ^{1}S$_0$ is completely decoupled from the nuclear spin I, due to the total absence of hyperfine interactions. A residual admixture of the higher-lying states ^{3}P$_1$ and ^{1}P$_1$ with $J = 1$ to the excited clock state ^{3}P$_0$ is caused through hyperfine and spin orbit coupling (see Section 1.2). However, to leading order, also ^{3}P$_0$ exhibits vanishing hyperfine coupling [111]. The spin dependence of the interaction potential observed in alkali atoms is caused by the quantum exchange interaction of the orbital part of the wavefunction. Thus, the absence of orbital angular momentum in the AEA clock states also entails a spin-independence of the interactions [58]. Formally, the interaction Hamiltonian becomes invariant under SU(N) transformations with $N = 2F + 1$. That is, it commutes with all nuclear-spin permutation operators

$$\hat{S}_a^b = \int \mathrm{d}^3 r\, \hat{\psi}_a^\dagger(\mathbf{r})\hat{\psi}_b(\mathbf{r}) \tag{1.57}$$

acting on the spinors $\hat{\psi}_\sigma$ of dimension $2F+1$ ($\sigma = -F, ..., F$), and satisfying the SU(N) algebra $[\hat{S}_a^b, \hat{S}_c^d] = \delta_{bc}\hat{S}_a^d - \delta_{da}\hat{S}_c^b$ [58, 66]. A single interaction channel is then enough to describe the scattering between atoms in the same electronic orbital. In Eq. (1.56), the a_{F_p} is replaced by a single scattering length a.

For ^{173}Yb, ^{174}Yb and ^{171}Yb, available measurements for the s-wave scattering lengths are listed in Table 1.1. It includes values for both intraorbital (a_{gg} and a_{ee}) and interorbital (a_{eg}) scattering between the clock states ^{1}S$_0$ or ^{3}P$_0$. A collection of all intra- and interisotope ground-state scattering lengths is presented in [100]. Most of the measured values are repulsive and of intermediate strength. One exception is a_{gg} for ^{171}Yb which is nearly two orders of magnitude smaller than for ^{173}Yb. For example, this could prove useful in the experimental realization of the Kondo lattice model (see Section 2.8).

Absence of spin-changing collisions The influence of the nuclear spin on the interactions only enters through the Pauli exclusion principle. Spin-changing collisions are then prohibited, and along with F_p and m_{F_p}, also the nuclear spin F and projection m_F of the individual

scattering partners are preserved [see Fig. 1.12(b)]. This permits us to produce "tunable" SU($N \leq 2I+1$) symmetry groups by only populating subsets of the N available spins.

The microscopic origin of the decoupling between nuclear and electronic angular momentum for the two clock states is discussed in [58]: In the course of a collision, the free particles are coupled to molecular electronic state at short distances. The dominant molecular states have vanishing projections of the electronic angular momentum onto the molecular axis. Yet, very weak coupling to states of non-zero angular momentum (mainly $^3P_1$), results in spin-changing processes. By modeling the scattering phase evolution in the short-range potential, Gorshkov et al. predict a residual relative nuclear-spin dependence of the scattering length $\delta a/a$ (for ^{87}Sr). For ground-state collisions, $\delta a_{gg}/a_{gg} \sim 10^{-9}$ is extracted, compared to $\delta a_{ee}/a_{ee} \sim \delta a_{eg}/a_{eg} \sim 10^{-3}$ for scattering between $^3P_0$ atoms, or between $^1S_0$ and $^3P_0$ [58].

In the case of ^{173}Yb, we have verified that spin-changing processes are suppressed on experimentally relevant timescales. By holding a $^1S_0$ two-component spin mixture ($m_F = -5/2, +5/2$) in a harmonic trap, and monitoring the relative population of all m_F states, an upper limit $\delta a_{gg}/a_{gg} < 10^{-4}$ could be extracted [97] (see Fig. 1.13). The SU(N) symmetry

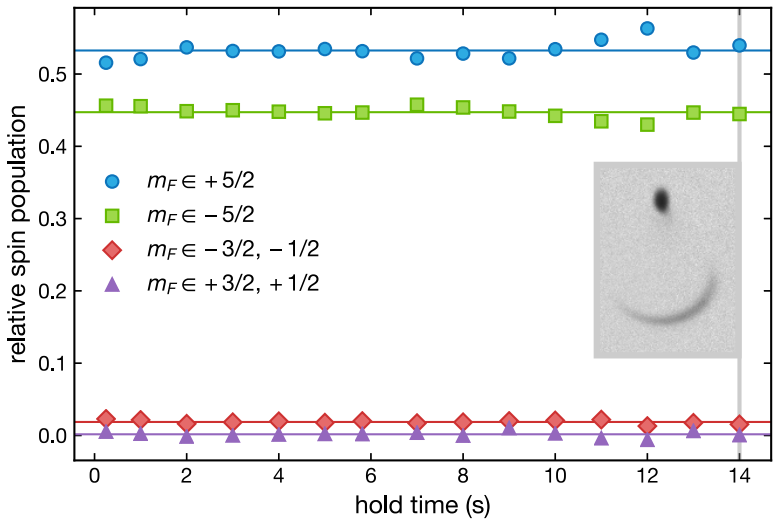

Figure 1.13 – Absence of collisional spin relaxation of ^{173}Yb in $^1S_0$: Relative population of the m_F levels after varying hold times. The initial state is a two-spin mixture $m_F = -5/2, +5/2$. The inset shows the m_F-resolved detection using optical Stern-Gerlach separation [Section 3.6.2]: No repopulation of additional m_F states is discernible. Figure adapted from [97].

of the $^3P_0$ collisions has been investigated spectroscopically, yielding an upper bound on the percent level, $\delta a_{ee}/a_{ee} < 10^{-2}$ [97].

Interacting SU(N)-symmetric many-body systems

Before we focus on the properties and symmetries of the interactions between the two clock state orbitals, we want to give a brief overview over the potential consequences and applications of the SU(N)-symmetric interactions for the simulation of large-spin systems. The

large nuclear spin of fermionic ^{173}Yb or ^{87}Sr in the ground state could provide access to high-symmetry analogs of well-known electronic SU(2)-symmetric models which are predicted to host novel phases of matter [62–66].

Two- or three-dimensional degenerate gases, realized by loading spin mixtures in optical dipole traps or one-dimensional optical lattices, could be used to study the physics of SU(N)-symmetric Landau-Fermi liquids. Significant modifications of the Fermi-liquid properties with the number of spin components N are expected [62, 65]. In one dimensional systems, deviations of a large-N spin liquid from the regular Luttinger liquid properties have already been observed experimentally [67]. In higher dimensions, the Fermi liquid can become unstable towards symmetry-braking phase transitions, so-called Pomeranchuk instabilities. A deformation of the SU(N)-symmetric Fermi surface could lead to a reduced symmetry of the ground state. A famous example for such an instability is the Stoner magnetism for repulsive interactions, leading to the formation of ferromagnetic domains and phase segregation. For attractive interactions, the Fermi surface becomes unstable towards BCS pairing. Both instabilities can be generalized to an SU(N)-symmetric setting and ultracold gases of AEA have been proposed as an ideal platform for studying these effects [62, 65, 66, 150].

The SU(N) Fermi-Hubbard model Interactions and correlations between ultracold atoms can be drastically increased by loading them into an optical lattice. Owing to the SU(N) symmetry of the interactions in AEA, the single scattering length a_{gg} is enough to describe the interactions between all spin states m_F of the atomic ground state ^{1}S$_0$. By expressing the interaction Hamiltonian Eq. (1.54) in terms of the lowest band Wannier functions of the optical lattice, and capturing the particle mobility in a nearest-neighbor tunneling term, we arrive at the SU(N)-symmetric Fermi-Hubbard model (FHM)

$$H_{\mathrm{FH}} = -t \sum_{\langle i,j\rangle, m_F} \hat{c}^\dagger_{im_F} \hat{c}_{jm_F} + \frac{U}{2} \sum_i \hat{n}_i(\hat{n}_i - 1)\,. \tag{1.58}$$

For a derivation of the tunnel matrix element t and the onsite interaction parameter U, see Section 2.1.4. $\hat{c}_i$ is the annihilation operator for a particle of spin m_F on site i, and the occupation number of a lattice site, independent of m_F, is given by $\hat{n}_i = \sum_{m_F} \hat{c}^\dagger_{im_F} \hat{c}_{im_F}$. Obviously, the Hamiltonian obeys the SU(N) symmetry in the nuclear spin. Again, this is guaranteed by the commutation with all spin permutation operators[13] $\hat{S}^b_a$.

While the SU(N)-symmetric FHM bears a strong formal resemblance with its standard spin-1/2 analogue[14], the enlarged spin space expresses itself in fundamentally different behavior, especially concerning magnetic order. An extensive discussion of the applicability of fermionic AEA for the simulation of the SU(N)-symmetric FHM is provided in [66]. The modified spin statistics significantly affect the high-temperature properties of the SU(N) Mott insulating phase [68, 151–153]. Notably, a strong influence on the adiabatic loading process from a 3D bulk sample into the lattice is found. Due to a Pomeranchuk-type cooling effect, lower

[13] In the Wannier basis, the spin-permutation operators from Eq. (1.57) take the form $\hat{S}^b_a = \sum_i \hat{c}^\dagger_{ia} \hat{c}_{ib}$.

[14] For a recent review on the experimental progress in simulating the rich phase diagram of the spin-1/2 FHM using ultracold fermions, see [44].

final temperatures are predicted for higher N. The most intriguing consequences, however, are expected for strong repulsive interactions, where an SU(N)-symmetric Mott insulator is formed. In the range of unit lattice filling, the system is well described by a SU(N)-symmetric variant of the Heisenberg model, capturing magnetic correlations at temperatures below the super-exchange scale [154, 155]. The characteristics of the ground state depend sensitively on the dimensionality and the number of spin components [66]. Recent studies suggest that the large-N limit ($N > 6$) is beneficial for the observation of SU(N) preserving phases. In particular, an SU(N)-breaking flavor-density wave is predicted for $N \leq 6$ [156], whereas for $N > 6$, an SU(N)-preserving staggered-flux pattern should be favored [62, 156]. Predictions for lower-spin systems include a flavor-density wave for $N = 3$ [156] and a valence bond solid for $N = 4$ [157]. Significant approximations are made in the mean-field and renormalization group treatment of the FHM, and quantum Monte-Carlo simulations are limited to particular lattice fillings. Ultracold AEA thus present themselves as a very promising candidate for the simulation of these models.

Repulsive interactions are naturally realized in the ground state of all AEA probed so far. Even in the absence of Feshbach resonances, varying the potential depth of the optical lattice allows one to tune the interaction to tunneling ratio, and to access the strongly interacting regime. Using ^{173}Yb, SU(6)-symmetric Mott insulators have recently been realized [68, 69]. In our experimental setup, we have probed the transition between a metal and SU($N \leq 6$) Mott insulating phase. The thermodynamic equation of state and its variations with N have been extracted from the local density distribution in the optical lattice. The lowest achievable temperatures are still above the super-exchange scale. Yet, indications of the onset of magnetic correlation have been observed [69, 98].

1.5.4 Two interorbital scattering channels

Above, we have discussed the low-energy scattering properties of AEA in a single electronic orbital where the nuclear spin projection is the only internal degree of freedom. The SU(N) symmetry of the interactions assure that only one scattering length is required per orbital, that is, a_{gg} (a_{ee}) for the scattering between $|g\rangle$ ($|e\rangle$) atoms. Because of the decoupling of orbital angular momentum and nuclear spin in both $|g\rangle$ and $|e\rangle$, also the interorbital collisions between $|g\rangle$ and $|e\rangle$ exhibit an SU(N) symmetry. Thus, the introduction of only two more scattering channels is enough. Now, the electronic orbitals can either be in an antisymmetric or symmetric configuration, $|eg^-\rangle \equiv (|eg\rangle - |ge\rangle)/\sqrt{2}$ or $|eg^+\rangle \equiv (|eg\rangle + |ge\rangle)/\sqrt{2}$. Because the scattering potentials and molecular states are in general not equal for the two electronic state combinations, also the associated scattering lengths a_{eg}^- and a_{eg}^+ differ. As demonstrated in [58], the difference of a_{eg}^- and a_{eg}^+ gives rise to a natural spin-exchange interaction between the orbitals. Along with the localization of the $|e\rangle$ orbital in our state-dependent lattice, this provides the basis for the simulation of Kondo-type models [see Section 2.8].

In total, four scattering channels are enough for the description of both intra- and interorbital s-wave interactions and the single-channel scattering pseudo-potential in Eq. (1.53) can

be generalized to

$$V(\mathbf{r}) = \frac{4\pi\hbar^2}{m}\delta_{\mathrm{reg}}(\mathbf{r})\sum_{\xi} a_\xi \mathcal{P}_\xi\,, \tag{1.59}$$

where $\xi \in \{gg, ee, eg^-, eg^+\}$ and $\mathcal{P}_\xi = |\xi\rangle\langle\xi|$ is the projector onto the respective scattering channel. The scattering properties are entirely determined by the orbital wavefunction. However, the nuclear spin must arrange in a spin singlet $|s\rangle$ or triplet $|t\rangle$ to ensure the antisymmetrization of the total fermionic wavefunction[15]. Considering a subset of two nuclear spin states, denoted as $|\uparrow\rangle$ and $|\downarrow\rangle$, we have the spin singlet $|s\rangle = (|\uparrow\downarrow\rangle - |\downarrow\uparrow\rangle)/\sqrt{2}$ and the triplet states $|t\rangle \in \{(|\uparrow\downarrow\rangle + |\downarrow\uparrow\rangle)/\sqrt{2}, |\uparrow\uparrow\rangle, |\downarrow\downarrow\rangle\}$. Including the spin degree of freedom, the four scattering channels are then given by

$$\begin{aligned} |gg\rangle &\equiv |gg\rangle \otimes |s\rangle, \\ |ee\rangle &\equiv |ee\rangle \otimes |s\rangle, \\ |eg^+\rangle &\equiv (|eg\rangle + |ge\rangle)/\sqrt{2} \otimes |s\rangle, \\ |eg^-\rangle &\equiv (|eg\rangle - |ge\rangle)/\sqrt{2} \otimes |t\rangle\,. \end{aligned} \tag{1.60}$$

Obviously, the nuclear spin configuration indirectly determines the available scattering channel, giving rise to effective spin-spin interactions. In particular, regarding the interorbital interactions, there is a unique mapping between the two available spin and orbital configurations with different scattering lengths. The orbital singlet $|eg^-\rangle$ is associated with a nuclear spin singlet $|s\rangle$, and the orbital triplet $|eg^+\rangle$ is accompanied by a nuclear spin triplet $|t\rangle$.

In the case of ^{173}Yb, the most precise measurements of a_{eg}^+ and a_{eg}^- have been achieved in our setup via recoil-free clock-line spectroscopy in a deep 3D optical lattice [59, 90]. The results are listed in Table 1.1. An unusually large value was found for the spin-singlet compared to the triplet channel, with $a_{eg}^+ \gg a_{eg}^-$ by nearly an order of magnitude. As with the ee interactions, the nuclear-spin independence and thereby the SU(N) symmetry of the eg interactions has been investigated by repeating the spectroscopic measurement for varying spin mixtures. Again, an upper bound on the percent level is extracted, $\delta a_{eg}^\pm / a_{eg}^\pm < 10^{-2}$ [59, 90, 97].

Recently, also fermionic ^{171}Yb has been investigated spectroscopically and a qualitatively different scaling has been discovered, namely $a_{eg}^- > a_{eg}^+$ [88, 158]. As a result, a different sign of the spin-exchange coupling will emerge in multiorbital models (see Section 2.8). A systematic study of the interorbital SU(2) symmetry has not yet been performed for ^{171}Yb.

The emergence of interorbital spin exchange

As we will see now, the difference between a_{eg}^- and a_{eg}^+ finally gives rise to spin-exchanging interactions between the orbitals. Let us represent the electronic orbitals $|g\rangle$ and $|e\rangle$ as a pseudo-spin-1/2 system with standard spin-1/2 operators $\hat{\mathbf{T}}_1$ and $\hat{\mathbf{T}}_2$ for a pair of atoms, as in [58]. $\mathbf{T}$ has the associated ladder operators $T^\pm$ acting as $T^+|g\rangle = |e\rangle$, $T^-|e\rangle = |g\rangle$, and the z-component acting as $T^z|g\rangle = -\frac{1}{2}|g\rangle$, $T^z|e\rangle = +\frac{1}{2}|e\rangle$. Using the relation $\hat{\mathbf{T}}_1 \cdot \hat{\mathbf{T}}_2 = \hat{T}_1^z \hat{T}_2^z +$

[15] Note, that for s-wave scattering, the spatial wave function is symmetric.

$(\hat{T}_1^+\hat{T}_2^- + \hat{T}_1^-\hat{T}_2^+)/2$, one can show that the projectors onto the *orbital* singlet and triplet states can be expressed as

$$\mathcal{P}_{eg}^{\pm} = \frac{1}{2} \pm \left(\frac{1}{4} - \hat{\mathbf{T}}_1 \cdot \hat{\mathbf{T}}_2\right). \tag{1.61}$$

The interorbital part of the interaction Hamiltonian Eq. (1.59) can then be written in the orbital pseudo-spin basis:

$$V_{eg}(\mathbf{r}) = \frac{4\pi\hbar^2}{m}\delta_{\mathrm{reg}}(\mathbf{r})\left(\frac{a_{eg}^+ - a_{eg}^-}{2}(\hat{T}_1^+\hat{T}_2^- + \hat{T}_1^-\hat{T}_2^+) + \frac{a_{eg}^+ + a_{eg}^-}{2}\right). \tag{1.62}$$

In this form, the emergence of an orbital exchange interaction is evident. In a final step, we reintroduce the pseudo-spin operator in second quantization, including also the nuclear spin degree of freedom, via $\hat{\mathbf{T}} = \sum_{\alpha,\beta,\sigma}\hat{\psi}_{\alpha\sigma}^\dagger(\mathbf{r})\boldsymbol{\tau}_{\alpha\beta}\hat{\psi}_{\beta\sigma}(\mathbf{r})$. Here, $\hat{\psi}_{\alpha\sigma}^\dagger$ creates a particle in the orbital $|\alpha\rangle$ ($\alpha \in \{e,g\}$) and nuclear spin σ. The vector of Pauli matrices $\boldsymbol{\tau}$ describes the orbital pseudo-spin-1/2 system. Substituting the respective ladder operators $\hat{T}^+ = \hat{T}^- = \sum_\sigma \hat{\psi}_{e\sigma}^\dagger(\mathbf{r})\hat{\psi}_{g\sigma}(\mathbf{r})$ into Eq. (1.62), yields the full interorbital interaction Hamiltonian $\hat{V}_{eg} = \hat{V}_{\mathrm{ex}} + \hat{V}_{\mathrm{d}} + \mathrm{const.}$, with

$$\begin{aligned}
\hat{V}_{\mathrm{ex}} &= \frac{4\pi\hbar^2}{m}\frac{a_{eg}^+ - a_{eg}^-}{2}\sum_{\sigma,\sigma'}\int \mathrm{d}^3r\, \hat{\psi}_{g\sigma}^\dagger(\mathbf{r})\hat{\psi}_{e\sigma'}^\dagger(\mathbf{r})\hat{\psi}_{g\sigma'}(\mathbf{r})\hat{\psi}_{e\sigma}(\mathbf{r}),\\
\hat{V}_{\mathrm{d}} &= \frac{4\pi\hbar^2}{m}\frac{a_{eg}^+ + a_{eg}^-}{2}\sum_{\sigma,\sigma'}\int \mathrm{d}^3r\, \hat{n}_{e\sigma'}(\mathbf{r})\hat{n}_{g\sigma}(\mathbf{r})
\end{aligned} \tag{1.63}$$

The two constituents are typically denoted as the exchange and direct interaction, in analogy to the scenario of interacting spin-1/2 alkali atoms with different interaction strengths in the spin-singlet and triplet channel [58]. In contrast to the direct interaction which depends only the density $\hat{n}_{\alpha\sigma} = \hat{\psi}_{\alpha\sigma}^\dagger\hat{\psi}_{\alpha\sigma}$ in the two orbitals, the exchange part induces interorbital spin-flip processes $|e\downarrow\rangle|g\uparrow\rangle \rightleftharpoons |e\uparrow\rangle|g\downarrow\rangle$. This is illustrated in Fig. 1.12(c). Note that the interorbital interactions $\hat{V}_{eg}$ commute with a generalized form of the spin-permutation operator Eq. (1.57) which involves the summation over the electronic orbitals [58]:

$$\hat{S}_\sigma^{\sigma'} = \sum_{\alpha=e,g}\int \mathrm{d}^3r\, \hat{\psi}_{\alpha\sigma}^\dagger(\mathbf{r})\hat{\psi}_{\alpha\sigma'}(\mathbf{r}). \tag{1.64}$$

Thus, the SU(N) symmetry in the nuclear spin is preserved.

Therefore, interorbital spin-exchange processes preserve the individual m_F populations. However, they can be redistributed over the two different orbitals: An initial spin-population imbalance between the orbitals equilibrates to the same spin distribution within each orbital. The exact dynamics of the spin equilibration process depends on the confinement, density, and energy of the atomic gas. For ^{173}Yb, coherent exchange dynamics have been observed for atomic pairs on isolated sites of a deep 3D optical lattice [60]. Reduced confinement in an array of quasi-2D "pancake" traps has been studied in our experiment. Here, the exchange dynamics occurs on longer timescales and the decoherence in the bulk system leads to damping

and a spin-equilibrated steady state [59]. In Chapter 5, we probe the same interorbital spin equilibration process in the setting of an orbital state-dependent lattice, where $|g\rangle$ and $|e\rangle$ particles start out on different lattice sites. As explained in Section 2.8, the lattice system can be described by a two-orbital FHM where the $|e\rangle$ atoms are localized and spin exchange is only enabled via the mobility of the $|g\rangle$ atoms, in analogy to the Kondo- or Kondo lattice model.

1.5.5 A magnetic Feshbach resonance for interorbital interactions

The SU(N) symmetry and the decoupling of the two interorbital interaction channels $|eg^+\rangle$ and $|eg^-\rangle$ relies on the absence of spin-dependent potentials. Magnetic fields, vector or tensor light shifts which couple differently to the available m_F states break the SU(N) symmetry and lead to a mixing between the orbital singlet and triplet states. The SU(N) symmetry is reduced to U$(1)^{N/2}$, that is, a conservation of spin along the magnetic quantization axis [34].

The non-interacting two-particle eigenstates of the Zeeman Hamiltonian induced by an external magnetic field are given by the spin-product states

$$\begin{aligned} |o\rangle &= (|g\uparrow; e\downarrow\rangle - |e\downarrow; g\uparrow\rangle)/\sqrt{2} \quad \text{and} \\ |c\rangle &= (|e\uparrow; g\downarrow\rangle - |g\downarrow; e\uparrow\rangle)/\sqrt{2}. \end{aligned} \tag{1.65}$$

These are referred to as open and closed scattering channels. The differential linear Zeeman shift between atoms in the two clock states $^3\mathrm{P}_0$ and $^1\mathrm{S}_0$ and in the nuclear spin projections $m_F^\uparrow$ and $m_F^\downarrow$ is caused by the differential Landé factor δg and is defined in Eq. (1.48). Thus, the closed scattering channel is positively detuned from the open channel by

$$\begin{aligned} \Delta\mu B &= [(g_e m_F^\uparrow + g_g m_F^\downarrow) - (g_e m_F^\downarrow + g_g m_F^\uparrow)]\mu_B B \\ &= -\delta g\, \Delta m_F\, \mu_B\, B \end{aligned} \tag{1.66}$$

if $\Delta m_F = m_F^\uparrow - m_F^\downarrow > 0$ and the open channel is energetically favored (see Fig. 1.14).

For ^{173}Yb in the two nuclear spin states $m_F^\uparrow = +5/2$ and $m_F^\downarrow = -5/2$, the differential magnetic moment becomes $\Delta\mu = 554(2)\,\mathrm{Hz/G}$. The quadratic differential Zeeman shift is spin independent and therefore does not enter the scattering problem.

The open and closed channel states are the symmetric and antisymmetric superpositions of the interaction eigenstates $|+\rangle \equiv |eg^+\rangle$ and $|-\rangle \equiv |eg^-\rangle$, such that

$$|\pm\rangle = (|o\rangle \mp |c\rangle)/\sqrt{2}. \tag{1.67}$$

When the differential Zeeman shift becomes comparable to the interaction energies, the interorbital interaction channels start to mix. In the presence of a deep external lattice confinement, the coupling leads to strong modifications of the discrete spectrum of the on-site interactions. A full T-matrix based treatment of the two interaction channels in the orbital state-dependent lattice is presented in Section 4.2.

In a bulk system, the same coupling mechanism, along with the differential Zeeman shift leads to the emergence of a Feshbach resonance in the s-wave scattering length [89–91]. In this so-called orbital Feshbach resonance, the two interaction channels are defined by the symmetry

in the electronic orbital degree of freedom, instead of the electronic spin in a classical, alkali-type magnetic Feshbach resonance [40]. The coupling to the bound states of the two scattering potentials determines the scattering amplitude. Notably, ^{173}Yb possesses an exceptionally large scattering length in the orbital triplet channel. Correspondingly, a shallow bound state emerges in the closed channel at a binding energy $E_b^c/h = -\frac{\hbar^2}{m a_c^2} \approx 19\,\mathrm{kHz}$, with $a_c = (a_{eg}^- + a_{eg}^+)/2$ the scattering length of the closed channel [89, 99]. Despite the small differential Zeeman shift[16], reasonably small magnetic fields are enough to shift the entrance energy of the scattering problem into resonance with this bound state. This is illustrated in Fig. 1.14 (a).

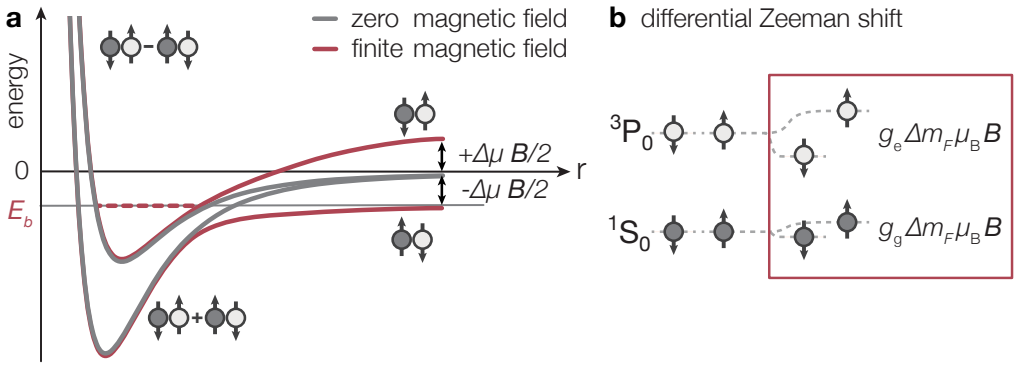

Figure 1.14 – Schematic of the scattering potentials and Zeeman shifts involved in the orbital Feshbach resonance: (a) The scattering potentials for the interorbital interactions at zero and finite magnetic field (gray and red, respectively). At short interparticle distance r, they are dominated by the orbital triplet and singlet channels $|\pm\rangle$. For large r, the spin-product states $|o\rangle$ and $|c\rangle$, as the Zeeman eigenstates, are the scattering entrance channels. The closed channel features a shallow orbital-triplet dominated bound state at E_b. (b) Differential linear Zeeman shift between the clock states causing an energy shift $\Delta\mu B = -\delta g\, \Delta m_F\, \mu_B\, B$ between $|c\rangle$ and $|o\rangle$.

Detailed theoretical descriptions of the orbital Feshbach resonance are presented in [89, 90, 99]. The T-matrix based treatment in [90] also includes the effect of potential external confinement on both the open and closed scattering channel. The magnetic field-dependence of the s-wave scattering length becomes

$$a(B) = \frac{1}{2} \frac{1/a_{eg}^+ + 1/a_{eg}^- - 2\xi(B)}{\left(1/a_{eg}^+ - \xi(B)/2\right)\left(1/a_{eg}^- - \xi(B)/2\right) - \xi^2(B)/4}, \tag{1.68}$$

with $\xi(B) \equiv \sqrt{m\Delta\mu B/\hbar^2}$. Finite scattering-energy dependence is captured in an effective range parameter

$$r_{\mathrm{eff}}(B) = -\frac{1}{\xi(B)} \left(\frac{1/a_{eg}^- - 1/a_{eg}^+}{1/a_{eg}^- + 1/a_{eg}^+ - 2\xi(B)} \right)^2. \tag{1.69}$$

At zero temperature (and scattering energy), the magnetic field position B_0 of the Feshbach

[16] compared to the one typically found in alkali atoms scaling with the Bohr magneton

resonance is given by the divergence of the scattering length in Eq. (1.68) under the condition

$$\Delta\mu B_0 = -E_b^c = \frac{\hbar^2}{m\, a_c^2}\,. \tag{1.70}$$

The magnetic field shifts the entrance energy such that the energy E_b^c of the bound state in the scattering potential of the closed channel matches the differential Zeeman shift. In contrast, the s-wave scattering length vanishes at the zero crossing of the resonance, at a field B_Δ with

$$\Delta\mu B_\Delta = \frac{\hbar^2}{4m}\left(\frac{1}{a_{eg}^+} + \frac{1}{a_{eg}^-}\right). \tag{1.71}$$

For ^{173}Yb, $\Delta m_F = 5$ and the scattering lengths in Table 1.1, we extract $B_0 \approx 33\,G$ and $B_\Delta \approx 238\,G$ [90, 99]. In units of magnetic field, the resonance shape is reasonably wide with $B_\Delta - B_0 \approx 200$ G.

For a quantitatively correct treatment of finite-energy scattering, the energy dependence of the two scattering channels needs to be taken into account. This is particularly important for the orbital singlet channel where the van-der-Waals length of the scattering potential is comparable to the scattering length. The van-der-Waals C_6 coefficient of ^{173}Yb is $C_6 = 2561$ a.u. [159]. An effective range parameter can be analytically deduced for a known C_6 and we obtain $r_{\text{eff}}^+ = 216a_0$ and $r_{\text{eff}}^- = 122a_0$ for the orbital triplet and singlet channel [90, 160]. A low-energy expansion of the scattering phase shift up to the effective range is captured in the replacement [90]

$$1/a_{eg}^\pm \mapsto 1/a_{eg}^\pm - \frac{1}{2} r_{\text{eff}}^\pm \frac{m}{\hbar^2}\left(E - \frac{\Delta\mu B}{2}\right). \tag{1.72}$$

In our setup, for typical atomic densities of $5 \times 10^{13}/\text{cm}^3$ and temperatures of $T \approx 0.3 T_F$ in a crossed dipole trap, the bare resonance position B_0 is shifted to an increased magnetic field of 55(8) G [90]. On resonance, we extract a relatively long $1/e$ lifetime of 348(4) ms, comparable to resonances in alkali elements [161]. The loss dynamics on resonance are well reproduced by a two-body loss model with a loss-rate coefficient $\beta_{eg}^\star = 2.2(3) \times 10^{-13}\,\text{cm}^3/\text{s}$ [99].

On resonance, the open channel effective range, Eq. (1.69), becomes large compared to the van-der-Waals radius of the interorbital scattering potential[17]. Therefore, despite its large width in terms of magnetic field strength, the orbital Feshbach resonance can be classified as (energetically) narrow or closed-channel dominated [40]. This classification also holds in terms of the resonance strength parameter s_{eff} defined by Chin et al., with $s_{\text{eff}} = 0.15 \ll 1$ [99]. In practice, this leads to a strong dependence of the resonant scattering properties on the collisional energy, and thus, the temperature. The narrow character of the resonance also affects the physics of strongly interacting Fermi gases around the BEC-BCS crossover. For example, a particularly high transition temperature to the Fermi superfluid is predicted on the BCS side of the resonance [162], and special polaron properties in AEA impurity systems are investigated [163–165].

[17] The effective range is $r_{\text{eff}}(B_0) \approx -960\,a_0$ compared to the van-der-Waals radius $r_0 = 80\,a_0$ [99].

The orbital Feshbach resonance enables wide-range tunability of the interorbital interactions by means of an external magnetic field, at the cost of breaking the SU(N) symmetry. We note that the differential Zeeman shift could also be generated by nuclear-spin-dependent ac Stark shifts, for example, by exploiting the optical transitions $^1S_0 \rightarrow {}^3P_1$ or $^3P_0 \rightarrow {}^3D_1$ (see Section 1.3.4). Experimentally, these artificial magnetic fields would be controllable on much shorter timescales, enabling fast quenches and Floquet-type engineering of the interactions [34].

CHAPTER 2

An orbital state-dependent optical lattice

Periodic potentials are an essential ingredient for the physics of many condensed-matter systems. Trapping ultracold atoms in periodically modulated optical potentials produced by counter-propagating laser beams, so-called optical lattices, is a common technique for replicating these systems in a well-controllable environment [39, 166]. In particular, the metastable clock state of AEA offers the intriguing possibility to construct a monochromatic lattice for two electronic orbitals with variable differential trap depth and mobility for the two "species". This state-dependent lattice (SDL) can be used to simulate Kondo and Anderson-type physics, that emerge in the presence of localized spins interacting with a bath of mobile atoms. In contrast, optical lattices on the so-called magic wavelength can produce state-independent confinement which can be used to eliminate spatially varying differential light shifts and thereby enable narrow clock-line spectroscopy.

In this section, we introduce the working principles of the optical lattices implemented in our experimental setup. We investigate the trapping properties for single particles in the state-dependent as well as the magic-wavelength lattices and introduce the notion of mixed on-site confinement for the two electronic orbitals. The underlying differential polarizability induced by the lattice light is quantified by means of clock-line spectroscopy and parametric heating techniques. Dissipative processes and dynamics limiting the lifetime of ground-state $^1S_0$ and metastable $^3P_1$ atoms in the SDL are studied. Finally, we review how the two-orbital SU(N) Fermi-Hubbard model is realized in the SDL and how Kondo-type models emerge in certain experimental parameter regimes. The accessibility of characteristic many-body phases in these models is discussed in the context of our SDL setup.

2.1 Optical lattices

As discussed in Section 1.3.4, laser light that is far detuned from all transitions induces a scalar light shift for an atomic level with negligible scattering. The shift is proportional to the intensity of the light and the scalar polarizability. In our setup, all lattice beams are produced by retroreflected monochromatic laser beams with linear polarization. For a single laser beam along z and with beam waist w_z, this leads to a standing-wave intensity pattern (Figure 2.1)

and an associated trapping potential[1]

$$V(x,y,z) = V_z e^{-2\frac{x^2+y^2}{w_z^2}} \cos^2(k_z z). \tag{2.1}$$

The maximum trapping potential V_z can be calculated from the peak intensity and the ac polarizability for a given wavelength λ_z (wavevector $k_z = 2\pi/\lambda$) using Eq. (1.31). Close to a single

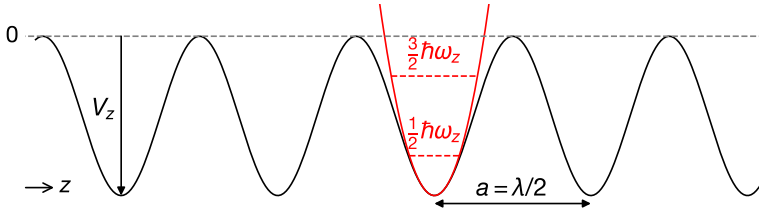

Figure 2.1 – Schematic of a red-detuned, attractive optical lattice potential ($V_z < 0$) with lattice spacing $a_z = \lambda_z/2$. Harmonic approximation of the on-site potential (solid, red) and two lowest single-particle eigenstates (dashed, red), valid for deep lattices.

atomic transition, one can distinguish between red and blue detuned light potentials, resulting from negative or positive detuning with respect to the transition, and leading to attractive ($V_z < 0$) or repulsive ($V_z > 0$) trapping potentials. In a multilevel system, multiple transitions become relevant and contribute to the overall light shift, as explained in Section 1.3.3.

Along the beam, the interference of the counter-propagating light fields leads to a subwavelength lattice spacing $a_z = \lambda_z/2$. Although in our experiments the lattice beams are focused onto the atoms, the Gaussian beam profile is large compared to the atom cloud size and, to good approximation, only causes a transverse harmonic confinement.

In the context of the experiments presented in this thesis, we mainly work with three-dimensional lattice setups produced by three orthogonal retroreflected laser beams with variable relative intensity. We assure that the individual axis do not interfere with each other by detuning the lattice beam light relative to each other or by employing orthogonal polarization (see Section 3.4). Then, the trapping potentials along the three spatial directions $r_i = x, y, z$ decouple and can simply be added to an overall potential

$$V_{\text{lat}}(x,y,z) = \sum_{i=1,2,3} V_{r_i} e^{-2\frac{r_{i+1}^2 + r_{i+2}^2}{w_{r_i}^2}} \cos^2(k_{r_i} r_i) \approx \sum_{i=1,2,3} \left(V_{r_i} \cos^2(k_{r_i} r_i) + \frac{1}{2}\omega_{0,r_i}^2 r_i^2 \right) \tag{2.2}$$

The second expression is the harmonic approximation for the Gaussian confinement around the atom position in the center of the beam and the associated trapping frequency along r_i is given by

$$\omega_{0,r_i} = \sqrt{\frac{4}{m}\left(\frac{V_{r_{i+1}}}{w_{r_{i+1}}^2} + \frac{V_{r_{i+2}}}{w_{r_{i+2}}^2}\right)} \tag{2.3}$$

[1]The harmonic confinement along the laser beam caused by the finite Rayleigh length of the Gaussian beam has been neglected, since it is much larger than the atomic cloud size for reasonably large beam waists.

It is induced by the finite waists $w_{r_{i+1}}$ and $w_{r_{i+2}}$ of the two perpendicular lattice beams. Note that in the approximation above, we ignore the spatially varying depth of the sinusoidal lattice confinement. Also, we assume circular beams, but the calculation can easily be generalized to arbitrary ellipticity. A sketch of the total light potential created by two perpendicular lattice beams is shown in Fig. 2.9.

The presence of an additional harmonic confinement along with the homogeneous lattice confinement can be both an advantage and a drawback in our experiments. Preparing and probing homogeneous interacting systems is difficult in these systems, especially for large fermionic samples with finite Fermi radius. Typically, the maximum available laser power along with Gaussian beams limits the minimum trap frequency to around 10–100 Hz and many observables are prone to developing a shell structure. Yet, for weak confinement, within the validity of the local density approximation, one can map the radial position in the trap to a local chemical potential. In principle, this can allow us to extract a full thermodynamic equation of state from a single image of the atomic distribution in the trap. We have used this technique, e.g., for determining the equation of state of the SU(N) symmetric Fermi Hubbard model over a wide range of interaction strengths [69, 98]. Also, in Chapter 6, we directly probe the oscillations of the atomic cloud in the harmonic confinement to investigate the mobility properties in the state-dependent lattice.

2.1.1 Band structure and mobility

The optical lattice potential significantly alters the mobility of trapped particles. The single-particle non-interacting Hamiltonian is given as a sum of the free-particle dispersion and the trapping potential from Eq. (2.2):

$$H_0 = \frac{p^2}{2m} + V_{\mathrm{lat}}(x, y, z). \tag{2.4}$$

Weak optical lattices only lead to minor modifications of the free-particle dispersion relation and modified transport properties can be captured by an enhanced effective mass. However, increasing lattice depth leads to the opening of a band gap and the formation of a sinusoidal band structure in the so-called tight binding limit. In the limit of very deep lattices, the mobility is suppressed such that the lattice sites can be treated as individual harmonic oscillators (h.o.).

The Bloch theorem is helpful for understanding the single-particle physics in an optical lattice potential of arbitrary depth[2]. It states that the Schrödinger equation for the periodic potential can be solved by delocalized eigenfunctions, the so-called Bloch waves

$$\phi_{q,n}(z) = \sum_l c_l^{q,n} e^{i(q+2lk_z)z}, \quad l \in \mathbb{Z} \tag{2.5}$$

which are superpositions of plane waves with wave vectors containing the quasimomentum q (lattice momentum) and the reciprocal lattice vectors $2lk_z$.

[2]For details of the derivation we refer to existing literature [167, 168].

Inserting the plane-wave decomposition into the Schrödinger equation allows us to extract the coefficients $c_l^{q,n}$ and thereby the eigenspectrum by numerical diagonalization. The resulting band structure for a sinusoidal lattice potential at typical lattice depths in our experiments is shown in Fig. 2.2.

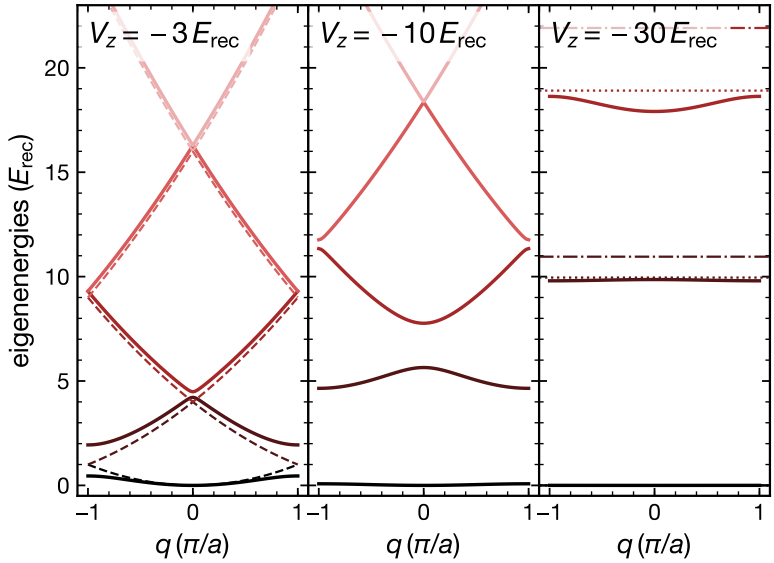

Figure 2.2 – The band structure of a homogeneous 1D optical lattice for different depths V_z (solid lines). The weak lattice ($V_z = -3E_{\mathrm{rec}}$) is compared to the free particle dispersion (dashed). The flat bands in a deep lattice ($V_z = -30E_{\mathrm{rec}}$) are compared to the spectrum of an on-site h.o. model (dash-dotted) and to the harmonic-oscillator model including a first-order correction in the quartic part of the sinusoidal lattice potential (dotted). The ground-state energy is subtracted from all energies.

The eigenfunctions can be grouped into bands n with increasing energy and quasimomentum q. Due to the discrete translational invariance of the lattice, the band structure $E(q)$ is periodic in q and only the first Brillouin zone $q \in [-\pi/a, \pi/a]$ is plotted. Apart from the periodicity of the eigenspectrum, increasing lattice depth leads to flattening of the dispersion relation, compared to the free-particle dispersion, and the associated opening of increasingly large band gaps. Already at $V_z = -3\,E_{\mathrm{rec}}$, the first band gap has become larger than the lowest band width.

Note that the lowest band of a 1D lattice opens around the energy $E(q = \pm\pi/a) = 1\,E_{\mathrm{rec}}$ for arbitrary low lattice depth. To prevent population of higher bands when loading atoms from an optical dipole trap, the Fermi energy in the dipole trap needs to stay below the lattice recoil energy. In a cubic 3D lattice setup, the problem is separable into the three spatial directions and the eigenfunctions can be written as products of 1D solutions. In case of a symmetric cubic lattice, the first band gap then only opens around $V_z \approx 2.2\,E_{\mathrm{rec}}$ [169].

For most of our experiments, we try to avoid the population of higher lattice bands and the mobility of particles is described by the lowest-band physics. Figure 2.3 (a) shows the transition from a parabolic into a sinusoidal dispersion relation for increasing lattice depth. For weak potentials, there is an extended range of quasimomenta around $q = 0$ where the dispersion

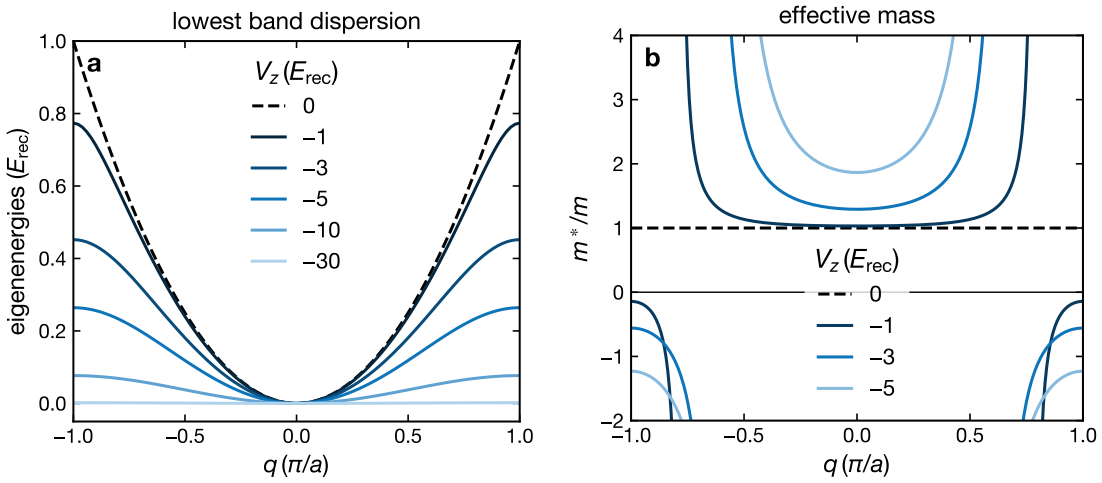

Figure 2.3 – (a) Dispersion relation of the lowest band of a homogeneous 1D optical lattice for different depths V_z (solid lines). The parabolic free particle dispersion (dashed) is compared to the increasingly flat and sinusoidal spectrum for large V_z. (b) Quasimomentum dependent effective mass m^* (solid lines) obtained from the lattice dispersion relation, in units of the bare particle mass m (dashed).

relation can still be approximated by a parabolic free-particle dispersion, but with reduced curvature. The modified curvature can be absorbed into the definition of a momentum-dependent inertial effective mass [170]

$$m^* = \left[\frac{1}{\hbar^2}\frac{\partial^2 E(q)}{\partial q^2}\right]^{-1} \tag{2.6}$$

The momentum and lattice depth dependence of the effective mass m^* in units of the bare particle mass m is depicted in Figure 2.3 (b).

2.1.2 Harmonic and quartic on-site approximation

In the limit of deep lattice potentials, the modified free-space picture becomes increasingly inadequate. Instead, regarding the individual lattice sites as independent, deep potential wells, as sketched in Fig. 2.1, provides a good approximation. We expand the 1D, on-site lattice potential up to sixth order in z:

$$V(z) = V_z \cos\left(k_z^2 z^2\right) = V_z\left(1 - k_z^2 z^2 + \frac{1}{3}k_z^4 z^4 - \frac{2}{45}k_z^6 z^6\right) \tag{2.7}$$

The leading, harmonic term leads to an approximation of the band gaps in terms of a constant h.o. spacing

$$\hbar\omega_z = \sqrt{\frac{2\hbar^2|V_z|k_z^2}{m}} = 2\sqrt{|V_z|E_{\mathrm{rec}}} \tag{2.8}$$

scaling with the square root of the lattice depth. In Fig. 2.2, we observe that the harmonic approximation fits the lowest band gaps from the exact diagonalization results relatively well for

$V_z = -30\,E_{\mathrm{rec}}$. Yet, there is an offset of $1\,E_{\mathrm{rec}}$ for the lowest band gap and $2\,E_{\mathrm{rec}}$ for the second band gap which remains, even if the lattice depth is increased further (see also Fig. 2.10).

This discrepancy is a contribution of the quartic term from the polynomial expansion in Eq. (2.7). First order perturbation theory of the h.o. model in this term leads to a correction $\Delta E^{(4)}(n)$ of the eigenenergies that is independent of lattice depth but depends on the band index n as

$$\Delta E^{(4)}(n) = -\frac{2n(n+1)+1}{4}\,E_{\mathrm{rec}}\,, \tag{2.9}$$

yielding

n	0	1	2	3	4
$\Delta E^{(4)}(n)/E_{\mathrm{rec}}$	-1/4	-5/4	-13/4	-25/4	-41/4

for the lowest bands. This results in a constant correction for the band gaps $\Delta E^{(4)}(n+1) - \Delta E^{(4)}(n) = -(n+1)\,E_{\mathrm{rec}}$. Adding this correction to the h.o. model leads to a significantly improved approximation for the on-site eigenenergies that becomes exact for increasing lattice depth[3]:

$$E(n) = (1+2n)\sqrt{|V_z|E_{\mathrm{rec}}} + \Delta E^{(4)}(n) + V_z\,. \tag{2.10}$$

This quartic correction is also shown in Fig. 2.2.

2.1.3 Wannier functions and the tight-binding regime

One of the main benefits of using optical lattices in ultracold gases experiments is the ability to faithfully simulate Hubbard-type models. By including only nearest or next-nearest neighbor tunneling as well as on-site interactions, these models are able to capture spin-correlations and electron mobility at the same time [43]. In order to realize these models, the optical lattice needs to be in a regime where it is not only a minor perturbation to the free-particle dispersion relation but the mobility of particles is rather described by quantum mechanical tunneling of localized wave packets through potential barriers between adjacent lattice sites. This so-called tight-binding regime, where only hopping between neighboring particles needs to be considered, is reached for lattice depths larger than $3-5\,E_{\mathrm{rec}}$.

Wannier functions The Wannier functions form a natural basis to treat the on-site and next-neighbor tunneling physics in the tight binding-regime. They can be constructed from a Fourier transform of the Bloch functions[4]

$$w_n(z-z_i) = \sum_q e^{iqz_i}\phi_{q,n}(z)\,. \tag{2.11}$$

[3] Perturbative corrections due to higher-order terms in the lattice potential expansion, starting from the sixth-order term, vanish with increasing lattice depth.

[4] The Wannier functions are an orthonormal basis set and thus one needs to be careful with the proper normalization of the Fourier transform. In particular, for infinite system size, the sum is replaced by an integral.

For the lowest bands, the Wannier functions should only depend on the distance from a given lattice site z_i and the band index n and should be localized as much as possible. Every Bloch wave in the superposition carries a free phase degree of freedom that can be varied to construct these maximally localized states. A complete description of Wannier functions in a separable cubic 3D system is given in [171]. It is shown that for arbitrary bands, there exists a unique Wannier function that is real and localized exponentially on the lattice site.

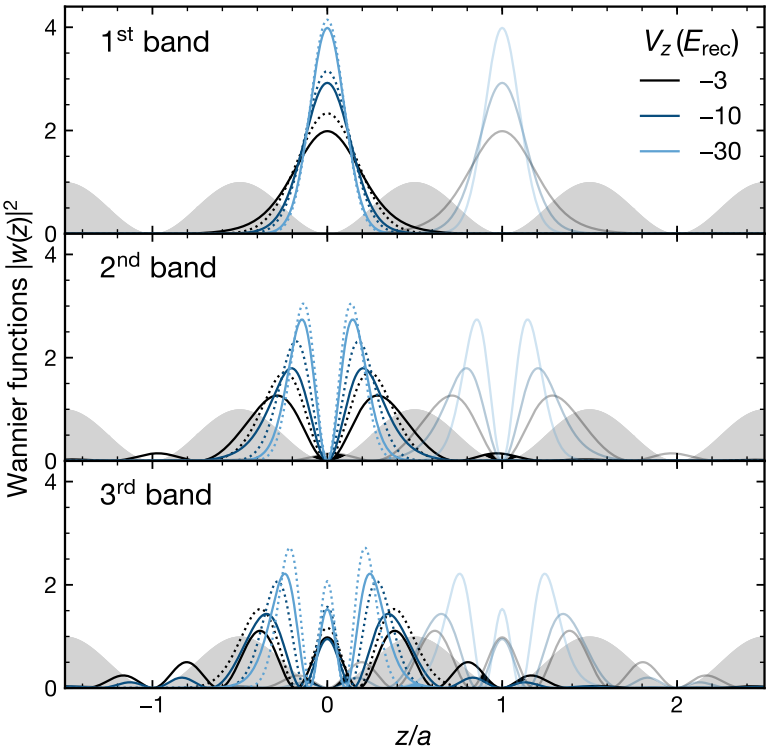

Figure 2.4 – Wannier functions for the lowest three bands of a one-dimensional lattice potential (shaded gray) and typical lattice depths V_z used in the experiment. The absolute square of the Wannier function centered around $z = 0$ (solid) is compared to the on-site harmonic approximation (dotted). Decreasing lattice depth and increasing bands lead to larger discrepancy with the harmonic approximation and increased wavefunction overlap with the neighbouring site ($z/a = 1$).

Following this procedure, we numerically construct the Wannier functions which are used to estimate the nearest and next-nearest neighbor tunneling rates in the lattice. In Fig. 2.4, the Wannier functions of the lowest three bands are compared to the wave functions from the on-site h.o. approximation introduced in Eq. (2.7). As expected, the h.o. approximation works increasingly well for larger lattice depth and lower bands where the more localized wave functions probe less of the anharmonic part of the lattice confinement. However, note that, like the lattice band energies above, the Wannier functions do not converge uniformly to the h.o. wavefunctions [38].

Single-particle mobility The lower the lattice depth, the larger the overlap of neighboring Wannier functions becomes. The tunneling rate of single particles between lattice sites can be calculated by evaluating the transition matrix element of the lattice Hamiltonian, Eq. (2.4), between Wannier functions on different lattice sites, namely

$$t_n^{(d)} = -\int \mathrm{d}z\; w_n^*(z-z_i)\left(-\frac{\hbar^2\nabla_z^2}{2m}+V(z)\right)w_n^*(z-z_{i+d}) \tag{2.12}$$

Indeed, the Hamiltonian can be cast into second-quantized form in the basis of the Wannier functions and $t_n^{(d)}$ turns out to be the prefactor of the tunnel matrix element between sites i, j separated by $d = j-i$ lattice sites in the band n [38]:

$$H_0 = \sum_{i,j}\left(-t_n^{(d=j-i)}c_i^\dagger c_j + h.c.\right) \tag{2.13}$$

where c_i is the annihilation operator on site i.

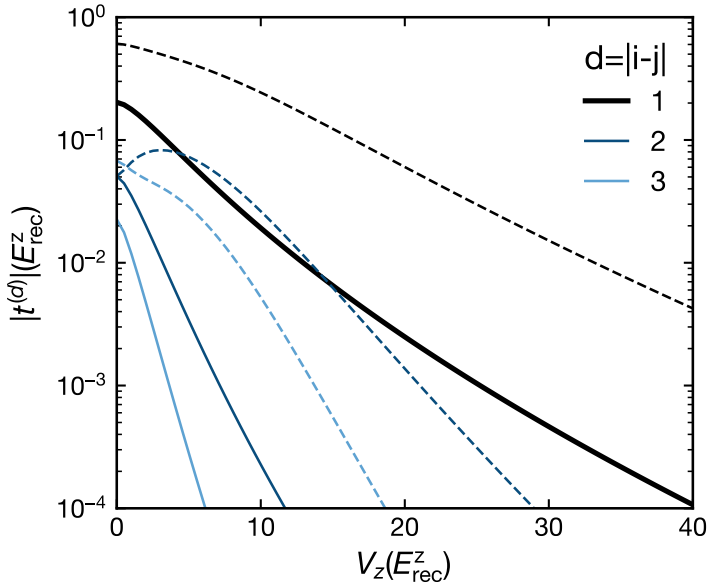

Figure 2.5 – Tunnel matrix element for typical lattice depths V_z used in the experiment in units of lattice recoil energy. Comparison of nearest-neighbor ($d = 1$, black thick) with next-nearest neighbor tunneling rates ($d > 1$, blue). The tunneling rate in the lowest lattice band (solid) is compared to the first excited band (dashed).

The tunnel strength can be calculated numerically[5] from Eq. (2.12) and one finds that it decreases approximately exponentially with the lattice depth as well as with the inter-site distance (see Fig. 2.5). Increasing the lattice depth also increases the ratio between nearest- and next-nearest neighbor tunneling.

For many relevant Hubbard models, one is only interested in short-range hopping in a single band, limited to at most one or two lattice sites. This so-called tight-binding regime

[5] Alternatively, it can be obtained from the Fourier transform of the band structure $E^{(n)}(q)$ in quasimomentum space, which is less numerically demanding [38]: $t_n^{(d)} = \sum_q e^{iqd}E^{(n)}(q)$.

is reached for lattice depths around $V_z \geq 3\,E_{\mathrm{rec}}$ where the next-nearest neighbor tunneling is suppressed by roughly a factor 10. The dispersion relation in the lowest band becomes fully cosinusoidal with

$$E^{(0)}(q) = -2t\cos(qa)\,, \tag{2.14}$$

as sketched in Fig. 2.3 with a band width of $4t$ in terms of the tunneling matrix element. One can define a characteristic timescale for the mobility in the lattice, the nearest-neighbor tunneling time (hopping time)

$$\tau = \frac{\hbar}{t}\,. \tag{2.15}$$

Note that we use the convention employing $\hbar$ to convert the energy to a time scale. This is different from the definition in our publication [172] where h/t is used as the tunneling time.

The optical lattice experiments presented in the following chapters partly work with relatively low lattice depths and the failure of the tight-binding approximation can directly observed in many observables below that limit.

2.1.4 Simulation of Hubbard models

The Fermi-Hubbard model (FHM) has first been introduced in the context of solid-state physics to extend pure band models as to also capture electron-electron interactions [35]. In ultracold atom experiments, optical lattices in the tight-binding regime have been successfully employed for the simulation of Hubbard-type models, both with fermionic and bosonic atoms [38, 44]. Using the Wannier basis introduced above, the FHM can be written in second quantization as the sum of three contributions

$$H = H_0 + H_{\mathrm{int}} + V\,. \tag{2.16}$$

The first term H_0 typically captures the mobility in the lowest lattice band. In the tight-binding approximation, Eq. (2.13) reduces to

$$H_0 = -\sum_{\langle i,j\rangle,\sigma} t_\sigma \left(c^\dagger_{i,\sigma} c_{j,\sigma} + h.c.\right) \tag{2.17}$$

with $\langle i,j\rangle$ indicating a sum over nearest neighbor sites, and t_σ the according tunnel matrix element for a (pseudo) spin σ.

An additional inhomogeneous trapping potential, like the weak h.o. potential induced by the Gaussian lattice beam envelope, can be included in

$$V = \sum_{i,\sigma} \nu_{i,\sigma} n_{i,\sigma}\,. \tag{2.18}$$

The energy offsets $\nu_{i,\sigma}$ can potentially depend on σ.

Finally, the on-site interactions are contained in

$$H_{\mathrm{int}} = \sum_{i,\sigma,\sigma'} U_{\sigma,\sigma'} n_{i,\sigma} n_{i,\sigma'} \tag{2.19}$$

where the interaction parameter $U_{\sigma,\sigma'}$ defines the on-site interaction energy for two particles in σ and σ' on the same lattice site. For weak s-wave interactions, justifying the pseudopotential approximation, it can be evaluated from overlaps of the on-site Wannier functions w_σ as

$$U_{\sigma,\sigma'} = \frac{4\pi\hbar^2 a_{\sigma,\sigma'}}{m} \int \mathrm{d}^3 r |w_\sigma|^2 |w_{\sigma'}|^2 \tag{2.20}$$

with $a_{\sigma,\sigma'}$ the scattering length. This expression can be obtained by inserting the localized Wannier wave functions into Eq. (1.54). However, if the interaction energy becomes comparable to the lowest band gap, the regularized interaction potential needs to be considered [139]. For ^{173}Yb, this is the case already at small lattice depths due to the large spin-singlet scattering length (see Chapter 4).

Note that in the standard electronic FHM, σ denotes the electronic spin and the interactions are typically SU(2) symmetric. In general, however, σ can be a placeholder for any quantum mechanical degree of freedom. In particular, it can also represent the electronic orbital of AEA, determining the mobility in our optical state-dependent lattice. In Section 2.8, the full two-orbital FHM, including the SU(N)-symmetric interorbital interactions will be introduced.

2.2 Orbital state-dependent mobility

In our experiments, the two clock states of ytterbium, separated in energy by optical frequencies, need to be trapped simultaneously in optical potentials. The implementation of our orbital state-dependent lattice (SDL) relies on the different ac polarizabilities of the ground state $^1\mathrm{S}_0$ ($|g\rangle$) and the metastable excited state $^3\mathrm{P}_0$ ($|e\rangle$), lying in different transition manifolds. The origin of the different polarizabilities of the clock states has been discussed in Section 1.3.4. A monochromatic laser beam at a selected wavelength can then produce qualitatively different confinements for the two internal states. While $|e\rangle$ and $|g\rangle$ see the same lattice spacing, they experience different potential depths, and thus, in general, different mobility.

Let us define the wavelength-dependent ratio of ac polarizabilities of the clock state as

$$p = \frac{\alpha(^3\mathrm{P}_0)}{\alpha(^1\mathrm{S}_0)} = V_e/V_g \tag{2.21}$$

where V_g and V_e are the light shifts induced for $|g\rangle$ and $|e\rangle$ atoms by the same laser intensity. Figure 2.6 shows the scalar ac polarizability ratio over a large range of wavelengths, estimated from the transition collections in Section 1.3.4 and from an ab-initio CI+MBPT calculation [125].

2.2.1 The magic wavelength

We can make out several distinct points in this plot. Particularly important in the context of precision clock-line spectroscopy are the so-called magic wavelengths which produce orbital state-*independent* optical potentials ($p = 1$). These wavelengths cancel the differential spectroscopic shifts induced by variations of laser intensity. For other wavelengths, inhomogeneous

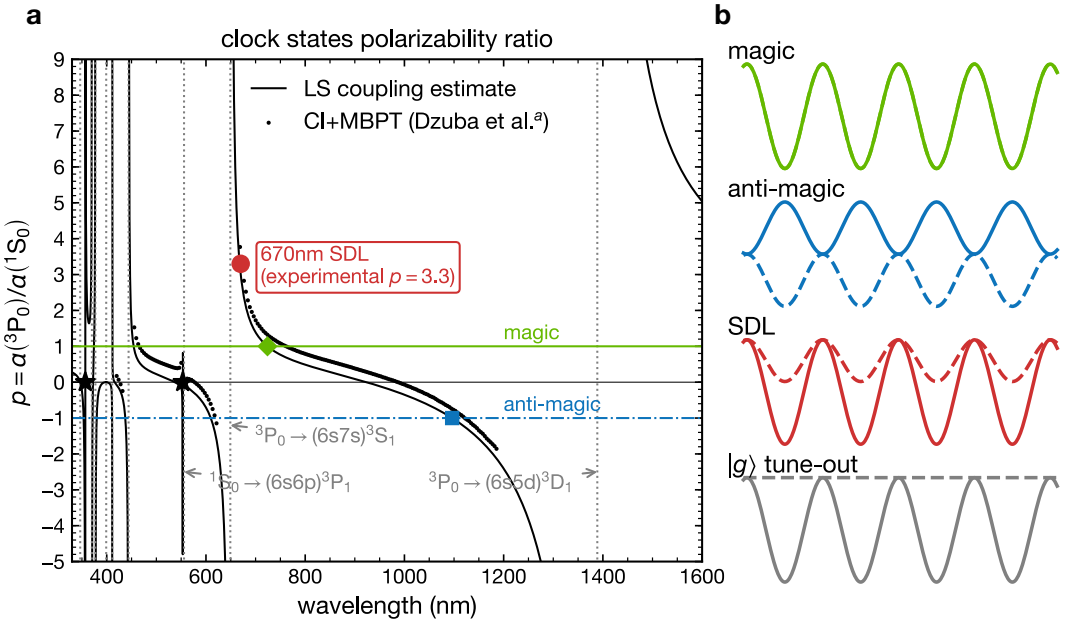

Figure 2.6 – (a) Ratio p of the scalar ac polarizabilities of the two clock states $^1S_0$ ($|g\rangle$) and $^3P_0$ ($|e\rangle$) determined from the LS coupling estimate (solid lines) in Section 1.3.4 and from ab-initio CI+MBPT calculations [a][125] (circles). Relevant optical transitions from Table B.1 are indicated by dotted lines. The measured magic wavelength 759.35(2) nm [129] ($p = 1$, diamond), the SDL wavelength of 670 nm ($p \approx 3.3$, circle), a potential anti-magic wavelength around 1100 nm ($p = -1$ square) and a tune-out wavelength for $|g\rangle$ ($V_g = 0$, asterisk) are marked. (b) Sketches of the lattice potentials experienced by $|g\rangle$ (dashed) and $|e\rangle$ (solid) for the indicated wavelength.

laser intensity over the extent of the atomic density distribution in the trap, or temporal fluctuations of trapping laser intensity lead to a broadening of the spectroscopic features which is particularly limiting for atomic clock experiments.

For ytterbium, magic wavelengths can be found, for example, at 413 nm, 465 nm, 552 nm [125] and 759 nm [173]. An experimentally well-accessible magic wavelength used in most experiments, and also in this work, is the one at $\lambda_m = 759$ nm. Precise values of this magic wavelength $\lambda_m = 759.35594(2)$ nm and $\lambda_m = 759.35374(7)$ nm for the isotopes ^{171}Yb and ^{174}Yb have been obtained in the lattice clock experiments [174] and [173].

The relatively large detuning from the closest transition $^3P_0 \rightarrow {}^3S_1$ ensures low photon scattering rates and thus and long lifetimes of the $|e\rangle$ atoms. Moreover, the frequency dependence of the differential ac Stark shift around this wavelength has been measured to be relatively low, with a linear shift slope of only $-22(2)$ mHz per GHz detuning and recoil potential depth (measured for ^{174}Yb and ^{171}Yb in [173, 174]). This leads to a very weak sensitivity on frequency fluctuations of the laser light.

A slightly smaller magic wavelength has been determined for ^{173}Yb in our setup [97]:

$$\lambda_m^{173} = 759.30(4)\,\text{nm}\,. \tag{2.22}$$

The wavelength was extracted from a measurement of the clock transition at different wave-

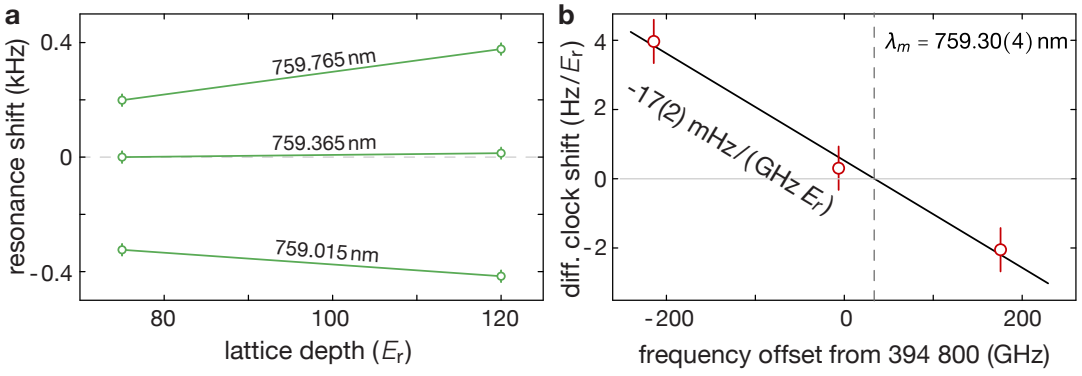

Figure 2.7 – (a) Shift of the measured clock transition frequency for different lattice light wavelengths and depths. (b) Differential clock shift normalized to lattice depth (slopes in (a)). The magic wavelength and a shift slope per recoil and detuning around this wavelength are extracted. Figure adapted from [97].

lengths and lattice depths, as depicted in Fig. 2.7.

This value is consistent with a higher-precision measurement $\lambda_m^{173} = 759.29(1)\,\mathrm{nm}$ in [175]. The discrepancy with the other isotopes can probably related to different hyperfine coupling strength of $^3P_0$. A linear shift slope $-17(2)\,\mathrm{mHz}/(\mathrm{GHz}\,E_{\mathrm{rec}})$ around the magic wavelength for ^{173}Yb has been measured in [97]. An incompatible value of $-52(1)\,\mathrm{mHz}/(\mathrm{GHz}\,E_{\mathrm{rec}})$ is obtained in [175] hinting at uncontrolled systematic errors in the experiments. However, an uncertainty of around 1 GHz in the lattice light frequency at a typical lattice depth of $30\,E_{\mathrm{rec}}$ only leads to clock-line shifts on the Hz level for both values. This is well below the current resolution of our clock laser setup. For more details on the experimental implementation of our magic wavelength lattices, see Section 3.4.

2.2.2 Anti-magic and tune-out wavelengths

The first proposals for orbital state-*dependent* trapping potentials for AEA have been made in the context of quantum information processing. Daley et al. suggest to use two independent lattices for the metastable electronic states of fermionic strontium, one for the storage of qubits and one for transport and gate operations [73]. Here, the two wavelengths are chosen such that one lattice traps only the $|g\rangle$ atoms and has zero polarizability for the $|e\rangle$ atoms ($V_e = 0$), and inversely for the other lattice ($V_g = 0$). These are sometimes referred to as *tune-out wavelengths*.

Gorshkov et al. suggest to use two tune-out wavelength lattices for the implementation of the Kondo-Lattice model, where excited-state atoms act as localized spins interacting with a bath of mobile ground-state atoms [58]. The independent lattices for $|g\rangle$ and $|e\rangle$ would even allow to tune the overlap of the on-site wavefunctions and thereby the strength of the spin-exchange interactions [58, 176].

As recently proposed in [84, 177, 178], mixed 1D or quasi-1D confinement for $|g\rangle$ and strong localization of $|e\rangle$ could provide access to the Kondo impurity model. This system could be realized by a single tune-out wavelength lattice for the $|g\rangle$ atoms that pins a dilute sample

of $|e\rangle$ impurities.

In strontium, tune-out wavelengths for both $|g\rangle$ (689 nm) and $|e\rangle$ (627 nm) are in a readily accessible wavelength regime and relatively close to each other[6]. For ytterbium, the largest tune-out wavelength for $|g\rangle$ can found below the transition to $^3P_1$, at 553nm[7]. However, the associated $|e\rangle$ polarizability is very weak (see Fig. 1.6), leading to large laser power requirements. An accessible tune-out wavelength for $|e\rangle$ with a reasonable residual polarizability for $|g\rangle$ can be found around 987 nm [125].

Another special setting can be produced with *anti-magic wavelength* lattices. Here, the two internal states experience optical potentials of equal magnitude but with opposing sign ($p = -1$, $V_e = -V_g$). Two sublattices form for the two states, shifted by $\lambda/4$ with respect to each other. The two clock states can then be coupled adiabatically on the clock transition to create a sub-wavelength lattice for the induced dressed states [179]. The reduced lattice spacing results in reduced timescales and temperature requirements for quantum information schemes and can be exploited for subwavelength, nuclear-spin dependent control in the simulation of quantum lattice models. Similarly, Gerbier and Dalibard [76] propose to use light-induced tunneling between the sublattices of an anti-magic lattice to simulate the Harper model, hosting strong artificial gauge fields. An experimentally accessible anti-magic wavelength for the clock states can be found, for example, around 1121 nm [125].

2.2.3 A state-dependent lattice for orbital lattice models

In addition to the spin-exchange coupling between orbitals, another essential ingredient for the implementation of the Kondo lattice model (KLM) is the presence of two lattice bands with distinct mobilities, localizing one orbital while leaving the other mobile. Preferably, the $|g\rangle$ atoms are used to simulate the mobile band of conduction electrons of solid-state systems, since ytterbium atoms in different nuclear-spin states of $|e\rangle$ undergo strong lossy collisions [59].

The two-species lattices described above require defined polarizability ratios and can therefore only be realized using unique wavelengths. Away from these special points, the ratio of the ac polarizabilities for the two clock states can take arbitrary values. Instead of employing two independent tune-out lattices, as proposed in [58] for the simulation of the KLM, we chose to produce the state-dependent confinement using a single, monochromatic optical lattice with a wavelength of around 670 nm.

This wavelength is in a range above the $^3P_0 \rightarrow (6s7s)^3S_1$ transition (649 nm) where the polarizability of $|e\rangle$ is enhanced compared to $|g\rangle$ (see Section 1.3.4). Using lattice modulation spectroscopy in Section 2.4, we determine a polarizability ratio of $p = 3.3(2)$ for the clock states at $\lambda = 670$ nm.

For our experiments working in the tight-binding regime of the optical lattices, the relevant scale for the relative mobility is the ratio of the $|e\rangle$ and $|g\rangle$ tunneling rates t_e/t_g. The

[6] The simulation of the KLM or the above-mentioned quantum information proposals require the two tune-out lattices to have an identical lattice spacing. This can be achieved by a relative angle of the lattice beams if the beams are sufficiently close in wavelength.

[7] Our LS coupling estimate in Section 1.3.4 predicts another tune-out wavelength around 357nm. However, the reliability of this estimate for the low-wavelength regime is unclear.

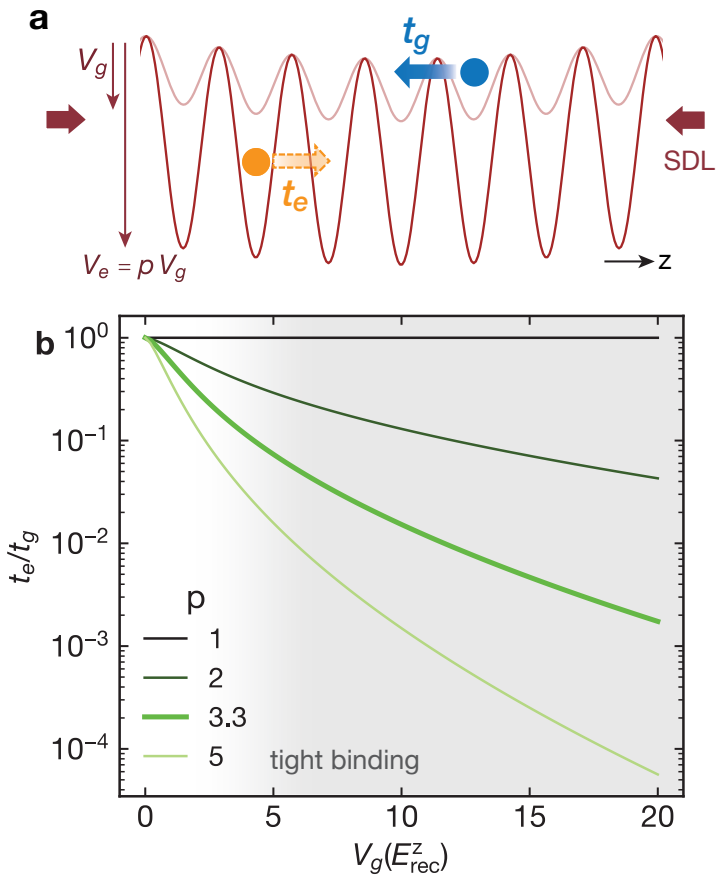

Figure 2.8 – Orbital state-dependent mobility: (a) Schematic of 670 nm state-dependent lattice potential experienced by ground-state (blue) and excited-state atoms (yellow). $|e\rangle$ atoms experience a deeper lattice potential by a factor $p \approx 3.3$ and a reduced tunneling rate t_e compared to t_g of $|g\rangle$ atoms for the same light intensity. (b) Ratio of tunneling mobilities t_e/t_g for varying $|g\rangle$ potential depth and polarizability ratio p. The thick line indicates the polarizability ratio $p \approx 3.3$ used in the experiment. In the tight-binding regime (gray area), a $\sim 10 - 100$ fold suppression of the tunneling rate ratio is reached.

dependence of this ratio on the ground-state lattice depth is illustrated in Fig. 2.8 for different polarizability ratios. Although, the relative lattice potential depth is only around three times larger for $|e\rangle$ at $\lambda = 670\,\mathrm{nm}$, the ratio takes a value of $t_e/t_g = 0.18$ already for $V_g = 3\,E_{\mathrm{rec}}$ and decreases further to $t_e/t_g = 0.015$ for $V_g = 10\,E_{\mathrm{rec}}$.

On the one hand, the residual mobility of the $|e\rangle$ atoms for a given lattice depth determines the maximum time scales on which the KLM can still be faithfully simulated without considering the $|e\rangle$ loss dynamics. On the other hand, physically relevant time scales of the lattice model are tied to the hopping rate of the $|g\rangle$ atoms. Therefore, an increased polarizability ratio p would be favorable, leading to an enhanced $|e\rangle$ lifetime or a speed-up of the $|g\rangle$ mobility for a given laser intensity. Obviously, the polarizability ratio increases if the transition $^3\mathrm{P}_0 \rightarrow (6s7s)^3\mathrm{S}_1$ is approached further. This would lead to an increased scattering lattice photon scattering rate, however. For $\lambda = 670\,\mathrm{nm}$, the ratio of dipole and radiative force on the

$|e\rangle$ atoms can be estimated to $\Delta/\Gamma \approx 9 \times 10^6$ [see Eq. (1.26)], roughly a factor of five lower than for the magic lattice wavelength. Also, the lower end of the tunability of our high-power Ti:Saph laser system is bounded at around 667 nm.

An alternative choice of wavelength for future implementations of a SDL could lie in the range above the $^3P_0 \rightarrow (6s5d)^3D_1$ transition. Around 1550 nm, narrow-linewidth, high-power laser options are available. The expected polarizability ratio $p \approx 6$ is larger than for 670 nm light. At the same time, the ratio between dipole and radiative force on the $|e\rangle$ atoms due to lattice photon scattering should also be enhanced, with $\Delta/\Gamma \approx 7 \times 10^7$ [Eq. (1.26)]. Because of the increased lattice spacing, however, the mobility in the lattice would be strongly reduced leading to prolonged physical time scales.

Preservation of nuclear spin Lattice potentials that are dependent on an internal atomic degree of freedom have been previously proposed and realized, using the spin of alkali atoms [180–182]. There, the spin dependence is induced by detuning the lattice lasers between the finestructure splitting of the D1 and D2 lines which produces different light shifts for the hyperfine components F of the ground state. These systems, however, suffer from strong heating rates and limited lifetimes in the lattice because of the close detuning to the atomic transitions. The heating is particularly severe for fermionic species like potassium or lithium which possess a relatively small finestructure splitting.

A way around this problem for alkali atoms has recently been demonstrated by Jotzu et al. [183]. They use a modulated magnetic field gradient to induce an oscillating force on the $F = 9/2$ manifold of potassium. In a Floquet picture, this induces an effective hopping rate that is tunable in amplitude and sign and depends on the Zeeman sublevel m_F. This scheme explicitly breaks the SU(2) symmetry of the lattice Hamiltonian in the spin sector and is therefore not well suited for the implementation of Kondo and Anderson lattice models, nor their possible SU(N) extensions using AEA. In the context of quantum information processing using AEA, spin-dependent lattices have been proposed for performing gate operations. These could be realized by adiabatically coupling the clock states using an optical lattice operating near the clock transition itself [74].

Instead, our implementation of an orbital SDL using far-detuned monochromatic laser light with $\lambda = 670$ nm preserves the SU(N) symmetry of the lattice Hamiltonians in both clock states. As shown in Section 1.3.4, the expected vector and tensor polarizabilities for the clock states with $F = 0$ are strongly reduced, on the order of 10^{-6} compared to the scalar light shift. Within the resolution of our clock-line spectroscopy of spin-polarized gases in the SDL, we have not been able to observe m_F-dependent light shifts.

2.3 Mixed anisotropic confinement

In this work, we employ a setup of three perpendicular and decoupled retroreflected lattice beams (see Fig. 3.5). The light potentials along the three dimensions can be added and lead to an overall trapping potential according to Eq. (2.2).

For most of the experiments, we work with two perpendicular, magic-wavelength lattice beams of equal strength $V_\perp = V_x = V_y$ along x and y, producing an array of cigar-shaped traps. For deep enough potentials, these can be regarded as decoupled quasi-1D systems. Along these tubes, we add an additional lattice potential of variable depth V_z which is either an orbital state-dependent lattice with polarizability ratio $p = 3.3$ or another magic-wavelength, state-independent lattice.

Figure 2.9 – Schematic of lattice potential experienced by ground-state (left) and excited-state atoms (right) in the presence of a 670 nm state-dependent lattice along z and a magic-wavelength lattice beam along x (dimensions not to scale). $|e\rangle$ atoms experience a larger potential depth by a factor $p = 3.3$ than $|g\rangle$ atoms along the SDL for the same light intensity while the perpendicular lattice confinement is identical for both species.

The resulting total lattice potential experienced by the $|g\rangle$ and $|e\rangle$ atoms is sketched in Fig. 2.9, for a SDL along z. The plot shows a cut through a lattice node of the y lattice and includes the effect of the gaussian beam envelope. In our experiments, the cold atomic samples populate the region in the center of the trap, where all three lattice axes contribute significantly. The overall confinement for both orbitals can be described as *anisotropic* and *mixed*.

Anisotropy In general, if $V_z \neq V_\perp$, the on-site confinement is anisotropic since it is different in the perpendicular direction and along z for both clock states. In the h.o. approximation, the system is described by two independent energy scales given by the oscillator frequencies

$$\hbar\omega_{z,s} \neq \hbar\omega_{\perp,s} \quad \text{for} \quad s \in \{g, e\}\,. \tag{2.23}$$

We can define the anisotropy ratio

$$\eta_s = \omega_{\perp,s}/\omega_{z,s} \neq 1 \quad \text{for} \quad s \in \{g, e\} \tag{2.24}$$

characterizing the ratio of the trapping frequencies. The characteristic length scales are the h.o. lengths

$$l_{z,s} = \sqrt{\hbar/m\omega_{z,s}} \quad \text{and} \quad l_{\perp,s} = l_{z,s}/\sqrt{\eta_s} \quad \text{for} \quad s \in \{g, e\} \tag{2.25}$$

describing the extent of the Gaussian wavefunction in the longitudinal and perpendicular directions. The on-site, single-particle eigenenergies are given by

$$E_s(n_z, n_\perp) = \left(n_z + \frac{1}{2} + \eta_s n_\perp + \eta_s\right)\hbar\omega_{z,s} \tag{2.26}$$

where n_z, $n_\perp$ denote the number of longitudinal and perpendicular band excitations.

Note that the anisotropy of the on-site confinement is not necessarily a consequence of the orbital state dependence of the lattice and is also present for imbalanced 3D state-independent lattices. In the limit of very weak lattice confinement along z, the system becomes quasi-1D and the residual h.o. frequency along the tubes is given by the Gaussian envelope of the perpendicular beams via Eq. (2.3).

In the absence of interactions, the different lattice directions can be treated separately and the additional energy scale compared to an isotropic system only changes the density of states and reduces the amount of degeneracies in the spectrum. However, as we will see in Chapter 4, the anisotropic confinement enters non-trivially in the calculation of the two-particle interactions.

Mixed confinement A direct consequence of the SDL is the so-called *mixed confinement* for the two orbitals. In our experiment configuration, the $|g\rangle$ atoms experience a weak lattice potential along z, always smaller than the perpendicular confinement. At the same time, the $|e\rangle$ atoms are localized in a deeper potential that can reach similar depths as the perpendicular lattices [see Fig. 2.8 (a)]. Since we do not employ a tune-out wavelength for the SDL, both orbitals experience a finite lattice potential and we cannot reach the configuration of entirely *mixed dimensions*[8]. In the tight binding regime, both species are subject to a 3D lattice, yet, with significantly different on-site anisotropy.

In Chapter 4, we will introduce a model for the on-site two-particle interactions in mixed confinements. Similar to the anharmonicity of the lattice potential, the mixed confinement leads to a coupling of relative and center-of-mass motion in the on-site two-particle problem.

2.4 Lattice-depth and polarizability calibration

The potential depth of the optical lattices is an important experimental parameter in the derivation of the lattice model Hubbard parameters. Common techniques to calibrate the lattice depth using fermionic AEA are via parametric excitation of lattice vibrational modes or clock laser sideband spectroscopy in the Lamb-Dicke regime.

Both techniques spectroscopically probe the band structure experienced by non-interacting atoms. By measuring the energy needed to transfer atoms between bands and comparing to a numerical band structure calculation, the lattice depth can be reconstructed. Figure 2.10 shows the theoretically expected band structure for the two orbitals in a 1D SDL. The band widths decrease with the lattice depth and are always smaller for the $|e\rangle$ atoms for a given

[8] This would be the case if $|g\rangle$ atoms were trapped in quasi-1D and $|e\rangle$ atoms were fully localized (quasi-0D) in 3D lattice potential wells.

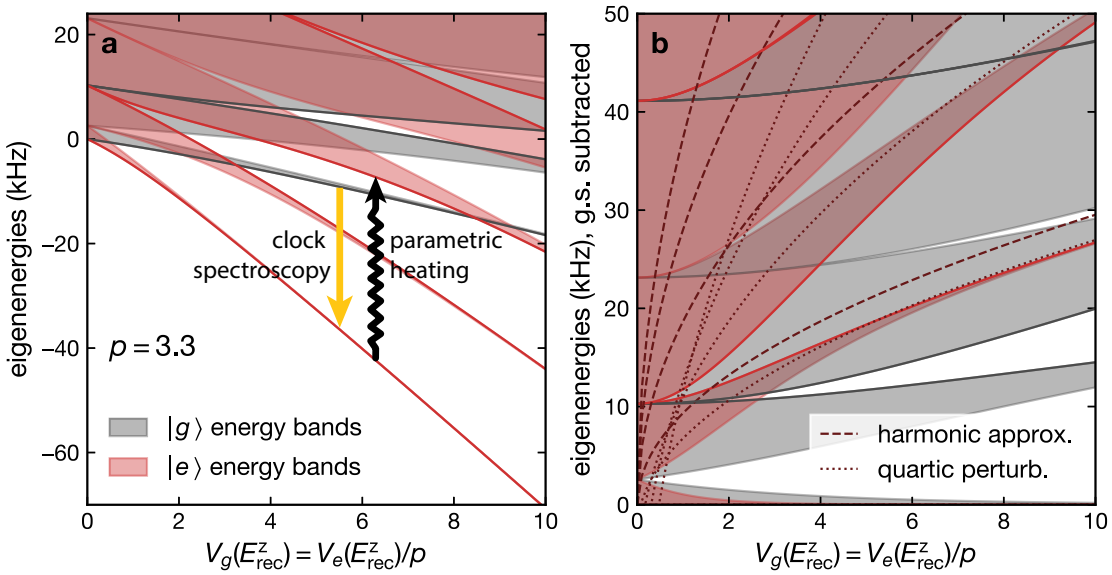

Figure 2.10 – Energy spectrum from the numerical band structure calculation for a 1D state-dependent lattice with polarizability ratio $p = 3.3$. Energy bands for $|g\rangle$ (gray) and $|e\rangle$ (red) produced by a fixed laser light intensity. Eigenstates with quasi momentum $q = 0$ are marked with solid lines. (a) Full spectrum including light shift. Clock spectroscopy between orbitals probes the differential light shift, whereas parametric heating probes the intra-orbital band structure. (b) Spectra with ground-state energy for both orbitals subtracted, compared with harmonic on-site approximation (dashed) and correction by first-order perturb. in quartic lattice potential term (dotted) from Eq. (2.10).

light intensity. Since neither of the techniques resolves the change in quasimomentum for a transition between bands, the band width ultimately limits the resolution of the calibration. The resonance signals result from an average over different initial and final quasimomenta in the trap. Therefore, the system should be probed with the largest possible lattice depths.

As illustrated in Fig. 2.10, the fundamental difference between the two approaches is that the parametric heating technique preserves the internal atomic state whereas the clock-laser sideband spectroscopy transfers atoms from $|g\rangle$ to $|e\rangle$. Lattice sideband spectroscopy can be used in our setup for the calibration of the magic-wavelength lattice copropagating with the clock laser. Probing the amplitude ratios of blue and red sidebands allows us to probe excitations of higher bands[9] [59]. However, for the clock line sideband spectroscopy in the SDL, one needs to consider line shifts and broadening due to the additional state-dependent ac Stark shift (Section 2.5). The SDL depth is therefore calibrated using parametric heating in our setup.

Parametric heating

Parametric heating can be employed to calibrate the lattice depth for $|g\rangle$ and $|e\rangle$ separately. Typically, we load a spin-polarized, non-interacting sample of fermions into a 3D lattice con-

[9] For an extensive review of clock spectroscopy physics in an optical lattice, see [184, 185].

figuration. A tiny sinusoidal temporal modulation is then applied to the depth of the optical lattice using an acusto-optical modulator. When the modulation frequency ν_{mod} matches the energy difference between lattice bands of equal parity, atoms can be parametrically excited into the higher band [186]. Experimentally, we employ the resonance between the lowest band $n = 0$ and the second excited band $n = 2$ [see Fig. 2.10 (a)]. The energy input into the system results in heating and a broadening of the momentum distribution. This can be detected after release and finite time of flight from the lattice, via an increased width of the atom cloud along the direction of the modulated lattice arm (or atom loss from the trap for large modulation amplitudes).

The perpendicular, magic-wavelength lattices can reach a maximum lattice depth of around $60\,E_{\mathrm{rec}}$, where the band structure is essentially flat and the parametric excitation becomes momentum independent. A residual resonance width remains because of inhomogeneous lattice potentials and finite intensity modulation amplitudes.

In the current configuration of the SDL, the potential depth for $|g\rangle$ is limited to around $10\,E_{\mathrm{rec}}$. There, the band width of the second excited band is on the order of 10 kHz and the third excited band is only separated by a band gap of around 1 kHz. So, the lattice modulation essentially probes an excitation into a continuum of states [see Fig. 2.10]. The resulting heat-

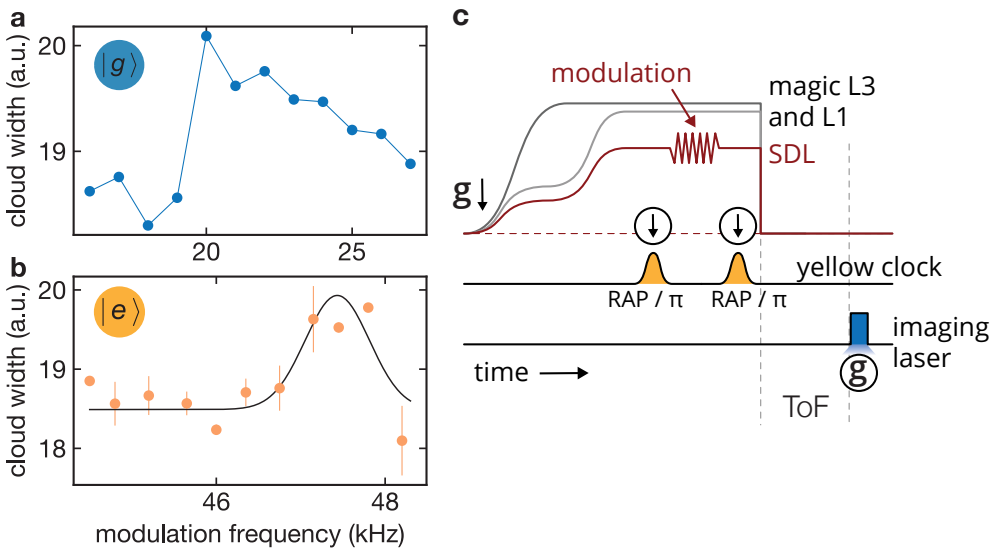

Figure 2.11 – State-dependent lattice depth calibration by parametric heating. (a) Width of an expanding $|g\rangle$ atom cloud after a $\sim$ 20 ms, 5% intensity modulation of the SDL at variable modulation frequency. (b) Same modulation with $|e\rangle$ atoms. Solid line is a Gaussian fit to the cloud width. (c) Sketch of experiment sequence used the parametric heating of $|e\rangle$ atoms in the SDL: the clock laser excites spin-polarized $|g\rangle$ atoms to $|e\rangle$ and deexcite after lattice modulation for imaging.

ing signal detected after finite time of flight is shown in Fig. 2.11. We can discern a relatively sharp flank at $\nu_{\mathrm{mod}} \approx 19.5\,\mathrm{kHz}$. That can be attributed to excitations to the lowest quasi-momentum states around $q = 0$[10] at a lattice depth $V_g \approx 9.5\,E_{\mathrm{rec}}$, from the numerical band

[10]The $q = 0$ state is the lowest-energy state in the second excited band.

structure calculation. Excitations into a continuum of higher energy states lead to a slowly decaying tail for higher modulation frequencies.

The same light intensity causes a significantly deeper potential for the $|e\rangle$ atoms. However, in order to observe the effect of the lattice modulation, the atoms first have to be excited to the $^3P_0$ state via a RAP or a high-power resonant π pulse on the clock transition. As depicted in Fig. 2.11(c), the modulation is then applied to the $|e\rangle$ atoms. Finally, another clock pulse transfers the atoms in $|e\rangle$ back to $|g\rangle$ and we can image the momentum distribution after time of flight. This leads to a roughly 1 kHz broad parametric heating resonance around $\nu_{\mathrm{mod}} \approx 47.4\,\mathrm{kHz}$, corresponding to $V_e \approx 31.3\,E_{\mathrm{rec}}$ in Fig. 2.11(b).

Polarizability ratio Under the assumption that the spatial distribution in the trap is comparable for the two orbitals, the experimentally ratio of the determined potential depths V_e and V_g should directly give access to the polarizability ratio defined in Eq. (2.21). We have repeated this type of measurement for several SDL depths and for a fixed wavelength of $\lambda_{\mathrm{SDL}} = 670.007\,\mathrm{nm}$ (frequency $\nu_{\mathrm{SDL}} = 447.447\,\mathrm{THz}$) and arrive at a value of

$$p(670\,\mathrm{nm}) = V_e/V_g = 3.3(2) \tag{2.27}$$

The relatively large uncertainty is due to an estimated 1 kHz uncertainty in the extraction of the $q = 0$ flank in the $|g\rangle$ parametric heating resonance. An improved precision could be achieved by employing deeper lattices with a flatter band structure, either by using more tightly focused lattice beams or by increasing the laser power.

2.5 Clock spectroscopy in the state-dependent lattice

In our experiments, the optical spectroscopy of the narrow clock line in optical lattice systems is a powerful tool for the coherent preparation and detection of interacting two-orbital systems. When magic-wavelength confinements are employed, the clock transition becomes independent of laser intensity which makes these systems robust against spatial and temporal intensity variations and well suited for precision spectroscopy and optical clocks [57]. In the following, we see and quantify how the presence of our orbital-state dependent lattice potential introduces an intensity and wavelength-dependent differential light shift for the clock-transition that needs to be controlled and accounted for in the spectroscopy and state preparation.

2.5.1 Doppler-free spectroscopy

Deep optical lattice systems can be used to ensure recoil-free optical spectroscopy, when the Lamb-Dicke condition is satisfied [187]. If the extent of the atomic wavefunction becomes much smaller than the wavelength $\lambda_c = 2\pi/k_c$ of the probing laser, the recoil-induced momentum shift of the line, i.e. the Doppler shift, is suppressed. The clock photon recoil energy and momentum are then increasingly absorbed by the confining potential in the form of lattice photons. In a reasonably deep optical lattice, where the on-site potential can be approximated

by a h.o., the extent of the wavefunction is given by the h.o. length $l = \sqrt{\hbar/m\omega}$. Then, the so-called Lamb-Dicke parameter can be defined as

$$\eta = lk_c/\sqrt{2} = \frac{1}{\sqrt{2V/E_{\mathrm{rec}}}} \tag{2.28}$$

and the Lamb-Dicke condition is satisfied for $\eta \ll 1$.

The state-dependent lattice depth is varied in a range where the $|g\rangle$ atoms experience a maximum trap depth of $V_g = 10\,E^z_{\mathrm{rec}}$. This is not enough to ensure recoil-free spectroscopy with the clock laser oriented along the SDL. Instead the clock laser is aligned along the horizontal magic-wavelength lattice beam (L1), perpendicular to the SDL, as shown in Fig. 2.12. The magic-wavelength lattices are typically regulated to a minimum depth of $V_\perp = 30\,E^\perp_{\mathrm{rec}}$ ensuring a maximum Lamb-Dicke parameter of $\eta \approx 0.13$.

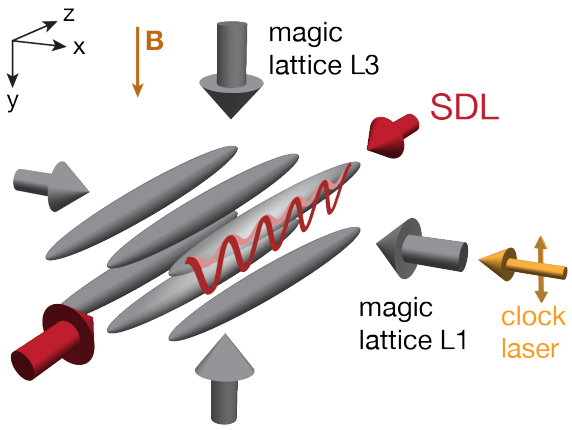

Figure 2.12 – Schematic of lattice and clock laser beam configuration: Two magic-wavelength lattices (vertical L3 along $\hat{y}$ and horizontal L1 along $\hat{x}$) create an array of quasi-1D traps (gray). The linearly polarized clock laser beam is oriented along L1 which ensures Lamb-Dicke conditions for the spectroscopy. The horizontal SDL beam along $\hat{z}$ is oriented perpendicular to all other beams and creates a state-dependent confinement along the state-independent quasi-1D systems.

Note that for an optical excitation along a weaker lattice potential (along $\hat{x}$ in Fig. 2.12), the coupling strength to the clock laser (also along $\hat{x}$) depends on the quasimomentum and band index via an effective Rabi frequency [59]

$$\Omega^{q,q'}_{n,n'} = \Omega_0 \int \mathrm{d}x \langle \phi^{n'}_{q'} | \mathrm{e}^{ik_c x} | \phi^{n}_{q} \rangle \,. \tag{2.29}$$

The clock laser photons can only induce transitions between bands n, n' of the coaligned lattice (L1) and couple quasimomenta q, q' along $\hat{x}$ differing by k_c. When the band widths of the coupled bands become smaller than the bare-particle Rabi coupling Ω_0, Eq. (1.37), the momentum dependence vanishes. For the typical bare Rabi frequencies $\Omega > 2\pi \times 100\,\mathrm{Hz}$ employed in our experiment, this happens already for a lattice depth $V_x \gtrsim 10\,E_{\mathrm{rec}}$. In contrast, the quasimomentum and band index in the SDL along $\hat{z}$, perpendicular to the clock laser, are always preserved.

2.5.2 Differential light shifts

Particles in the two orbitals $|g\rangle$ and $|e\rangle$ experience different ac Stark shifts which results in a shift of the clock transition frequency compared to a purely state-independent confinement. The magnitude of this differential clock-line light $\delta\nu_c$ depends on the SDL depth, its wavelength and the motional state of the atom.

In principle, the clock laser can drive transitions between the orbitals $|g\rangle$ and $|e\rangle$, between different quasi momenta q and q' as well as between different lattice bands n and n' along its propagation direction. We can calculate the resulting differential light shift as

$$\delta\nu_c = E(q', n', V_e = pV_g) - E(q, n, V_g) \tag{2.30}$$

where $E(q, n, V)$ are the eigenenergies from the numerical band structure calculation. For deep lattices, the band structure becomes momentum independent and within the harmonic on-site approximation (Eq. (2.10) with quartic correction), we have

$$\begin{aligned}\delta\nu_c(n \to n') = &\left[\left(1+2n'\right)\sqrt{|p|} - (1+2n)\right]\sqrt{|V_g|E_{\mathrm{rec}}} \\ &+ \Delta E^{(4)}(n') - \Delta E^{(4)}(n) \\ &+ (p-1)V_g\,.\end{aligned} \tag{2.31}$$

The clock laser beam in our experiment is preserves the quasimomentum and band index in the SDL. Yet, the clock transition frequencies are still sensitive to the motional state of the atoms in the band structure of the SDL. As illustrated in Fig. 2.10 for transitions in the lowest bands $n = n' = 0$, the main contribution to the clock line shift originates from the difference $(p-1)V_g$ in maximum lattice potential depth for the two orbitals. A second contribution comes from the difference in the on-site zero point energies, scaling with $\sqrt{V_g}$ [see Fig. 2.13(b)].

In Fig. 2.13(a), we show the results of a clock-line spectroscopy in the SDL. The atoms are confined in a 3D lattice setup with a deep magic-wavelength perpendicular confinement and a longitudinal SDL of variable depth and wavelength $\lambda = 670\,\mathrm{nm}$. The data points denote the spectroscopic features attributed to singly occupied, that is, non-interacting, lattice sites and are from two independent data sets (a spin-polarized and a two-spin mixture of similar densities and atom numbers). The expected differential clock-line light shift, Eq. (2.30), from the numerical band structure calculation is fitted to the data, with p and a global frequency offset as the free parameters.

In principle, one needs to consider imperfections in the retroreflection of the SDL laser beam. Let us assume that only a fraction β of the laser intensity contributes to the standing wave interference. The effect of the residual, non-interfering intensity fraction $(1-\beta)$ is reduced by a factor 4 compared to the lattice potential. Because the lattice depth V_e has been calibrated independently using parametric heating, we have to consider an additional light shift contribution

$$\delta\nu_c^{\mathrm{dip}} = \frac{1}{4}\frac{(1-\beta)}{\beta}(p-1)V_g \tag{2.32}$$

in Eq. (2.30). This term has the same linear dependence on V_g as the light shift caused by the (interfering) lattice potential and the fit parameters β and p become strongly correlated. Thus,

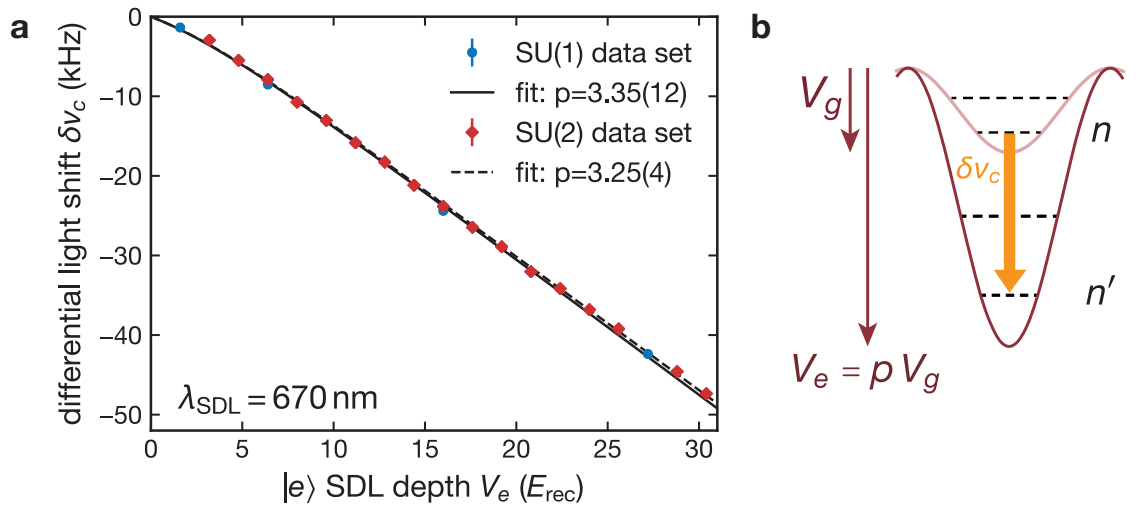

Figure 2.13 – (a) Differential light shift between the clock states, measured by clock spectroscopy of the $m_F = -5/2$ nuclear spin state on singly occupied lattice sites in the lattice lowest bands, in a sample of spin-polarized atoms (circles) and a two-spin mixture (squares, $m_F = \pm 5/2$). The constant magnetic diff. shift for the offset field of $B = 10\,$G is subtracted. The SDL lattice depth is variable and independently calibrated for $|e\rangle$. Perpendicular lattices $V_\perp = 30\,E_{\rm rec}^\perp$. Fits (solid and dashed lines) of the numerical band structure calculation yield estimates for the polarizability ratio p. (b) Schematic of clock spectroscopy in the lowest bands $n = 0$ and n' of the SDL.

for the fit in Fig. 2.13(a), we have neglected this term by setting $\beta = 1$. A 10% variation of β would lead to a 3% variation in the optimum value for p. The fit results for the polarizability ratio are shown in the figure and are compatible with the value obtained from the independent parametric heating experiment above.

Wavelength dependent clock shift In an additional measurement, we characterize the SDL wavelength dependence of the differential clock shift. The Ti:Sa laser systems allow us to tune the lattice wavelengths over a range of several nanometers. Again, we probe the differential shift by probing the light induced shift of the clock transition of a spin-polarized gas in a 3D lattice setup.

We vary the SDL wavelength in a range between 666.5 nm and 673.1 nm and extract the shift of the spectroscopic peaks with respect to a reference measurement in a pure magic-wavelength confinement (SDL depth $V_z = 0$ and magic $V_\perp = 30\,E_{\rm rec}^\perp$) [see Fig. 2.14(a)]. As expected from the theoretical estimates of the scalar polarizabilities in Section 1.3.4 and Fig. 2.6, the polarizability ratio, and thereby the differential clock shift $\delta\nu_c$, increase when approaching the transition $^3{\rm P}_0 \rightarrow {}^3{\rm S}_1$ around 649 nm.

We observe in Fig. 2.14(b) that in the investigated range of wavelengths around $\lambda = 670\,$nm, the dependence of $\delta\nu_c$ on the SDL frequency $\nu_{\rm SDL}$ is roughly linear and we extract a shift slope of $-50(10)h\,{\rm Hz}/(E_{\rm rec}{\rm GHz})$. The uncertainty is dominated by a relatively large estimated uncertainty of $1\,E_{\rm rec}$ for the $|g\rangle$ lattice depth in this measurement. The value is com-

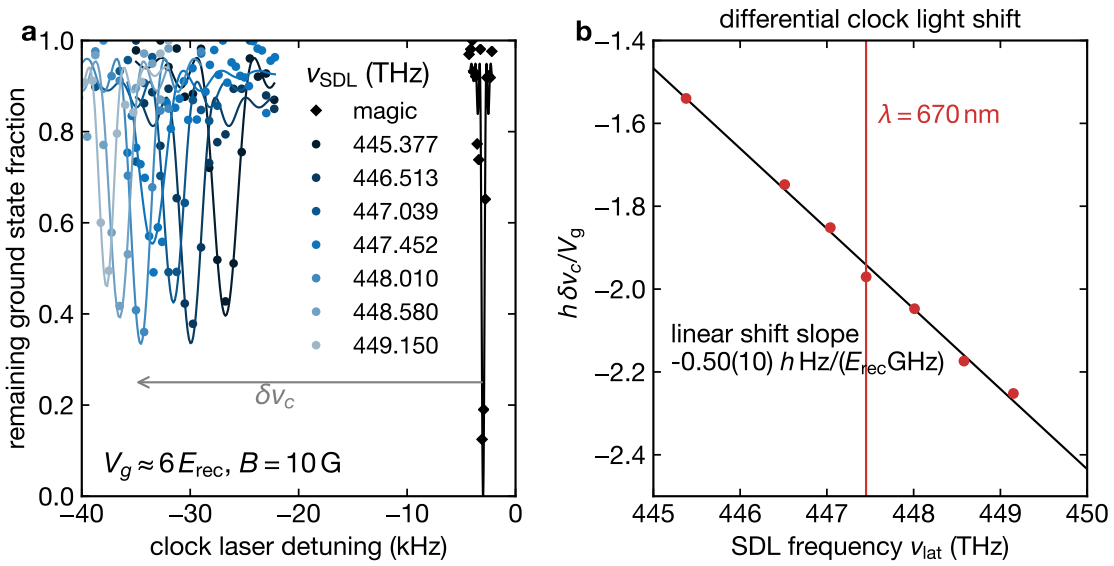

Figure 2.14 – Wavelength-dependent differential light shift of the clock transition in the SDL. (a) Spectroscopy signal (remaining $|g\rangle$ atoms after a clock π pulse on spin-polarized $m_F = -5/2$ atoms) for varying SDL light frequency ν_{SDL} and fixed SDL depth $V_g = 6(1)\,E_{\mathrm{rec}}$ (circles). Comparison with reference measurement in purely magic-wavelength lattice ($V_g = 0$) yields differential light shift $\delta\nu_c$. Measurement is done at magnetic offset field $B = 10$ G and clock laser detuning is with respect to zero-field resonance position. (b) Differential light shift from Rabi line shape fit to the resonances in (a), normalized to the $|g\rangle$ SDL lattice depth. A linear fit gives the shift slope of the clock transition per lattice depth in recoil and GHz detuning around the wavelength 670 nm.

patible with the prediction $-0.56\,h\,\mathrm{Hz}/(E_{\mathrm{rec}}\,\mathrm{GHz})$ from the CI+MBPT calculation in [125].

The shift slope is larger by over an order of magnitude compared to the one around the magic wavelength (see Section 2.2.1). Yet, a 1 GHz stability of the lattice light frequency at a typical $|g\rangle$ lattice depth of $10\,E_{\mathrm{rec}}$ still restricts the clock shifts to the 5 Hz level, below our clock laser resolution.

2.6 Single-particle lifetime in the SDL

The atomic lifetime in our lattice systems is limited by several decay and heating mechanisms. On longer timescales, this is the case already on the single-particle level, neglecting collisional decay. For both clock states, the lifetime is limited by the finite background pressure of the vacuum system and the lattice light leads to additional loss and decay of the $|e\rangle$ atoms, through photon scattering and repumping to $|g\rangle$.

Vacuum background losses Although the experiment is conducted at low pressures of around $P = 1.7 \times 10^{-11}$ mbar, the collisions with the residual background gas lead to a measurable loss rate. By holding a sample of degenerate spin-polarized fermions in a $\sim 3\,\mu$K deep, crossed optical dipole trap, we measure a loss rate (inverse of 1/e-lifetime τ) of $k_{\mathrm{vac}} = 1/106(12)s =$

9.4(9) mHz (see Fig. 2.15). The losses are largely independent of confinement depth and we expect them to be also independent of the electronic orbital. Due to a defective atomic beam shutter mechanism, most of the experiments in this work have been performed with the shutter permanently open. The associated decay rate was measured independently in different confinements, that is, a crossed 1064 nm dipole trap and a deep 3D magic-wavelength lattice ($V_{x,y,x} = 30\,E_{\mathrm{rec}}$). As shown in Fig. 2.15, the presence of the atomic beam during the hold time leads to an additional reduction in lifetime by a factor of three and we extract a working value $k_{\mathrm{vac}} \approx 29(1)$ mHz for the loss rate.

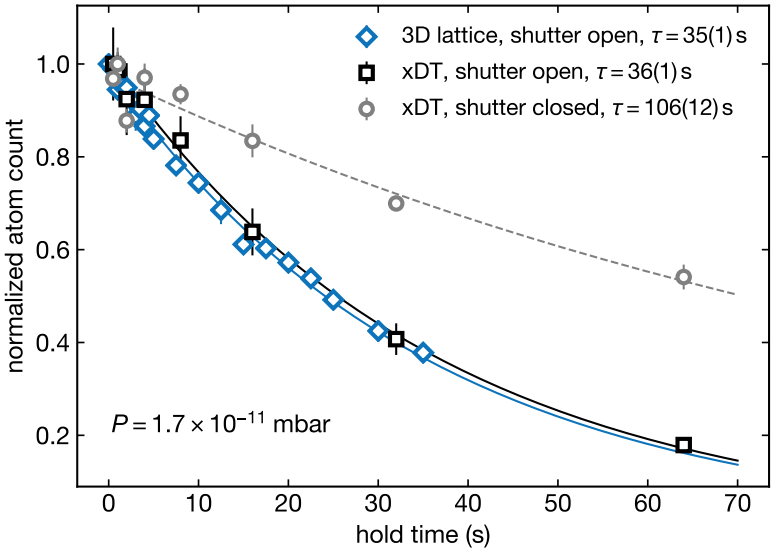

Figure 2.15 – The lifetime of a non-interacting degenerate $|g\rangle$ Fermi gas of $\sim 10^4$ spin-polarized ^{173}Yb atoms at a background pressure $P = 1.7 \times 10^{-11}$ mbar. The 1/e-lifetime τ in an isotropic 3D magic-wavelength lattice $V_{x,y,z} = 30\,E_{\mathrm{rec}}$ (diamonds) matches the one in a crossed 1064 nm optical dipole trap (squares). These lifetimes with the atomic beam shutter open are reduced by a factor 3 compared to the closed shutter case (squares).

Excited-state losses The $|e\rangle$ atoms are subject to additional single particle loss and decay processes. Independent of the confinement, the $|e\rangle$ atoms can decay spontaneously to $|g\rangle$, with a decay rate $k_n = 38$ mHz [106] given by the natural linewidth of the transition. This decay timescale is comparable to the loss rate from the vacuum background collisions. Moreover, both the magic-wavelength light and the 670 nm light of the SDL cause repumping to $|g\rangle$ and photon scattering on long timescales. The repumping occurs mainly via the transitions to the intermediate states $(6s5d)^3D_1$ and $(6s7s)^3S_1$. The SDL wavelength is significantly closer to the $^3P_0 \rightarrow {}^3S_1$ transition at 649.1 nm which should lead to an enhanced scattering and repumping rate.

We quantify the loss rates experimentally for a typical lattice configuration used for the spin-exchange and spectroscopy experiments in the next chapters (for the relative beam alignment, see Fig. 2.12). The SDL at a lattice depth of $V_z = 5.8\,E_{\mathrm{rec}}^z$ is aligned perpendicular to two

magic-wavelength lattices, both $V_\perp = 45\,E_{\mathrm{rec}}^{\perp}$ deep (for the beam alignment, see also Fig. 2.12). A spin-polarized sample of $|e\downarrow\rangle$ atoms is held for variable time in this configuration. The $|g\rangle$ atoms, populated through repumping and decay, and the $|e\rangle$ population are imaged separately [see Fig. 2.16(a)]. For comparison, a reference measurement is conducted using an isotropic, magic-wavelength 3D lattice. Using $V_{x,y,z} = 30\,E_{\mathrm{rec}}$, the total magic-wavelength light power $V_{\mathrm{m}} = 90\,E_{\mathrm{rec}}$ is maintained compared to the previous measurement.

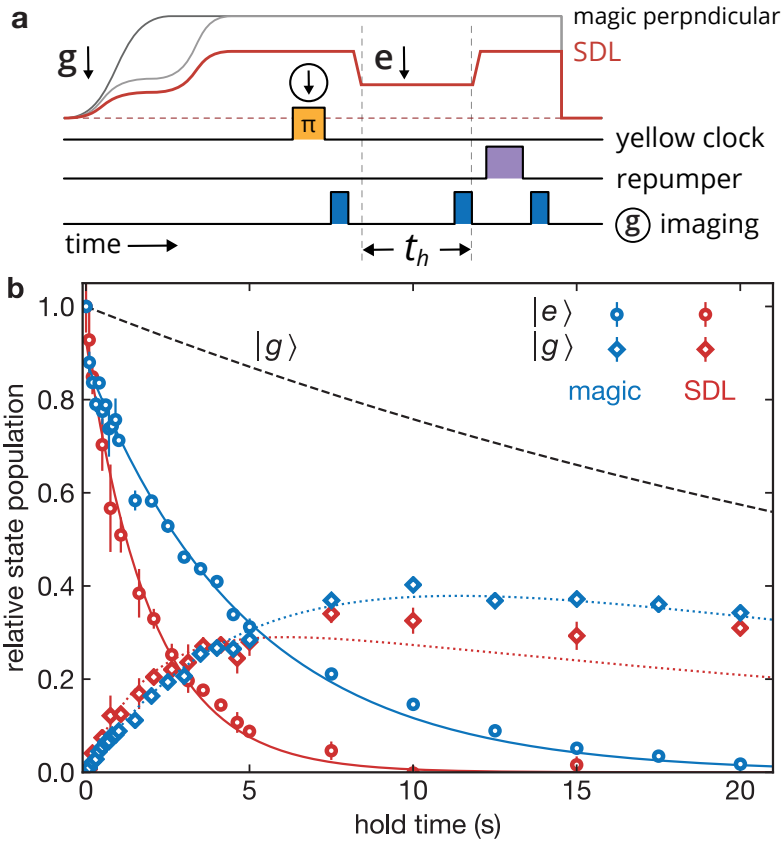

Figure 2.16 – (a) Experiment sequence for measuring the loss and repumping rates of spin-polarized $|e\rangle$ atoms in the SDL: A sample of $|g\downarrow\rangle$ atoms ($m_F = -5/2$) is excited to $|e\downarrow\rangle$ via a high-power π pulse (1 mW) and held for variable time t_h. The first imaging pulse clears away residual $|g\rangle$ before hold, the second pulse images the $|g\rangle$ population after the hold time, and the third pulse images the $|e\rangle$ population after being repumped to $|g\rangle$. (b) $|e\rangle$ losses due to photon scattering, repumping by lattice light, natural decay, and background collisions in a 3D lattice: Atom numbers in $|e\rangle$ (circles) and $|g\rangle$ (diamonds) for varying hold time in the 30 E_{rec} isotropic magic-wavelength lattice (blue) and in the 5.8 E_{rec}^{z} SDL with 45 E_{rec} perpendicular magic-wavelength confinement (green). Error bars indicate the standard error of the mean. Solid and dotted lines are fits of the one-body rate equation for the coupled eg decay dynamics. Dashed line shows the decay of $|g\rangle$ due to vacuum background collisions.

The time traces in Figure 2.16(b) show that the additional SDL potential induces an increased $|e\rangle$ loss rate compared to the magic-wavelength confinement. Loss rates can be extracted from the data by fitting a coupled system of rate equations for $|g\rangle$ and $|e\rangle$ atom numbers

n_e and n_g that includes possible single-particle loss processes:

$$\begin{aligned}\dot{n}_e &= -(k_{\mathrm{vac}} + k_n + k_{\mathrm{lat}})n_e \\ \dot{n}_g &= -k_{\mathrm{vac}} n_g + \xi\left[(k_n + \beta k_{\mathrm{lat}})n_e\right].\end{aligned} \tag{2.33}$$

The vacuum loss rate k_{vac} is the same for both orbitals and is taken from the independent measurement above. The clock state $|e\rangle$ can spontaneously decay to $|g\rangle$ at a rate k_n. Finally, light of a given lattice configuration induces a loss rate k_{lat} for $|e\rangle$ atoms where a fraction β is repumped to $|g\rangle$. The lattice induced loss rate $k_{\mathrm{lat}} = k_{\mathrm{m}} + k_{\mathrm{SDL}}$ has contributions k_{m} from the magic-wavelength light and k_{SDL} from the SDL. Unequal detection efficiencies in the detection of $|e\rangle$ and $|g\rangle$ atoms are captured by the parameter ξ.

For the SDL configuration specified above, the extracted overall 1/e-lifetime of a spin-polarized $|e\rangle$-sample is $\tau_e = 1/(k_{\mathrm{vac}} + k_n + k_{\mathrm{lat}}) = 2.0\,\mathrm{s}$, compared to 4.9 s for the purely magic confinement. This exceeds the experimentally relevant time scales for the experiments presented in the next chapters. Normalized by the total lattice potential depth, we obtain a relatively small $|e\rangle$ loss rate $k_{\mathrm{m}}/(V_m) = 1.5(1)\,\mathrm{mHz}/E_{\mathrm{rec}}^{\mathrm{m}}$ induced by the magic-wavelength lattices. However, the rate $k_{\mathrm{SDL}}/V_{\mathrm{SDL}}^{g} = 51(4)\,\mathrm{mHz}/E_{\mathrm{rec}}^{\mathrm{SDL}}$ caused by the SDL light could be a limiting factor when further increasing the lattice intensity or decreasing the lattice wavelength to obtain larger polarizability ratios.

2.7 Limiting excited-state losses

One essential idea behind the choice of 670 nm as the SDL wavelength is to localize atoms in the excited orbital $|e\rangle$ ($^3\mathrm{P}_0$), relative to atoms in $|g\rangle$ ($^1\mathrm{S}_0$). Dissipative dynamics via strong inelastic collisions of $|e\rangle$ atoms (*ee* losses) can thereby be reduced while maintaining the mobility of $|g\rangle$. This is particularly important for the realization of the Kondo lattice model where we do not only require dilute magnetic impurities but rather a half-filled lattice band of localized magnetic moments [58]. In the following, we will present an independent measurement of the *ee* loss, characterizing the setup used to study the interorbital spin exchange in the SDL (in Chapter 5). We will interpret the resulting dynamics in terms of the expectations from a dissipative Fermi-Hubbard model, similar to [188]. In this setting, *ee* losses are mediated by a relatively slow superexchange process and the possible buildup of spin correlations on the $|e\rangle$ superexchange time scale can further reduce the effective loss rate.

2.7.1 Excited-state losses in a 3D lattice

To our knowledge, the microscopic origin behind the *ee* loss process has not been investigated systematically. However, recently measured particle loss dynamics in quasi-2D bulk systems [97] as well as in a 3D optical lattice [188] are compatible with rate equations based on a two-body loss process. By measuring particle loss rates of a nuclear-spin balanced mixture of $|e\rangle$ atoms in a 1D optical lattice, Scazza et al. have determined a two-particle loss coefficient of $\beta_{ee} = 2.2(6)\times10^{-11}\,\mathrm{cm}^3/\mathrm{s}$ for ^{173}Yb [59, 97]. A comparable value of $\beta_{ee} = 5(3)\times10^{-11}\,\mathrm{cm}^3/\mathrm{s}$ has been obtained for ^{171}Yb [95].

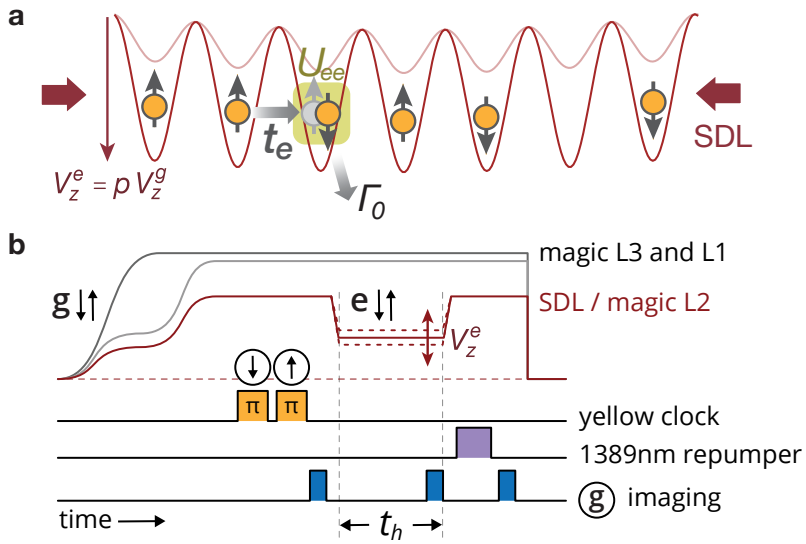

Figure 2.17 – (a) Excited-state collision process in the SDL with close to half $|e\rangle$ filling. Effective dissipative dynamics are controlled by nearest-neighbor tunneling t_e, on-site interaction U_{ee} and loss rate Γ_0. (b) Experiment sequence for measuring the collisional excited-state losses of a two-spin $|e\rangle$ mixture in the SDL: $|g\downarrow\rangle$ and $|g\uparrow\rangle$ ($m_F = \pm 5/2$) are excited to $|e\downarrow\rangle$ and $|e\uparrow\rangle$ via two high-power π pulses and held for time t_h at variable SDL depth V_z^e. The first imaging pulse clears away residual $|g\rangle$ before hold, the second pulse images the $|g\rangle$ population after the hold time, and the third pulse images the $|e\rangle$ population after a 2 ms repumping pulse to $|g\rangle$.

As depicted in Fig. 2.17(a), we are typically working with $|e\rangle$ densities of $n_e = n_{e\uparrow} + n_{e\downarrow} \leq 1$, avoiding doubly occupied sites. Yet, for low depths of the SDL, collisions mediated by next-neighbor $|e\rangle$ tunneling cannot be neglected. As described in [188], the ee losses in such lattice experiments are well characterized by an on-site loss process in the so-called dissipative Hubbard model. Along with tunneling t_e and on-site interaction U, on-site losses are captured by a loss rate Γ_0. As long as the scattering dynamics happens in the lowest lattice band, the two-particle loss coefficient β can be related to an on-site loss rate via [143]

$$\Gamma_0 = \beta \int \mathrm{d}^3 r\, |w_1(\mathbf{r})|^2 |w_2(\mathbf{r})|^2 \,. \tag{2.34}$$

Here, $w_{1/2}$ are the lowest band Wannier functions of the collision partners. Note that these can in general be different for mixed confinement, e.g. for interorbital (eg) collisions in the SDL. Like the on-site interaction strength U_{ee}, the on-site loss rate Γ_0 scales linearly with the two-particle overlap. Using the measured scattering length $a_{ee} = 306(10)\,a_0$ for ^{173}Yb [59], we obtain a ratio

$$\alpha \equiv \frac{U_{ee}}{\hbar \Gamma_0} = 3.4(9)\,, \tag{2.35}$$

independent of the lattice depth.

Along with the nearest-neighbor tunneling t, this ratio is a critical parameter entering the scaling of the dynamics in the dissipative Fermi Hubbard model. The exact dynamics of the

system can be obtained from the solution of an appropriate master equation, as attempted in [188] for small system sizes. However, in the limit of small tunnel mobility ($t_e \ll U_{ee}$ and $t_e \ll \hbar\Gamma_0$), the particle number dynamics can be described in a simplified model, where intermediate interacting states are integrated out as virtual states. Following [143, 188], the system can then be described by a rate equation for the on-site density

$$\dot{n}_e(t) = -p_N \kappa(t)\, n_e^2(t) - k_1 n_e(t) \tag{2.36}$$

with a time-dependent two-body loss coefficient $\kappa(t) = 4q\Gamma g^{(2)}(t) n_e(0)$. The initial state is described by the on-site density $n_e(0)$, the factor $q = 2$ gives the number of nearest neighbors in a 1D setup and $p_N = \frac{N-1}{N}$ is the probability of the neighboring atom being in a different nuclear spin state, in a balanced, uncorrelated mixture of N spin states. Further, the loss coefficient is governed by the effective loss rate [143, 189, 190]

$$\Gamma = 4\frac{t_e^2}{\hbar U_{ee}} \frac{\alpha}{1+4\alpha^2} \tag{2.37}$$

which depends on the fixed on-site parameter $\alpha = U_{ee}/\hbar\Gamma_0$ determined above. Additionally, we will see that the loss dynamics is further influenced by time-dependent spin correlations, defined by the standard nearest-neighbor correlation coefficient $g^{(2)}$ [191].

Two qualitatively different regimes can be identified for this "superexchange-type" loss process. If $\alpha \ll 1$, the virtual intermediate state is governed by the inelastic scattering rate $\hbar\Gamma_0$ and the effective loss rate scales as $\Gamma \propto t_e^2/(\hbar^2\Gamma_0)$. This regime is often called the quantum Zeno regime because one can interpret the inelastic process as a continuous measurement process of the doubly occupied site population, effectively inhibiting losses [143]. Notably this mechanism has been successfully employed to suppress lossy chemical reactions between KRb molecules [189, 190] in weak lattice systems.

In the other extreme $\alpha \gg 1$, where elastic interactions dominate the intermediate state, the effective loss rate Γ vanishes again, in this case due to the formation of a Mott insulating state with reduced mobility.

The experimentally determined ratio $\alpha = 3.4(9)$ for the ee losses in ^{173}Yb is described by an intermediate regime where both inelastic and elastic collisions contribute significantly. The loss rate in Eq. (2.37) can be specified in units of the superexchange time scale $\tau^e_{\mathrm{SE}} = \hbar U_{ee}/t_e^2$ for the $|e\rangle$ atoms, as $\Gamma \approx 0.29/\tau^e_{\mathrm{SE}}$. Sponselee et al. study this intermediate regime of the dissipative Fermi-Hubbard using two and six-spin mixtures of ^{173}Yb in an array of 1D magic-wavelength lattice systems. The ee loss dynamics is modeled in terms of a master equation and the simplified rate equation approach described above [188]. When removing the effect of single particle $|e\rangle$ losses, they find that after an initial decay happening on the superexchange timescale, the two-particle loss process stops and the $|e\rangle$ atom number settles to a finite plateau. This is attributed to the buildup of spin correlations in a sample of initially uncorrelated atoms with $g^{(2)}(0) = g_0^{(2)} = 1$ by means of the atom loss process. The measured loss dynamics is only compatible with an exponential decay to zero of the nearest-neighbor correlation function

$$g^{(2)} = g_0^{(2)} e^{-t/\tau_2} \tag{2.38}$$

on a timescale $\tau_2 \propto \tau^e_{\mathrm{SE}}$, which is also suggested by their master equation approach. A final value of $g^{(2)} = 0$ could be an indicator for a state without nearest neighbors, a ferromagnetically ordered state or more complicated entangled states. By numerically studying the spin correlations, they find that the long time steady state with $g^{(2)} = 0$ should indeed be given by a highly entangled Dicke state[11], as predicted before for purely inelastic collisions in two-spin fermionic mixtures [81].

2.7.2 Measurement results

In order to quantify the collisional *ee* losses in our setup, we prepare a balanced $|e\uparrow\rangle$-$|e\downarrow\rangle$-mixture at densities comparable to the spin-exchange measurements in Chapter 5. The experiment sequence is illustrated in Fig. 2.17. By means of clock-line interaction spectroscopy, we ensure that the initial spin mixture of $|g\uparrow\rangle$ and $|g\downarrow\rangle$ ($m_F \in \pm 5/2$) in the lattice is balanced and that lattice sites are mainly singly occupied. The temperature of the degenerate $|g\rangle$ atoms is estimated to $T/T_F \approx 0.2$ in units of the Fermi temperature before the loading into the lattice. This should lead to an initial spin distribution with close to half filling ($n_g = n_\uparrow + n_\downarrow = 1$ particle per lattice site). The perpendicular confinement is fixed to $V_\perp = 30\, E^\perp_{\mathrm{rec}}$. The depth of the SDL along the remaining direction can be varied and the potential depth experienced by the $|e\rangle$ atoms is given by V^e_z. Both spin states are excited individually to $|e\uparrow\rangle$ and $|e\downarrow\rangle$ using short subsequent π pulses (Rabi frequency $\Omega = 2\pi \times 1.6\,\mathrm{kHz}$ at a quantization B-field of 10 G) in a deep SDL with $V^e_z = 28.8\, E^z_{\mathrm{rec}}$ that prevents tunneling during the state-preparation. A $20\,\mu$s imaging pulse on the $^1\mathrm{S}_0 \rightarrow {}^1\mathrm{P}_1$ transition removes residual $|g\rangle$ atoms after the preparation. The SDL depth is then lowered in a fast 1 ms ramp to different probe depths where the $|e\rangle$ spin mixture is held for variable time t_h. During this hold time, $|g\rangle$ can be repopulated through repumping by the lattice light, natural decay of $|e\rangle$ (as described in Section 2.6) or possibly the *ee* inelastic collision process. These $|g\rangle$ atoms are imaged and removed at the end of the hold time. Finally, the SDL is ramped up again for the detection of the $|e\rangle$ atoms which is performed using a 2 ms repumping pulse on the 1389 nm transition and subsequent imaging of the repumped $|g\rangle$ atoms.

The resulting dynamics for the $|e\rangle$ and $|g\rangle$ population is shown in Fig. 2.18. For every SDL depth, the data are normalized to the initial $|e\rangle$ atom count $n_e(0)$. Due to the finite length of the state preparation and detection, the initial atom number varies slightly with the confinement. For vanishing SDL depth, the dynamics happens faster leading to a lower initial atom number. For completeness, the unnormalized time traces are shown in Fig. D.1(a-b).

Considering the logarithmic time scale of Fig. 2.18, it becomes clear that the $|e\rangle$ loss for most confinements can be described by a fast initial loss rate followed by a slow long-term decay, comparable to the behavior observed in [188]. In the limit of vanishing SDL (quasi-1D systems), the $1/e$ decay time is on the order of 100 ms, much faster than the expected single-particle loss rates (dotted lines) for the given lattice depths. For increasing SDL depth, the initial loss rate decreases and the overall losses are dominated by the single-particle loss.

[11] A highly entangled state with a spin wave function that is spatially symmetric around $\hat{z}$ and carries maximum possible total angular momentum S and a minimal uncertainty in S_z.

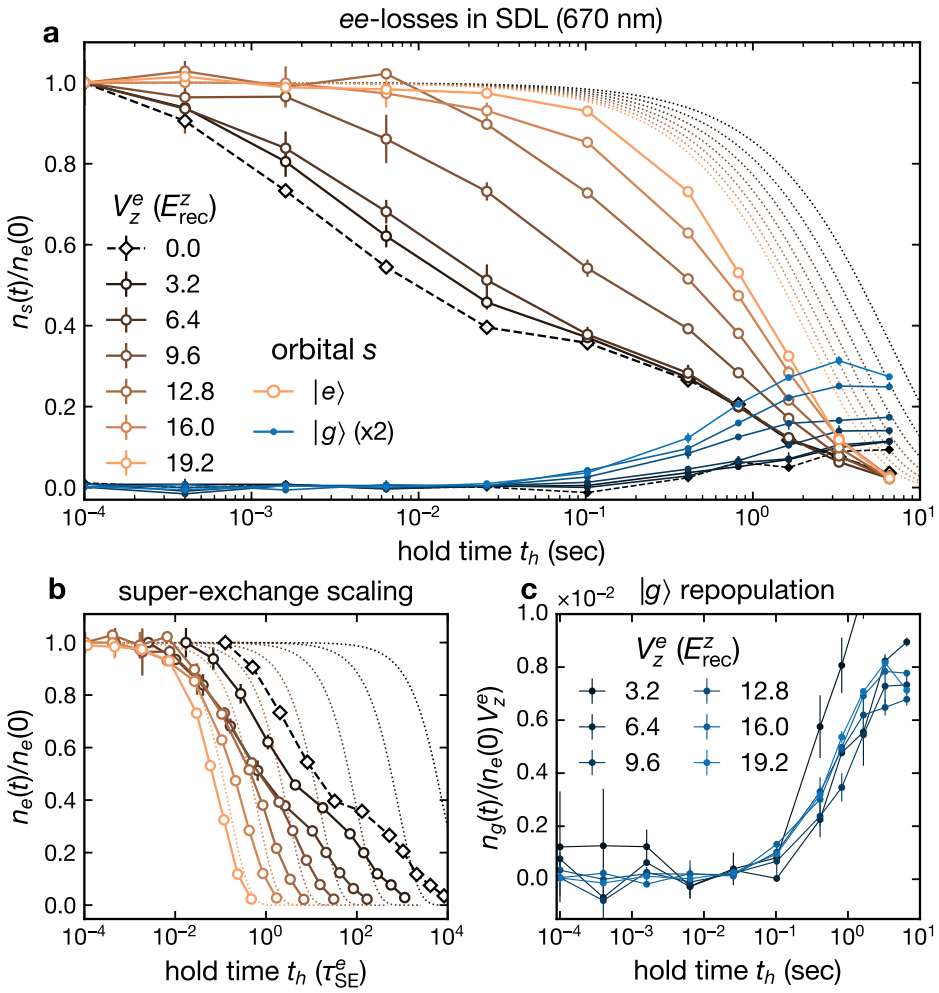

Figure 2.18 – Measured excited-state loss dynamics in a two-spin $|e\rangle$ mixture. (a) Dynamics of the $|e\rangle$ (empty markers) and $|g\rangle$ (full markers) population, normalized to the initial atom number $n_e(t=0)$ for different SDL depths V_z^e and fixed perpendicular magic lattice confinement $V_\perp = 30\,E_{rec}^\perp$. Dotted lines in (a) and (b) show the expected single-particle loss dynamics from Section 2.6 for comparison. (b) Data from (a) with hold time scaled in units of the superexchange time scale τ_{SE}. (c) $|g\rangle$ population, normalized to SDL light intensity. All data are the mean of two realizations. Error bars denote the standard error of the mean.

In order to verify the superexchange mediated loss model introduced above, we plot the loss dynamics in units of the lattice-depth dependent $|e\rangle$ superexchange time scale τ^e_{SE} in Fig. 2.18(b). We observe that the initial loss dynamics roughly coincide for the lower SDL depths. In deeper lattice systems, the superexchange time scale τ^e_{SE} for the two-body collisions becomes comparable to the single-particle lifetime and it becomes harder to disentangle the two time scales.

The repopulation of the $|g\rangle$ atoms is shown in Fig. 2.18(a). As expected from pure lattice repumping dynamics, an increased repopulation rate is measured for deeper SDL. In Fig. 2.18(c) we show the same data, normalized to the SDL depth. For large V^e_z where the single-particle losses are dominated by the SDL intensity, the normalized $|g\rangle$ repopulation dynamics coincide. Note, that this would indeed be the expected behavior in the absence of *ee* collisional losses. However, the final $|g\rangle$ population after a given hold time is the result of an integration of all repopulation rates over previous times. In the low-lattice depth regime, increased *ee* losses lead to a much faster drop in the $|e\rangle$ atom number and therefore, a smaller $|g\rangle$ repopulation fraction through single-particle effects should be expected at large times. From the data, a significant creation of trapped $|g\rangle$ atoms as a product of the *ee* collision process can be excluded since a measurable repopulation occurs only after a fixed absolute time $t_h \sim 100$ ms, independent of lattice depth.

To obtain more quantitative information on the *ee* loss process and separate it from the single-particle dynamics, we carry out a fit of the superexchange based rate equation Eq. (2.36) to the same data. Instead of "normalizing" the data to the single particle losses, as done in [188], we fit the full rate equation, including the single-particle losses. The solution of Eq. (2.36) for the $|e\rangle$ population dynamics can be given analytically as

$$n_e(t) = n_e(0)\frac{(1+k_1\tau_2)e^{-k_1 t}}{1+k_1\tau_2+p_N\tau_2\kappa(0)\left(1-e^{-t(k_1+1/\tau_2)}\right)}. \tag{2.39}$$

We choose the correlation buildup time τ_2, the initial decay rate $\kappa(0)$ and the single-particle loss rate k_1 as free fit parameters. In Fig. 2.19, the fit results are presented. We find very good agreement with the data for all lattice depths and realize that the $|e\rangle$ loss takes place within the first superexchange time. For visual separation of the two- and single-particle loss process, the effect of the extracted single-particle loss is subtracted from both the fit and the measured data[12]. Similar to [188], we find that the fast initial two-particle loss then stops after a time $\tau_2 < \tau^e_{\mathrm{SE}}$ and, with the single particle loss subtracted, the $|e\rangle$ population settles on a plateau

$$n_e(t\to\infty) = \frac{n_e(0)}{1+p_N\kappa(0)\tau_2} \tag{2.40}$$

that can directly be related to the decay time. In contrast to [188], we probe a wider range of lattice depths and find a significant variation of τ_2, and thereby the remaining atom number. Deep lattices lead to faster correlation decay times and larger remaining $|e\rangle$ population[13].

[12] Note that we do not show the data set $V^e_z = 19.2\,E^z_{\mathrm{rec}}$. There, k_1 and $1/\tau_2$ are on the same order and the fit parameters become strongly entangled.

[13] A trend in the same direction can actually also be read off the plotted data in [188].

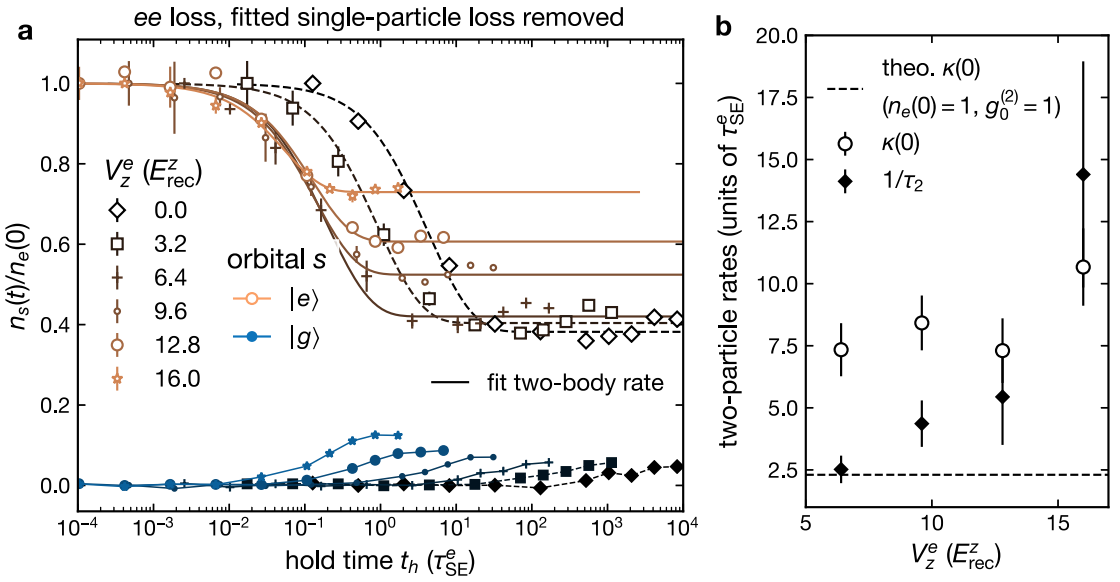

Figure 2.19 – (a) Fit (solid lines) of the rate equation solution Eq. (2.39) for the ee loss process to the measured $|e\rangle$ population data (empty symbols) from Fig. 2.18. The free fit parameters are the correlation buildup time τ_2, the initial decay rate $\kappa(0)$ and the single-particle loss rate k_1. The effect of the extracted single-particle loss is subtracted from both the fit and the measured data for visual separation of the two-body loss process. The lattice superexchange model is invalid for the lowest lattice depths (dashed). Repopulated $|g\rangle$ density (filled symbols) is shown for comparison. (b) Extracted two-body loss coefficients versus SDL depth. Error bars are the standard errors of the fit. Dashed line indicates theoretically expected $\kappa(0)$ for balanced, uncorrelated two-spin mixture at half filling.

Figure 2.19(b) shows the extracted two-particle loss coefficients and their dependence on lattice depth. The superexchange model, based on the lowest-band 3D Wannier functions, is only justified in the tight binding regime and we therefore ignore the two weakest lattice configurations. A description for these systems, close to quasi-1D, could be given in terms of a dissipative Lieb-Liniger model [192]. The derivative of $n_e(t)$ at zero time is given by $\dot{n}_e(0) = -k(0)p_N\, n_e(0)$ and should be independent of τ_e. It should depend only on density and correlation properties of the initial state and is proportional to the effective loss rate $\Gamma \propto 1/\tau_{SE}^e$. Indeed, we find an approximately constant rate $\kappa(0) \approx 8/\tau_{SE}^e$, independent of the lattice depth. This initial decay rate is faster than the theoretically expected $\kappa(0) \approx 2.3/\tau_{SE}^e$ for an initially balanced and uncorrelated two-spin mixture. The same discrepancy is found in [188] and further research on the loss model will be required. The model does note include potential repopulation of $|g\rangle$ through the ee loss process, and therefore also potential additional strong eg losses on short timescales are ignored. A more complete model should also include scattering in multiple lattice bands, modifying effective densities and enabling more scattering channels [190].

Comparison with magic-wavelength lattice In the realization of Kondo-type models, the relevant time scales are given in units of the $|g\rangle$ tunneling time $\tau_g = \hbar/t_g$. The polarizability

ratio of our SDL is chosen such that $|e\rangle$ atoms are more localized than $|g\rangle$, and during several $|g\rangle$ tunneling times, the $|e\rangle$ population is preserved. In contrast, the simulation of the multiorbital Fermi-Hubbard model, as proposed for example in [193] for the realization of long-range ferromagnetic order, requires state-independent confinement. There, $|g\rangle$ and $|e\rangle$ have the same mobility and *ee* losses can significantly limit the attainable time scales.

The *ee* losses in the magic-wavelength lattice have been measured in a sequence analogous to the one in the SDL, with the longitudinal SDL replaced by a magic-wavelength lattice. The full data for a large range of lattice depths can be found in Fig. D.1(c-d). In these plots, loss rates identical to the SDL setting are found for small times in units of the $|e\rangle$ tunneling time τ_e. Only at large times or large intensities, the photon-scattering induced $|e\rangle$ losses are reduced compared to the SDL.

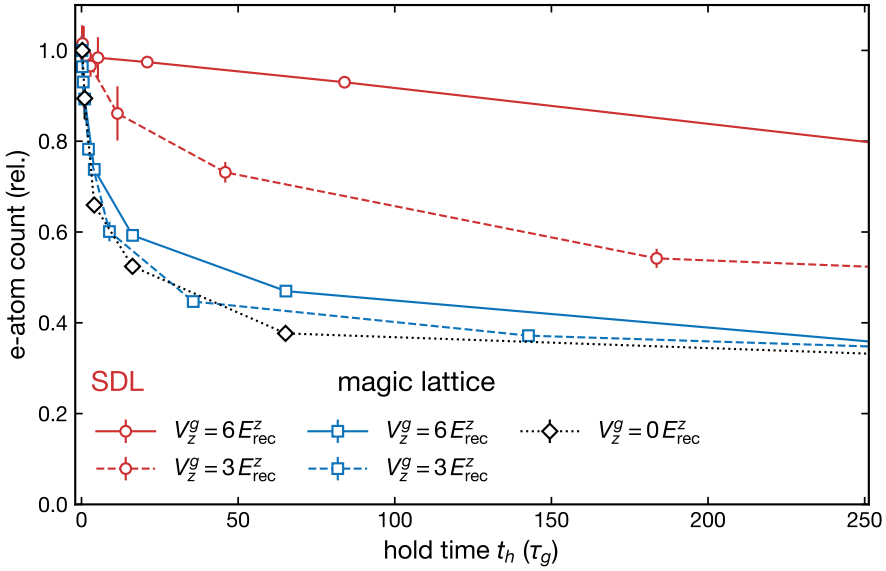

Figure 2.20 – Comparison of measured excited-state loss dynamics in the longitudinal SDL (circles) and magic-wavelength lattice (squares) with identical $|g\rangle$ mobility. Atom count is normalized to the initial atom number $n_e(t=0)$. The hold time is in units of the $|g\rangle$ tunneling time $\tau_g = \hbar/t_g$ along the longitudinal lattice of variable depth V_z^g. Perpendicular magic confinement is fixed to $V_\perp = 30\,E_{\rm rec}^\perp$.

In Fig. 2.20, we compare the $|e\rangle$ lifetime in the SDL and the magic-wavelength lattice, given the same $|g\rangle$ mobility, that is the same $|g\rangle$ potential depth $V_z^g/E_{\rm rec}^z$. After around 50 $|g\rangle$ tunneling times in a $V_z^g = 6\,E_{\rm rec}^z$ magic-wavelength lattice, half of the $|e\rangle$ atoms are lost in a fast initial loss process (in the superexchange model for the losses introduced above, this is roughly the *ee* correlation buildup time τ_2). In comparison, the SDL localizes the $|e\rangle$ particles and only $\sim 5\%$ are lost in the same time, enabling the study of several $|g\rangle$ superexchange times $\tau_{\rm SE}^g$ in Chapter 5.

2.8 Multiorbital physics in the state-dependent lattice

Above, we have characterized the state-dependent mobility and lifetime of separate single-orbital spin mixtures in the SDL. Utilizing AEA mixtures in two electronic orbitals instead could prove valuable insights into the physics of two-orbital many-body systems governed by spin-orbital interactions [58]. Notably, this includes the simulation of the (anti-)ferromagnetic Kondo lattice model (KLM) and Kugel-Khomskii model which are used to describe orbital magnetism and Kondo coupling in heavy fermion compounds, as well as colossal magnetoresistance (CMR) in manganites and other transition-metal oxides with perovskite structure [4, 21, 22]. Recently, the realization of a Kondo impurity model with varying coupling anisotropy has also been proposed in the context of dilute two-orbital AEA mixtures [34].

In this section, we first introduce the two-orbital version of the SU(N) FHM, providing a microscopic description of the interorbital interactions in the presence of the SDL. We will briefly review the Kondo impurity and Kondo lattice model and the hallmark features of the strongly correlated low-temperature phases. It will be demonstrated how both models are naturally realized experimentally as limiting cases of the two-orbital FHM in our setup. Possible state-preparation techniques and observables of characteristic phases are discussed.

2.8.1 The two-orbital Fermi-Hubbard model

In Section 1.5.4, we have shown how a spin-exchanging interaction between the electronic orbitals $|g\rangle$ and $|e\rangle$ emerges from the two independent scattering channels $|eg^-\rangle$ and $|eg^+\rangle$. The direct and exchange part of the interorbital interactions can be expressed in second quantization as in Eq. (1.63). Thus, when treating mixtures of $|g\rangle$ and $|e\rangle$ atoms in an optical lattice, a single-orbital Hubbard model [Eq. (1.58)] is not sufficient and all four interaction channels $|gg\rangle$, $|ee\rangle$, $|eg^+\rangle$, $|eg^-\rangle$ need to be taken into account. This is accomplished by the two-orbital Fermi-Hubbard model (2FHM) proposed in [58], which also captures the orbital state-dependent mobility in the SDL.

To arrive at this model, we express the field operators $\hat{\psi}_{\alpha\sigma}(\mathbf{r}) = \sum_j w_{i\alpha}\hat{c}_{i\alpha\sigma}(\mathbf{r})$ in Eq. (1.63) in the basis of the lowest-band Wannier functions $w_{i\alpha}$. Here, $\hat{c}^\dagger_{i\alpha\sigma}$ creates a particle on site i, in the electronic orbital $|\alpha\rangle$ ($\alpha \in \{e, g\}$) and the nuclear spin projection $\sigma \in \{-F, -F+1, ..., F\}$, with the corresponding number operator $\hat{n}_{i\alpha\sigma} = \hat{c}^\dagger_{i\alpha\sigma}\hat{c}_{i\alpha\sigma}$. Neglecting the Gaussian intensity envelope of the optical lattice, the total Hamiltonian describing eg mixtures in the SDL becomes

$$\begin{aligned}\hat{H}_{\mathrm{2FHM}} = &- \sum_{\alpha,\langle i,j\rangle,\sigma} t_\alpha \hat{c}^\dagger_{i\alpha\sigma}\hat{c}_{j\alpha\sigma} + \sum_{\alpha,i}\frac{U_{\alpha\alpha}}{2}\hat{n}_{i\alpha}(\hat{n}_{i\alpha}-1) \\ &+ V_{\mathrm{d}}\sum_i \hat{n}_{ig}\hat{n}_{ie} + V_{\mathrm{ex}}\sum_{i,\sigma,\sigma'}\hat{c}^\dagger_{ig\sigma}\hat{c}^\dagger_{ie\sigma'}\hat{c}_{ig\sigma'}\hat{c}_{ie\sigma},\end{aligned} \tag{2.41}$$

with $\langle i, j\rangle$ indicating neighboring lattice sites. The first term describes the state-dependent tunnel mobility, with $t_e \ll t_g$ in our implementation of the SDL. The second and third term model the intraorbital and direct interorbital interactions, respectively. Both are spin-independent

and depend only on the total on-site occupation numbers $\hat{n}_{i\alpha} = \sum_\sigma \hat{n}_{i\alpha\sigma}$ of the orbitals $|\alpha\rangle$. In contrast, the last term lifts the degeneracy in the spin degree of freedom and constitutes an on-site interorbital spin-exchange interaction. However, an overall SU(N) symmetry of the Hamiltonian remains as it commutes with the generalized spin-permutation operator, defined in Eq. (1.64): $\hat{S}_\sigma^{\sigma'} = \sum_{i\alpha} \hat{c}^\dagger_{i\alpha\sigma}\hat{c}_{i\alpha\sigma'}$.

The Hubbard interaction parameters can be obtained from the Wannier function overlaps [see Eq. (2.20)]

$$U_{\alpha\alpha} = \frac{4\pi\hbar^2}{m} a_{\alpha\alpha} \int \mathrm{d}^3 r\, |w_\alpha(\mathbf{r})|^4 \quad \text{and} \quad U^{\pm}_{\mathrm{eg}} = \frac{4\pi\hbar^2}{m} a^{\pm}_{\mathrm{eg}} \int \mathrm{d}^3 r\, |w_{\mathrm{g}}(\mathbf{r})|^2 |w_{\mathrm{e}}(\mathbf{r})|^2 \tag{2.42}$$

yielding

$$\begin{aligned} V_{\mathrm{d}} &= \frac{1}{2}\left(U^{+}_{\mathrm{eg}} + U^{-}_{\mathrm{eg}}\right), \\ V_{\mathrm{ex}} &= \frac{1}{2}\left(U^{+}_{\mathrm{eg}} - U^{-}_{\mathrm{eg}}\right). \end{aligned} \tag{2.43}$$

Note that this derivation is only valid in the lowest-band, tight-binding approximation. As we will see in Chapter 4 and Chapter 5, the scattering properties in weak SDL potentials can be significantly altered by the lattice band structure, due to the large orbital triplet scattering length of ^{173}Yb. Notably, additional on-site bound states become energetically accessible enabling tunability of the exchange interactions.

Neglecting additional tuning mechanisms, the interaction strengths are largely fixed by the scattering lengths for a given atomic species and isotope. Slight variability is enabled through the scaling of the Wannier functions with the external confinement. The ratio between the on-site interactions and the tunneling rate, however, can be widely tuned by means of the lattice depth. The same holds for the ratio of the tunneling rates t_g/t_e (see Section 2.2.3).

The exchange energy V_{ex} in Eq. (2.41) quantifies the energy difference between an on-site orbital triplet $|eg^+\rangle$ and singlet $|eg^-\rangle$. When two nuclear spin states are occupied, the interorbital interactions are indirectly determined by the spin state through the fermionic antisymmetrization (see Section 1.5.4). In the case of ^{173}Yb, the on-site spin triplet is lower in energy, with $V_{\mathrm{ex}} > 0$, indicating ferromagnetic (FM) exchange interactions [59, 60]. The opposite sign of the exchange interactions $V_{\mathrm{ex}} < 0$ is found for ^{171}Yb, leading to anti-ferromagnetic (AFM) coupling [88, 158].

This 2FHM, naturally realized with fermionic AEA in a SDL, features both orbital state-dependent mobility and spin-orbital coupling. The realization of orbital magnetism in the full 2FHM using AEA is discussed, for example, in [193, 194]. In the following, we will focus on the possible implementation of the Kondo impurity model and KLM, emerging from the 2FHM for different lattice band fillings, in the limit of a fully localized $|e\rangle$ orbital (see Fig. 2.21).

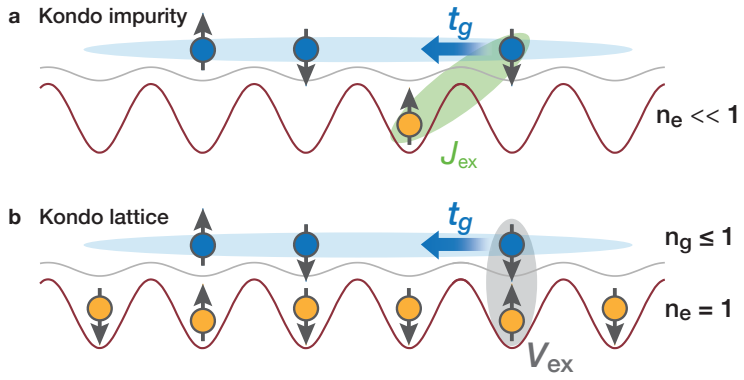

Figure 2.21 – Simulation of Kondo models using AEA in the orbital state-dependent lattice. (a) In the Kondo impurity model, dilute ($n_e \ll 1$) localized $|e\rangle$ impurities (yellow) are subject to spin-exchange coupling (J_{ex}) with itinerant $|g\rangle$ atoms (blue). $J_{\mathrm{ex}} \propto t_g^2/U_{\mathrm{eg}}^+ - t_g^2/U_{\mathrm{eg}}^-$ is mediated via next-neighbor super-exchange processes (see Chapter 5). (b) The Kondo lattice model features a unit-filled lattice of localized $|e\rangle$ magnetic moments ($n_e = 1$) undergoing on-site spin-exchange interactions $V_{\mathrm{ex}} = (U_{\mathrm{eg}}^+ - U_{\mathrm{eg}}^-)/2$ with mobile $|g\rangle$ atoms of variable filling n_g.

2.8.2 The Kondo impurity model

Exchange interactions between different electronic orbitals play a central role in many solid-state systems. One famous example is the Kondo effect, originally observed in the context of a resistivity anomaly in dilute magnetic alloys [1]. A logarithmic increase of the resistivity for low temperatures occurs in these materials that can be attributed to a quenching of impurity magnetic moments and the formation of a local Fermi liquid [195]. The physics of the Kondo effect, and more general, the physics of spin-flip scattering between a bath of mobile conduction electrons and dilute, localized impurities can be captured by the Kondo impurity model[14] [1, 4]:

$$\hat{H}_{\mathrm{K}} = \sum_{k,\sigma} \epsilon(k)\, \hat{c}^{\dagger}_{kg\sigma} \hat{c}_{kg\sigma} + \frac{J}{2M} \sum_{k,k',\sigma,\sigma'} (\hat{\mathbf{S}} \cdot \boldsymbol{\tau}_{\sigma\sigma'})\, \hat{c}^{\dagger}_{k'g\sigma'} \hat{c}_{kg\sigma} \tag{2.44}$$

Here, $\hat{\mathbf{S}} = (\hat{S_x}, \hat{S_y}, \hat{S_z})$ denotes a localized impurity spin and $\boldsymbol{\tau} = (\tau_x, \tau_y, \tau_z)$ is the vector of Pauli matrices associated with the spin of the bath atoms. Spin-flip scattering can occur between momenta k, k' of the conduction electron bath with a band dispersion $\epsilon(k)$. The system size (number of lattice sites) is given by M.

This isotropic version of the Kondo Hamiltonian has been formulated for the description of low-energy scattering in s-d compounds, where mobile s electrons scatter from localized d orbitals. The minimum microscopic model describing these materials is the Anderson impurity model, modeling the weak hybridization of the conduction electrons with the localized moments along with a strong Coulomb repulsion of the localized orbitals [2, 4]. A Schrieffer-Wolff transformation that integrates out the charge fluctuations can be employed to obtain the Kondo impurity model as the low-energy realization of the Anderson model [196]. In this case,

[14] For the definitions of the spin operators in the Kondo models, we follow the conventions used in [34].

an AFM exchange coupling $J > 0$ naturally emerges, leading to Kondo spin-singlet screening of the impurities. Using renormalization group methods, the critical temperature for the onset of Kondo singlet screening, the Kondo temperature, is determined as

$$k_B\, T_{\mathrm{K}}(J) = \mathcal{D}\sqrt{|J|\,\rho}\,\exp\left(-\frac{1}{J\,\rho}\right), \tag{2.45}$$

with $[-\mathcal{D}, \mathcal{D}]$ the band width and ρ the density of states at the Fermi energy[15] [4, 14]. The Kondo temperature vanishes exponentially with the coupling J. The many-body ground state of the AFM Kondo model at low-temperatures $T \ll T_K$ is a strongly correlated Kondo singlet, with zero impurity magnetization $\langle S_z \rangle \approx 0$. The impurity spin is screened from external perturbations and small external magnetic fields do not break up the Kondo singlet [4].

In contrast, when the Kondo impurity model exhibits FM exchange coupling $J < 0$, fundamentally different behavior emerges. The many-body ground state becomes a spin doublet and the impurity spin is not fully screened [3]. The presence of an infinitesimal quantization field lifts the ground-state degeneracy and the impurity magnetization in equilibrium takes a finite value. The characteristic temperature T_0, below which the system displays FM behavior, takes the same form as the Kondo temperature: $T_0(J) = T_K(J)$ [197]. However, due to the sign difference, the scaling with the coupling strength $|J|$ is fundamentally different and T_0 diverges with $J \to \infty$.

A peculiarity of the FM coupling regime is that the magnetic properties of the ground state depend crucially on the anisotropy of the Kondo coupling, which can, for example be introduced by an external magnetic field. A generalized, anisotropic version of the Kondo impurity model can be written as [198]:

$$\hat{H}_{\mathrm{K}} = \sum_{k,\sigma} \epsilon(k)\, \hat{c}^{\dagger}_{kg\sigma} \hat{c}_{kg\sigma} + \frac{1}{M} \sum_{k,k',\sigma,\sigma'} \left[\frac{J_z}{2} (\hat{S}_z \tau^z_{\sigma\sigma'}) + \frac{J_\perp}{2} (\hat{S}_x \tau^x_{\sigma\sigma'} + \hat{S}_y \tau^y_{\sigma\sigma'}) \right] \hat{c}^{\dagger}_{kg\sigma'} \hat{c}_{kg\sigma}\,. \tag{2.46}$$

Two independent coupling coefficients $J_\perp$ and J_z account for the anisotropy and broken SU(2) rotational symmetry compared to the isotropic model in Eq. (2.44). The sign of J_z now decides about the microscopic character, FM or AFM, of the Kondo impurity model[16] [4, 198]. Figure 2.22 illustrates the poor man's scaling renormalization group flow, obtained from second order perturbation theory for varying coupling strength and anisotropy [198]. For the FM Kondo impurity model ($J_z < 0$), one needs to distinguish between the easy-plane ($|J_z| < |J_\perp|$) and easy-axis ($|J_\perp| < |J_z|$) configuration. In the easy-axis system, as well as in the SU(2) symmetric case ($|J_\perp| = |J_z|$), the coupling flow goes into the weakly interacting FM fixed points ($J_\perp = 0$) where the impurity spin effectively becomes decoupled from the bath. In contrast, on the easy-plane side, the coupling exhibits a non-trivial flow towards the strong-coupling AFM fixed point ($J \to +\infty$). This finally leads to the formation of a Kondo singlet ground-state, as in the Kondo impurity model with AFM microscopic coupling.

[15] In 1D, we have $\mathcal{D} = 2t_g$ and $\rho \propto 1/(2\pi t_g)$ [34, 88].

[16] The sign of $J_\perp$ can trivially be changed by a rotation around the z-axis.

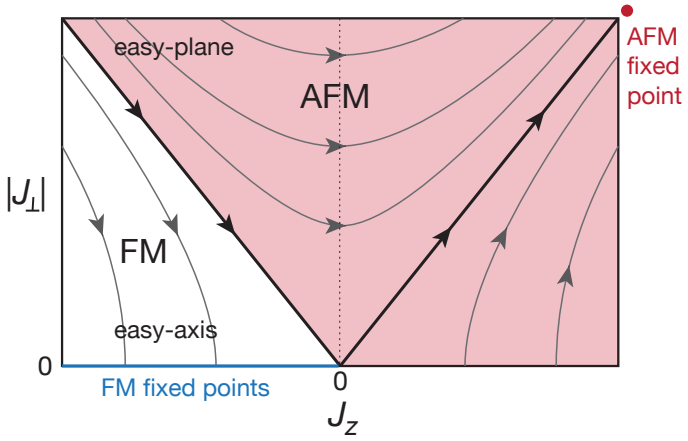

Figure 2.22 – Schematic of the poor man's scaling renormalization group flow (arrows) in the anisotropic Kondo impurity model, as obtained in [198]. J_z and $J_\perp$ are the z-component and the "spin-flip" component of the Kondo coupling. The couplings in the white, FM easy-axis regime ($J_z < 0$ and $|J_z| > |J_\perp|$) flow towards the weak-coupling FM fixed points ($J_\perp = 0$), whereas in the red (AFM) region, the flow goes into the large-coupling AFM fixed point. This holds even for ferromagnetic coupling $J_z < 0$ in the easy-plane coupling regime ($|J_z| < |J_\perp|$). Figure is qualitatively reproduced from [34].

Simulation of the Kondo impurity model with AEA

Extensive theoretical and experimental efforts have led to a very comprehensive understanding of the equilibrium properties of the Kondo model [4]. Yet, recent transport measurements in mesoscopic quantum dot systems and spectroscopic studies of the electromagnetic response of correlated materials [24–29] have motivated theoretical efforts to understand the physics of out-of-equilibrium systems with spin-orbital coupling [32, 33]. The dynamical timescales of electronic systems are very fast and real-time access to spin correlations is particularly demanding [28, 33].

In this regard, the simulation of the Kondo impurity model using AEA in optical lattices could prove as a helpful tool. Recent theoretical studies have investigated the use of ^{173}Yb or other AEA in a SDL, and they derive the effective Kondo model parameters from the 2FHM [34, 84]. The system configuration proposed in [34] requires a dilute concentration of localized $|e\rangle$ impurities interacting with a bath of mobile $|g\rangle$ atoms in different nuclear spin states, as depicted in Fig. 2.21(a). In contrast to the implementation of the Kondo lattice model presented below, SDL sites start out in a singly occupied state. Because of the large interorbital on-site interactions $U_{\mathrm{eg}}^{\pm} \gg t_g$ in Eq. (2.41), at least for the fermionic ytterbium isotopes, low-energy spin-exchange processes are mediated via virtual-tunneling. In Chapter 5 and [172], we present our experimental realization of such a lattice systems. In this context, we derive the effective Kondo interaction from a Schrieffer-Wolff transformation in a simplified state-dependent double-well model. In the absence the observed confinement-induced tuning mechanism, we arrive at an isotropic coupling [see Eq. (5.13)]

$$J = J_z = J_\perp \propto t_g^2/U_{\mathrm{eg}}^{+} - t_g^2/U_{\mathrm{eg}}^{-}. \tag{2.47}$$

Although the Kondo coupling is not caused directly by the spin-exchanging on-site interactions,

its sign and strength still emerge from a competition of the orbital singlet and triplet scattering channels. In the case of ^{173}Yb, we have $U_{\mathrm{eg}}^{+} \gg U_{\mathrm{eg}}^{-}$ and the virtual tunneling process goes predominantly via the on-site orbital singlet state which exhibits a spin-triplet character. Thus, a natural FM Kondo coupling constant emerges. Instead, AFM coupling is expected for ^{171}Yb with $U_{\mathrm{eg}}^{-} > U_{\mathrm{eg}}^{+}$. In Chapter 5, we demonstrate how in a weak SDL, additional on-site bound states becomes energetically accessible for special confinements. Virtual tunneling to these states enables tunability of the exchange interactions and could allow for an inversion of the coupling sign [172].

For a more detailed derivation of the low-energy interaction parameters from the 2FHM, including the full lattice dispersion we refer to [34, 199]. The authors present a new time-dependent variational approach which is able to solve equilibrium as well as long-time non-equilibrium problems of anisotropic spin-impurity problems. By applying their method to the setting of AEA in a SDL, it is found that external static and modulated Zeeman fields could be used to tune the anisotropy and strength of the Kondo coupling. Various equilibrium and dynamical observables are studied that could provide experimental access to the phases of the anisotropic Kondo model.

The nature of the phase transition between easy-axis and easy-plane FM systems could be investigated by measuring the characteristic spin-susceptibility of the impurities discussed above. Further, quench-type experiments are proposed where a spin-polarized impurity is initially decoupled from the fermionic bath and interactions are suddenly switched on. The magnetization dynamics of the impurity are then monitored, exhibiting qualitative differences in the expected spin-relaxation dynamics [34]. This is closely related to the optical spectroscopy protocols performed in electronic systems [28]. In Chapter 5, we study a similar scenario with AEA in the SDL: Local $|e\rangle$ moments are prepared in an initially spin-polarized state and we monitor the global spin-relaxation dynamics after the spin-exchange coupling with the mobile $|g\rangle$ atoms is enabled abruptly.

The long-time impurity spin relaxation dynamics in the easy-axis regime of the FM Kondo impurity model should obey the famous Korringa law, first observed in nuclear magnetic resonance experiments [12, 200]. Poor man's scaling RG predicts a freezing of the impurity spin at zero temperature since the coupling flows into the FM fixed points where the spin-flip scattering term vanishes ($J_{\perp} = 0$). At finite temperatures, the RG flow does not entirely reach the FM points resulting in a slow exponential decay of the impurity magnetization with a rate that scales linearly with temperature [200]. Small polynomial quantum corrections to the linear decay rate dependence have been predicted which could potentially be verified in cold atom setups [34, 201].

Polarization dynamics in the AFM Kondo impurity model have been studied in the context of quantum-dot experiments with time-dependent gate voltages and a relaxation on the Kondo time scale $\hbar/k_B T_K$ is found [30, 31, 202]. Non-trivial long-time relaxation dynamics are expected for the FM Kondo model in the easy-plane regime, where the RG flow crosses over from the FM to the AFM coupling side [34]. Exploiting the single-site resolution of modern quantum gas microscopes, time-dependent spin correlations between the impurity and bath atoms could be probed. This would provide direct access to the formation dynamics of the

Kondo screening cloud correlations [33, 34].

2.8.3 The Kondo lattice model

The Kondo lattice model (KLM) has been introduced by Doniach for the description of solid-state magnetic materials, where mobile conduction electrons interact with spins in localized f-orbitals [13]. It has since been successfully applied to the description of heavy-fermion compounds, as well as manganites and other transition-metal oxides with perovskite structure [4, 21, 22]. The KLM can be regarded as the lattice generalization of the Kondo impurity model, with a localized spin on every lattice site. The basic form of the KLM can be written as [13, 203]

$$\hat{H}_{\mathrm{KLM}} = -t_g \sum_{\langle i,j\rangle,\sigma} \hat{c}^\dagger_{ig\sigma}\hat{c}_{jg\sigma} + J\sum_i \hat{\mathbf{S}}_i \cdot \hat{\mathbf{s}}_i \tag{2.48}$$

where t_g is the tunnel matrix element of the mobile electrons. The on-site spin-exchange coupling J occurs between the orbitals $|g\rangle$ and $|e\rangle$. In second quantization, the spin operators for the localized and mobile magnetic moments on site i can be expressed as $\hat{\mathbf{S}}_i = \frac{1}{2}\sum_{\sigma,\sigma'} \hat{c}^\dagger_{ie\sigma}\boldsymbol{\tau}_{\sigma\sigma'}\hat{c}_{ie\sigma'}$ and $\hat{\mathbf{s}}_i = \frac{1}{2}\sum_{\sigma,\sigma'} \hat{c}^\dagger_{ig\sigma}\boldsymbol{\tau}_{\sigma\sigma'}\hat{c}_{ig\sigma'}$, respectively. Here, $\boldsymbol{\tau}$ is the vector of Pauli matrices. The KLM then is expressed as

$$\hat{H}_{\mathrm{KLM}} = -t_g \sum_{\langle i,j\rangle,\sigma} \hat{c}^\dagger_{ig\sigma}\hat{c}_{jg\sigma} - \underbrace{\frac{J}{2}}_{=-V_{\mathrm{ex}}} \sum_{i,\sigma,\sigma'} \hat{c}^\dagger_{ig\sigma}\hat{c}^\dagger_{ie\sigma'}\hat{c}_{ig\sigma'}\hat{c}_{ie\sigma}, \tag{2.49}$$

Note, that we have chosen the same labels for the electronic orbitals as in the definition of the two-orbital FHM in Eq. (2.41) for the description of AEA in the SDL. Indeed, a direct mapping between the two models exists under the replacement $-2V_{\mathrm{ex}} \mapsto J$ and the omission of the excited-state tunneling t_e, the on-site intraorbital and direct interorbital interactions, U_{gg}, U_{ee} and V_{d}.

In the physics of intermetallic compounds, the KLM provides an effective low-energy model for the interactions between localized electrons in partly filled f-orbitals of rare-earth or actinide impurities with mobile electrons in s, p or d orbitals. Analogous to how the Kondo impurity model emerges as the low-energy limit of the Anderson model, the weak-coupling KLM is obtained perturbatively from the periodic Anderson model in the high Coulomb-repulsion limit[17] via a Schrieffer-Wolff transformation [2, 196, 204].

Despite its formal simplicity, the KLM features a very rich phase diagram resulting from the interplay of charge, spin and orbital degree of freedom. Apart from the lattice structure and dimensionality, the KLM has only two free parameters, namely the ratio J/t_g between exchange coupling and tunnel mobility and the density n_g of the itinerant species. Qualitative differences emerge in the phase diagrams for different dimensionality D and sign of the interactions J.

[17] A weak hybridization of the mobile and localized orbitals along with strong Coulomb repulsion in the f orbital.

Antiferromagnetic Kondo lattice model

At low temperatures, the physics of the antiferromagnetic KLM (AFKLM) with coupling $J > 0$ ($V_{\mathrm{ex}} < 0$) is determined by the competition of Kondo singlet coupling and magnetic order mediated by Ruderman-Kittel-Kasuya-Yosida (RKKY) interactions. The AFKLM has been extensively studied in the description of heavy-fermion compounds, in particular, regarding the quantum phase transition connecting the strong and weak coupling regime [205]. Figure 2.23 (a) depicts the famous finite-temperature phase diagram introduced by Doniach in the context of 1D "Kondo necklace" systems [13]. In the strong-coupling limit $J/t_g \gg 1$, it is favorable for the localized spins to undergo singlet coupling with the conduction electrons. This so-called static Kondo screening leads to the emergence of a paramagnetic phase featuring heavy-fermion (HF) properties. For $D > 1$, a Femi liquid with heavy quasiparticles, a so-called heavy-Fermi liquid (HFL), forms due to the hybridization with the strongly localized moments. The massive quasiparticles must be included in the conduction electron Fermi volume, making the HFL a "large Fermi surface" state [4, 14]. At half filling n_g, the Kondo exchange dominated HFL develops into a fully insulating state, the spin-gapped Kondo insulator [14, 203] [see Fig. 2.23(b)]. The HF properties in the KLM can be explained by a lattice band hybridization on the mean-field level [80, 81, 206] (see also Chapter 6). The critical energy scale for the onset of Kondo screening in the KLM is again given by the Kondo temperature T_{K} of the impurity model [Eq. (2.45)].

In contrast, in the low-coupling limit, $J/t_g \ll 1$, so-called RKKY interactions become the dominant interaction process [210–212]: Through Friedel oscillations induced in the itinerant electrons, a second order spin-spin interaction is mediated between the localized moments. The critical temperature scales as [14]

$$T_{\mathrm{RKKY}} = J^2 \rho \,. \tag{2.50}$$

For low temperatures $T < T_{\mathrm{RKKY}}$, the RKKY interactions cause long-range order which may be ferro- (FM) or antiferromagnetic (AFM), depending on the density of the conduction electrons. This is illustrated in Fig. 2.23(b,c), where we review the ground-state ($T = 0$) phases of the KLM, characterized by the local spin-spin correlations $\langle \hat{\mathbf{S}}_i \hat{\mathbf{S}}_j \rangle$. The Doniach phase diagram Fig. 2.23(a) compares the critical temperatures for the competing Kondo and RKKY coupling. A transition point $T_K \sim T_{\mathrm{RKKY}}$ occurs for intermediate coupling $J/t_g \approx 1$. The phase transition between the magnetically ordered and Fermi liquid phase has been the subject of extensive theoretical and experimental studies, fueled by the discovery of unconventional superconductivity in rare-earth HF compounds [5–7] and the emergence of exotic non-Fermi liquid behavior (NFL) [17] around a quantum critical point (QCP) at $T = 0$ [205].

A theoretical treatment of the KLM Hamiltonian is demanding, particularly in higher dimensions $D > 1$ and in the strongly correlated intermediate-coupling regime, and often restricted to an approximate mean-field treatment [4, 14]. Although the 1D KLM is not thought to be directly realized in solid state materials, it has served as a theoretical prototype for higher-dimensional systems since it is traceable with numerically exact techniques, like DMRG or exact diagonalization for small enough system sizes [203, 207, 209]. As depicted in its $T = 0$

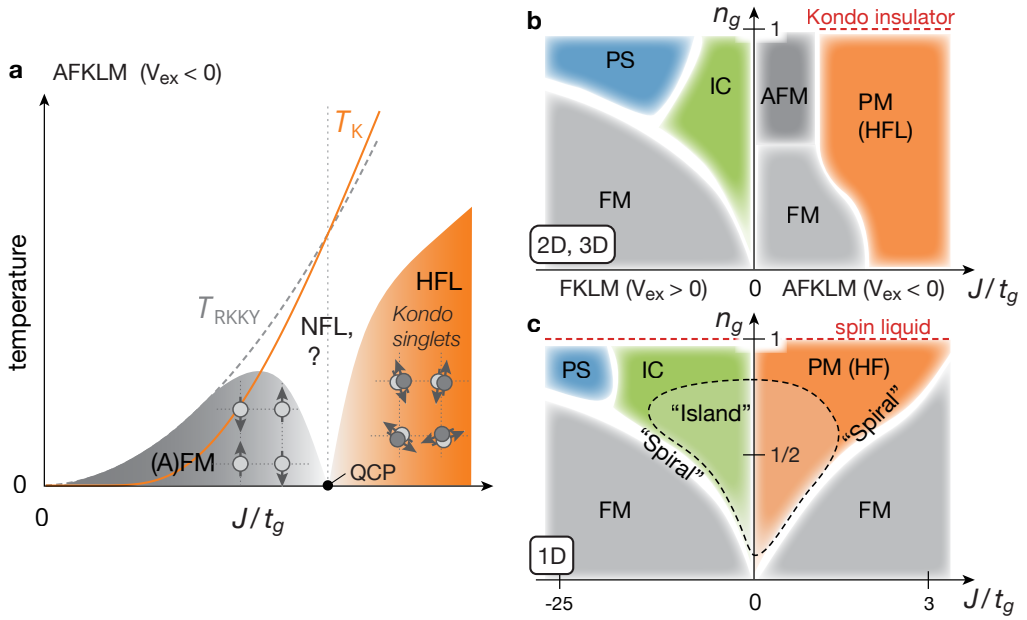

Figure 2.23 – Schematic phase diagrams of the ferro- (FKLM) and antiferromagnetic (AFKLM) Kondo lattice models. (a) Doniach phase diagram for the AFKLM ($V_{\mathrm{ex}} < 0$, $J > 0$), dominated by a competition of RKKY and Kondo coupling for varying coupling strength J [13, 14]. The critical temperatures are T_{RKKY} (dashed) and T_{K} (solid), respectively. For strong coupling, such that $T_{\mathrm{K}} > T_{\mathrm{RKKY}}$, and low temperatures $T < T_{\mathrm{K}}$, a heavy Fermi liquid (HFL) forms. Kondo singlet pairing ensures paramagnetism (PM). The HFL becomes unstable against RKKY magnetism at weak coupling ($T_{\mathrm{RKKY}} > T_{\mathrm{K}}$) causing FM or AFM order in the localized moments. A quantum critical point (QCP) emerges at $T = 0$ between the magnetic and the HFL phase [205]. The quantum critical region is predicted to feature non-Fermi liquid (NFL) behavior at $T > 0$ [8, 11, 17, 205]. (b,c) Ground-state phase diagrams for varying mobile band filling n_g in the FKLM ($J < 0$) and AFKLM ($J > 0$), characterized by magnetic order. PS denotes a regime with phase separated FM and AFM correlations; IC has incommensurate correlations. HF properties are found in the PM phases. (b) 2D, 3D systems: At half-filling ($n_g = 1$) and large J, a Kondo insulator appears (red dashed). The FKLM phase diagram is qualitatively based on the results in [207, 208], the AFKLM side on [81, 206]. (c) 1D systems: A spin-gapped spin liquid exists for all J at $n_g = 1$. Quasi-long-range "spiral" and "island"-type correlations appear for intermediate J. The phase diagram is qualitatively reproduced from the numerically exact DMRG results in [209].

phase diagram in Fig. 2.23(c), the 1D KLM differs from its higher-dimensional analogs in some qualitative aspects: A spin-polarized ground state (FM) instead of a PM phase is found in the strong-coupling limit, independent of n_g. Instead, the PM phase extends to the low-coupling regime. Although the Fermi-liquid picture breaks down at low energies in 1D, the PM phase is still expected to feature HF properties, qualitatively understandable through a hybridization mean-field decoupling [81, 203, 206]. At half filling $n_g = 1$, analogous to the Kondo insulator in $D > 1$, the ground state of the 1D KLM is a spin-gapped spin-liquid phase. In 1D, no critical J separates the spin-liquid phase from the magnetically ordered phases and it even exists in the ferromagnetic KLM [203].

Ferromagnetic Kondo lattice model

While the ferromagnetic KLM (FKLM), with $J < 0$ ($V_{\mathrm{ex}} > 0$), has in the past received less attention than its AFM counterpart, it has more recently attracted considerable interest in the context of colossal magnetoresistance in manganese and other transition-metal oxides with perovskite structure [18–22]. For these materials, the FKLM describes the competition between kinetic energy of itinerant electrons and a double-exchange (Hund) exchange coupling with localized spins [213, 214]. When the Hund coupling becomes large compared to the conduction electron band width, it causes electrons to align with localized moments in spin triplet states. Then, the conduction electron mobility depends strongly on the magnetic texture of the local moments, becoming large in the case of FM order and vanishing for AFM order [213]. The high sensitivity of the conductivity on an external magnetic field, changing the magnetic structure of the localized moments, is denoted as colossal magnetoresistance.

In the weak-to-intermediate coupling regime, the FKLM, like the AFKLM, exhibits a rich structure in its magnetic $T = 0$ phase diagram [Fig. 2.23(b,c)]. Here, different dimensionalities are qualitatively comparable [203, 207]. At low filling, a FM ordered phase emerges, prevailing also at larger fillings for increased coupling strengths. For larger fillings, a phase separation (PS) regime is identified, which hosts coexisting regions of undoped AF and hole-rich FM order, along with incommensurate correlations (IC). The 1D problem has been investigated using numerically exact methods, and additional, more exotic phases, such as "spiral" or "island"-type correlations have been recovered. In their DMRG study of the 1D KLM, Garcia et al. find a remarkable similarity between the FM and AFM exchange coupling side, with similar phase boundaries separating the FM state and the island and spiral phases also extending to the $J > 0$ side of the phase diagram [209].

Simulation of the KLM with AEA

As noted above, the KLM emerges non-perturbatively from the 2FHM under the assumption that the terms scaling with t_e, U_{gg}, U_{ee} and V_{d} can be omitted [58]. In contrast to the Kondo impurity model, half-filling ($n_e = 1$) of the $|e\rangle$ lattice orbital is required for the simulation of the Kondo lattice model [see Fig. 2.23(b)]. The implementation of our SDL ensures that t_e is the smallest energy scale and tunneling of the $|e\rangle$ atoms is strongly suppressed. Additionally, at half filling, the strong on-site ee interactions $U_{\mathrm{ee}} \gg t_e$ further reduce next-neighbor $|e\rangle$ tunneling, as well as ee losses, through the formation of an insulating state (see Section 2.7). The direct interorbital interaction V_{d} is present on every lattice site and therefore only produces a constant energy offset. An experimental sequence to prepare the half-filled lattice of $|e\rangle$ atoms, along with a filling $n_g \leq 1$ of mobile $|g\rangle$ atoms, is presented in [80, 81] and a more detailed discussion can be found in [97]. The underlying idea is to initialize a $|g\rangle$ mixture of two nuclear spin states in a deep SDL. For a given harmonic confinement of the trap the total $|g\rangle$ atom number can be adjusted such that the $|g\rangle$ density in the trap center is between $n_g = 1$ (half filling) and $n_g = 2$ (band insulator). Then, the clock transition is used to independently excite all singly occupied sites and one atom on every doubly occupied lattice site.

In the case of ^{173}Yb, the ground-state scattering length a_{gg} is relatively large, and U_{gg}

always remains sizeable compared to the mobility t_g in our implementation of the SDL. For a comparison of the energy scales in our setup, see Fig. 5.2(b). However, it stays small compared to the interorbital exchange $U_{gg} \ll V_{\mathrm{ex}} \approx U_{\mathrm{eg}}^{+}$. A finite interaction of the itinerant species in the AFKLM can be included the so-called Kondo-Hubbard model. Numerical studies suggest that the standard Hubbard interaction further localizes the conduction electrons which favors Kondo screening of the localized spins, and shifts the magnetic instability to lower critical exchange coupling strengths [85, 215, 216]. Experimentally, a reduction of the ground-state interactions could be achieved by increasing the eg polarizability ratio of the lattice light, essentially approaching a $|g\rangle$ tune-out wavelength (see Section 2.2). This would allow us to lower the $|g\rangle$ lattice depth while maintaining strong $|e\rangle$ localization. Alternatively, fermionic ^{171}Yb could be used which offers a near-vanishing a_{gg}.

The on-site exchange coupling V_{ex} emerges directly from the 2FHM, and already for small SDL depths in the tight-binding regime, it becomes large compared to t_g. Thus, the strong-coupling regime of the KLM is naturally realized. This is favorable concerning the temperature requirements for both magnetically ordered phases and heavy-Fermi liquid phases [see Eqs. (2.45) and (2.50)]. ^{171}Yb with an AFM exchange coupling V_{ex} presents itself as an excellent candidate for the simulation of the AFKLM [88]. For their implementation of a 1D KLM using ^{171}Yb in a comparable monochromatic SDL setup, Ono et al. have recently estimated a Kondo temperature of around $T_{\mathrm{K}} \sim 10\,\mathrm{nK}$ in the $V_{\mathrm{ex}} \gtrsim t_g$ regime where Eq. (2.45) is valid [88]. This temperature range should be accessible in our setup, considering typical reduced temperatures of $T/T_F \approx 0.1 - 0.2$ and Fermi temperatures $T_F \approx 100\,\mathrm{nK}$ before the lattice loading [59, 69].

Heavy fermion properties in the strong-coupling regime could therefore become accessible in AEA setups. The hallmark feature of the HFL is the existence of heavy quasiparticles around the Fermi energy. Using the weak harmonic confinement of an optical lattice, the enhanced effective mass could be detected via a reduced dipole oscillation frequency of artificially induced collective dynamics [80, 81]. In Chapter 6, we characterize the collective mobility as an observable in our SDL setup. Independently, the enlarged Fermi surface of the HFL could be probed directly by monitoring the in-trap momentum distribution using a band-mapping technique.

For a half-filled $n_g = 1$ lattice, the non-conducting Kondo insulator should be realized. In the presence of a harmonic confinement, the local density varies significantly over the extent of the atomic distribution in the optical lattice. Then, an integer-filling shell structure similar to the Mott insulator density plateaus is predicted, both in 1D and 2D [80, 81, 217, 218]. Notably, in 1D, also the FKLM features an insulating spin-liquid phase, and it is numerically found to exhibit insulating signatures in its shell structure [218]. High-resolution in-situ imaging should give access to the local density distribution and thereby the vanishing compressibility in the insulating phase [98].

The natural on-site exchange interactions of ^{173}Yb have been found to be large and ferromagnetic [59, 60], and can be used to realize the strong-coupling regime of the FMKLM. Reminiscent of colossal magnetoresistance in magnanites, a recent proposal for AEA in an SDL suggests to probe the competition of the strong triplet coupling with externally induced AFM

order [219]. Exotic spin-orbit coupled metallic states are predicted that could be observed via the local dynamics of spin-charge excitations.

The large nuclear spin $I = 5/2$ of ^{173}Yb allows us to work with an increased number $N \geq 2$ of spin states m_F [see Section 1.5.4]. The SU(N) symmetry of the interorbital interactions ensures that a selected subset of N spin states is preserved under collisions. Using $N > 2$ spin states directly realizes the so-called Coqblin-Schrieffer model, the SU($N = 2I + 1$) symmetric analogue of the KLM which is believed to describe the low-temperature physics in alloys with cerium impurities [4, 58, 220, 221]. Notably, as recently investigated in HF and carbon nanotube quantum dot systems [222, 223], one expects an exponential increase of the Kondo temperature with N [4, 221].

CHAPTER 3

Experimental setup and techniques

In this chapter, our experimental apparatus and techniques for producing, manipulating and probing ultracold samples of ytterbium are introduced. We describe the configuration of laser beams and magnetic fields used to trap and cool the atoms. In particular we focus on the implementation of the lattice setup, including the 670 nm state-dependent optical lattice potential, used for the realization of Kondo-type Hamiltonians. Furthermore, we give an overview of the optical techniques used to create degenerate samples of ^{173}Yb, manipulate their nuclear spin and orbital degree of freedom, as well as detect the atomic in-trap distribution.

3.1 A setup overview

An overview of the experimental apparatus, including magnetic fields and laser beams is provided in Fig. 3.1. The schematic is reduced to the components most relevant to this work. For additional components as well as further technical details about the experiment setup, consider references [97–99].

The displayed configuration is centered around the position of the trapped atoms in the main vacuum chamber. This octagonal steel chamber is evacuated using an ion pump and a titanium sublimation pump. With an atomic beam shutter installed, the resulting background pressure of around 10^{-11} mbar limits the lifetime of a degenerate Fermi gas to around 100 s (see Fig. 2.15). Optical access is provided via six viewports in the horizontal plane and two viewports on the vertical axis.

The flux of all isotopes of ytterbium, produced in an oven, enters the main chamber through the increasing-field Zeeman slower coil (C_{ZS}) and counter-propagates the 399 nm Zeeman slower light beam (ZS). The atoms are then trapped in a magneto-optical trap (MOT) in the center of the main chamber by 6 counter-propagating, circularly polarized 556 nm beams and magnetic field gradients produced by the coils C_{TV} and C_{MOT} in anti-Helmholtz configuration. Horizontal and vertical homogeneous magnetic fields B_{TV} and B_z at the position of the atoms can be generated by the same coils in Helmholtz configuration.

Atoms in the electronic ground state $^1S_0$ can be cooled to quantum degeneracy through evaporative cooling in a pair of crossed optical dipole traps (1064 nm DT). We also employ a pair of 759 nm state-independent dipole traps (magic DT) for trapping both clock states simultaneously. A set of three perpendicular, retro-reflected 759 nm laser beams (magic L1, L2,

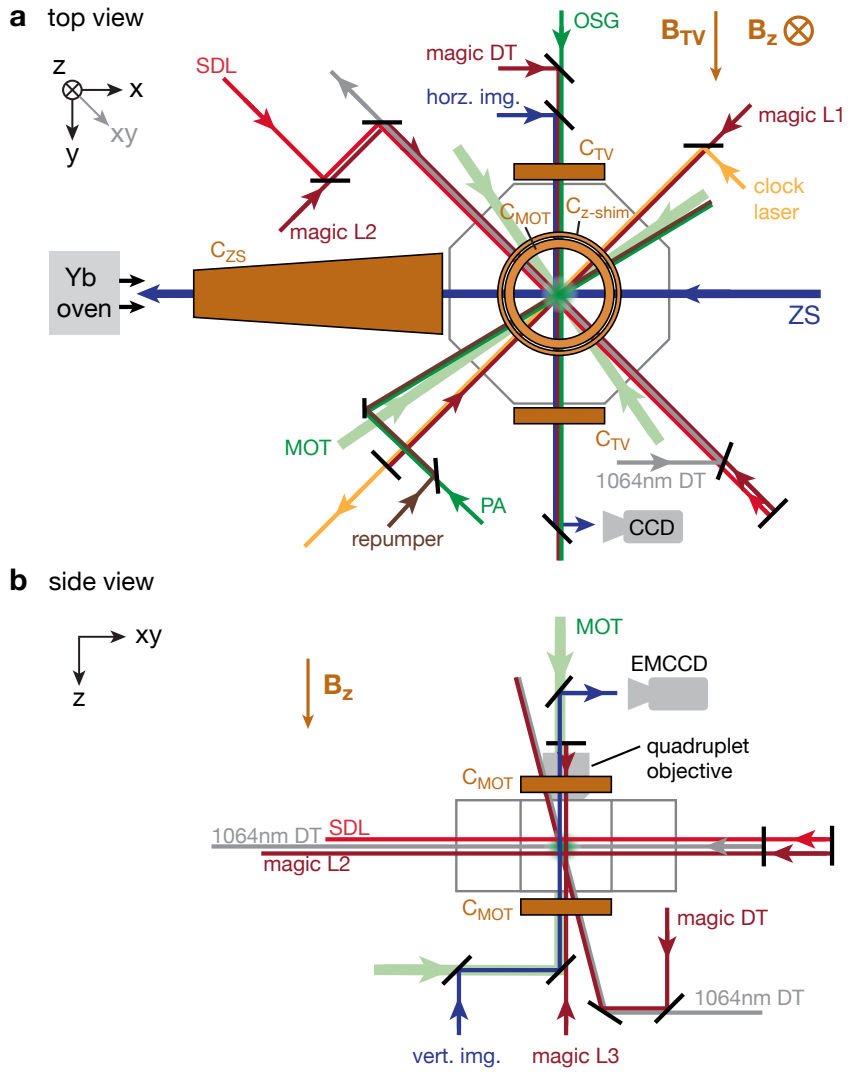

Figure 3.1 – Schematic of the experiment setup, including relevant laser beam paths (arrows) and magnetic fields, viewed (a) from the top and (b) from the side, perpendicular to the state-dependent lattice (SDL). All beams are centered onto the atom position in the middle of an octagonal steel vacuum chamber (gray) with 6 horizontal and 2 vertical viewports. A cubic state-independent optical lattice can be produced by the beams L1, L2 and L3, where L2 is aligned along the SDL. In addition to 1064 nm dipole traps, we employ state-independent dipole traps (magic DT). Coils C_{TV} and C_{MOT} produce magnetic fields B_{TV} in the horizontal plane and B_z in the vertical direction. Atoms can be imaged in-situ from the top or horizontally after time of flight. Compared to the original setup in [97], a 670 nm state-dependent lattice and a 1389 nm optical repumper for the clock state have been added. Dimensions are not to scale.

L3) forms a state-independent optical lattice potential, variable between 1D lattice (stacked pancakes), 2D lattice (array of tubes) and 3D cubic lattice geometries. Moreover a 670 nm beam (SDL), coaligned and retroreflected together with magic L2, creates an orbital state-dependent lattice potential for $^1S_0$ and $^3P_0$.

The clock transition is addressed by a linearly polarized 578 nm beam (clock laser) copropagating with magic L1 and perpendicular to the magnetic field B_z providing the nuclear-spin quantization axis.

In our setup, absorptive imaging of the ground-state atoms is performed on the horizontal or vertical axis using 399 nm light. Only small magnification is used on the horizontal axis to capture the momentum distribution of the atoms in time-of-flight imaging and to perform an optical Stern-Gerlach technique (OSG) using a 556 nm beam coaligned with the imaging beam. Instead, in-situ imaging is done from the top, through a high-resolution objective. Detection of the orbital excited state $^3P_0$ is enabled through a newly added 1389 nm laser beam (repumper) along the magic L1 axis, that repumps $^3P_0$ to $^1S_0$.

3.2 Magnetic fields and Zeeman shifts

While inhomogeneous magnetic fields are needed for Zeeman slowing and magneto-optical trapping, most later stages of the experiment require precisely controlled homogeneous fields. These are used for state preparation and detection as well as for controlling the atomic interaction properties. Several sets of coils are used to generate homogeneous magnetic fields, mostly to set a quantization axis for the nuclear spin and enable Zeeman-energy selective addressing of the different m_F components.

The transverse coils C_{TV} can produce fields B_{TV} up to 25 G in the direction of the horizontal OSG and imaging beams. The MOT coils C_{MOT} have recently been upgraded to handle large currents and generate a vertical magnetic field strength of B_z up to 1200 G [98, 99]. While the ground-state scattering properties do not depend on the magnetic field, the interorbital interactions between the two clock states are governed by a magnetic Feshbach resonance [90, 91]. The large fields allow us to explore a significant range of interactions strengths between the clock states [90, 99]. The vertical magnetic field is also used in conjunction with the vertically polarized clock laser light to ensure pure π polarization and nuclear-spin selectivity of the clock transition through the differential Zeeman shift between $^1S_0$ and $^3P_0$. Similarly, the preparation of different nuclear-spin mixtures employs a Zeeman-energy selective optical pumping scheme on the $^1S_0 \rightarrow {}^3P_1$ intercombination line. The circularly polarized vertical MOT beams in the presence of vertical fields allow us to address σ transitions between adjacent m_F components. Also, the Zeeman shift of the $^1S_0 \rightarrow {}^1P_1$ transition enables nuclear-spin dependent imaging at high magnetic fields in the vertical direction.

Additional low-current shim coils (up to ~ 2 A) in all three spatial directions are individually controllable to cancel magnetic stray fields (up to ~ 2 G), from magnetic parts on the setup or from the earth magnetic field[1].

[1] The total earth magnetic field strength in Munich is 485 mG, composed of 211 mG, 14 mG and 437 mG in x,

Field ramps and rotations In particular, the vertical shim coil C_z^{shim} is used to set a permanent offset field $B_z^0 \approx 1\,\mathrm{G}$ in the same direction as B_z generated by the MOT coils. Our orbital spin-exchange experiments require weak offset fields, large enough compared to ambient field noise to preserve the quantization axis, but small compared to other energy scales of the physical problem. Utilizing the full dynamic range of the smaller power supplies for the shim coils enables more precise control for weak magnetic fields.

To perform an OSG measurement or imaging on the horizontal axis, the magnetic field needs to be rotated slowly from the vertical to horizontal orientation. This needs to happen adiabatically for the nuclear-spin to follow and not induce Larmor precession. In contrast, for the spin-exchange experiments in Chapter 5, we want to ramp the magnetic field strength from relatively high amplitudes ($> 20\,\mathrm{G}$) to zero as fast as possible after the state preparation. The required minimum ramp time is $< 10\,\mathrm{ms}$, faster than the tunneling dynamics of the atoms in the deep SDL. Therefore, we shunt the current in the MOT coils using a MOSFET based circuit. Here, the permanent vertical offset field produced by C_z^{shim} prevents the loss of the quantization axis due to negative overshoots of the field produced by $\mathrm{C_{MOT}}$.

3.2.1 Calibration of magnetic fields

In order to calibrate the vertical magnetic field strength B_z at the position of the atoms, we perform spectroscopy on the $^1\mathrm{S}_0 \rightarrow {}^3\mathrm{P}_1$ transition, as in [129, 132]. In contrast to the differential Zeeman effect for the clock transition, the m_F-dependent Zeeman splitting for these two states can be calculated ab initio to good precision by means of a Breit-Rabi calculation, assuming bare Russel Saunders (RS), that is, uncoupled LS coupling eigenstates $^1\mathrm{S}_0$ and $^3\mathrm{P}_1$. Modifications on the one percent level are obtained when spin-orbit coupling of $^3\mathrm{P}_1$ with $^1\mathrm{P}_1$ is taken into account in a full diagonalization of the combined Zeeman and Hyperfine coupling Hamiltonian (see Section 1.2).

Performing the spectroscopy for various magnetic fields and different m_F components allows us to also extract the strength of potential background fields and laser frequency offsets. Fig. 3.2 shows a typical spectroscopic result and fit determining the magnetic coil and offset field calibration. By using only the transitions $m_F = \pm 5/2 \rightarrow \pm 7/2$ on the stretched states of $^3\mathrm{P}_1$ (F=7/2), we can exclude a quadratic Zeeman shift of the transition within the measurement precision. The expected residual quadratic coupling of at maximum 100 Hz [Fig. 3.2(c)] for the employed fields comes from Zeeman coupling with $m_F = 7/2$ states of $^3\mathrm{P}_2$. Therefore, it sufficient to consider only the linear shift from the Landé factors in Eq. (1.10), modified by spin-orbit coupling, instead of fitting the full Zeeman, spin-orbit and hyperfine cross-coupling model from Section 1.2. Experimentally, the absence of higher order Zeeman shifts helps in distinguishing the non-linearities in the regulation of the coil currents from a quadratic Zeeman shift. The uncertainty for the coil calibration given in Fig. 3.2 is only the standard fit error of the respective models and certainly underestimates the real experimental uncertainty. The magnetic field resolution is limited to around 0.5% by the analog control of the power supplies,

y and z-direction of the experiment setup in Fig. 3.1 (values derived from NGA World Magnetic Model 2015).

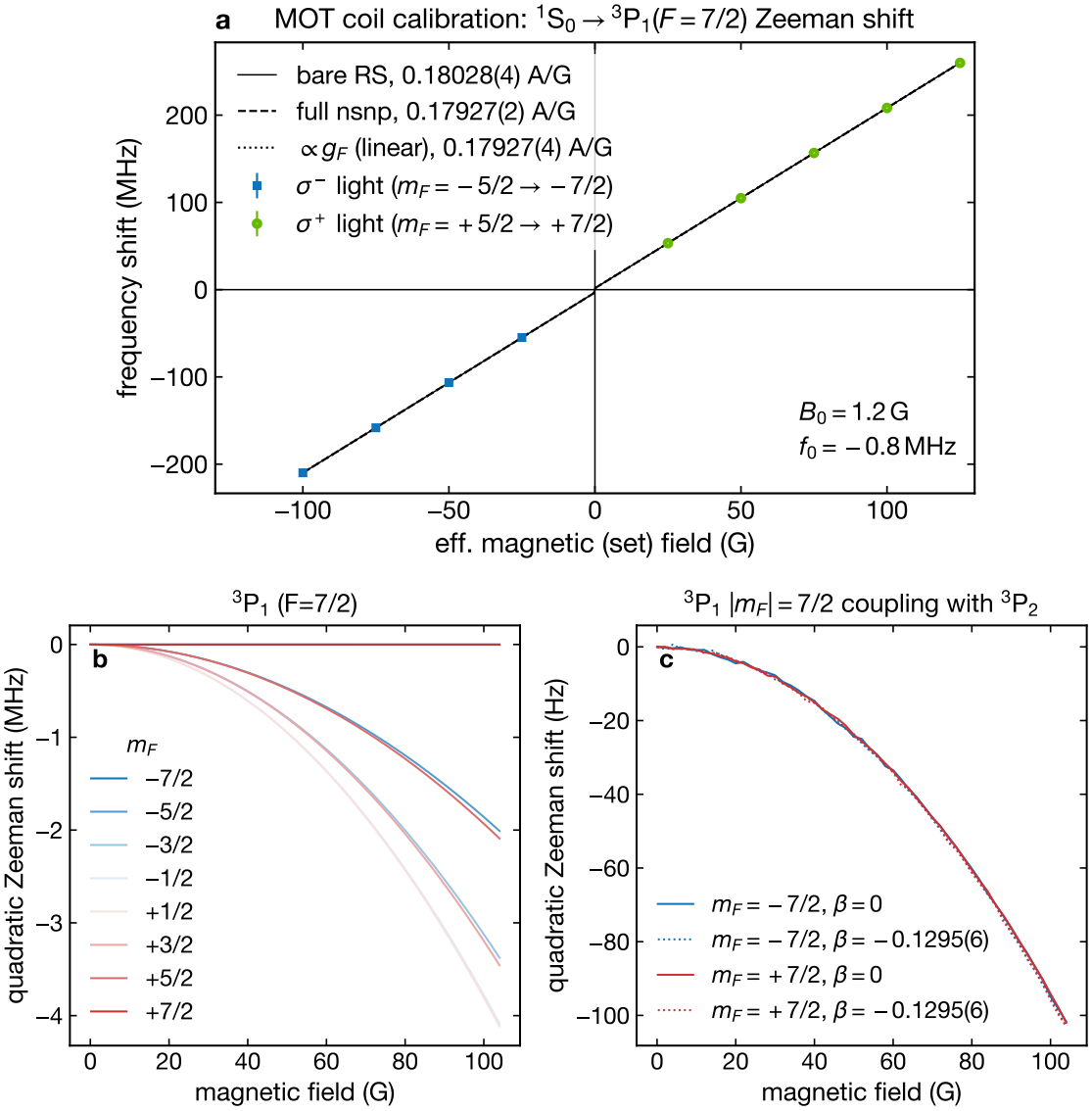

Figure 3.2 – (a) Calibration of the vertical magnetic field produced by the MOT coils. Squares (circles) indicate resonances from spectroscopy on the $^1S_0 \rightarrow {}^3P_1$ transition using σ^- (σ^+) light and starting from $m_F = -5/2$ ($m_F = 5/2$). The use of different m_F components at different set values for the magnetic field (coil current) allows to distinguish a laser frequency offset f_0 from a background B-field offset B_0. The fit functions are the expected linear Zeeman shift for uncoupled RS states (solid line), the shift expected from the Zeeman, spin-orbit and hyperfine cross-coupling model in Section 1.2 (dashed line) and the linear shift expected from the Landé factors Eq. (1.10) modified by spin-orbit coupling. (b-c) Expected quadratic Zeeman shift for $^3P_1$ $|m_F| = 7/2$, the final states in (a), is only from Zeeman coupling with $^3P_2$ and thus strongly suppressed compressed compared to other m_F.

and by repeated spectroscopic measurements of the clock transition we observe fluctuations of the ambient magnetic field of around 100 mG.

3.2.2 Measurement of the differential clock state Zeeman shift

The magnetic field dependence of the clock transition $^1S_0 \rightarrow {}^3P_0$ is induced by hyperfine and Zeeman coupling of $^3P_0$ with $^3P_1$ and $^1P_1$, making it hard to calculate ab initio. Predicted accuracies from CI+MBPT calculations are only on the few-percent level [137]. The differential clock state Zeeman shift enters directly into the two-channel scattering model for the interorbital interactions (see Chapter 4). Therefore, its independent and precise determination is helpful for making accurate theoretical predictions of the interatomic scattering properties.

In principle, one can determine the differential Zeeman shift experimentally by performing clock spectroscopy at different magnetic fields. However, the final accuracy is limited by the calibration of the external magnetic field at the position of the atoms. In previous experiments, we have relied on the magnetic field calibration obtained from the spectroscopy of the intercombination transition which is easier to model theoretically (Section 3.2.1). However, we cannot exclude systematic errors of the calculation on the percent level.

Instead, we employ a field-insensitive differential measurement technique similar to the one in [111] to extract the linear differential clock shift for ^{173}Yb. The idea behind the technique is to spectroscopically probe σ^- and σ^+ transitions between the clock states, starting from different m_F states [Fig. 3.3(a)]. The measured resonance positions can then be combined in a way that eliminates the dependence on the external magnetic field B and the quadratic Zeeman shift. We can then extract a value for differential Landé factor δg that depends only on the nuclear Landé factor g_I via the nuclear magnetic moment μ_I [Eq. (1.4)].

The underlying assumption for the scheme to work is that we can split[2] the differential Zeeman shift into a linear m_F-dependent part and a quadratic shift $\Delta_Z^{(2)}(B)$ that is independent of m_F. The transition frequency is then given by

$$\nu^{\pm}(B, m_F) = \nu_0 - \delta g(m_F \pm 1)\mu_0 B - g_I(\pm 1)\mu_0 B + \Delta_Z^{(2)}(B) \tag{3.1}$$

where $(\pm)$ indicates the light polarization and ν_0 is the center frequency for zero field, including potential measurement offsets.

In the experiment, we measure the frequency of three transitions: $\nu_1(B) = \nu^-(B, m_1)$, $\nu_2(B) = \nu^+(B, m_1)$ and $\nu_3(B) = \nu^-(B, m_2)$, starting from two different m_F values $m_1 = -3/2$ and $m_2 = 5/2$. Now, taking the differences

$$\begin{aligned} \Delta_a(B) &= \nu_3(B) - \nu_1(B) = -\delta g(m_2 - m_1)\mu_0 B, \\ \Delta_b(B) &= \nu_2(B) - \nu_1(B) = -2(\delta g + g_I)\mu_0 B \end{aligned} \tag{3.2}$$

between the transition frequencies leaves only the linear magnetic field dependence of the

[2] We have checked the validity of the calibration scheme for fields up to at least 10^4 G, using the hyperfine and Zeeman coupling model for the (6s6p) manifold, introduced in Section 1.2. See Fig. A.1 for more details.

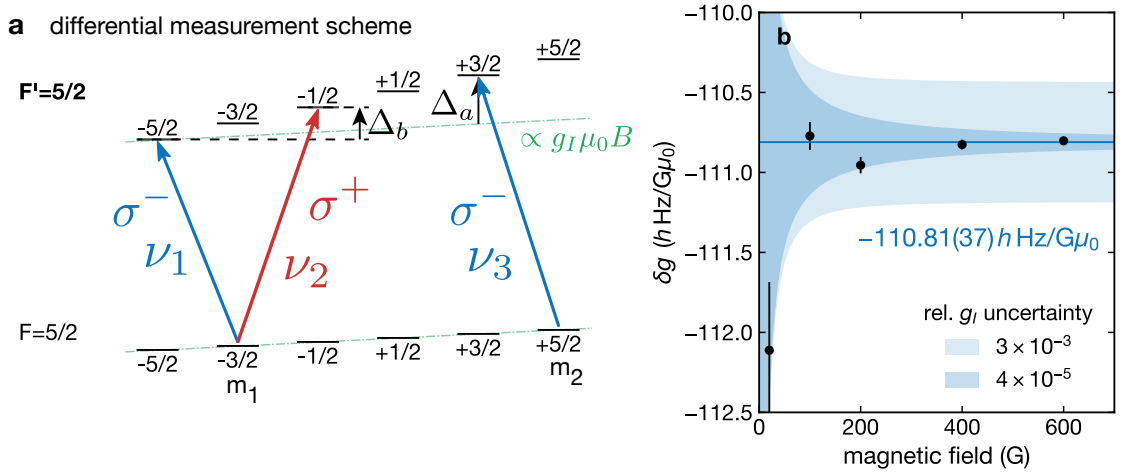

Figure 3.3 – Measurement of the linear differential Zeeman shift of the clock transition $^1S_0 \rightarrow {}^3P_0$. (a) Differential measurement scheme involving the measurement of two σ^- transition frequencies ν_1 and ν_3 and one σ^+transition ν_2, starting from two different m_F states m_1 and m_2. The differential Landé factor δg can be determined from the ratio Δ_b/Δ_a of the frequency differences, which is independent of the quadratic Zeeman effect and the magnetic field. (b) Differential shift δg determined from clock spectroscopy at different magnetic fields (circles) and assuming $g_I(^{173}\mathrm{Yb}) = -207.30(1)\,h\,\mathrm{Hz/G}\mu_0$ (from $\mu_I(^{173}\mathrm{Yb}) = -0.67989(3)\mu_N$ [120]). Error bars are propagated standard fit errors for the center of a Rabi line shape. Shaded areas are theoretically expected uncertainties for 50 Hz uncertainty in the resonance positions and different rel. uncertainties of g_I: from [120] (dark region), or from difference of μ_N values in [117] and [120] (bright region). The indicated value for δg is from a weighted average of all data points, including the larger g_I uncertainty.

clock states. Finally, we define the ratio

$$r \equiv \frac{\Delta_b(B)}{\Delta_a(B)} = \frac{2(\delta g + g_I)}{\delta g (m_2 - m_1)}, \tag{3.3}$$

a measured quantity, independent of magnetic field which relates the differential shift to the nuclear magnetic moment via

$$\delta g = g_I \frac{2}{r(m_2 - m_1) - 2}. \tag{3.4}$$

In the experiment, we are limited by the finite linewidth and short-term stability of the clock laser frequency and the magnetic fields. We assume a fixed uncertainty of $\sigma_\nu \approx 50\,\mathrm{Hz}$ for the measured resonance positions. Another source of uncertainty $\sigma(g_I)$ is in the independently measured nuclear Landé factor g_I [120]. The estimated relative uncertainty of the determined δg scales as

$$\frac{\sigma(\delta g)}{\delta g} = \frac{1}{g_I}\sqrt{\sigma^2(g_I) + h^2 \frac{4(\delta g + g_I)^2 + \delta g^2 (m_2 - m_1)^2}{2\,\delta g^2\,(m_2 - m_1)^2 \mu_0^2 B^2}\sigma_\nu^2} \tag{3.5}$$

In principle, the ratio r can be measured at a single arbitrary magnetic field. However, the achievable precision scales favorably with increasing B. With our spectroscopic resolution, we require magnetic fields of around 500 G to reach a relative uncertainty of 10^{-3} in δg.

In Figure 3.3(b), we display the experimentally determined differential Landé factor δg for a range of magnetic fields along with the predicted accuracy from Eq. (3.5). The spectroscopy of the three transitions for every magnetic field has been performed in an interleaved measurement as to reduce the effect of potential magnetic field drifts. For large fields, the achievable accuracy is limited by the uncertainty in g_I. If we assume a rather conservative uncertainty, given by the difference of the higher-precision value by Stone [120] and the older value from [117], we extract

$$\delta g = -110.81(37)\, h\,\mathrm{Hz/G}\mu_0\,, \tag{3.6}$$

still with an improved, sub-percent accuracy[3].

3.3 Cooling spin mixtures to degeneracy

In order to realize multi-orbital Hubbard models using ytterbium in optical lattices, we require degenerate Fermi gases in a well-controlled nuclear spin configuration. In the context of this work, we are mainly interested in the cooling and loading of balanced two-spin mixtures in the atomic ground-state. The orbital degree of freedom can later be manipulated in the optical lattice by addressing the clock transition. These spin mixtures are produced using standard techniques for AEA, which we will review briefly in the following. A detailed description of the atom loading and cooling techniques in our setup can be found in [97–99].

3.3.1 Zeeman slower and magneto-optical trap

The initial deceleration of the 340 m/s fast atoms from the atomic oven section is performed by an increasing-field Zeeman slower operating on the broad, dipole-allowed $^1\mathrm{S}_0 \rightarrow {}^1\mathrm{P}_1$ transition (399 nm). The magneto-optical trap uses magnetic field gradients produced by the coils C_{TV} and $\mathrm{C}_{\mathrm{MOT}}$ in anti-Helmholtz configuration and six counter-propagating laser beams addressing the green transition $^1\mathrm{S}_0 \rightarrow {}^3\mathrm{P}_1$ (556 nm). On the one hand, the narrow linewidth of the intercombination transition leads to a relatively low capture velocity of 8 m/s. On the other hand, the achievable cooling temperature, the Doppler temperature of 4.4 μK, is also low. After a loading time of around 8 s from the ZS into the MOT, a subsequent trap compression is applied, where the detuning and intensity of the MOT beams are reduced and the magnetic field gradient is increased. For ^{173}Yb, the phase space compression leads to a transfer of around 5×10^7 atoms into the crossed 1064 nm optical dipole trap (xODT), at an initial temperature of 22 μK [99].

Loading different isotopes requires that the respective isotope shifts are included in the laser detuning of the ZS and MOT. Our setup has recently been upgraded to allow the simultaneous loading of two isotopes [158]. A large-bandwidth electro-optical modulator is used to induce sidebands onto the MOT light, such that the carrier and one of the sidebands simultaneously address different isotopes. We have successfully transferred cold mixtures of ^{174}Yb

[3] A previous measurement in our setup had concluded $\delta g = -112(1)\, h\,\mathrm{Hz/G}\mu_0$ [97].

and ^{171}Yb into the xODT where the bosonic ^{174}Yb is used to sympathetically cool and produce degenerate samples of ^{171}Yb during forced evaporation.

3.3.2 Evaporation in the dipole traps

After cooling in the MOT, a nuclear spin-balanced sample of atoms is transferred into a deep crossed optical dipole trap for forced evaporative cooling. A high power commercial 1064 nm laser generates a pair of horizontal and vertical trap beams (1064 nm DT) intersecting at their focus point in the center of the vacuum chamber. This wavelength creates a low-scattering, attractive dipole potential for the ground state atoms (see Section 1.3.4). The vertical dipole trap (vDT) has a circular beam waist of 168 μm, whereas the horizontal dipole trap (vDT) is strongly elliptic with a horizontal waist of 154 μm and a vertical waist of 20 μm.

At the beginning of the evaporation, the maximum laser power of 10 W in the horizontal and 1 W in the vertical trap generate a trap depth of 75 μK. The associated trap frequencies are $\omega/2\pi = (14, 124, 952)$ Hz (along hDT, perp. to hDT, along z). The light power in hDT in then lowered in an approximately exponential ramp which gradually reduces the confinement against gravity. The power in vDT is increased such that the final trap geometry becomes similar to the harmonic confinement of the 3D lattice. The presence of multiple spin-components in ^{173}Yb during the evaporation ensures thermalization through s-wave scattering. Employing ramp times of around 15 seconds is enough to produce degenerate gases of arbitrary mixtures of spin components, in a final trap depth below 1 μK. Typical trap frequencies after the evaporation are $\omega/2\pi = (22, 33, 191)$ Hz. At these temperatures, the Fermi gas can be transferred into the 3D optical lattice setup with only few vacancies.

A recent addition to the setup is a pair of crossed magic-wavelength dipole trap beams (see Fig. 3.1). Operating on the magic wavelength (759 nm) for the two clock states ^{1}S$_0$ and ^{3}P$_0$, they create orbital state-independent bulk confinement. These magic-wavelength dipole traps have been employed to study the bulk properties of the recently discovered interorbital Feshbach resonance [90, 99]. Although not used in this work, one could also make use of these traps for simultaneous evaporation of the two clock states, exploiting the tunable interactions for enhanced thermalization and cooling of interorbital mixtures.

3.3.3 Preparation of ground-state spin mixtures

For the experiments presented in the next chapters, probing the interorbital interaction, we typically work with degenerate mixtures of two m_F components. The temperature, balance and overall atom number of these mixtures needs to be controlled well. Initially, the loading from the MOT into the xODT leaves us with fully spin-scrambled mixtures [97], with six m_F states equally populated for ^{173}Yb. In order to manipulate the spin balance, individual m_F components need to be removed or converted to other m_F states.

To this end, experiments with ultracold alkali atoms usually drive transitions within a hyperfine manifold using microwave radiation. This is not possible with AEA where the ground state ^{1}S$_0$, with $J = 0$, possesses no hyperfine structure. Instead, the optical intercombination

transition $^1S_0 \rightarrow {}^3P_1$(F=7/2) is used to spin-selectively address and manipulate the ground state. In contrast to the MOT setup, we use a large homogeneous magnetic field of 50 G along $\hat{z}$ (produced by C_{MOT} in Helmholtz configuration) to generate an m_F-dependent differential Zeeman splitting between $^1S_0$ and $^3P_1$. The ground state $^1S_0$ is only subject to the weak nuclear Zeeman shift of $207\,h\,\mathrm{Hz/G} \times m_F$ [see Eq. (1.11)], whereas $^3P_1$ (F=7/2) splits with $597\,h\,\mathrm{kHz/G} \times m_F$. The full hyperfine structure of $^3P_1$ and the m_F-dependent Zeeman shifts are shown in Fig. 1.4. For the given magnetic field, the transitions between different m_F are energetically separated by multiple natural linewidths. We use the vertical MOT beams along $\hat{z}$ to address σ^+ and σ^-, and the horizontal beams to address π transitions.

Depending on the depth of the xODT, two qualitatively different regimes can be distinguished. In the limit of a deep xODT, as in the beginning of the evaporation, multiple 556 nm photons ($E_{\mathrm{rec}} = 3.7kHz$) can be scattered until the accumulated recoil energy is enough to expel the atoms from the trap. A sequence of light pulses can then be used to transfer population between different m_F by optical pumping. Note that the pulse time or light power has to be adapted to the varying Clebsch-Gordan coefficients in the hyperfine manifold, as in Fig. 1.9. In this way, arbitrary spin mixtures and imbalances can be prepared without losing a significant amount of atoms [97]. During evaporation, the xODT depth is lowered and the remaining atoms thermalize through collisions. The SU(N) symmetry of the ground-state s-wave interactions on experimental time scales ensures the preservation of the spin composition [see Section 1.5.3]. The detection of nuclear spin-state populations is performed by means of an optical Stern Gerlach technique, described in Section 3.6.2. Fig. 3.10 (b) shows examples of different spin-polarized and two-spin mixtures after evaporative cooling, produced by means of optical pumping.

In the limit of small trap depth, that is after the evaporation in the xODT, scattering of single pump light photons already leads to an expulsion from the trap. In the experiment, we employ short, resonant "push pulses" during a final hold time to remove residual unwanted spin components. This is particularly helpful for the generation of spin-polarized or strongly imbalanced mixtures. The evaporation is then carried out with a spin-balanced mixture, ensuring thermalization, and subsequent push pulses are used to create the desired spin configuration.

3.3.4 Measuring temperatures

Since the equation of state for an interacting many-body state is often unknown, measuring the temperature of strongly interacting Fermi gases is a non-trivial problem. In particular, this holds for optical lattice systems where the tight confinement boosts the interactions to a scale comparable to the mobility. In contrast, the atomic densities and interaction energies in the harmonic confinement provided by a weak xODT after the evaporation are strongly reduced. Even in the presence of the intermediate ground state scattering length, this enables us to fit a non-interacting equation of state to the atomic density.

A review of the physics of interacting and non-interacting Fermi gases in the presence of a trapping potential is provided in [41]. In Appendix C, we have compiled a short summary of the experimentally relevant thermodynamic observables in non-interacting systems. The

local optical density in an absorption image is proportional to the column integrated atomic density along the imaging direction. Figure 3.4(a) shows a typical, absorption image after long expansion time ($t \gg 1/\omega$), released from a shallow xODT (trap configuration as in Section 3.3.2 after evaporation). The strongly anisotropic initial in-trap density distribution

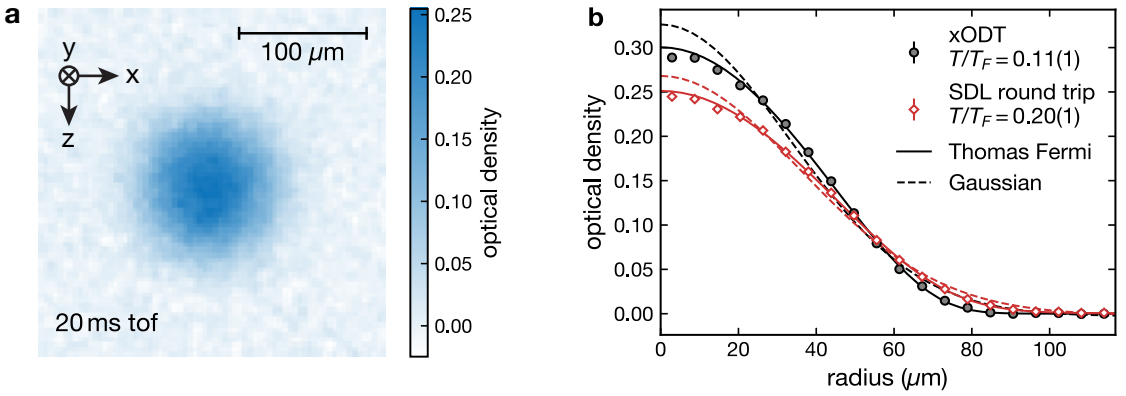

Figure 3.4 – (a) Absorption image (optical density) of a degenerate two-spin mixture (2.7×10^4 atoms) after 20 ms time of flight from xODT. After round trip from shallow xODT into the lattice (9 E_{rec} deep SDL, 30 E_{rec}perp. magic confinement), a hold time of 100 ms, and loading back into shallow xODT. (b) Reduced temperatures T/T_F from fit of Thomas Fermi profile to optical density images as in (a). Diamonds show higher-temperature data from SDL round-trip experiment [Section 3.4.3], circles are from direct release from a shallow xODT. Shown is the azimuthal average of the fit (dashed) and the data (markers) around the atom cloud center. For comparison, a fit of a 2D Gaussian distribution (dashed) shows clear deviations for the degenerate gases.

has been mapped to an isotropic momentum distribution. The low density during expansion ensures non-interacting dynamics and the final optical density is low enough to allow for non-saturated absorption imaging.

The expected column density measured in an absorption image, either in the trap or after release and expansion from the trap, is given in terms of the local density approximation, by Eq. (C.16). In a least squares approach we fit the equation of state (Thomas-Fermi distribution) to extract the fugacity $z = \exp(\mu/k_B T)$ as a measure of the quantum degeneracy. The fugacity can directly be related to the reduced temperature $T/T_F = (-6\mathrm{Li}_3(-z))^{-1/3}$ and thereby the per-particle entropy $S/(Nk_B) \approx \pi^2 T/T_F$ in lowest order Sommerfeld approximation (see Appendix C).

The fit results for two different experimental samples are shown in Fig. 3.4(b). The Thomas-Fermi approximation matches the data very well, and reduced temperatures $T/T_F \lesssim 0.2$ are extracted for the investigated two-spin mixtures. In comparison, the best fit of a non-degenerate, thermal distribution (a 2D Gaussian) strongly overestimates the density in the wings and in the cloud center, even for the higher-temperature sample.

For very small atom numbers, it can be advantageous to determine the temperature from a fit to the in-situ density distribution. The vertical imaging path in our setup provides much larger resolution and magnification (see Section 3.6.1). As illustrated in Appendix C, the functional shape of the atomic density distribution is independent of the expansion time apart

from a rescaling of the main axes. Neglecting the effect of residual interactions, the extracted fugacity and reduced temperature should be equal. Indeed, we find compatible results for both approaches. Care has to be taken in order to correctly compensate for corrections to the Lambert-Beer absorption law, in case of high imaging light intensity [98].

Weak interactions In principle, finite interactions between the atoms can heavily influence the in-trap density and momentum distribution. Bruun and Burnett [224] study the effect of strong contact interactions in the presence of a harmonic confinement along with the consequences for the validity of the Thomas-Fermi approximation. Weak interactions in a Fermi gas can be captured in Landau's Fermi-liquid picture [41] and the characteristic interaction parameter for 3D scattering in the dipole trap is $k_F a$. The relative correction to the energy per particle in first order perturbation theory is $10/(9\pi) \times k_F a$ [41]. The Fermi momentum k_F is determined by the typical Fermi energies of $E_F = \hbar^2 k_F^2/2m \approx 2\,\mathrm{kHz}$ [see Eq. (C.6)] in our experimental configuration (in Fig. 3.4). Together with the scattering length $a_{gg} = 199.4(2.1)\,a_0$ for the atomic ground state, the effective interaction parameter stays small, with $k_F a \approx 0.1$. However, finite interactions could explain the residual discrepancies in the fit to the density profile in the center of the cloud in Fig. 3.4(b).

3.4 Optical lattices

The working principles of our orbital state-dependent and independent optical lattices have been reviewed in Chapter 2. In the following, we give an overview over the experimentally available lattice configurations in our setup. In particular, the optical setup and the resulting range of available trap depths and frequencies are documented.

3.4.1 Laser sources and lattice geometry

As depicted in Fig. 3.1, three perpendicular magic-wavelength lattices are available in our setup (L1, L2, L3). We use a tunable commercial Ti:Saph ring laser as a source of the 759 nm light. The total available light power of approx. 5 W is distributed into the three lattice beams. The polarization vectors of the magic lattice beams all lie in the horizontal plane of the experiment [see Fig. 3.5(a)]. In order to prevent interference, the individual lattice beams are detuned on the 100 MHz scale with respect to each other [97]. Considering the 100 Hz resolution of our clock laser, the resulting state-dependence below the Hz level (Section 2.2.1) of the lattice can be neglected.

The light for the newly implemented state-dependent lattice (SDL) is produced by another commercial Ti:Saph ring laser[4]. At an operating wavelength of 670 nm, a maximum power of around 0.6 W can be reached on the experiment table. The short term frequency stability of the SDL laser is provided by locking it to an integrated reference cavity (1.5 GHz FSR, <50 kHz relative linewidth). On longer timescales, the length of the reference cavity is stabilized to

[4] M Squared SolsTis 18W SRX-XS, optimized for the lowest possible near-IR wavelength range.

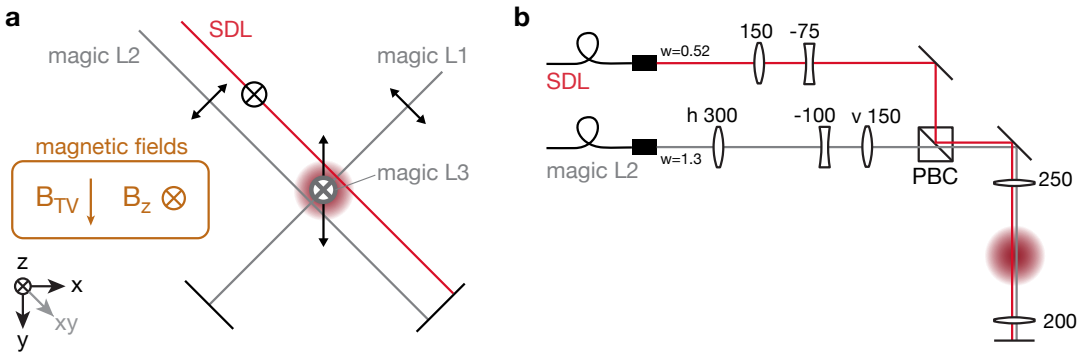

Figure 3.5 – (a) Schematic of the lattice beam setup, the state-independent lattices (magic L1, L2, L3) and state-dependent lattice (SDL). The black arrows denote the polarization with respect to the propagation directions (red) and magnetic fields (orange). The coordinate system is as in Figure 3.1 (a), centered around the position of the atoms (red). While all three magic-wavelength lattice polarization vectors lie in the xy plane, the SDL polarization is along z. (b) Beam shaping optics for focusing the copropagating L2 and SDL onto the atoms in the experiment setup. Numbers indicate lens focal lengths and beam waists (w) in mm. A telescope with horizontal and vertical (h, v) cylindric lenses is used to produce a narrow waist of L2 along the direction of gravity. A large and symmetric focus for the SDL minimizes spatially varying light shifts.

the absolute light frequency provided by a high precision wavelength meter[5]. The SDL beam copropagates with the horizontal magic-wavelength L2 and shares a common retro-reflection mirror. Figure 3.5(b) shows how the optical setup on the experiment table is used to overlap the two beams using a polarizing beam splitter. The polarization of the SDL is oriented vertically and orthogonal to all other lattice beams.

Regarding the spin-dependence of the optical lattice potentials: The linear polarization of all laser beams eliminates the possibility of vector light shifts (see Section 1.3.3). As obvious from Eq. (1.31), the overall tensor light shift for laser beams in three spatial directions cannot be completely eliminated. However, the estimated tensor light shift for the clock states in Section 1.3.4 does not exceed a relative strength of 10^{-6} compared to the scalar shift, and stays well below our clock laser resolution.

3.4.2 Trap depths and frequencies

The beam geometries together with the balancing of the laser power in the individual lattice arms determine the dimensionalities that can be simulated with the optical lattice setup. As explained in Section 2.3, the cubic lattice setup can produce every configuration between quasi-2D (pancakes), quasi-1D (cigar-shaped) or full 3D lattice systems. Different ac polarizabilities for the clock states $^3P_0$ and $^1S_0$ in the SDL (with a polarizability ratio $p \approx 3.3$ for 670 nm light) additionally allow us to realize mixed orbital confinements.

The maximum achievable trap depths and associated lattice properties (like band gap or width) in the current setup are listed in Table 3.1. Trap depths are given in units of recoil energies of the given lattice wavelength and are calibrated using the parametric heating technique,

[5]HighFinesse Wavelength Meter WS-7, 60 MHz absolute accuracy.

introduced in Section 2.4. An additional harmonic confinement frequency perpendicular to the propagation direction is induced by the finite lattice beam waists, as in Eq. (2.3). These are calibrated by measuring collective oscillatory dynamics (center-of-mass oscillations) of spin-polarized gases. The horizontal magic lattice beams have elliptical beam profiles, as to match the horizontal dipole trap aspect ratio. The vertical lattice beam is circular. The SDL beam is circular, too, with a relatively large beam waist. As a compromise, this constrains the maximum lattice depth but also spatially inhomogeneous differential light shifts for the clock states (see Section 3.5.2).

lattice	L1	L2	L3	SDL	
wavelength	magic wavelength 759 nm			670 nm (p=3.3)	
				$\|g\rangle$	$\|e\rangle$
beam waists (μm)	(40, 153)	(40, 160)	127	231	
max. depth (E_{rec})	50	30	50	9	30
trap freq. (Hz)	(121, 32)	(94, 23)	38	10	18
band width (h Hz)	0.2	3.7	0.2	249	5.0
band gap (h kHz)	26.1	19.6	26.1	10.7	25.0

Table 3.1 – Properties of the optical lattices. For relative beam orientation, see Fig. 3.5. Beam waists at the position of the atoms estimated from in-trap collective motion dynamics (sloshing) and Gaussian beam propagation. Two values (vertical and horizontal waist) are given for the horizontal elliptic beams L1, L2. The maximum lattice depths are limited by the overall laser power. The trap frequencies (along the beam waists), band width and gap are for the respective lattice alone, at the indicated max. depth. For the SDL, properties are given for both clock states $|g\rangle$ and $|e\rangle$ with polarizability ratio $p = 3.3$.

3.4.3 Lattice loading

After the evaporation in the xODT, the degenerate Fermi gas should be transferred to the lattice setup in a way that adds as little entropy as possible. Qualitatively, the profile of the handover ramps in [97, 98] is maintained, with only minor adjustment to the timing. First, the vertical lattice (L3) intensity is smoothly ramped up (in a 100 ms s-shaped ramp) while both 1064 nm dipole trap intensities are reduced to zero. The vertical lattice must be deep enough to hold the atoms against gravity. Experimentally, we determine that confinements $\geq 15E_{\mathrm{rec}}$ are sufficient. This limits the minimum perpendicular magic-wavelength depth used in the following sections. In a next step, the horizontal lattices, L1 and the SDL, are ramped in a two-step 200 ms ramp to their final depth, where the experiments are performed.

Entropy in the lattice An upper limit for the temperature, or entropy, in the lattice setup can be estimated by performing a round-trip experiment [225]. The atoms are loaded from the xODT into the lattice and back into the dipole trap in a symmetric way. The temperature can then be extracted in-situ or after time-of-flight expansion by fitting a Thomas-Fermi profile as in Section 3.3.4. Assuming thermalization of the sample after the transfer ramps, the extracted

reduced temperature should give an upper limit on the entropy in the lattice setup. For an ideal adiabatic process, the temperatures before lattice loading and after reloading into the xODT should be equal. In practice, we typically measure increases in the reduced temperature T/T_F below 0.1 , which can probably be attributed to non-optimal design of the transfer ramps. For example, Fig. 3.4 shows the final Thomas-Fermi distribution after round-trip loading into a deep SDL configuration. The fit yields a maximum $T/T_F = 0.2$ for the two-spin ground state mixture, insensitive to short variations of the intermediate hold time in the lattice.

Our in-situ imaging system allows us to access the horizontal profile of the in-trap density distribution, that is, the distribution in the SDL and L1. However, we are looking at the vertical column integration over several lattice planes. The number of populated planes is determined by the initial transfer from the xODT into L3, where the lattice confinement essentially freezes out the vertical distribution in the dipole trap. Assuming adiabatic loading and non-interacting Fermi gases, we simulate the loading process as in [97]. The total particle number and the entropy are fixed, and the 3D bulk equation of state is transformed into a vertical stack of independent 2D systems, each with a local chemical potential determined by the vertical trap frequency of the xODT. For the trap configuration given in Table 3.1, we estimate that 17% of the atoms occupy the central plane and only 7 planes have an atom number larger than 5% of the total atom number.

3.5 Addressing the second orbital

The excited orbital, the clock state $^3P_0$, can be accessed through coherent atom-light coupling on the ultranarrow clock transition. Details on the implementation and characterization of our clock laser can be found in [97, 226]. In this section, we will briefly review its main features regarding clock spectroscopy in our state-dependent lattice setup. In particular, we will discuss the consequences of the spatially inhomogeneous differential light shift and how to cope with it in the experiment.

3.5.1 The clock laser

The clock laser light is initially produced by a 1156.8 nm external cavity diode laser with a linewidth below 100 kHz. Frequency doubling to 578 nm yellow light is done using a periodically poled lithium tantalate crystal for second-harmonic generation. Via a Pound-Drever-Hall locking technique, the laser is stabilized to an ultralow-expansion glass reference cavity. A high-bandwidth control loop reduces the laser linewidth to around 60 Hz after frequency doubling [97]. This is multiple orders of magnitudes larger than commonly achieved in state-of-the-art clock laser setups [57]. Yet, the resolution is sufficient for our experiments, considering that for fast state preparation and detection schemes, we deliberately induce power broadening on the kHz scale.

With the current beam configuration, the laser intensity at the position of the atoms is

around $3\,\mathrm{W/cm^2}$. This corresponds to a maximum Rabi coupling[6] of $\Omega = 2\pi \times 2\,\mathrm{kHz}$ (see Section 1.4) or a π pulse time of $250\,\mu s$. A beam waist of around $200\,\mu\mathrm{m}$ (at a light power of 2 mW) ensures near-homogeneous intensity over the typical atom cloud extent.

The dipole coupling of the clock light to adjacent atomic transitions leads to a frequency shift of the clock transition itself, often referred to as the probe Stark shift in optical clock experiments [57, 128, 135]. From the ac polarizability calculation in Section 1.3.4, we estimate a probe Stark shift of $\sim 17\,\mathrm{Hz}$ per $1\,\mathrm{W/cm^2}$ yellow light intensity for ^{173}Yb. This is slightly below our clock laser resolution for the employed light powers.

3.5.2 Orbital state preparation in the state-dependent lattice

In Section 2.5, we have discussed the differential light shift in the presence of the SDL. The clock transition is red-shifted, with an amplitude that scales with the SDL depth [Eq. (2.30)]. The typical alignment of the clock laser with respect to the lattice setup is shown in Fig. 2.13. The clock beam polarization is vertical and aligned along the quantizing B-field. Copropagation with the deep magic-wavelength lattice L1 ensures Lamb-Dicke conditions with a typical Lamb-Dicke parameter of $\eta = 0.13$ for a $30\,E_{\mathrm{rec}}$ deep lattice.

Apart from the overall light shift of the clock line, the distribution of atoms in an inhomogeneous SDL potential leads to a broadening of the transition. The two-spin, low atom number (7×10^3 atoms) samples prepared in Chapter 5 exhibit an estimated Fermi radius of $7\,\mu\mathrm{m}$ after adiabatic loading into a SDL and magic perpendicular confinement (for the trapping configuration in Table 3.1 and Fig. 3.5). This results in a differential light shift varying by around 0.1 kHz over the atom distribution in the trap for the maximum available SDL depth. The available clock laser power is enough to generate a power broadening Ω_0 on the few kHz scale and, in practice, addresses at least 80% of the atoms by resonant π pulses.

Note that for some of the earlier experiments, we have used a more tightly focused beam profile for the SDL (allowing for a larger maximum lattice depth). For example, the measurement presented in Fig. 1.11 was performed with 1.7 times smaller SDL beam waists, resulting in a roughly three times larger inhomogeneous light shift for the same extension in the trap. Only around 60% of the spin-polarized sample could be excited by resonant π pulses in this measurement.

Rapid adiabatic passages In such trapping configurations, it can be beneficial to compensate the inhomogeneous light shifts with an additional dipole trap beam that has an inverted ac polarizability ratio (trapping $^1\mathrm{S}_0$ stronger than $^3\mathrm{P}_0$). Alternatively, in our experiment, we have tested a clock excitation scheme relying on a large-range rapid adiabatic passage (RAP) across the resonance (e.g., in the lattice depth calibration measurement in Fig. 2.11). By not only ramping the clock light detuning but also modulating its intensity, we can achieve good

[6] In a recent upgrade to the clock laser setup, we have integrated a tapered amplifier for the 1112 nm light which allows for significantly increased Rabi couplings, on the order of $\Omega = 10\pi \times 2\,\mathrm{kHz}$ for the same beam configuration.

transfer efficiencies with moderate ramp frequency amplitudes. This is important as to retain some spectroscopic resolution in the m_F-dependent state preparation. Compared to the constant-intensity RAP presented in [227], we can then address single spin components in a multi-spin mixture using only small Zeeman splitting.

Starting from the atom-light coupling Hamiltonian for an atomic two-level system (bare states $|g\rangle$ and $|e\rangle$) in Eq. (1.36), one can derive a differential equation for the dynamics of the state vector $|\psi\rangle = c_g|g\rangle + c_e|e\rangle$, for a time-varying light detuning Δ and bare Rabi coupling Ω_0 [121, 228]:

$$\partial_t \begin{bmatrix} c_g \\ c_e \end{bmatrix} = -i \begin{bmatrix} 0 & \Omega_0(t)/2 \\ \Omega_0(t)/2 & -\Delta(t) \end{bmatrix} \begin{bmatrix} c_g \\ c_e \end{bmatrix} \tag{3.7}$$

The idea behind the RAP is to start with light far detuned from resonance compared to the Rabi frequency ($|\Delta| \gg \Omega_0$), such that the dressed states with energies $E_\pm$ [Eq. (1.39)] coincide with the bare atomic states.

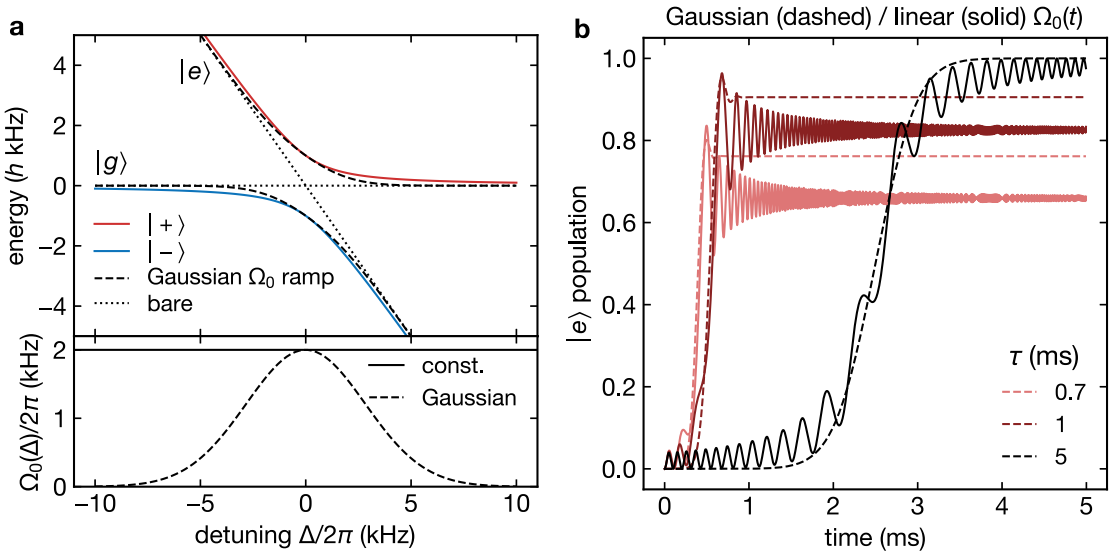

Figure 3.6 – (a) Dressed states $|+\rangle$ and $|-\rangle$ (solid) of the two-level atom-light coupling model for typical bare Rabi coupling $\Omega = 2\pi \times 2$ kHz, compared to dressed states for Gaussian detuning dependent coupling $\Omega_0(\Delta)$ (dashed). Dotted lines are bare atomic states. The lower panel shows the Gaussian detuning dependence of Ω_0 in the experimental RAP. (b) Time traces of the excited-state population during RAP, for different detuning and coupling sweep times τ. Constant Rabi coupling (solid) and Gaussian dependence on detuning (dashed) are compared. Full population transfer is reached for $\tau \gg 1/\Omega_0$.

This is illustrated in Figure 3.6(a) for typical experimental parameters ($\Omega_0 = 2\pi \times 2$ kHz, initial detuning $-\Delta_0 = -2\pi \times 10$ kHz). The light detuning is then slowly swept across the resonance as to transfer the initial $|g\rangle$ population to $|e\rangle$ and inversely:

$$\Delta(t) = -\Delta_0 + \frac{2\Delta_0}{\tau} t \quad \text{for} \quad 0 < t \leq \tau\,. \tag{3.8}$$

The ramp speed τ needs to be slow compared to the Landau-Zener velocity, determined by the gap size Ω_0.

The solid lines in Fig. 3.6(b) are the numerical solutions obtained from Eq. (3.7) for a constant clock laser intensity, or Rabi coupling Ω_0, and different ramp speeds for the detuning. Obviously, although $\tau \gg 1/\Omega_0$ for the slowest ramp, there are residual oscillations in the transferred population. These originate from the small initial detuning and a projection of the bare atomic state onto the dressed states. We resolve this issue by performing a Gaussian-profile ramp of the laser intensity that is dependent on detuning, with a maximum at $\Delta = 0$ [see dashed lines in Fig. 3.6]:

$$\Omega_0 \rightarrow \Omega_0(t) = \Omega_0 e^{-\frac{(t-\tau/2)^2}{2[\tau/(4\pi)]^2}}. \tag{3.9}$$

This increases the effective initial detuning and the overlap of bare and dressed states at the beginning of the ramp, and thereby removes the oscillatory dynamics. In practice, with RAP ramp times of around 5 ms in the trap configuration of Table 3.1, we achieve transfer efficiencies of above 90% for individual spin components. This is on par with the high-power resonant π pulses, yet, at the cost of larger state-preparation times.

3.5.3 A repumper for the clock state

In a recent upgrade to the experiment, we have implemented a repumper laser for the excited clock state $^3P_0$ that enables repumping to the imageable atomic ground state $^1S_0$. The laser operates on the 1388.19 nm transition $^3P_0 \rightarrow (5d6s)^3D_1$. The state $^3D_1$ can decay into multiple lower lying states (see Fig. 1.2). Without taking hyperfine structure into account, the estimated branching ratios into the final states $^3P_0$, $^3P_1$ and $^3P_2$ are 0.64, 0.35 and 0.01 (see Table B.1). Atoms in $^3P_1$ further decay to $^1S_0$ whereas $^3P_0$ can be repumped again and $^3P_2$ is a dark state of the repumping scheme. The expected maximum efficiency of the repumping scheme is 97.5% with only 8 photons required for a >95% repumping efficiency [227, 229].

Technical details on the setup, similar to the implementation in [227], can be found in [229]. The repumper light is provided by a commercial DFB laser[7] with an output power of 30 mW. A light power of around 5 mW and a beam waist of 0.8 mm lead to a peak intensity of 0.5 W/cm^2 at the position of the atoms. The natural width of the repumper line is $\Gamma = 2\pi \times 309(6)$ kHz [105] and the strong saturation broadens the transition to a FWHM of around 0.30 GHz.

In practice, this makes the repumper efficiency less susceptible to laser temperature variations. The experimentally determined sensitivity is 16.5(2) MHz/mK, and the laser temperature is only stabilized on the few 10 mK level [229]. The repumper beam is π polarized and aligned under a small angle with respect to the lattice L1 and the yellow clock laser beam path (see Fig. 3.1), ensuring Lamb-Dicke conditions in the presence of a deep L1. The repumper beam is expected to scramble the m_F components with rates and branching ratios depending on the addressed hyperfine state. For the hyperfine and Zeeman substructure of $^3D_1$, see the spectrum in Fig. A.5.

With the current experimental configuration, we find that a pulse time of 2 ms is enough to reach maximum repumping efficiency for all spin components. Figure 3.7(a) shows a typical

[7] NTT Electronics NLK1E5GAAA

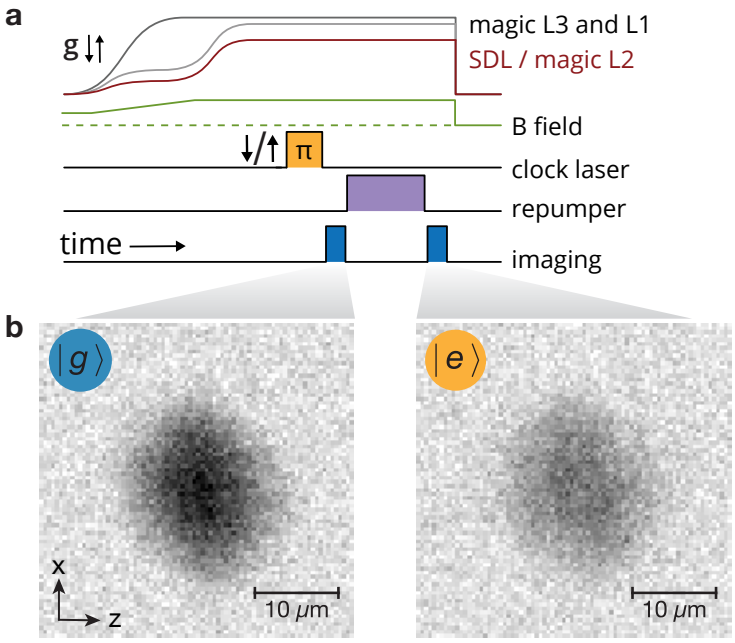

Figure 3.7 – (a) Schematic of clock spectroscopy experiment using clock laser π pulses to excite $|g\rangle$ to $|e\rangle$ and the repumper to detect $|e\rangle$. Two imaging pulses are used to image $|g\rangle$ and $|e\rangle$ separately using the "multi-stripe" imaging technique. (b) Typical in-situ images of the $|g\rangle$ population after clock excitation and $|e\rangle$ after repumping, on the $m_F = -5/2$ clock line resonance. Experiment as in Fig. 3.8.

experimental sequence used for repumping clock line spectroscopy of a two-spin mixture in the lattice confinement. The atoms are loaded adiabatically to the lattice confinement, with roughly unit filling, while the magnetic field is ramped high enough to resolve the different m_F levels. Then, a clock laser π pulse performs the orbital excitation at a given frequency and the remaining $|g\rangle$ atoms are imaged in a first "stripe" of our multi-stripe imaging technique (Section 3.6.1). Subsequently, atoms are repumped and the $|g\rangle$ atoms are imaged again. Examples for resulting in-situ absorption images on resonance are shown in Fig. 3.7(b) and a typical high-power clock-line spectrum is presented in Fig. 3.8. We observe that the short repumping pulse does not significantly broaden the in-trap distribution. Also, the sum of $|g\rangle$ and $|e\rangle$ atoms remains constant over the entire spectrum within the SNR, as expected for close to 100% repump efficiency. The ac Stark shift caused by the SDL confinement is small compared to the power-broadened repumper line width and does not measurably influence the repumping rate. Note that the required pulse time is much longer than expected for the aforementioned scattering rate, probably due to off-resonant scattering. A direct stabilization of the laser frequency should help to improve the repumping rate.

3.6 State detection

In the previous sections, it was illustrated how nuclear spin-mixtures in different electronic orbitals are prepared using resonant atom-light coupling. Here, we present our experimen-

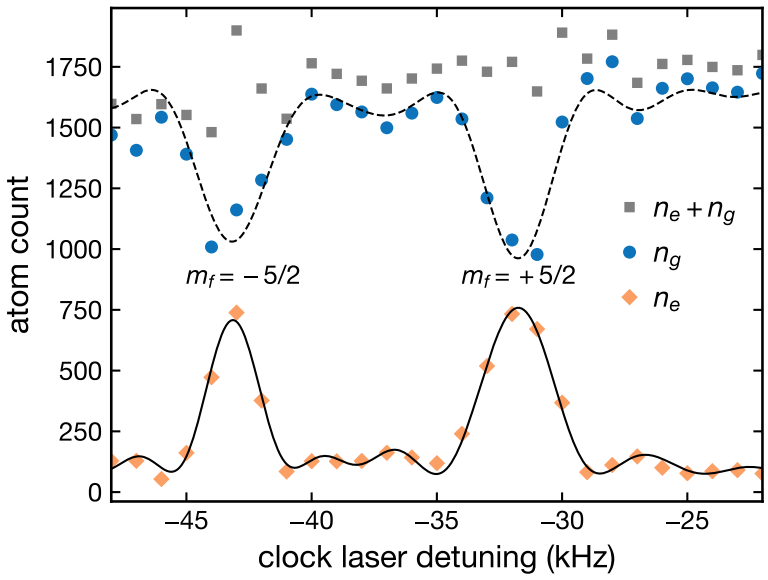

Figure 3.8 – Clock spectrum of a degenerate two-spin mixture (balanced $m_F \in \pm 5/2$) in a the SDL (8 E_{rec}, with 45 E_{rec} perpendicular L1 and L3, no double occupancies). Clock excitation of $|g\rangle$ (circles) with π pulses ($\Omega_0 = 2\pi \times 1.6\,\mathrm{kHz}$, excitation fraction ~ 0.8) $|e\rangle$ atoms (diamonds) repumped with 2ms pulses, all at 20 G magnetic field. Sum of detected $|g\rangle$ and $|e\rangle$ atoms (squares) is constant over entire spectrum. Dashed and solid lines are fits of two Rabi line shapes (Eq. (1.42)) to $|g\rangle$ and repumped $|e\rangle$ population.

tal techniques for extracting information on the atomic density in the trapping potential. Combining resonant absorption imaging with an optical Stern Gerlach technique and a clock state shelving technique, allows us to determine the spin and orbital composition of multi-component Fermi gases.

3.6.1 Absorption imaging

Imaging in our setup is based on resonant absorption imaging on the dipole-allowed ${}^1\mathrm{S}_0(F = 5/2) \rightarrow {}^1\mathrm{P}_1(F = 7/2)$ transition. The large linewidth of $\Gamma \approx 2\pi \times 29$ MHz and photon scattering rate allow for short imaging pulse times in the few μs range.

As illustrated in Fig. 3.1, our experiment setup possesses two main imaging paths. A horizontal imaging path with low magnification ($3.9 \times 10^{-6}\,\mu\mathrm{m/px}$) is used to perform time-of-flight imaging from the side after expansion from the trap. The reduced optical density after time of flight permits us to image atomic samples with high in-trap density. Long time of flight compared to the trap frequencies gives access to the in-trap momentum distribution, and thereby to the reduced temperature (see Section 3.3.4). It is also used to probe the spin-dependent momentum kick generated by the OSG beam.

Along the vertical axis, high resolution in-situ imaging provides spatial resolution of in-trap density distributions. The optical properties of this imaging setup have been characterized in [69]. There, the in-situ resolution of $\sim 1.2\,\mu$m with a numerical aperture NA=0.27 has proven to be enough to resolve spatial structure over few lattice sites and analyze the equation of state

of the SU(N) Fermi-Hubbard model [98]. A schematic of the in-situ imaging setup is shown in Fig. 3.9(a). The current magnification (0.47×10^{-6} μm/px on the EMCCD sensor) slightly oversamples the optical resolution[8].

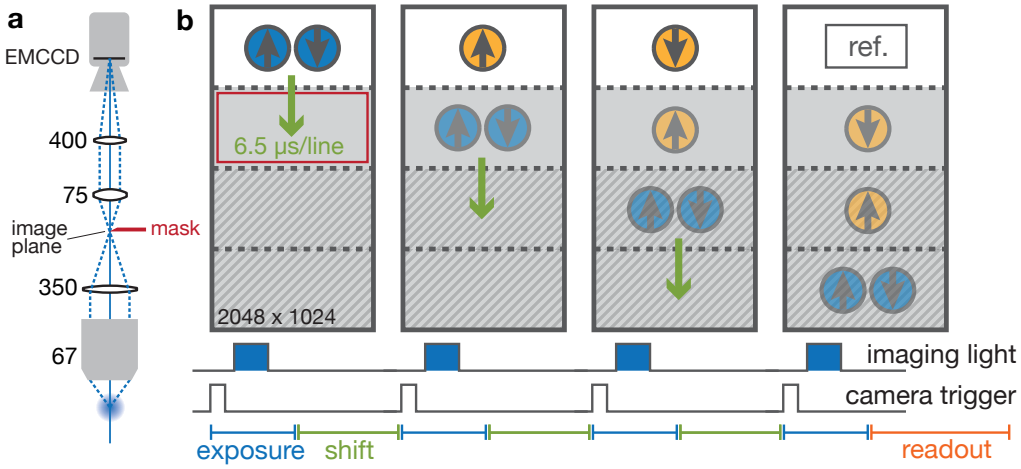

Figure 3.9 – (a) Schematic of the in-situ imaging setup. Numbers indicate lens focal lengths in mm. A quadruplet objective (custom design by Lens-Optics GmbH) with NA=0.27 is focused on the atoms. An achromatic lens produces a first image plane P that is imaged via a second magnifying telescope (total magnification ~ 28) on the EMCCD camera. A razor blade in plane P enlarges the dark region of the CCD. (b) Multi-stripe imaging sequence: The CCD is subdivided into 4 stripes. The lower half is masked on the sensor. An additional mask in P increases the dark area (red). External triggers start the preset CCD exposure time and subsequent vertical pixel shifts by one stripe (green arrow). The first three stripes capture different spin/orbital components. The last trigger produces an empty reference image and starts readout.

Multi-stripe imaging

Absorptive imaging in our setup is a destructive process. For a typical image pulse length of 10 μs and a maximum scattering rate of $\Gamma/2$ (see Section 1.3.7), we estimate around 900 scattered photons. The associated recoil energy is enough to expel an atom even from deep optical lattice confinement. Short imaging pulses can therefore be used to remove ground-state atoms from the trap and image them at the same time.

This gives us the ability to image multiple spin or orbital components in one experimental cycle. The benefits of this "differential" measurement are an increased signal-to-noise ratio for many relative observables and an improved effective cycle time. For example, in Chapter 5, we measure the relative $|g\rangle$, $|e\downarrow\rangle$ and $|e\uparrow\rangle$ population after a certain spin-exchange time. The fundamental requirement for this technique to be useful, is that the sequence of images is taken fast compared to residual physical dynamics.

In principle, the m_F-dependent Zeeman shift of the imaging transition could be used for spin-resolved detection. A magnetic field of around 80 G is needed to split m_F-adjacent transi-

[8] We calibrate the magnification by probing the atomic density modulation in a bichromatic lattice [69]. The summed potentials of the copropagating magic-wavelength lattice L2 (759 nm) and the state-dependent lattice (670 nm) lead to a 2.84 μm periodic horizontal modulation pattern, larger than the optical resolution.

tions (see Fig. A.2). However, technical limitations of the imaging laser frequency lock scheme strongly limit the maximum ramp speed of the laser frequency, and we cannot easily tune it to be resonant with multiple m_F components in one sequence. Instead, we typically image the atoms at low magnetic field where the m_F-dependent Zeeman shift of the imaging transition is unresolved. Using π-polarized light we ensure balanced sensitivity for $m_F = \pm 5/2$ (see Fig. 1.9). Shelving of atoms in the excited clock state still enables both spin and orbital selectivity. E.g., in Chapter 5, spin-selective clock laser pulses are used to subsequently transfer excited state atoms back to the ground state where they can be imaged.

On the camera side, fast image sequences need to be recorded. We make use of the "Fast Kinetics Mode" of our EMCCD camera[9] and an enlarged dark sensor region to capture up to three independent images, each with a capture time on the ms scale. This is illustrated in Fig. 3.9. External triggers to the camera start the preset exposure time during which a first image is taken. Thereafter, the pixels are shifted downward on the CCD by a quarter of the sensor size. The maximum shift speed (6.5 μs per line) depends on the vertical CCD bias voltage. This process is repeated three times and the final trigger starts the comparatively slow (300 ms) readout of the entire CCD.

High-intensity absorption imaging

In-situ imaging of our dense degenerate atomic samples in the optical lattice and dipole trap requires saturation of the imaging transition. In the high saturation limit, the photon scattering rate is bounded by the transition linewidth and the effective optical density is reduced (see Section 1.3.7). A modern review on saturated in-situ absorption imaging techniques is given in [230]. We follow the approach in [231] to calibrate the intensity dependent scattering cross section $\sigma(I)$.

In order to extract the correct atomic densities, a modified version of the classical Lambert-Beer law needs to be considered, taking into account the transition saturation:

$$\frac{\partial I}{\partial z} = -n(z)\,\sigma\left(I(z)\right) I(z) \quad \text{with} \quad \sigma(I) = \sigma_{\text{eff}} \frac{1}{1 + I/I_{\text{eff}}^{\text{sat}}}\,. \tag{3.10}$$

The resonant scattering cross section σ_0 and saturation intensity I_0^{sat} from Eq. (1.44) are modified by a factor α, such that $\sigma_{\text{eff}} = \frac{\sigma_0}{\alpha}$ and $I_{\text{eff}}^{\text{sat}} = \alpha I_0^{\text{sat}}$. This unknown parameter takes into account the sampling of the Zeeman substructure of the imaging transition by a given light polarization.

By integration of Eq. (3.10) along the imaging direction z, we arrive at an expression for the atomic column density $\int \mathrm{d}z\, n(z)$ and the optical depth map:

$$OD(x,y) \equiv \sigma_0 \int \mathrm{d}z n(z) = -\alpha \ln\left(\frac{I_f(x,y)}{I_i(x,y)}\right) + \frac{I_i - I_f}{I_0^{\text{sat}}}\,. \tag{3.11}$$

The two-level saturation intensity is $I_0^{\text{sat}} = 60.0\,\text{mW/cm}^2$ for our imaging transition. Typical in-situ imaging intensities in our setup are around $I \approx I_0^{\text{sat}}$[10]. In practice, one needs to convert the

[9] Andor iXon, water cooled, optimized version for blue light

[10] with a beam waist of 220 μm

intensities in Eq. (3.11) to counts on the camera. Therefore, the intensity at the position of the atoms needs to be calibrated independently. Knowledge about the atom density distribution in the trap can be exploited, as in [69], where a unit-filled Mott insulating phase in a 3D lattice is prepared.

The parameter α can be determined experimentally by demanding a fixed optical depth (or atomic column density) for varying light intensity [230, 231]. Its value can vary depending on the light polarization, the actual spin composition of the atomic sample as well as the pulse length. For example, for the in-situ measurements in Chapter 5, we independently determine $\alpha = 1.44$ for $m_F = +5/2$ and $\alpha = 1.27$ for $m_F = -5/2$. Alternatively, intensity-dependent momentum transfer through photon scattering can be used to calibrate the imaging cross section [232].

3.6.2 Optical Stern-Gerlach detection

When in-situ resolution is not required, a straight-forward way to access the global spin composition of the atomic ground state in our setup is a Stern Gerlach technique. The reduced magnetic sensitivity of the two clock states prohibits a standard magnetic gradient technique. Instead, we employ an optical Stern Gerlach technique [233], as first realized for ytterbium in [234].

The operating principles are illustrated in Fig. 3.10 (a). A strong m_F-dependent dipole force gradient is generated at the position of the atoms by means of a horizontal 556 nm laser beam. The force generates a momentum kick which can be probed after time-of-flight expansion and the spin components become spatially separated.

The detuning is chosen close to the $^1\mathrm{S}_0 \rightarrow {}^3\mathrm{P}_1$(F=7/2) transition such that the light shifts are dominated by the according Clebsch-Gordan coefficients given in Fig. 1.9. Depending on the light polarization, the dipole force can be dominated by the vector or the tensor light shift, as shown in Fig. 1.7.

When σ^+ polarized light is used, the vector shift dominates and all m_F components experience different forces. This is shown in Fig. 3.10(b) for different spin mixtures after expansion from the xODT. Note that the slightly attractive force for $m_F = -5/2$ stems from the light shift contributions of the other two hyperfine states. Typically, the quantization axis in our experiments is provided by the vertical magnetic field B_z. For σ polarization, the field and atomic spins therefore have to be adiabatically rotated (on the few 100 ms time scale) to the horizontal B_{TV} before the OSG pulse.

In order to still have fast access to multiple spin components, in the context of the spin-exchange experiments, we make use of a π polarized OSG beam. The light shift is then predominantly tensorial and only varies for different values of $|m_F|$. Figure 3.10(c) shows a typical momentum distribution picture of an $m_F \in (-5/2, +3/2)$ mixture obtained after π polarized OSG, directly from a deep optical lattice setup. The increased momentum spread in the optical lattice leads to a blurred signal. We are uncertain about the origin of the substructure of the $m_F = -3/2$ signal. It could be caused by imperfect polarization together with a weak vertical quantization field of 2 G. Yet, we have verified in an independent measurement, that

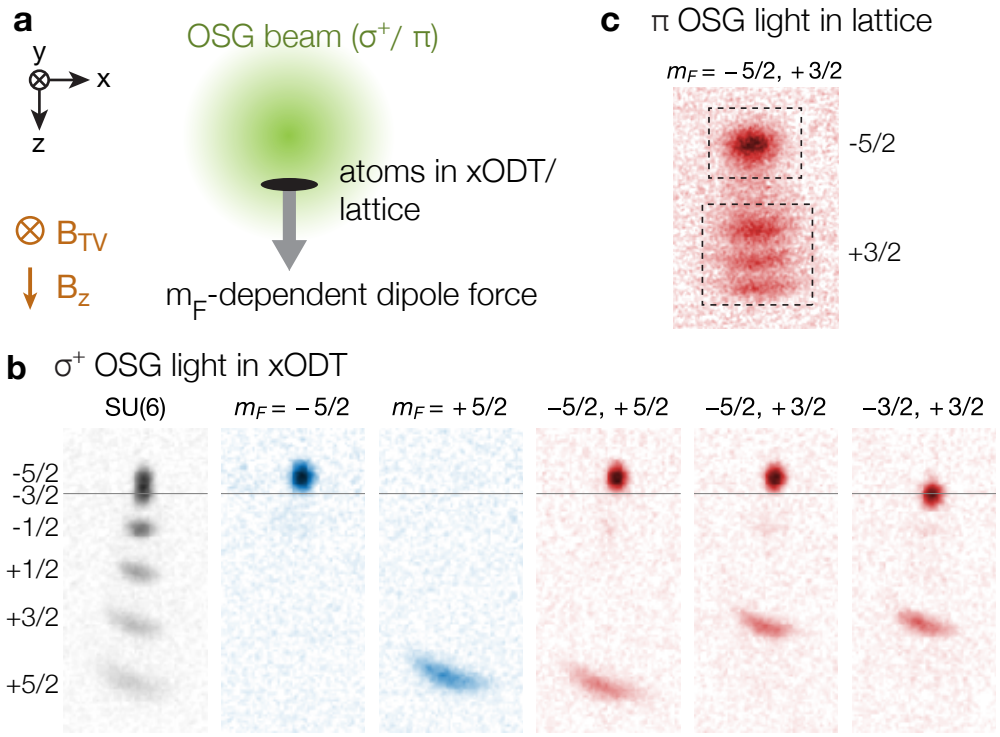

Figure 3.10 – (a) Optical Stern Gerlach (OSG) technique for nuclear spin detection in the crossed optical dipole trap or a lattice system. The coordinate system is as in Fig. 3.1 (a). The horizontal OSG laser beam (along $\hat{y}$) creates an intensity gradient that induces an m_F-dependent, vertical dipole force onto the atoms. The quantization axis is set either by the magnetic field B_{TV}, yielding σ^+ light for right-circular polarization – or by the vertical field B_z, yielding π light with linearly polarized light. (b) Split m_F states by OSG force for a balanced 6 spin mixture (gray), or after optical pumping to one (blue) or two (red) m_F states. Absorption images are after 12 ms time of flight, for horizontal magnetic field $B_{\mathrm{TV}} = 20$ G, after a 1 ms, σ^+ light pulse from a $\sim$ 40 mW beam ($\sim 100\,\mu$m waist on the atoms), 0.9 GHz detuning from the $^1\mathrm{S}_0 \rightarrow {}^3\mathrm{P}_1$(F=7/2) resonance. The gray line indicates the atom position without light force. (c) Absorption image after π light OSG on $m_F \in (-5/2, +3/2)$ mixture in optical lattice (30 E_{rec} deep L1 and L3). Blurred signal from momentum spread in lattice, after 8 ms time of flight, vertical magnetic field $B_z = 2$ G.

the two rectangular areas in Fig. 3.10(c) can be uniquely identified with the two prepared spin components.

CHAPTER 4

Interorbital interactions in mixed confinement

In this chapter, we introduce a theoretical model for the two-particle interorbital interactions in the orbital state-dependent lattice (SDL). From this model, we derive the Hubbard on-site interaction parameters for our 1D SDL system. The interorbital scattering is described by two scattering channels, the orbital singlet and triplet channel (or the nuclear spin triplet and singlet channel, respectively). The strong orbital triplet scattering of ^{173}Yb in the confinement of the SDL necessitates a simultaneous treatment of the interactions and the on-site trapping potential. The presented approach from our publication [172], is an approximative model for the scattering in mixed confinement for the two orbitals and is based on the exact solution of two particles interacting in an anisotropic harmonic oscillator potential [235]. Notably, a set of shallow spin-singlet bound states is predicted, which are induced by the lattice confinement. These underlie the tuning mechanism for the effective spin-exchange coupling, describing the magnetization dynamics in the next chapter.

Moreover, in this chapter, we discuss a direct spectroscopic characterization of the interorbital interactions in the SDL. Clock line spectroscopy is used to probe the low-energy eigenspectrum of a strongly interacting fermionic two-spin mixture. The measurement is performed over a range of magnetic fields across the orbital Feshbach resonance, where the two interorbital scattering channels become strongly coupled. We compare the experimental results to a full coupled two-channel model for the interactions in the SDL.

4.1 Interactions in mixed anisotropic confinement

The nature of the confinement for non-interacting particles in our SDL setup has been discussed in Section 2.3. An array of quasi-1D systems[1] is produced by two perpendicular magic-wavelength lattices of depth $V_\perp$. In the longitudinal direction z, a SDL of variable depth $V_z \equiv V_{z,g}$ for the ground state atoms and $V_e = p\,V_z$ (eg polarizability ratio $p = 3.3$) for the excited-sate atoms is superimposed (Fig. 2.9). In the case of fully localized $|e\rangle$ atoms, a sen-

[1] We employ the common prefix "quasi" for reduced dimensionalities which are produced by perpendicular confinement strong enough to fully restrict kinematics in this direction, but weak enough such that the excluded dimensions still enter the scattering process [40].

sible theoretical description would be provided by scattering models employing fully mixed dimensions [236–238]. Such interaction models tailored to our SDL setup have recently been proposed featuring, e.g., fully localized or quasi-0D $|e\rangle$ impurities interacting with a bath of mobile $|g\rangle$ particles in 1D or quasi-1D [84, 177, 178].

Instead, since the eg lattice depth ratio $p = 3.3$ is relatively moderate, we consider it reasonable to treat the $|g\rangle$ and $|e\rangle$ confinement in the same dimensionality for modelling the interorbital interactions. On-site quasi-0D confinement is assumed for both orbitals, which, in general, is different (mixed) and spatially anisotropic for both clock states $|g\rangle$ and $|e\rangle$. For simplicity, we will treat the two-body interactions in the harmonic oscillator (h.o.) approximation for an individual lattice site (see Section 2.1.2). The lattice anharmonicities and mixed confinement, leading to coupling between center-of-mass and relative motion will be included on a perturbative level.

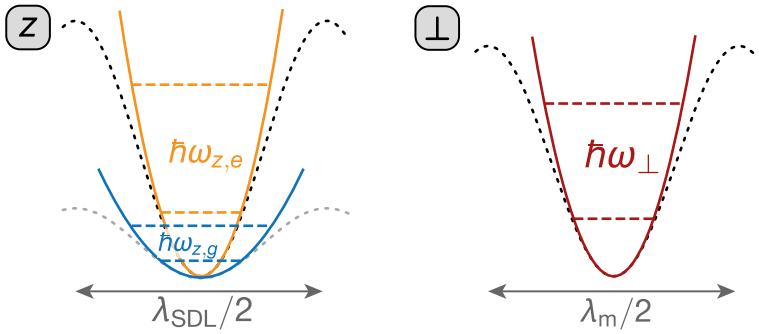

Figure 4.1 – Mixed, anisotropic lattice on-site confinement (dotted) in the SDL (along z, $\lambda_{\mathrm{SDL}} = 670\,\mathrm{nm}$) with two deep perpendicular magic-wavelength lattices ($\perp$, $\lambda_m = 759\,\mathrm{nm}$). Mixed confinement along z with two distinct frequencies $\omega_{z,g/e}$ for $|g\rangle$ (blue) and $|e\rangle$ (orange) in harmonic approximation (solid). H.o. frequency $\omega_\perp$ along $\perp$ lattices.

4.1.1 The on-site interaction model

As illustrated in Fig. 4.1, the on-site confinement is dominated by three independent energy scales given by the oscillator frequencies for $|g\rangle$ and $|e\rangle$ in the longitudinal and perpendicular direction, determined by the individual lattice depths via Eq. (2.8):

$$\hbar\omega_{z,g} = 2\sqrt{V_z E_{\mathrm{rec}}^z}, \quad \hbar\omega_{z,e} = \sqrt{p}\,\hbar\omega_{z,g} \quad \text{and} \quad \hbar\omega_\perp = 2\sqrt{V_\perp E_{\mathrm{rec}}^\perp}. \tag{4.1}$$

Let us consider the interactions between one $|g\rangle$ and one $|e\rangle$ particle in the presence of this potential. For our low-temperature atomic samples, we assume only s-wave collisions between distinguishable fermions. Interorbital interactions in ^{173}Yb can happen both in the weakly interacting spin-triplet channel with 3D scattering length a_{eg}^-, or in the strongly interacting spin-singlet channel with $a_{eg}^+ \gg a_{eg}^-$ (Section 1.5.4). Although the perpendicular lattice confinement is deep in the tight-binding regime, it stays comparable to the longitudinal $|e\rangle$ confinement and we model the on-site interactions in 3D. The true finite-range interatomic

scattering potentials are replaced by zero-range Fermi-Huang pseudopotentials [138]

$$V_{\mathrm{int}}^{\pm}(\mathbf{r}) = \frac{4\pi\hbar^2 a_{eg}^{\pm}}{m}\delta(\mathbf{r})\frac{\partial}{\partial r}r\,. \tag{4.2}$$

This is a valid approximation, since the range of the interaction potential (the van der Waals length) stays small compared to the separation of the particles, that is, the h.o. length. The regularized pseudopotential is required instead of a bare delta potential for a correct treatment of the strongly-interacting spin-singlet channel. In particular, it supports a spectrum of loosely bound molecular states [139].

Without a magnetic field that couples the two interaction channels, independent Hamiltonians can be constructed for eg pairs in a spin singlet or triplet sate. Cylindrical coordinates ($z_{e/g}$ and $\rho_{e/g}$ along the long./perp. confinement) capture the symmetry of the confinement and we obtain

$$\hat{H}^{\pm} = -\frac{\hbar^2}{2m}\left[\nabla_g^2 + \nabla_e^2\right] + \frac{m}{2}\left[\omega_\perp^2\left(\rho_g^2+\rho_e^2\right) + \omega_{z,g}^2 z_g^2 + \omega_{z,e}^2 z_e^2\right] + V_{\mathrm{int}}^{\pm}(\mathbf{r}_g - \mathbf{r}_e). \tag{4.3}$$

Motivated by the fact that the interactions only depend on the interparticle distance, let us now switch to center-of-mass (CM) and relative (rel.) coordinates $\mathbf{R} = (\mathbf{r}_g + \mathbf{r}_e)/2$ and $\mathbf{r} = \mathbf{r}_g - \mathbf{r}_e$, using

$$\begin{aligned} \nabla_g^2 + \nabla_e^2 &= {\nabla_{\mathbf{R}}}^2/2 + 2{\nabla_{\mathbf{r}}}^2\,, \\ \rho_g^2 + \rho_e^2 &= 2\rho_{\mathrm{CM}}^2 + \rho^2/2\,, \\ z_{g/e} &= Z \pm z/2 \end{aligned} \tag{4.4}$$

The total Hamiltonian can be split into three parts:

$$\hat{H}^{\pm} = \hat{H}_{\mathrm{CM}} + \hat{H}_{\mathrm{rel}}^{\pm} + \hat{H}_{\mathrm{mix}}\,. \tag{4.5}$$

The CM part of the two-particle system is a non-interacting h.o. with the total mass $M = 2m$:

$$\hat{H}_{\mathrm{CM}} = -\frac{\hbar^2}{2M}{\nabla_{\mathbf{R}}}^2 + \frac{M}{2}\left[\omega_\perp^2\rho_{\mathrm{CM}}^2 + \bar{\omega}_z^2 Z^2\right]. \tag{4.6}$$

The rel. motion part of the Hamiltonian is described by an interacting h.o.

$$\hat{H}_{\mathrm{rel}}^{\pm} = -\frac{\hbar^2}{2\mu}{\nabla_{\mathbf{r}}}^2 + \frac{\mu}{2}\left[\omega_\perp^2\rho^2 + \bar{\omega}_z^2 z^2\right] + V_{\mathrm{int}}^{\pm}(\mathbf{r}) \tag{4.7}$$

with the reduced mass $\mu = m/2$ and an effective trapping frequency $\bar{\omega}_z^2 \equiv (\omega_{z,g}^2 + \omega_{z,e}^2)/2$ along the SDL. Additionally, a CM-rel. coupling term

$$\hat{H}_{\mathrm{mix}} = \frac{m}{2} Z z \Delta\omega^2 \tag{4.8}$$

emerges because of the mixed confinement, scaling with the difference in the trap frequencies

$$\Delta\omega^2 = \omega_{z,e}^2 - \omega_{z,g}^2 = (p-1)\omega_{z,g}^2 \tag{4.9}$$

and vanishing in the case of state-independent potentials (p=1).

It the framework of this h.o. theory, it is convenient to give all energies in units of the longitudinal h.o. spacing $\hbar\bar{\omega}_z$. The h.o. length $\ell_z = \sqrt{\hbar/\mu\bar{\omega}_z}$ is employed as the relative coordinate length unit and $L_z = \sqrt{\hbar/M\bar{\omega}_z}$ as the CM length unit. Then, the parts of the Hamiltonian Eq. (4.5) can be simplified to[2]

$$\begin{aligned}\hat{H}_{\mathrm{CM}} &= -{\nabla_{\mathbf{R}}}^2/2 + \left[\eta^2\rho_{\mathrm{CM}}^2 + Z^2\right]/2 \\ \hat{H}_{\mathrm{rel}}^{\pm} &= -{\nabla_{\mathbf{r}}}^2/2 + \left[\eta^2\rho^2 + z^2\right]/2 + 2\pi a_{eg}^{\pm}\delta(\mathbf{r})\frac{\partial}{\partial r}r \\ \hat{H}_{\mathrm{mix}} &= \frac{1}{2}\frac{\Delta\omega^2}{\bar{\omega}_z^2}Zz = \frac{p-1}{p+1}zZ\,.\end{aligned} \tag{4.10}$$

The average anisotropy of the lattice site potential for both orbitals is specified using the parameter $\eta = \omega_\perp/\bar{\omega}_z$. In our experimental setup, it can be varied by changing the lattice depth ratio of longitudinal and perpendicular lattices and typically varies within the range $0.7 < \eta < 2.3$.

Lattice anharmonicities The h.o. oscillator approximation is the lowest order approximation to the on-site potential of a sinusoidal lattice. In weak lattice systems, corrections due to higher order expansion terms should be considered. More coupling terms emerge between the CM and rel. coordinates. The anharmonic corrections, neglected in the derivation above are

$$\hat{H}_{\mathrm{anh}} = \sum_{i,s} V_s^i\left[\sin^2(k_i r_{i,s}) - k_i^2 r_{i,s}^2\right], \quad i \in \{x,y,z\} \quad \text{and} \quad s \in \{g,e\} \tag{4.11}$$

with $V_s^i k_i^2 = \omega_{i,s}^2 m/2$, $k_x = k_y = k_\perp$ and $\omega_{x,s} = \omega_{y,s} = \omega_\perp$.

To fully treat the on-site interactions, one would need to take into account corrections to the non-interacting h.o. Hamiltonian from the anharmonic part of the lattice potential $\hat{H}_{\mathrm{anh}}$ and the coupling through mixed confinement $\hat{H}_{\mathrm{mix}}$, leading to a total correction $\hat{H}_c = \hat{H}_{\mathrm{mix}} + \hat{H}_{\mathrm{anh}}$. The emergence of the coupling terms can be seen from a series expansion in the rel. and CM coordinates: Along the direction of the mixed confinement with polarizability ratio p, and using a fourth-order expansion in the lattice potential (see Section 2.1.2), we obtain

$$\begin{aligned}\hat{H}_c = \frac{p-1}{p+1}zZ - \frac{1}{6\sqrt{2(1+p)}}\sqrt{\frac{E_{\mathrm{rec}}^z}{V_z}}\left[(z^4 + 6z^2Z^2 + Z^4) + \frac{p-1}{p+1}(4z^3Z + 4zZ^3)\right] \\ + \frac{1}{90(1+p)}\frac{E_{\mathrm{rec}}^z}{V_z}\left[(z^6 + 15(z^4Z^2 + z^2Z^4) + Z^6) + \frac{p-1}{p+1}(20z^3Z^3 + 6(z^5Z + zZ^5))\right].\end{aligned} \tag{4.12}$$

The second order coupling due to the mixed confinement is independent of lattice depth while the fourth (sixth) order corrections scale with $V_z^{-\frac{1}{2}}$ (V_z^{-1}). Note that the higher order terms of the lattice potential expansion alone contain only even powers in z, Z whereas the mixed

[2]Note that we keep the existing variable names for the dimensionless variables. The scattering lengths, as part of the interaction Hamiltonian in the relative coordinates, are in units of ℓ_z.

confinement causes odd-power coupling terms. This enables the coupling between odd and even h.o. eigenfunctions or lattice bands, respectively.

Overall we have mapped the setting of anisotropic and mixed confinement for an eg pair to a sum of effective h.o. problems in reduced CM and rel. coordinates. A coupling between the coordinates is caused by the mixed confinement as well as the anharmonic lattice potential.

4.1.2 A solution to the uncoupled problem

Apart from the anisotropy, this problem is very similar to the one investigated by Deuretzbacher et al. in the context of heteronuclear mixtures in optical lattices [239]. There, the mixed confinement arises not only because of different polarizabilities but also different masses of the atomic species. The authors develop a numerical, exact diagonalization technique to treat the mixed confinement coupling terms as well as corrections due to the lattice potential.

In our anisotropic setting, no exact solution is available to our knowledge for the coupled h.o. problem. Although the polarizability ratio of $p = 3.3$ for the SDL causes a considerable coupling of $\Delta\omega_z^2/\overline{\omega}_z^2 = 2(p-1)/(p+1) \approx 1$, we neglect all coupling terms between CM and rel. coordinates in a first step. Then, the separable anisotropic h.o. problem with contact interactions can be solved exactly, as demonstrated in [235]. The approach is a generalization of the analytical solution to the spherically symmetric case, obtained by Busch et al. [139].

In the absence of CM-rel. coupling, the eigenstates are given by separable wavefunctions $\Psi(\mathbf{r},\mathbf{R}) = \psi_{\mathrm{CM}}(\mathbf{R})\psi_{\mathrm{rel}}(\mathbf{r})$ and a total eigenenergy

$$E = E_{\mathrm{CM}} + E_{\mathrm{rel}}\,. \tag{4.13}$$

The CM part of the problem is simply a non-interacting, anisotropic 3D h.o. with eigenenergies

$$E_{\mathrm{CM}} = (\eta + 1/2) + n_z + n_\perp\,\eta\,, \tag{4.14}$$

and $E_0^{\mathrm{CM}} = \eta + 1/2$ the CM ground-state energy. Note that we stay in the natural h.o. units specified above. n_z and $n_\perp = n_X + n_Y$ count the longitudinal and perpendicular CM band excitations. The associated 3D wavefunction is the product of independent 1D h.o. eigenfunctions [235]:

$$\psi_{\mathrm{CM}}(\mathbf{R}) = \frac{\sqrt{\eta}}{\pi^{3/4}} e^{-\frac{\eta\rho_{\mathrm{CM}}^2+Z^2}{2}} \prod_{i=X,Y,Z} \sqrt{\frac{1}{2^{n_i} n_i!}} H_{n_i}(\eta_i \mathbf{R}_i) \tag{4.15}$$

with $\eta_{X/Y} = \eta$ for the perpendicular directions X and Y, and $\eta_Z = 1$. H_n are the n-th order Hermite polynomials.

In the relative coordinate, the interacting Schrödinger equation is solved by inserting a wavefunction expanded in the basis of 3D non-interacting h.o. functions [Eq. (4.15)]. Only states with vanishing angular momentum $m_z = 0$ along the z-axis experience the s-wave contact interactions[3] [235] and the associated eigenenergies of the relative motion Hamiltonian are

$$E_{\mathrm{rel}} = \eta + 1/2 + \epsilon\,. \tag{4.16}$$

[3] This is analogous to the criterion $l = 0$ for the total angular momentum of the h.o. in the isotropic case [139].

Relative to the ground-state energy $E_0^{\mathrm{rel}} = \eta + 1/2$ of the non-interacting h.o., the effect of the interactions is captured in ϵ. The trap potential causes a discrete energy spectrum which is obtained from the equation [235]

$$\mathcal{F}_\eta(-\epsilon/2) = 1/a \tag{4.17}$$

with

$$\mathcal{F}_\eta(x) \equiv -\frac{1}{\sqrt{\pi}} \int_0^\infty dt \left[\frac{\eta e^{-xt}}{(1-e^{-t\eta})\sqrt{1-e^{-t}}} - \frac{1}{t^{3/2}} \right]. \tag{4.18}$$

The above integral only converges for $x > 0$, that is, for energies below the ground state energy $E < E_0^{\mathrm{rel}}$. Yet, by analytic continuation, the following recursive formula can be used for $E > E_0^{\mathrm{rel}}$ [235]:

$$\mathcal{F}_\eta(x+\eta) - \mathcal{F}_\eta(x) = \frac{1}{\sqrt{\pi}} \int_0^\infty dt \frac{\eta e^{-xt}}{\sqrt{1-e^{-t}}} = \frac{\eta \Gamma(x)}{\Gamma(x+1/2)}. \tag{4.19}$$

Equation (4.17) provides an exact solution to the interacting anisotropic h.o. problem [235]. The integral in the function $\mathcal{F}$ can be evaluated numerically for arbitrary anisotropy ratio η. The authors in [235] also provide an associated exact expression for the interacting wavefunction in the form of a series expansion:

$$\psi_{\mathrm{rel}}(\rho, z; \epsilon) = \frac{\eta e^{-\eta\rho^2/2}}{2\pi^{3/2} e^{\epsilon/2}} \sum_{m=0}^{\infty} 2^{\eta m} \Gamma\left[\frac{2\eta m - \epsilon}{2}\right] L_m\left[\eta\rho^2\right] D_{\epsilon - 2\eta m}\left[|z|\sqrt{2}\right], \tag{4.20}$$

where L_m are the Laguerre polynomials, D_ν the parabolic cylinder functions and $\Gamma(x)$ the Euler gamma functions. In order to gain a better qualitative understanding of the resulting spectrum, we will discuss several relevant limiting cases in the following, as well as evaluate the spectrum numerically for different anisotropy ratios.

The 3D isotropic case ($\eta = 1$)

For isotropic confinement $\eta = 1$, we recover the well-known solution obtained by Busch et al. [139] where Eq. (4.17) reduces to

$$\frac{1}{a} = \mathcal{F}_1(-\epsilon/2) = \frac{2\Gamma(-\epsilon/2)}{\Gamma(-\epsilon/2 - 1/2)}. \tag{4.21}$$

In our previous work on the ^{173}Yb orbital Feshbach resonance, this two-particle interaction model has been used for the theoretical two-channel description in the presence of an isotropic 3D lattice potential [90, 99]. Perturbative corrections for the anharmonic lattice potential as well as effective range corrections have yielded very good quantitative agreement with the measurement data in the limit of deep lattices.

Equation (4.21) features a discrete energy spectrum, as illustrated in Fig. 4.2 for different ratios of 3D scattering length a and harmonic confinement length ℓ. In Fig. 4.2(a), only the

relative motion eigenenergies $\epsilon = E_{\mathrm{rel}} - E_0^{\mathrm{rel}}$ with respect to the non-interacting case are plotted. We note that the regularized delta potential induces a bound state ψ_b with $\epsilon < 0$, both for positive and negative scattering length. The higher lying states can be attributed to h.o. eigenstates with $m_z = 0$ and are spaced by roughly $2\hbar\omega$.

In contrast, for scattering in free space, a bound state with energy $E_b^{\mathrm{free}} \propto -1/a^2$ emerges for positive a only [40]. However, in h.o. units, we exactly recover this free-space bound state ψ_b^{free} in the large ϵ limit of Eq. (4.21) [139]. Large binding energies occur either for small scattering length or weak confinement ($\ell \gg a$). For strong confinement or large scattering length, the trapping potential shifts the binding energy upwards.

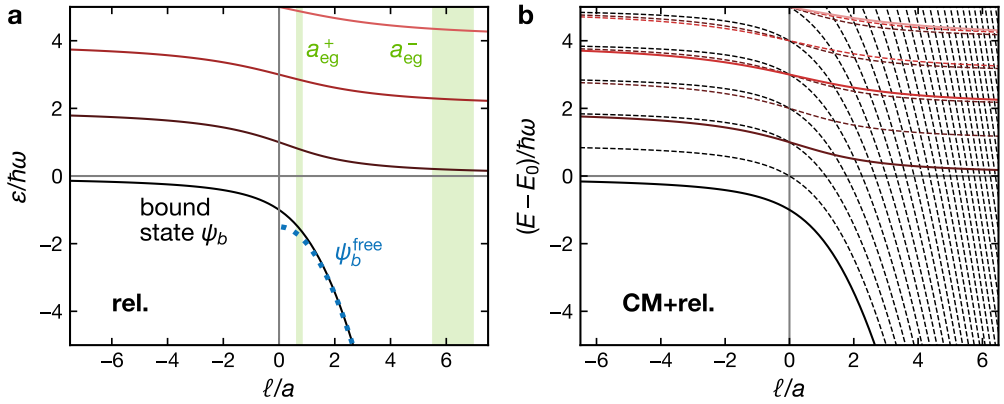

Figure 4.2 – Spectrum of the isotropic h.o. with contact interactions (s-wave scattering length a) in h.o. units (h.o. length ℓ and frequency ω). (a) Interaction energies ϵ of the rel. motion Hamiltonian H_{rel}: a bound state ψ_b (with $\epsilon < 0$) is induced for all ℓ/a by the trap (black, solid). The free-space scattering bound state ψ_b^{free} (dashed) exists for $a > 0$. Discrete higher trap states with $\epsilon > 0$ (red, solid). Green bands show $\ell/a_{\mathrm{eg}}^{\pm}$ regimes sampled with ^{173}Yb in $V = 20 - 50\, E_{\mathrm{rec}}$ deep 3D lattice. (b) Complete spectrum of uncoupled CM and rel. coordinate Hamiltonian $H = H_{\mathrm{CM}} + H_{\mathrm{rel}}$, relative to non-interacting ground-state energy E_0. Dashed lines are CM band excitations of all interacting states.

Different parts of the spectrum can be accessed not only by tuning the scattering length, but also by varying ℓ and $\hbar\omega$ via the lattice depth V. However, since $V \propto \ell^{-4}$, the experimentally accessible tuning range for the eigenenergies can be rather limited. For the fixed two interorbital scattering channels of ^{173}Yb, we indicate the parameter space probed by typical, deep magic-wavelength confinements in Fig. 4.2(a) (for a $V = 20 - 50\, E_{\mathrm{rec}}$ deep 3D lattice). The large spin-singlet scattering length a_{eg}^+ leads to a shallow bound state, with a binding energy on the order of the band gap $\hbar\omega$, whereas the spin-triplet bound state lies much deeper.

Up to now, we have only considered the relative coordinate. Figure 4.2(b) illustrates the complete eigenspectrum, including the non-interacting CM part of the wavefunction. The total ground-state energy $E_0 = E_0^{\mathrm{CM}} + E_0^{\mathrm{rel}}$ of the non-interacting Hamiltonian is subtracted. Effectively, an infinite number of CM-excited copies of the rel. motion eigenstates exist at higher energies, spaced by the band gap $\hbar\omega$. Because the slope of the bound state ψ_b at $a > 0$ is much steeper, its band excitations cause a lot of level crossings with $\epsilon > 0$ trap states as well as the non-interacting particle energy E_0. Now, adding a coupling mechanism between

rel. and CM coordinate leads to the emergence of avoided crossings and enables adiabatic transitions between the states [240].

The quasi-1D limit ($\eta \to \infty$)

In our SDL setup, the confinement in the longitudinal direction is typically smaller than in the perpendicular state-independent axes, i.e., $\eta > 1$. For vanishing SDL intensity, both $|g\rangle$ and $|e\rangle$ particles experience a quasi-1D potential. In this limit of $\eta \gg 1$, the bound state energy E_b^{1D} can be obtained from an approximation of Eq. (4.17) as [235]

$$\frac{1}{a} = \mathcal{F}_{\eta\gg1}(-E_b^{1D}/2) \approx -\sqrt{\eta}\zeta(1/2, -E_b^{1D}/(2\eta)), \tag{4.22}$$

where ζ is the Hurwitz zeta function. This corresponds to the result for a quasi-1D waveguide[4] found by Olshanii [241, 242]. The lowest excited trap states ($\epsilon > 0$) converge to a continuum of states and can be described by an effective 1D scattering length $a_{1D} = -1/(\eta a) - \zeta(1/2, 1)/\sqrt{2\eta}$ [235] which also agrees with the findings for the quasi-1D waveguide in [241, 242]. Figure 4.3(c) shows the quasi-1D approximation for the bound state from Eq. (4.22), compared to the exact numerical solution of Eq. (4.17) for varying anisotropies. For $\eta = 10$, the bound-state results become almost indistinguishable and we notice the emergence of the state continuum for $E > E_0$. A similar analogy can be made in the opposite limit of $\eta \ll 1$, recovering the results derived independently for quasi-2D confinement [243].

Intermediate anisotropy

In case the SDL depth becomes comparable to the perpendicular confinement, both the longitudinal and perpendicular h.o. energy scales ($\hbar\omega_\perp$ and $\hbar\bar{\omega}_z$) are relevant and enter the CM and rel. motion spectrum. A numerical evaluation of the spectrum for different anisotropy ratios η can be found in Fig. 4.3 where we compare the fully isotropic case to an intermediate anisotropy setting ($\eta = 2.3$), typical for our experimental setup, and a near quasi-1D setting ($\eta = 10$). The "interacting spectrum" in the rel. coordinate is shown along with the four lowest perp. and long. CM excitations of the bound state. The rel. coordinate eigenstates with $m_z = 0$ are spaced by multiples of $2\hbar\omega_z$ and $2\hbar\omega_\perp$ in the non-interacting limit $\ell_\perp/|a| \to \infty$ [Fig. 4.3(b)]. Clearly, for $\eta \neq 1$, we also break the degeneracy in the band excitation energies and a much denser total spectrum emerges. As we will see in the following, coupling of the rel. and CM coordinate leads to the emergence of avoided crossings and further modifications of the spectrum which are therefore more likely to occur in the anisotropic setting.

4.1.3 On-site relative and center-of-mass motion coupling

Describing the on-site physics of an optical lattice in a h.o. picture is obviously an idealization. As discussed in Section 4.1, a correction $\hat{H}_c$ emerges because of the anharmonicity of the lattice

[4] This is obvious when written in units of the transverse h.o. where the anisotropy parameter cancels out, giving $\frac{\ell_\perp}{a} = \zeta(1/2, -E_b^{1D}/2\hbar\omega_\perp)$.

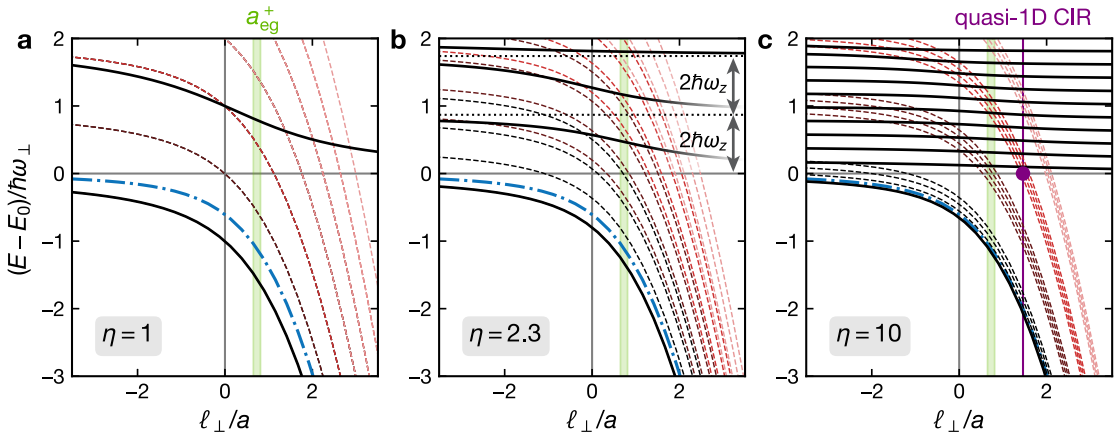

Figure 4.3 – Spectrum of two particles with contact interactions (s-wave scattering length a in units of perp. h.o. length $\ell_\perp$) in a h.o. potential, for different anisotropy ratios $\eta = \omega_\perp/\bar{\omega}_z$. (a) Isotropic trap, (b) intermediate and (c) strong quasi-1D like anisotropy. Interaction energies of the rel. motion Hamiltonian H_{rel} (solid) are in units of the perp. h.o. frequency $\omega_\perp$, relative to non-interacting ground-state energy E_0. Dashed lines are the 4 lowest perp. and long. CM band excitations of the bound state. The quasi-1D bound state energy $E_b^{1\mathrm{D}}$ is shown for comparison (dash-dotted), as well as the elastic confinement-induced resonance (CIR) position (purple marker) from $\ell_\perp/a \approx 1.460$ [241]. Green bands show $\ell_\perp/a_{\mathrm{eg}}^{+}$ sampled with ^{173}Yb in $V_\perp = 20 - 50\, E_{\mathrm{rec}}$ deep perp. lattices.

site, and potentially mixed confinement. An expansion of $\hat{H}_c$ in CM an rel. coordinates (as in Eq. (4.12)) shows that it leads to coupling between the two. Overall, there are two main consequences: First, it leads to quantitative corrections of the h.o. spectrum. Second, it causes avoided crossings between different spectral branches. An exact treatment of the full, coupled on-site problem is non-trivial and in the following we will review existing approaches.

For the scenario of isotropic confinement, Deuretzbacher et al. perform an exact, numerical solution of the on-site two-particle problem, using an exact diagonalization approach for the coupling perturbation [239]. They study the effect of mixed confinement caused by different masses in heteronuclear mixtures and an expansion of the lattice potential up to sixth order[5]. Good quantitative agreement is observed with the measured spectrum of strongly interacting gases in isotropic 3D optical lattices across a Feshbach resonance [245]. The deviation from the scenario of particles with identical mass is largest for the excited trap states in the positive scattering length regime. Still, even for strong interactions ($a = 4\ell$) and relatively low lattice depths ($V = 10E_{\mathrm{rec}}$), the mixed confinement $\Delta\omega^2/\overline{\omega}^2 \approx 0.65$ and the anharmonicity only lead to a total energy correction on a 10% scale.

Inelastic and elastic confinement-induced resonances On-site CM-rel. coupling also becomes relevant in the context of so-called *inelastic confinement-induced resonances* (CIR), as first analyzed by Sala et al. [240, 246]. Their model explains the observed particle loss and

[5]Sextic potentials have been found to be well-suited approximations for both the on-site confinement of a sinusoidal lattice as well as Gaussian beams [244] in the context of CM-rel. coupling.

heating in a deep *anisotropic* 3D optical lattice where the eigenspectrum is well reproduced by a h.o. model [247]. At the positions in the spectrum where the CM excitations of the bound state cross the higher-lying trap states, avoided crossings are opened due to the coupling term [see Fig. 4.4(a)]. Then, transitions between the two rel. motion eigenstates are enabled. Starting

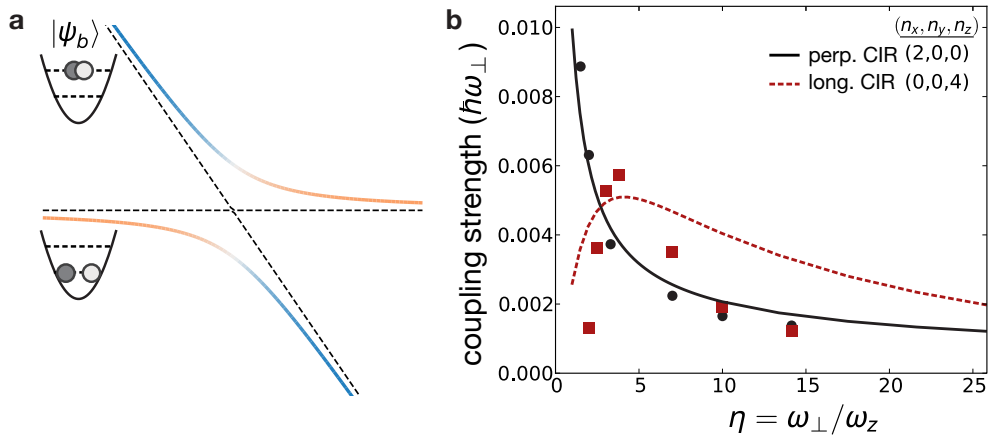

Figure 4.4 – (a) Avoided crossing (solid lines) between bare CM band excited bound state $|\psi_b\rangle$ and unbound trap state without CM excitation (dashed) is caused by CM-rel. coupling. (b) Figure adapted from [240]: CM-rel. coupling strength in h.o. confinement with varying anisotropy η, to different CM excitations (n_x, n_y, n_z) of $|\psi_b\rangle$. Coupling strength to longitudinal CM excitations has non-monotonous behavior (see main text). Symbols from exact ab initio calculation, lines from perturbative approach.

with non-bound atoms, an occupation of the molecular bound state becomes possible because the excess binding energy can be converted to kinetic energy, in the form of a CM excitation. This is the signature of an inelastic process. In the many-body context, this can trigger heating or losses from the trap, since collisions between bound-state pairs or with other unbound atoms can lead to a deexcitation into deeply bound molecular states [240]. The inelastic CIR have also been suggested as a tool for coherent molecule formation in the absence of magnetic Feshbach resonances [244].

In contrast, classical *elastic* CIR have been proposed in the context of quasi-1D waveguides ($\omega_z = 0$) to explain a resonant behavior of the 1D coupling g_{1D} with varying perpendicular confinement [241, 242]. These are resonances in the elastic scattering channel and occur for a specific ratio between transverse confinement length and scattering length, namely $\ell_\perp/a = -\zeta(1/2, 0) \approx 1.460$. The resonance in the scattering amplitude can be interpreted as the result of a Feshbach resonance-like model where the open and closed channels are represented by different transverse trap modes. This mechanism does *not* rely on the CM-rel. coupling induced by the trap anharmonicity or the mixed confinement. Note that with the available transverse confinement depth in our lattice setup the condition for the quasi-1D elastic CIR cannot be met by either of the interorbital scattering lengths [see Fig. 4.3(c)].

Numerical treatment of anharmonicities In their study of the coupling-induced inelastic CIR, Sala and Saenz compare several numerical approaches for treating lattice anharmonicities in a fully anisotropic setting, yet, not in mixed confinement. The energetic position of coupling

resonances as well as their strength is determined. An exact formalism, based on the full six-dimensional numerical solution of the stationary Schrödinger equation [248], is compared to first-order perturbative approaches.

Concerning the position of a given resonance, it is found that for low numbers of excitations, the crossing of the CM excited bound states with the lowest repulsive trap state is very well captured by the perturbative approach. For small anisotropy $\eta \approx 1$, even the pure h.o. model already produces quantitatively good results, consistent with the findings in [239]. In first order perturbation theory, the correction to the interacting h.o. eigenenergies is given by $\int d\mathbf{R}d\mathbf{r}\,|\psi_{\mathrm{rel}}(\mathbf{r},\epsilon)|^2\,|\psi_{\mathrm{CM}}(\mathbf{R})|^2\,\hat{H}_c$. However, in contrast to the treatment of an isotropic lattice potential [249], the numerical evaluation of the anisotropic interating h.o. wavefunction ψ_{rel} [Eq. (4.20)] is prohibitively demanding and only approximative forms are considered in [240]. It is found that for intermediate anisotropies, quantitatively reasonable values for the resonance positions can already be obtained when only the non-interacting CM part of the wavefunction is perturbed with the anharmonic lattice potential.

We generalize the approach in [240] to mixed confinement by employing the anharmonic lattice potential terms from Eq. (4.12) up to sixth order. This leads to a perturbatively corrected, total CM excitation energy

$$\Delta_{\mathrm{CM}} = \sum_{i=x,y,z} \hbar\bar{\omega}_i \left[n_i - \frac{1}{16}\frac{\hbar\bar{\omega}_i}{\bar{V}_i}(n_i^2+n_i) + \frac{1}{576}\left(\frac{\hbar\bar{\omega}_i}{\bar{V}_i}\right)^2 (2n_i^3+3n_i^2+4n_i)\right] \tag{4.23}$$

with n_i indicating the number of excitations in the respective direction. The mixed confinement enters via the polarizability ratios p_i in the renormalized trapping frequencies $\bar{\omega}_i \equiv \omega_i^g\sqrt{(p_i+1)/2}$ and lattice potential depths $\bar{V}_i \equiv V_i^g(p_i+1)/2$. In our setup, mixed confinement with $p_z \neq 1$ is only given along z, whereas $p_x = p_y = 1$. This anharmonic correction will be employed below for the comparison with our experimental interaction spectroscopy and the results from the measurement of the spin exchange dynamics in Chapter 5.

Considering the strength of the CM-rel. coupling, several qualitative observations are made in [240]. Obviously, the higher order terms of the lattice expansion can only lead to coupling with bound states that carry an even number of CM excitations. Moreover, the coupling strength decreases with the number of CM band excitations because excited-state wavefunctions feature stronger oscillations and thus, a decreased overlap. In stark contrast to the quasi-1D elastic CIR, the presence of a lattice along z also enables coupling to longitudinal band excitations. Here, a non-monotonic behavior is found for the coupling strength when varying the anisotropy [see Fig. 4.4 (b)]. Intuitively, this can be explained by the competition of two effects [240]: for $\omega_z \to 0$, the longitudinal lattice confinement vanishes along with the possibility of exciting a CIR along that direction. Conversely, for deep lattices with $\omega_z \to \infty$, the anharmonicity of the potential vanishes, reducing the CM-rel. coupling strength.

Finally, we note that neither of the CM-rel. coupling models presented above fully captures the on-site physics in our SDL. While the treatment in [239] treats lattice anharmonicities and mixed confinement exactly, it is only valid for isotropic confinement. The models studied in [240] are valid for arbitrary anisotropy of the trap. However, they do not include the coupling induced by mixed confinement. A full generalization of both approaches should certainly be

feasible, albeit at the expense of increased numerical effort.

4.1.4 Regularized Hubbard interaction parameters

In the tight-binding regime, we would like to describe our lattice system in the form of a Hubbard Hamiltonian. Two-particle contact interactions are used to derive the on-site interaction parameters U. In the standard approach, the Fermi-Huang pseudo potential is replaced with a simple delta potential and one neglects the influence of higher bands [42]. Then the interorbital interaction strengths are given by the overlap $U_{eg} = \frac{4\pi\hbar^2 a_{eg}^{\pm}}{m} \int \mathrm{d}^3 r |w_e|^2 |w_g|^2$ of the lowest-band Wannier functions, as in Eq. (2.20). Note that the Wannier functions for the two electronic orbitals differ along the SDL. However, this is valid only in the limit of weak interactions which do not significantly disturb the non-interacting Wannier functions. The condition $|a|/d \ll 1$ is imposed on the scattering length a and the lattice spacing d. More stringently, U needs to stay small compared to the lowest band gap [250, 251]. For ^{173}Yb in the SDL, this conditions is only fulfilled for interorbital scattering in the spin-triplet channel with $a_{eg}^{-}/d = 0.03$, as well as gg and ee scattering with $a_{\mathrm{gg}}/d = 0.03$ and $a_{\mathrm{ee}}/d = 0.05$.

On the contrary, this does neither hold for the naturally large ^{173}Yb spin-singlet scattering length, with $a_{eg}^{+}/d = 0.3$, nor can we make this approximation in the vicinity of a Feshbach resonance. Then, the regularized pseudopotential needs to be considered. In contrast to the delta potential, it supports a spectrum of bound states including a loosely bound molecular state for large scattering lengths. Büchler performs a microscopic derivation of an effective Hubbard interaction U by comparing the exact scattering amplitude in a 3D lattice potential with the formal one of the Hubbard model [251]. The model is valid for low-energy scattering and it includes the influence of higher bands and the renormalized bound state-energies. It is shown that even in the presence of a Feshbach resonance, U stays bounded for $a \to \pm\infty$. The same holds for the bare lattice bound state energies. In turn, for deeper lattices, these are well approximated by the h.o. model introduced above.

Instead of deriving an effective Hubbard parameter for the low energy scattering, we treat the accessible on-site bound states as different "scattering channels", using their energy as the Hubbard interaction parameters U. Virtual occupation of the interacting bound states will dominate the observed spin-exchange dynamics in the next chapter. We restrict ourselves to the spectrum of the anisotropic h.o. without CM-rel. coupling. Then, an eg atom pair on a lattice site might be in different rel. and CM motion states of the spin-triplet or spin-singlet configuration. The relevant, low-energy Hubbard interactions will be U^{+} and U^{-} for the first excited trap states, as well as U_b^{+} for the molecular spin-singlet bound state. The molecular spin-triplet bound state is deeply bound with $U_b^{-}/h < -1\,\mathrm{MHz}$ and not accessible by low-energy scattering.

In Figure 4.5, we compare these parameters to the ones obtained from the standard Wannier overlap calculation. Moreover, the ground-state and excited-state interactions U_{gg} and U_{ee} are displayed, which are on the order of U^{-}. The interaction energies depend on the lattice depths and are calculated for typical experimental lattice configurations. As expected, the strongest discrepancies with the result from the calculation involving the on-site Wannier

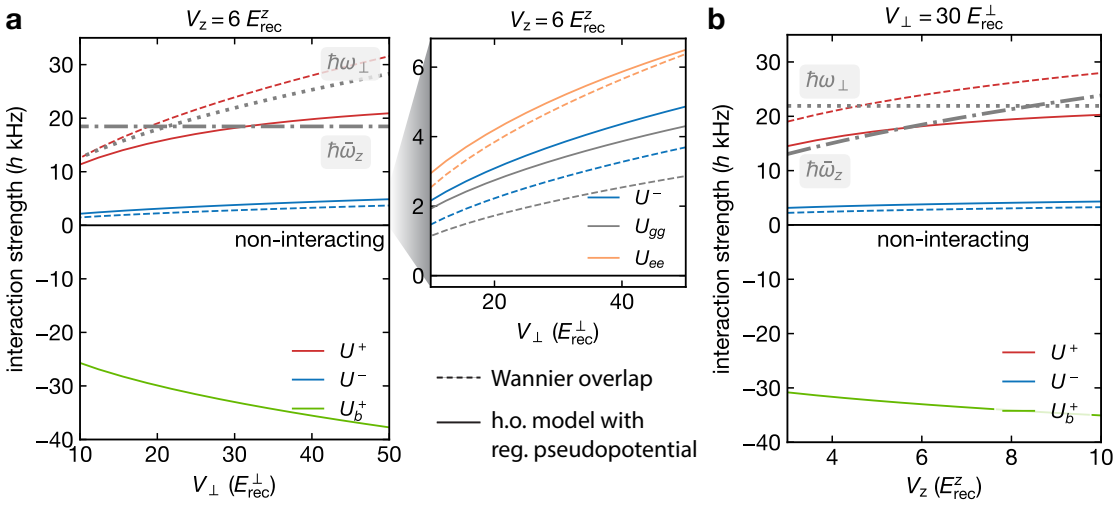

Figure 4.5 – On-site interaction energies for typical SDL confinements. (a) Fixed longitudinal SDL depth $V_z = 6\,E^z_{\mathrm{rec}}$ and varying perpendicular magic-wavelength lattice depth $V_\perp$. Interorbital interactions $U^\pm$ for $|e\rangle|g\rangle$ pairs in the spin-singlet and triplet excited trap states and in the spin-singlet molecular state (U_b^+); gg and ee interaction for comparison. Solid lines are from h.o. model with Fermi-Huang pseudopotential scattering, dashed lines are from lowest-band Wannier function overlap. The lowest longitudinal ($\hbar\bar{\omega}_z$, dash-dotted) and perpendicular ($\hbar\omega_\perp$, dotted) band gap are comparable to U^+. (b) Same for fixed $V_\perp = 30E^\perp_{\mathrm{rec}}$ and varying V_z.

function overlaps are found in the spin-singlet channel. The additional molecular bound state energy $|U_b^+|$ becomes comparable to U^+ and U^- for the given confinement. Also, when increasing the anisotropy η by increasing the perp. lattice depth, U^+ quickly becomes comparable to the lowest band gap ($\hbar\bar{\omega}_z$ for most η) and starts to saturate compared to the non-regularized result. For the weakly interacting scattering channels, the h.o. model with eigenfunctions more localized than the Wannier functions, overestimates the interaction energies.

4.2 Multi-channel mixing in anisotropic traps

As long as the two interorbital scattering channels $|\pm\rangle$ (with scattering lengths $a_{\mathrm{eg}}^\pm$) of fermionic ^{173}Yb remain uncoupled, we may use the model above to obtain an on-site spectrum and Hubbard parameters independently for both channels. However, this is not the case in the presence of a finite magnetic field. The differential magnetic moment $\Delta\mu$ between the clock states will mix the singlet and triplet states and couple the orbital and spin degree of freedom (see Section 1.5.5). This becomes relevant in the next section, where we perform interaction spectroscopy on the clock transition at finite magnetic fields.

We will now introduce a full two-channel model for the interorbital interactions at finite magnetic field. The T-matrix based approach is analogous to the one presented in our publication [90] for an isotropic 3D lattice, but generalized to an on-site confinement with arbitrary anisotropy. It accounts for energy-dependent collisions and includes the full effect of the con-

finement on both the open and closed scattering channel.

The non-interacting system at finite fields has the spin-product states

$$\begin{aligned} |o\rangle &= (|g\uparrow; e\downarrow\rangle - |e\downarrow; g\uparrow\rangle)/\sqrt{2} \quad \text{and} \\ |c\rangle &= (|e\uparrow; g\downarrow\rangle - |g\downarrow; e\uparrow\rangle)/\sqrt{2} \end{aligned} \tag{4.24}$$

as the eigenbasis, referred to as open and closed channel. These can be transformed to the orbital singlet and triplet states $|\mp\rangle$ via the unitary transform

$$R = \frac{1}{\sqrt{2}}\begin{pmatrix} 1 & 1 \\ 1 & -1 \end{pmatrix} \tag{4.25}$$

The CM and rel. coordinates can be decoupled, and in the rel. basis, we split the Hamiltonian $\hat{H}_{\text{rel}} = \hat{H}_0 + \hat{V}$ into a non-interacting part

$$\hat{H}_0 = \sum_{\mathbf{n}} \epsilon_{\mathbf{n}} |o, \mathbf{n}\rangle\langle o, \mathbf{n}| + \sum_{\mathbf{n}} (\epsilon_{\mathbf{n}} + \Delta\mu B)\, |c, \mathbf{n}\rangle\langle c, \mathbf{n}| \tag{4.26}$$

in the product state basis and an interaction part

$$\hat{V} = \sum_{\mathbf{n},\mathbf{n}'} \varphi_{\mathbf{n}}(0)\varphi_{\mathbf{n}'}(0) \left\{ U^+ |+, \mathbf{n}\rangle\langle +, \mathbf{n}'| \; + U^- |-, \mathbf{n}\rangle\langle -, \mathbf{n}'| \right\} \tag{4.27}$$

in the natural singlet-triplet basis. The positive differential shift $\Delta\mu B = -\delta g\, \Delta m_F\, \mu_B\, B > 0$ is applied only to the closed channel. Here, $\mathbf{n} = (n_x, n_y, n_z)$ is an index for the non-interacting, anisotropic h.o. eigenstates occupied by the atom pair in the rel. coordinate. These are $m_z = 0$ states (the ones affected by short-range interactions) and their wavefunction[6] at the origin is $\varphi_{\mathbf{n}}(0)$. The associated eigenenergies are $\epsilon_{\mathbf{n}}/\hbar\bar{\omega}_z = 2(n_z + \eta n_\perp)$, with $n_\perp = n_x + n_y$ and relative to the ground-state energy E_0^{rel}. The triplet and singlet bare coupling strengths[7] are $U^\pm$.

With the Hamiltonian set up, we determine the two-body spectrum by inserting a general wavefunction

$$|\psi\rangle = \sum_{\mathbf{n}} \left(b_{\mathbf{n}}^+ |+, \mathbf{n}\rangle + b_{\mathbf{n}}^- |-, \mathbf{n}\rangle \right) \tag{4.28}$$

in the singlet-triplet basis into the Schrödinger equation $H_{\text{rel}}|\psi\rangle = E|\psi\rangle$:

$$R \begin{pmatrix} \epsilon_{\mathbf{n}} - E & 0 \\ 0 & \epsilon_{\mathbf{n}} + \Delta\mu B - E \end{pmatrix} R \begin{pmatrix} b_{\mathbf{n}}^- \\ b_{\mathbf{n}}^+ \end{pmatrix} + \varphi_n(0) \begin{pmatrix} U^- & 0 \\ 0 & U^+ \end{pmatrix} \sum_{\mathbf{n}'} \varphi_{\mathbf{n}'}(0) \begin{pmatrix} b_{\mathbf{n}'}^- \\ b_{\mathbf{n}'}^+ \end{pmatrix} = 0\,. \tag{4.29}$$

Then, by summing over the possible excitations $\mathbf{n}$ and replacing the bare coupling $U^\pm$ with the scattering lengths $a_{eg}^\pm$, we arrive at a matrix equation:

$$\left[\boldsymbol{\tau}_0^{-1} + \boldsymbol{\Pi}(E) \right] \boldsymbol{\Psi}_{\text{reg}} = 0 \tag{4.30}$$

[6] Effectively, a product of three independent 1D wavefunctions, rescaled with the h.o. lengths, like Eq. (4.15).

[7] related to the s-wave scattering length via the Lippmann-Schwinger equation $(U^\pm)^{-1} = \frac{m}{4\pi\hbar^2 a_{\text{eg}}^\pm} - \sum_k \frac{1}{2\epsilon_k}$.

defining the regular part of the two-channel wave function [252]. Here, we have introduced the interaction matrix

$$\boldsymbol{\tau}_0 = -\frac{\sqrt{m}}{\hbar}\begin{pmatrix} a_{eg}^- & 0 \\ 0 & a_{eg}^+ \end{pmatrix} \tag{4.31}$$

and the one-loop polarization bubble

$$\boldsymbol{\Pi}(E) = \frac{\Pi(E)}{2}\begin{pmatrix} 1 & 1 \\ 1 & 1 \end{pmatrix} + \frac{\Pi(E-\Delta\mu B)}{2}\begin{pmatrix} 1 & -1 \\ -1 & 1 \end{pmatrix} \tag{4.32}$$

containing the renormalized pair propagator for anisotropic harmonic confinement [235]

$$\Pi(E) = \frac{\hbar}{\sqrt{m}\ell_z}\mathcal{F}_\eta(-E/2\hbar\bar{\omega}_z)\,. \tag{4.33}$$

The function $\mathcal{F}$ from Eq. (4.18) is valid for arbitrary anisotropy. For $\eta = 1$, we recover the isotropic pair propagator used in [90].

Overall, the interaction matrix and the polarization bubble define the T-matrix $\mathcal{T}(E) = [\boldsymbol{\tau}_0^{-1} + \boldsymbol{\Pi}(E)]^{-1}$ which has the same general shape as the one characterizing free-space scattering in the two-channel model in [90, 99]. Finally, the solutions to Eq. (4.30) define the interacting eigenstates of H_{rel} and those can be attributed to the poles of the T-matrix:

$$\det\left(\mathcal{T}^{-1}(E)\right) = \det\left(\boldsymbol{\tau}_0^{-1} + \boldsymbol{\Pi}(E)\right) \stackrel{!}{=} 0\,. \tag{4.34}$$

This evaluates to the condition

$$\prod_{i=\pm}\left[\frac{2\ell_z}{a_{\mathrm{eg}}^i} - \mathcal{F}_\eta\left(\frac{-E}{2\hbar\bar{\omega}_z}\right) - \mathcal{F}_\eta\left(\frac{-E+\Delta\mu B}{2\hbar\bar{\omega}_z}\right)\right] \stackrel{!}{=} \left[\mathcal{F}_\eta\left(\frac{-E}{2\hbar\bar{\omega}_z}\right) - \mathcal{F}_\eta\left(\frac{-E+\Delta\mu B}{2\hbar\bar{\omega}_z}\right)\right]^2 . \tag{4.35}$$

Note that the term on the right-hand side is only present for finite magnetic field coupling the two scattering channels. For $B = 0$, the equation decomposes into a simple product of independent conditions, in the form of Eq. (4.17), for the singlet and triplet channel.

Energy-dependent scattering

The derivation above was done for true zero-range interaction potentials. However, the singlet s-wave scattering length a_{eg}^- is only slightly larger than the van-der-Waals length of the interaction potential (see Section 1.5.4). The validity of the pseudopotential can be improved by including an energy dependence in an effective scattering length, as in [253]. In the two-channel model, we have to make the interaction matrix $\boldsymbol{\tau}_0^{-1}$ energy-dependent, that is, introduce scattering phase shifts $\delta_{eg}^{\pm}$ for the two channels which depend on the collisional energy E_c [254]:

$$\boldsymbol{\tau}_0^{-1} \mapsto \boldsymbol{\tau}^{-1}(E_c) = \sqrt{E_c}\begin{pmatrix} \cot\delta_{eg}^+(E_c) & 0 \\ 0 & \cot\delta_{eg}^-(E_c) \end{pmatrix}. \tag{4.36}$$

Note that the collisional energy $E_c = E - \frac{\Delta\mu B}{2} + E_0^{\mathrm{rel}}$ with $E \propto k^2$ also includes the zero-point energy $E_0^{\mathrm{rel}} = (\eta + 1/2)\hbar\bar{\omega}_z$ of the anisotropic h.o. . The energy-dependence of the scattering process is introduced by keeping an additional term in the low-energy expansion of the phase shift [254]:

$$\frac{\sqrt{mE_c}}{\hbar}\cot\delta_{eg}^{\pm}(E_c) \simeq -\left(a_{eg}^{\pm}\right)^{-1} + \frac{1}{2}r_{\mathrm{eff}}^{\pm}\frac{mE_c}{\hbar^2}\,, \tag{4.37}$$

proportional to the effective range[8] parameter $r_{\mathrm{eff}}^{\pm}$. Finally, the low-energy expansion of τ_0 is equivalent to replacing

$$\left(a_{eg}^{\pm}\right)^{-1} \mapsto \left(a_{eg}^{\pm}\right)^{-1} - \frac{1}{2}r_{\mathrm{eff}}^{\pm}\frac{m}{\hbar^2}\left(E - \frac{\Delta\mu B}{2} + (\eta + 1/2)\hbar\bar{\omega}_z\right) \tag{4.38}$$

in Eq. (4.31), and in Eq. (4.35) for the interaction energies[9]. The effect on the eigenspectrum resulting from a finite effective range is quantified in the next section where it leads to better agreement with the measured bound-state energies.

4.3 Interaction spectroscopy in mixed confinement

As discussed above, the presence of a 3D optical lattice leads to a discrete two-body interaction spectrum. Experimentally, the optical clock transition allows us to directly probe this spectrum by transferring an initial two-spin sample of weakly interacting $|g\rangle$ atoms to an eg mixture. In the limit of deep lattices, we make the approximation of considering the interactions on decoupled individual lattice sites and the validity of the on-site interaction model can be investigated. For these measurements, we employ high atom numbers, such that lattice sites can be occupied by both one or two particles. Discrete features in the spectral response can then be attributed to interacting or non-interacting eigenstates of the two-particle problem. The identification is done by comparing to the expected behavior for varying magnetic fields and external confinement, both influencing the interorbital interactions.

Spectroscopic shift In an isotropic, magic-wavelength setting, such a measurement has been performed in [90, 99]. One of the lattice axes is now replaced with a SDL, causing anisotropic and mixed confinement which influence the interactions. Yet, already on the single particle level, the SDL influences the clock line spectroscopy by imposing a differential light shift compared to a pure magic-wavelength confinement. The expected spectral shifts, which increase with the SDL depth and are independent of m_F, are quantified in Section 2.5.2. The external magnetic field B, setting the quantization axis, produces a linear differential Zeeman shift $\Delta\mu B$ between the employed m_F components (the two m_F states are labeled as $|\uparrow\rangle$ and $|\downarrow\rangle$).

This linear shift makes it easy to identify the spectroscopic features belonging to singly occupied lattice sites and we reference our spectra relative to the $|g\downarrow\rangle \rightarrow |e\downarrow\rangle$ transition frequency ν_s [see Fig. 4.6(d)].

[8] The effective range can be measured or estimated from the van-der-Waals coefficients of the scattering potential (see Section 1.5.5).

[9] In rel. h.o. units ℓ_z and $\hbar\bar{\omega}_z$, the replacement becomes $1/a_{eg}^{\pm} \mapsto 1/a_{eg}^{\pm} - r_{\mathrm{eff}}^{\pm}\left(E - \frac{\Delta\mu B}{2} + \eta + 1/2\right)$.

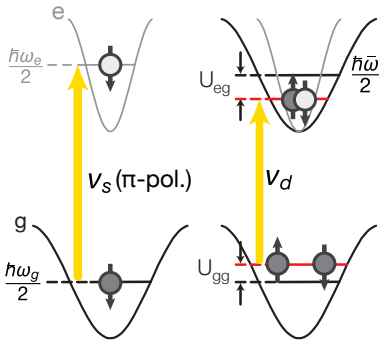

Figure 4.6 – Clock line interaction spectroscopy scheme on singly (left) and doubly (right) occupied lattice sites provides discrete spectral features at frequencies ν_s and ν_d. $|g\rangle$ (dark) and $|e\rangle$ (bright) atoms see different zero-point energies in the SDL. Interorbital interaction energy U_{eg} is probed relative to $|g\rangle$ interactions U_{gg}.

In contrast, interacting states on doubly occupied sites are probed by exciting one of the two $|g\rangle$ atoms on a lattice site to $|e\rangle$. The starting configuration is already weakly interacting with an on-site energy U_{gg} depending on the confinement. The interaction energy U_{eg} in the final state, and thereby the transition frequency ν_d, depends on the spin-configuration, the magnetic field and the confinement strength [see Fig. 4.6].

Relative to the signal ν_s from the singly occupied lattice sites, which already contains the differential light shift, the measured spectroscopic shift becomes

$$\Delta\nu = \nu_d - \nu_s = U_{eg} - U_{gg} + \hbar(\bar{\omega}_z - \omega_{z,g}) - \frac{1}{2}\hbar(\omega_{z,e} - \omega_{z,g})\,. \tag{4.39}$$

Here, we have considered the difference in zero-point energies in the SDL direction (z) for the single particle and two-particle scenario. The measured results can be compared directly to the interaction energies from the h.o. model in Eq. (4.35).

Spectroscopic contrast The contrast of the spectral features depends on the overlap of initial and final state and can also be used for an assignment of spectroscopic features to physical states. After the initial state preparation, the $|g\,g\rangle$ doubly occupied sites are necessarily in an orbital triplet state. To insure the fermionic anti-symmetry, the associated nuclear-spin must be in a spin-singlet state, such that the total wavefunction becomes

$$|\psi_i\rangle = |g\,g\rangle \otimes \frac{1}{\sqrt{2}}\left(|\uparrow\downarrow\rangle - |\downarrow\uparrow\rangle\right). \tag{4.40}$$

In contrast, after the coherent clock excitation, the eg pair can take on different nuclear-spin states. For vanishing external magnetic field, the eigenspectrum is composed of spin singlet and triplet states which evolve into the open and closed channel spin-product states at high fields. In our spectroscopy experiments, we employ π-polarized clock laser light and two opposite m_F levels ($m_F = \pm 5/2$). According to the single-particle dipole matrix element Eq. (1.34), the Clebsch-Gordan coefficients for the two m_F states are of equal magnitude but opposite sign. When generalized to a two-particle matrix element, it can be shown that the

coupling between spin-singlet states vanishes [97]. Therefore, the excitation into spin-singlet $|eg\rangle$ states

$$|\psi_i\rangle \not\to |+^{(n)}\rangle = \frac{1}{\sqrt{2}}(|eg\rangle + |ge\rangle) \otimes \frac{1}{\sqrt{2}}(|\uparrow\downarrow\rangle - |\downarrow\uparrow\rangle) \otimes |n\rangle \tag{4.41}$$

is forbidden and only the transitions to a spin triplet

$$|\psi_i\rangle \to |-^{(n)}\rangle = \frac{1}{\sqrt{2}}(|eg\rangle - |ge\rangle) \otimes \frac{1}{\sqrt{2}}(|\downarrow\uparrow\rangle + |\uparrow\downarrow\rangle) \otimes |n\rangle \tag{4.42}$$

exhibit finite spectroscopic contrast. At large magnetic field, the coupling with the interorbital open and closed channel states is equally strong. This symmetry argument, relevant for the low-field regime, also holds for all possible CM band excitations $|n\rangle$ as well as the molecular bound states $|\pm_b\rangle$. Further, using spin-selective imaging, adjacent m_F levels and σ-polarized light, one can uniquely identify the spin nature of the trap states. We have previously performed such measurements in a 3D isotropic magic-wavelength lattice [99].

The clock light coupling strength also depends on the spatial overlap of the initial and final state wavefunction, as in Eq. (2.29). This becomes particularly relevant for probing the molecular bound state of the interorbital scattering channels. The stronger the binding energy, the more localized the associated wavefunction and the smaller the overlap with the weakly interacting gg pair.

Bound-state spectroscopy

As we will see in Chapter 5, the existence and confinement dependence of a shallow spin-singlet bound state underlies the tuning mechanism for the spin-exchange coupling in the SDL. In the following, we will present a direct spectroscopic measurement of the bound-state energy in the anisotropic and mixed confinement of the SDL. The interactions will be tuned both by varying the confinement depth as well as the external magnetic field.

The general experiment sequence and setup used for the clock line spectroscopy are described in Section 3.5.2 and Fig. 2.12. Here, we employ a lattice setup with two perpendicular, magic-wavelength lattices of equal depth $V_\perp = 30E_{\text{rec}}^\perp$ and a longitudinal SDL ($\lambda_{\text{SDL}} = 670\,\text{nm}$) of variable depth V_z for the $|g\rangle$ atoms. A total of 8×10^4 atoms in a balanced mixture of $m_F \in \{-5/2, 5/2\}$ is loaded into this lattice configuration, at a reduced temperature of around $T/T_F = 0.25$ (measured in the 1064nm crossed dipole trap, after a round-trip loading into the SDL and back). Subsequently, a clock laser pulse of variable light frequency probes the interacting eigenspectrum. For the pulse duration and power, we have to strike a compromise between good resolution and coupling strength. Obviously, the spacing of the eigenenergies should be larger than the resolution of the clock spectroscopy. At the same time, stronger light intensities and the associated power broadening are required for coupling to the tightly bound molecular state, and to reduce the sensitivity to inhomogeneous differential light shift in the SDL. For the purely magic confinement we use 1 sec long pulses at a relatively low power of 0.5–1 μW, coupling incoherently to the clock transition. In the presence of the SDL, we employ higher-power, coherent π pulses (0.5-1 mW, bare single-particle Rabi coupling $\Omega_0 = 2\pi \times 0.75$–$1.5\,\text{kHz}$). The

remaining $|g\rangle$ atoms after the clock pulse are then imaged spin-independently at low magnetic field.

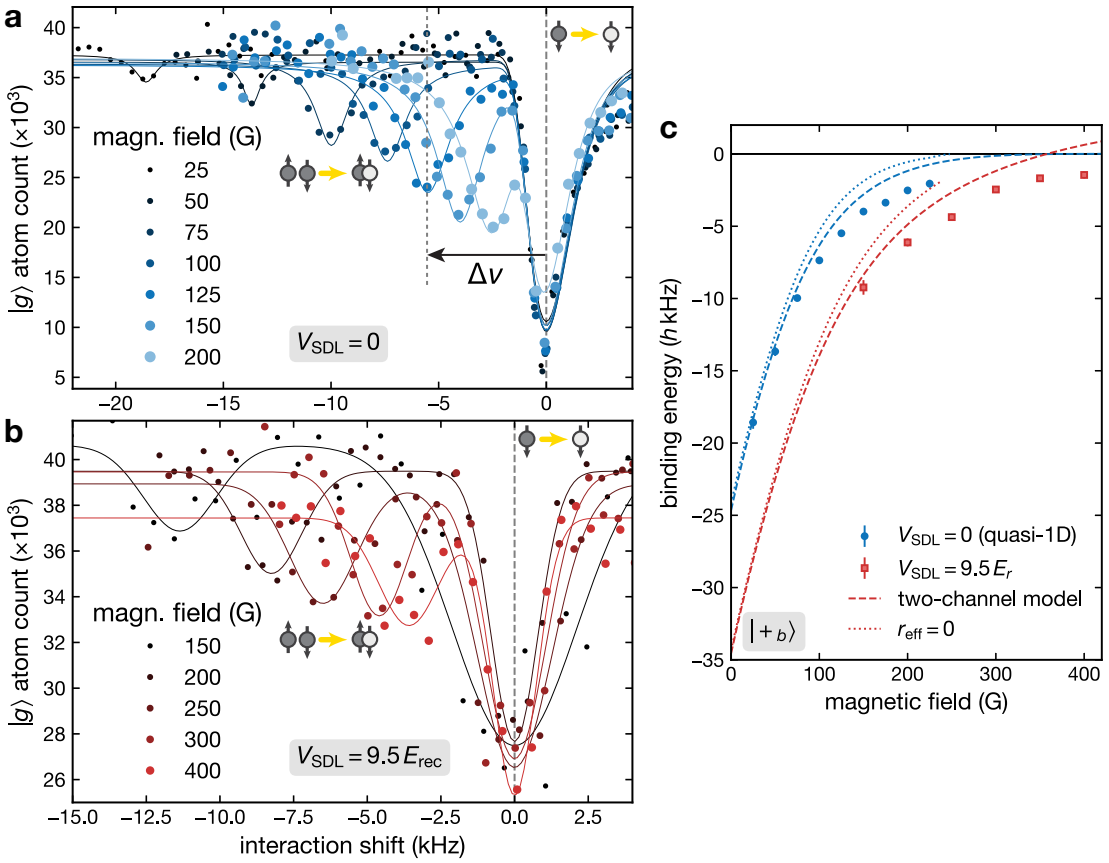

Figure 4.7 – (a-b) Interaction spectroscopy of the negative energy molecular bound state $|\psi_b\rangle$, rel. to the $|g\downarrow\rangle \rightarrow |e\downarrow\rangle$ transitions, for varying magnetic field. Comparison of (a) magic-wavelength quasi-1D and (b) a deep SDL configuration. Solid lines are fits to spectroscopy features (see main text), used to determine spectroscopic shifts $\Delta\nu$ between single-particle excitation and molecular bound state resonance. $V_\perp = 30E_{\text{rec}}^\perp$ perp. confinement. (c) Molecular bound state interaction energy E_b, rel. to two non-interacting particles, extracted from $\Delta\nu$ in (a-b) in quasi-1D (circles) and in the SDL (squares). Two-channel h.o. model for comparison, including effective range correction (dashed), and without (dotted). Error bars are standard fit errors for the spectroscopic shift $\Delta\nu$ of the interaction peak.

We probe the part of the spectrum below and including the single-particle transition $|g\downarrow\rangle \rightarrow |e\downarrow\rangle$ for a wide range of magnetic fields across the (free space) orbital Feshbach resonance. Figure 4.7 displays the resulting spectra for a quasi-1D and a deep SDL configuration ($V_z = 9.5\,E_{\text{rec}}^z$), including the highest-lying molecular bound state. As expected from our two-channel h.o. model introduced above, the bound state is more tightly bound at small magnetic fields[10]. The strong binding goes along with a decrease in the spectroscopic contrast. Note that despite the higher pulse power, the excitation fraction is significantly reduced in the presence of the

[10]Qualitatively, crossing the orbital Feshbach resonance from low to high magnetic fields, implies tuning the inverse scattering length from positive to negative values [99], effectively going from right to left in Fig. 4.3.

SDL and the SNR is only sufficient to follow the bound state down to magnetic fields of 150 G.

Obviously, in the quasi-1D case, the system does not actually form an array of isolated two-atom pairs but rather a "true" interacting many-body system. As a consequence, in Fig. 4.7(a), we observe an asymmetry of the single-particle transition that can be attributed to the interactions in the 1D scattering continuum. We interpret the minimum in the spectroscopy signal as the energetic onset of the scattering continuum.

The resonance positions ν_s and ν_d, belonging to the single-particle transition and the negative-energy bound state are extracted by fitting a sum of two displaced line shape profiles[11]. The extracted relative spectroscopic shift $\Delta\nu = \nu_d - \nu_s$ can be related to the two-particle interaction energy U_{eg} via Eq. (4.39), with the ground-state interaction $U_{gg}/h = 3.1\,\mathrm{kHz}$ estimated in the h.o. approximation. A comparison of the experiment data to the expected bound-state energy is shown in Fig. 4.7(c). The h.o. model is based on the known interorbital scattering lengths and effective ranges (Section 1.5) and has no further free parameters. The measured resonance position is in good agreement with the higher-lying molecular bound state, connecting to the spin-singlet state $|+_b\rangle$ at vanishing magnetic field. We extract an associated binding energy of $E_b^+/h = -24.7\,\mathrm{kHz}$ in the quasi-1D, and $E_b^+/h = -34.6\,\mathrm{kHz}$ in the deep SDL configuration. The spin-singlet nature of the state is also responsible for the decreased spectroscopic contrast at low fields. Note that we do not probe the spin-triplet molecular bound-state which is much more deeply bound, with a predicted energy $E_b^-/h < -1\,\mathrm{MHz}$ for the range of studied magnetic fields and SDL depths. At higher magnetic fields, there is a stronger discrepancy with the measured data which we attribute to the increasing effect of the lattice anharmonicity on the weakly bound wavefunction.

In addition to varying the interaction strength via the magnetic field, it can be tuned by the external confinement strength. Figure 4.8(a) displays the measured binding energy versus SDL depth V_{SDL}, at high magnetic fields where the bound state can still be resolved spectroscopically. We recover a relatively weak dependence on V_{SDL}. This is to be expected, as V_{SDL} enters only weakly into the h.o. length ℓ_z leading to small modifications of the critical interaction parameter ℓ_z/a. Again, it can be observed that the agreement with the h.o. model is significantly improved for the more deeply bound configurations. Figure 4.7(c) and Figure 4.8(a) also portrait the influence of the finite effective range, particularly at higher magnetic fields, leading to energy corrections on the kHz level.

Coupling to longitudinal center-of-mass excitations

As discussed in Section 4.1.3, the lattice potential anharmonicity and the mixed confinement lead to a coupling of the rel. and CM motion. Especially for anisotropic on-site confinement ($\eta \neq 1$), we expect a large density of level crossings between CM-excited molecular bound states and the lowest excited trap states [see Fig. 4.3]. The finite CM-rel. coupling should turn them into avoided crossings. Indeed, we can observe these features spectroscopically in the

[11] Empirically, we find good agreement using the sum of a symmetric Lorentzian and an asymmetric Gumbel distribution for the incoherent excitation in the quasi-1D case. For the coherent excitation in the SDL, two Gaussians are used for the fit.

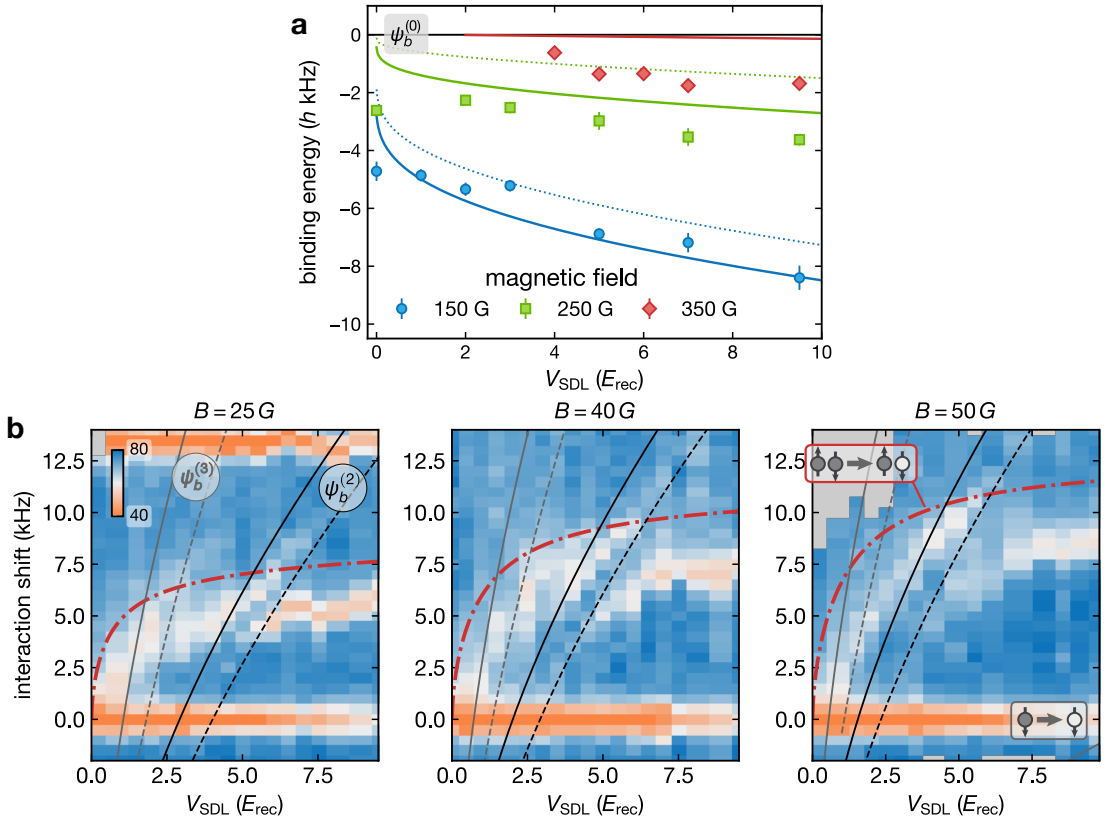

Figure 4.8 – (a) Measured interaction energy of molecular bound state $\psi_b^{(0)}$ in the CM ground state, for varying SDL depth and different magnetic field strengths. Two-channel h.o. model for comparison, including effective range correction (solid), and without (dotted). Error bars are standard fit errors for the spectroscopic shift $\Delta\nu$ of the interaction peak. (b) Clock-line spectroscopy of positive interaction energies, in a SDL of variable depth, at three different magnetic fields (from left to right). The number of residual $|g\rangle$ atoms after the clock laser pulse is plotted for varying detuning relative to the $|g\downarrow\rangle \rightarrow |e\downarrow\rangle$ transition. The dash-dotted line is the lowest positive-energy interacting trap state (spin triplet for $B = 0$) from the h.o. theory. The solid lines are n-th order longitudinal CM excitations $\psi_b^{(n)}$ of the rel.-motion molecular bound state $\psi_b^{(0)}$ in (a). For the dashed lines, the perturbative anharmonicity corrections for the CM excitation from Eq. (4.23) is included.

experiment configuration described above. We have probed the negative interaction energies of the highest-lying molecular bound state $\psi_b^{(0)}$, without CM excitations [see Fig. 4.8(a)]. Now, by scanning the clock laser detuning in the positive-energy range above the $|g\downarrow\rangle \rightarrow |e\downarrow\rangle$ transition, we can access the lowest-lying interacting trap state. In Fig. 4.8(b), it branches off from the repulsive quasi-1D scattering continuum when the lattice depth is increased. On a qualitative level, it matches the lowest eigenstate from the h.o. theory (dash-dotted), which evolves into the spin-triplet $|-^{(0)}\rangle$ with finite spectroscopic contrast for vanishing magnetic fields.

Clearly, around an intermediate SDL depth $V_{SDL} \approx 5E_{rec}^z$, a strong avoided crossing structure distorts the lowest trap state resonance, growing in width with the magnetic field. Energetically, the position and slope match with the crossing between $|-^{(0)}\rangle$ and the molecular bound state with two longitudinal CM excitations $\psi_b^{(n_z=2)}$. Including the first-order pertur-

bative anharmonicity correction from Eq. (4.23) reduces the energy of the CM excitations in $\psi_b^{(n_z=2)}$ and improves the agreement with the avoided crossing structure. Note that weak signatures of coupling with higher-order CM excitations can be discerned at lower SDL depths. However, an assignment of a specific order is not attempted. The anharmonicities of the lattice potential expansion should only couple states differing by even number of CM excitations [240]. In the SDL however, the mixed confinement breaks the CM-rel. symmetry of the coupling Hamiltonian Eq. (4.12), potentially leading to coupling between states of different symmetry.

Conclusion and remarks We have found that the two-channel h.o. model for two particles with contact interactions in mixed confinement provides a good approximation for the spectroscopically determined bound-state energies in the tight-binding regime. Due to the large spin-singlet scattering length, already the lowest longitudinal CM excitations of the shallow bound state can come into resonance with the repulsive on-site trap states for specific external confinement and magnetic fields. There, the anharmonic potential terms lead to the emergence of strong avoided crossings in the spectrum. The position of the resonances is approximately reproduced by the h.o. model. Yet, a full treatment of the anharmonic trap potential and coupling terms, including also the rel. motion part of the wavefunction, would be required to improve the agreement for the higher-lying trap states and to predict the CM-rel. coupling strength.

CHAPTER 5

Tunable spin exchange in an orbital state-dependent lattice

In the previous chapter, we have characterized the strong interorbital interactions of fermionic ^{173}Yb in the state-dependent lattice. The interactions can happen in two scattering channels, attributable to the symmetric and antisymmetric superpositions of the electronic clock state orbitals, or the nuclear spin singlet and triplet, respectively. The large spin-singlet scattering length compared to the spin-triplet leads to a strong ferromagnetic exchange coupling both in free space as well as for most external confinements [59, 60]. In this section, we demonstrate how the repulsive on-site interactions can be combined with orbital state-dependent mobility to engineer an effective next-neighbor spin-exchange coupling between mobile and localized magnetic moments, analogous to the Kondo coupling arising from the Anderson impurity model. The resulting exchange dynamics are observed directly by probing global magnetization dynamics in out-of-equilibrium spin mixtures. Notably, we find that variations in the external confinement can be used to resonantly tune the underlying exchange coupling. This tuning mechanism is attributed to resonant coupling with longitudinal center-of-mass excitations of the weakly bound spin-singlet, enabled by the mixed confinement and anharmonicity of the SDL potential. Details on this measurement can also be found in our publication [172][1].

5.1 Experimental setting

In our experimental setting, atoms in the two clock state orbitals $|e\rangle$ and $|g\rangle$ are confined in an array of state-independent quasi-1D traps, produced by perpendicular magic-wavelength lattice beams. Along the remaining direction, the SDL is superimposed, which effectively localizes the $|e\rangle$ atoms on experimentally relevant time scales [see Fig. 5.1(a)]. The SDL depth is independent of the nuclear spin m_F and it is reduces by a factor $p = 3.3$ (for $\lambda_{\mathrm{SDL}} = 670\,\mathrm{nm}$) for $|g\rangle$ compared to the $|e\rangle$ atoms. Thus, atoms in $|g\rangle$ retain their mobility and are free to undergo spin-changing collisions with the localized magnetic $|e\rangle$ moments. For details on the implementation of the SDL system and the mixed confinement properties, see Chapter 2. For the measurements presented in the following, we focus on intermediate SDL depths where

[1] Parts of the experiment and model description in this chapter are reproduced with permission from Phys. Rev. Lett. 120, 143601, © 2018 American Physical Society [172].

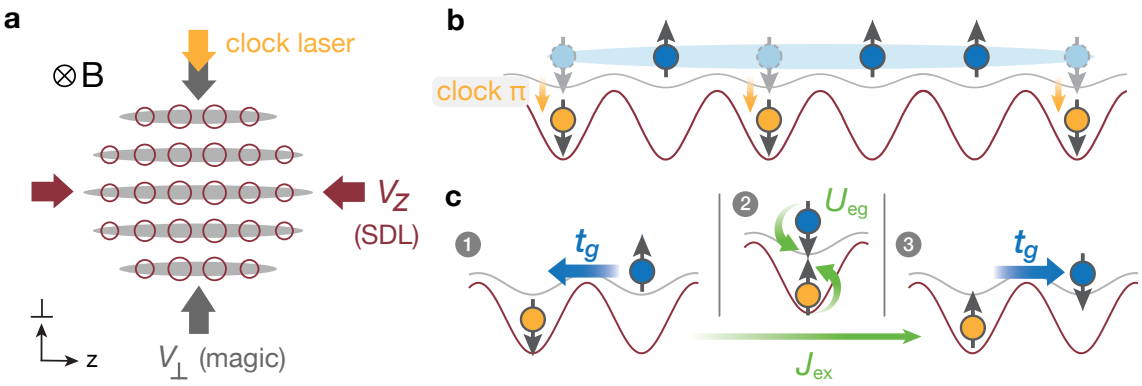

Figure 5.1 – Schematic of the experiment configuration and the spin-exchange process, adapted from [172]. (a) Lattice of isolated quasi-1D tubes, with perp. magic-wavelength confinement $V_\perp$, and longitudinal SDL. $|e\rangle$ atoms are mobile in a shallow potential (gray) whereas $|e\rangle$ atoms remain localized (red). (b) Initial state preparation in the SDL with singly occupied sites. A clock laser π pulse creates a spin imbalance within the two orbitals $|g\rangle$ (blue) and $|e\rangle$ (yellow). (c) Interorbital spin exchange between $|g\rangle$ and $|e\rangle$ on adjacent lattice sites via a second-order $|g\rangle$ tunneling process.

both orbitals are in the tight-binding regime and a state-dependent Hubbard model in the longitudinal direction z is realized. Then, the repulsive on-site interorbital interactions U_{eg} become dominant compared to the $|g\rangle$ tunnel coupling t_g. The lattice filling is chosen such that particles are on different lattice sites initially and both $|g\rangle$ and $|e\rangle$ populations are fully spin-polarized [Fig. 5.1(b)]. In this scenario, spin-flip scattering processes can only be mediated through second-order processes, where a $|g\rangle$ atom tunnels to a neighboring $|e\rangle$ site and back. Such a superexchange-like process is illustrated in Fig. 5.1(c).

We employ two out of six possible nuclear spin components of ^{173}Yb ($m_F = \pm 5/2$) to realize the spin degree of freedom ($|\uparrow\rangle$ or $|\downarrow\rangle$). Because of the SU(N) symmetry of the interactions and the absence of spin-changing processes, this can be considered an effective spin-1/2 system on the relevant timescales. For now, we neglect the influence of molecular bound states. Then, the possible intermediate interacting states of the superexchange process are the spin singlet and triplet trap states [see Section 1.5.4]

$$\begin{aligned} |+\rangle &= \frac{1}{\sqrt{2}}(|eg\rangle + |ge\rangle) \otimes \frac{1}{\sqrt{2}}(|\uparrow\downarrow\rangle - |\downarrow\uparrow\rangle) \\ |-\rangle &= \frac{1}{\sqrt{2}}(|eg\rangle - |ge\rangle) \otimes \frac{1}{\sqrt{2}}(|\downarrow\uparrow\rangle + |\uparrow\downarrow\rangle) \end{aligned} \tag{5.1}$$

as illustrated in Fig. 5.2(a). In Chapter 4, we have studied the on-site interactions in the mixed confinement setting of the SDL and have deduced approximate lowest band Hubbard parameters U^+ and U^- for the two interorbital scattering channels.

Overall, an effective ferromagnetic (FM) next-neighbor exchange coupling

$$J_{\mathrm{ex}}^0 = -\frac{t_g^2}{U^-} + \frac{t_g^2}{U^+} \approx -\frac{t_g^2}{U^-} < 0 \tag{5.2}$$

emerges from second-order perturbation theory in the low-energy regime. A derivation of

the exchange coupling from a state-dependent double-well model is performed below in Section 5.3.3, where we also take into account the influence of the spin-singlet molecular bound state. The perturbative treatment of the next-neighbor exchange interactions is justified in the limit $t_g \ll U^{\pm}$. In contrast, the on-site spin-exchanging interaction on doubly occupied lattice sites is simply given as $V_{\mathrm{ex}} = (U^+ - U^-)/2 > 0$ [59, 60].

In Fig. 5.2(b), we compare the on-site interactions to the ground- and excited-state mobility $t_{g/e}$ and quantify the resulting contributions $t_g^2/U^{\pm}$ to the exchange coupling. E.g., for the experimentally sampled range of SDL depths $V_z = (3...8)E_{\mathrm{rec}}^z$ and a typical perp. confinement $V_\perp = 30E_{\mathrm{rec}}^\perp$, we obtain a dominant spin-triplet coupling $t_g/U^- = (0.13...0.03)$. In the same range, the spin-singlet energy U^+ is nearly an order of magnitude higher and the associated exchange process is suppressed accordingly. Note that the dominant triplet exchange energy is comparable to the $|e\rangle$ tunneling rate, which limits the observable time scale on which we can assume the $|e\rangle$ atoms to remain localized and not undergo lossy *ee* collisions. An increased SDL polarizability ratio could help to mitigate this limitation. The interaction energies are shown relative to the zero-point energy

$$E_0^{\mathrm{os}} = (2\eta + 1)\hbar\bar{\omega}_z \tag{5.3}$$

of the two-particle, noninteracting harmonic oscillator. We use it as the entrance energy of the scattering process starting with two particles on separate sites[2]. Here, $\bar{\omega}_z$ is the mean longitudinal trapping frequency and $\eta = \omega_\perp/\bar{\omega}_z$ is the anisotropy of the on-site harmonic oscillator (h.o.) confinement, as defined previously.

5.2 Probing spin-equilibration dynamics

In a many-body setting, the spin-exchange coupling in the Kondo impurity model can lead to complex long-time relaxation dynamics of initially polarized magnetic impurities. The time evolution of the magnetization and the formation of the spin screening cloud have been studied numerically, and qualitatively different behavior is predicted in the context of ferro- (FM) and antiferromagnetic (AFM) Kondo models with varying coupling anisotropy [30–32, 34, 202]. Experiments with ultracold quantum gases exhibit slow dynamical timescales compared to most electronic condensed matter systems which should allow the real-time study of Kondo dynamics [34]. In particular, the next-neighbor interorbital exchange coupling realized between spin mixtures in our SDL could form the basis for the realization of Kondo-type physics. The global magnetization in the two electronic orbitals represents a useful tool for probing the exchange dynamics.

In our setup, localized as well as mobile magnetic moments are initially prepared in a polarized state, distributed on singly occupied lattice sites. The experimental sequence for state preparation and detection is displayed in Fig. 5.3. By means of optical pumping, a balanced

[2] In fact, the exact free-particle energy of one $|g\rangle$ and $|e\rangle$ atom on separate sites is $E_0^{\mathrm{os}} = (\eta\hbar\bar{\omega}_z + \frac{1}{2}\hbar\omega_{z,g}) + (\eta\hbar\bar{\omega}_z + \frac{1}{2}\hbar\omega_{z,e}) = \hbar\bar{\omega}\left(2\eta + \frac{1}{\sqrt{2}}\frac{1+\sqrt{p}}{\sqrt{1+p}}\right)$. However, the difference from the on-site zero-point energy is only on the one-percent level for the given polarizability ratio p of the SDL and becomes 0 for $p = 1$.

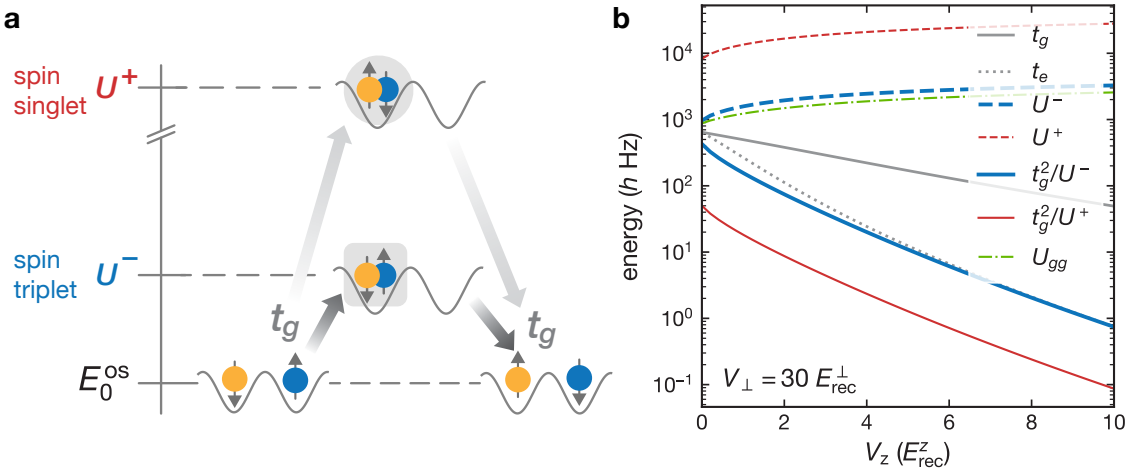

Figure 5.2 – (a) Interorbital spin exchange mediated by superexchange process ($\propto t_g^2/U$) via a repulsively interacting nuclear spin singlet $|+\rangle$ and a far-detuned triplet $|-\rangle$. On-site interaction energies $U^\pm$ are relative to a pair of noninteracting atoms on separate lattice sites E_0^{os}. (b) On-site interactions $U^\pm$ (red and blue dashed) and superexchange couplings $t_g^2/U^\pm$ (red and blue solid) compared to the state-dependent tunnelling rates t_g (gray solid), t_e (dotted) and the on-site ground-state interaction U_{gg} (dash-dotted), for typical variations of SDL depth V_z. Fixed perpendicular lattice depth $V_\perp = 30\, E_{rec}^\perp$.

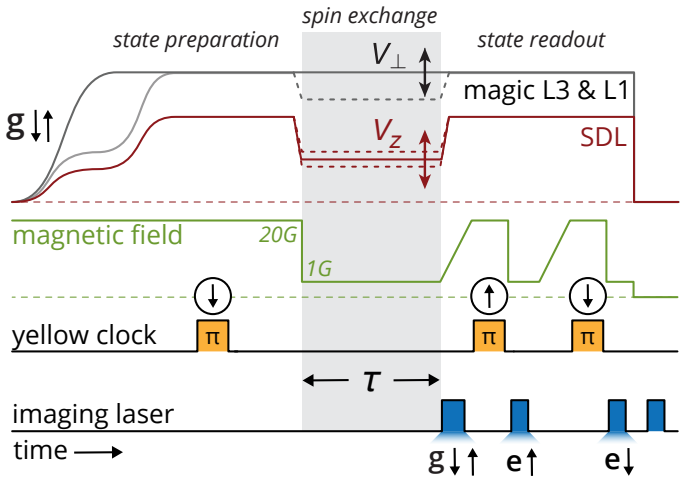

Figure 5.3 – Schematic of the experiment sequence for initiating and probing the interorbital spin-exchange dynamics after a mixture of $|g\uparrow\rangle$- and $|g\downarrow\rangle$-atoms is loaded into the SDL.

mixture of $|g\downarrow\rangle$ and $|g\uparrow\rangle$ ($m_F = \pm 5/2$) ^{173}Yb atoms is produced, with relatively low atom numbers ($N = 3.3\times10^3$ per spin state) and a reduced temperature of $T \approx 0.2\,T_\mathrm{F}$ in the optical dipole trap after evaporation [see Section 3.4.3]. The Fermi gas is transferred into a deep 3D lattice ($V_z = 8\,E^z_\mathrm{rec}$ and $V_\perp = 45...50\,E^\perp_\mathrm{rec}$) at a low atom density, such that the repulsive interactions between the fermions in the lattice suppress double occupancies. We verify this experimentally via clock-line spectroscopy, showing no peaks attributable to interacting states[3]. An average filling of around 21 atoms per tube is estimated. Applying a magnetic bias field of 20 G produces a differential Zeeman shift large enough to then selectively transfer the $|g\downarrow\rangle$ atoms to $|e\downarrow\rangle$ via a clock laser pulse. The fast π-pulse is performed at high intensities ($\Omega = 2\pi\times2.0$ kHz) to compensate spatially varying differential light shifts of the clock transition due to the harmonic confinement of the SDL beam. Until now, the magnetic field suppresses undesired spin-exchange dynamics energetically. Moreover, the mobility of the $|g\rangle$-atoms is reduced by the deep SDL, with a hopping rate of $t_g/h = 80$ Hz.

In order to initiate the spin-exchange dynamics, the perpendicular magic-wavelength lattice and the longitudinal SDL depth are rapidly lowered (1 ms ramp) to the values of interest, $V_\perp$ and V_z, defining the confinement during a variable hold time τ. Simultaneously, the magnetic field is ramped to a small bias value of 1 G. The field is high enough to preserve the nuclear spin quantization axis while at the same time inducing only small Zeeman energies ($h\cdot275$ Hz) compared to the on-site interaction energies (e.g., $U^- = h\cdot3.7$ kHz for $V_\perp = 30\,E^\perp_\mathrm{rec}$ and $V_z = 6\,E^z_\mathrm{rec}$). The mobility of the $|g\rangle$ atoms then allows them to reach $|e\downarrow\rangle$ sites by longitudinal tunneling, leading to spin-flip processes $|e\downarrow\rangle|g\uparrow\rangle \rightleftharpoons |e\uparrow\rangle|g\downarrow\rangle$ during a variable hold time τ.

Finally, before we image both $|e\rangle$ spin components separately to monitor the evolution of the exchange dynamics, we also image the entire $|g\rangle$ population by means of a high-intensity imaging pulse. This allows us to quantify the $|g\rangle$ atom loss and also defines the end point for the spin-exchange dynamics by removing the $|g\rangle$ atoms from the trap. Moreover, we rapidly increase the lattice depth again (1 ms ramp) as to suppress $|e\rangle$ tunnel mobility during the imaging process. The $|e\uparrow\rangle$ atoms populated through the spin-exchange process are imaged first, after ramping the magnetic field back up to 20 G (10 ms ramp time), spin-selective deexcitation to $|g\uparrow\rangle$ with a π-pulse and quenching the field back to 1 G. By imaging the deexcited $|e\uparrow\rangle$ atoms they are also removed from the lattice. This procedure is repeated analogously for the $|e\downarrow\rangle$ atoms. A modified Lambert-Beer law, independently calibrated for both spin components, accounts for saturated imaging pulses [see Section 3.6.1]. The column densities of the atomic in-situ distributions are captured within one camera frame, as described in Section 3.6.1. Overall, we are able to count the $|g\rangle$, $|e\uparrow\rangle$ and $|e\downarrow\rangle$ atom numbers in a single experimental realization[4].

[3] Note that this is in stark contrast to the measurements in Chapter 4. There, large atom numbers lead to many double occupancies which allows us probe the on-site interactions spectroscopically.

[4] In addition to probing the spin populations in the $|e\rangle$ orbital by subsequent deexcitation to $|g\rangle$ and detection pulses, the $|g\rangle$ population can also directly be probed spin-selectively by means of the optical Stern-Gerlach technique described in Section 3.6.2. An exemplary measurement of the spin-equilibration dynamics in the ground state is presented in Fig. D.3.

In-situ exchange dynamics In contrast to experiments conducted in isolated double-well systems [94, 255], or isolated doubly-occupied sites of a 3D lattice [60], we do not expect coherent collective dynamics of the magnetization after the field and lattice depth quench. Rather, the trap averaging over multiple "SDL tube" systems with varying atomic densities should lead to a global dephasing. Due to the global SU(N) symmetry of the interorbital interactions, the overall $|\uparrow\rangle$ and $|\downarrow\rangle$ population in both orbitals is conserved. However, the spin-flip processes should cause an equilibration of the individual magnetization of the $|e\rangle$ "impurities" and the $|g\rangle$ bath atoms, similar to the dynamics observed previously in 2D bulk systems [59].

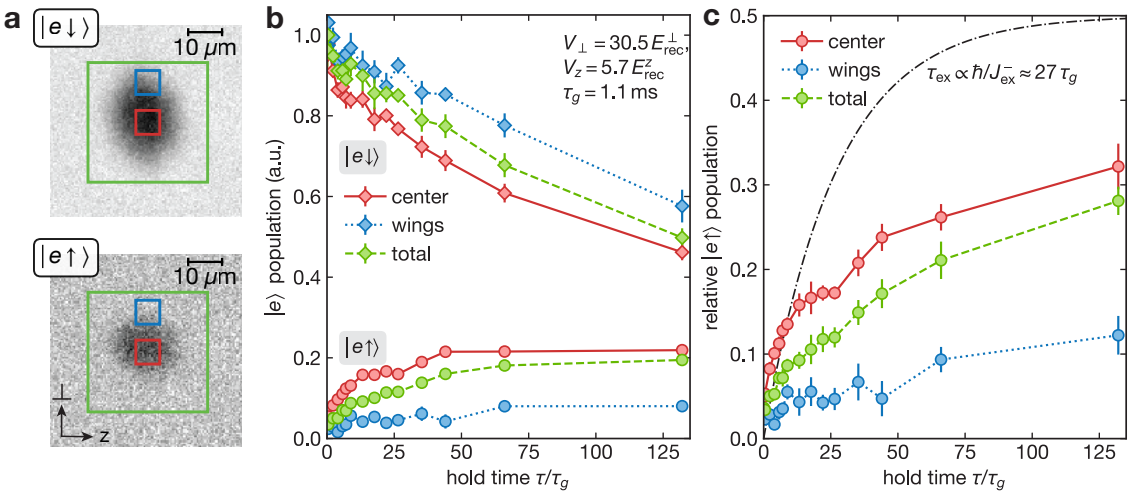

Figure 5.4 – In-situ observation of spin-exchange dynamics. (a) Separate in-situ absorption images (atomic column density) of the $|e\downarrow\rangle$ and $|e\uparrow\rangle$ population after a hold time $\tau = 40$ ms. Squares indicate areas with different atomic densities. (b) Time dependence of the $|e\downarrow\rangle$ ($|e\uparrow\rangle$) population relative to the initial, total $|e\rangle$ atom number is shown as diamonds (circles). The dynamics are evaluated for the regions specified in (a). They are faster in the trap center (red) compared to the wings (blue). The confinement $V_z = 5.7\,E_{rec}^z$, $V_\perp = 30.5\,E_{rec}^\perp$ is chosen such that CM-excited bound states are off-resonant. (c) $|e\uparrow\rangle$ normalized to total $|e\rangle$ atom count (circles). Exponential spin equilibration (dash-dotted) on time scale $\tau_{ex} = \hbar/J_{ex}^-$ for comparison. Each point is the average of at least four individual measurements. Data points less than τ_g apart are binned to reduce visual clutter. Error bars indicate the standard error of the mean.

Figure 5.4 depicts the measured equilibration dynamics in the $|e\rangle$ orbital for an intermediate SDL and perpendicular confinement depth. The in-situ imaging allows us to access the dynamics in different regions of the trap, and thereby probe different atomic densities independently. The red rectangle in Fig. 5.4 denotes an area in the center of the trap, covering 33% of the atomic cloud size[5]. The atomic density in this region is significantly larger than in the cloud wings (blue rectangle) and the initial state, governed by repulsive on-site interactions, should correspond to a spin chain with few vacancies. Out of the total $|e\rangle$ count (green rectangle), 15% percent are concentrated in the central trap region compared to 6% in the

[5]This is with respect to the area πr_F^2, where the Fermi radius is approximated as the σ with of a 2D Gaussian fit to the in-trap atomic column density.

wing region of equal size.

In Fig. 5.4(b), the $|e\uparrow\rangle$ and $|e\downarrow\rangle$ population in the different trap regions are plotted for varying hold time in units of the $|g\rangle$ tunneling time $\tau_g = \hbar/t_g = 1.1\,\mathrm{ms}$. The $|e\uparrow\rangle$ fraction, initially unpopulated, increases its relative weight over time while the number of $|e\downarrow\rangle$ atoms decreases. Clearly, the exchange dynamics are fastest in the trap center. This is true in particular during the first few $|g\rangle$ tunneling times. On longer time scales, a spin-independent loss process can be made out, affecting the total $|e\rangle$ atom number. The loss process is not symmetric in the orbital degree of freedom, with around 13% of the $|e\rangle$ atoms lost after $\tau = 50\,\tau_g$, compared to 7% of the $|g\rangle$ atoms (compare circles in Fig. 5.12). Figure 5.4(c) again shows the $|e\uparrow\rangle$ fraction, but this time normalized to the total, decaying $|e\rangle$ atom number. We have chosen a confinement where no CM-excited bound state becomes resonant with the entrance energy of the scattering process. Thus, the spin exchange should be dominated by the spin-triplet on-site interaction U^-. Indeed, the initial spin redistribution happens on a time scale that is compatible with the associated superexchange time

$$\tau_{\mathrm{ex}}^0 \equiv \hbar U^-/t_g^2 \approx 27\tau_g\,. \tag{5.4}$$

This is illustrated by the dash-dotted line in Fig. 5.4(c) which shows an exponential spin equilibration to a balanced mixture on that time scale. For comparison, the exchange rates extracted from a linear fit to the initial dynamics (up to $6\,\tau_g$) are 17.7(14) Hz for the trap center, 4.6(20) Hz for the wing region and 10.2(8) Hz for the total cloud. In the following, if not indicated otherwise, we restrict our treatment to the central trap region.

5.3 Tunable exchange coupling

Assuming the spin-exchange process that is only mediated via the lowest-band Hubbard parameters $U^{\pm}$, only a weak dependence of the exchange rate on the perpendicular confinement is expected, scaling with the on-site wavefunction overlap. Instead, we find that it can be strongly modified for certain values of the transverse confinement: The blue curves in Fig. 5.5(a) depict much faster exchange dynamics for values of $V_\perp$ that only differ slightly from the measurement presented above (black). Along with the exchange rate, also the loss rate of both excited-state species is amplified. Fig. 5.5(b) shows the dynamics of the $|e\uparrow\rangle$ fraction normalized to the total $|e\rangle$ atom number for a larger range of perpendicular confinements. We find that the exchange process is resonantly enhanced with a maximum around $V_\perp = 37\,E_{\mathrm{rec}}^\perp$ and displays an asymmetric resonance profile with a sharp flank on the low-$V_\perp$ side. This is also illustrated in Fig. 5.5(c), where an exchange rate is extracted from a linear fit to the initial dynamics. On resonance, the displayed maximum hold time of around $50\,\tau_g$ is enough to reach a full equilibration of the spin components.

We attribute the origin of this resonance to resonant coupling with a longitudinal CM excitation of the bound state of the spin-singlet scattering potential. This becomes clear when we map out the resonance position dependence on both perpendicular as well as longitudinal confinement. In Fig. 5.6(a), the growing $|e\uparrow\rangle$ fraction after a short hold time $\tau \propto \hbar U^-/t_g^2$

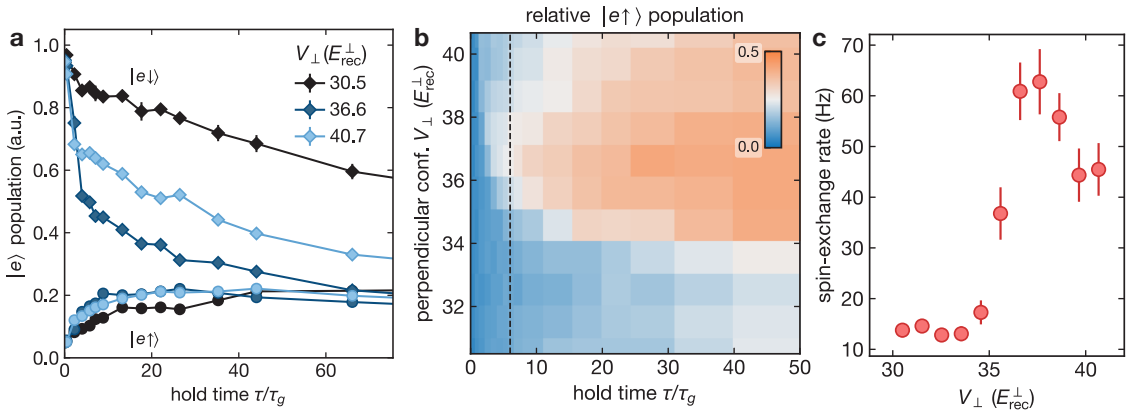

Figure 5.5 – Dependence of the spin-exchange dynamics on perpendicular confinement. Figure adapted from [172]. (a) Time dependence of the $|e\downarrow\rangle$ ($|e\uparrow\rangle$) population relative to the initial, total $|e\rangle$ atom number is shown as diamonds (circles). Each point is the average of at least four individual measurements. Data points less than τ_g apart are binned to reduce visual clutter. Error bars indicate the standard error of the mean. (b) Resonant population dynamics of $|e\uparrow\rangle$ relative to the total $|e\rangle$ population for varying perp. confinement. (c) Rate of increase of the $|e\uparrow\rangle$ fraction, determined by a linear fit to the short-time dynamics (up to $\tau = 6\tau_g$, dashed line in (b)). Error bars indicate the 1σ uncertainties of the fits. All atom numbers from trap center region, as in Fig. 5.4. SDL depth is fixed to $V_z = 5.7\, E^z_{\mathrm{rec}}$.

is plotted. This scaling of τ is motivated by the characteristic timescale of the superexchange model. Varying both confinement strengths, we identify two resonance branches in the experimentally accessible parameter regime where the exchange rate is enhanced. Figure 5.6(b) shows a cut through the raw data[6] underlying (a) along $V_\perp = 35.6\, E^\perp_{\mathrm{rec}}$, evaluated for different regions of the trap. The spin populations are normalized to the total $|e\rangle$ atom count in that region, for confinement parameters outside of the resonance branches. We observe that also the resonant dynamics happen faster in the region of high average atomic density. The resonance branches exhibit similar properties in terms of contrast and asymmetry. The steeper flank is found on the large-V_z side.

5.3.1 Resonant bound-state coupling

A tunable spin-exchange interaction for AEA in a SDL, which depends on the perpendicular confinement has been proposed in [84]. There, the tunability is caused by a perpendicular CIR in the interorbital scattering of fully localized impurities interacting with a $|g\rangle$ bath in a quasi-1D confinement. As we will see below, such a classical CIR can be ruled out for the achievable lateral confinements. Instead, the experimentally observed resonances are induced by the longitudinal mixed confinement in the SDL. Recent theoretical proposals also take the harmonic longitudinal confinement of the impurity into account. However, they consider fully mixed dimensions, with bath atoms confined in a pure 1D [256] or quasi-1D potential [178]. Both models neglect the lattice confinement of the $|g\rangle$ atoms as well as anharmonicities of the

[6] The full measurement data, featuring the independent $|e\uparrow\rangle$ and $|e\downarrow\rangle$ counts are summarized in Fig. D.2.

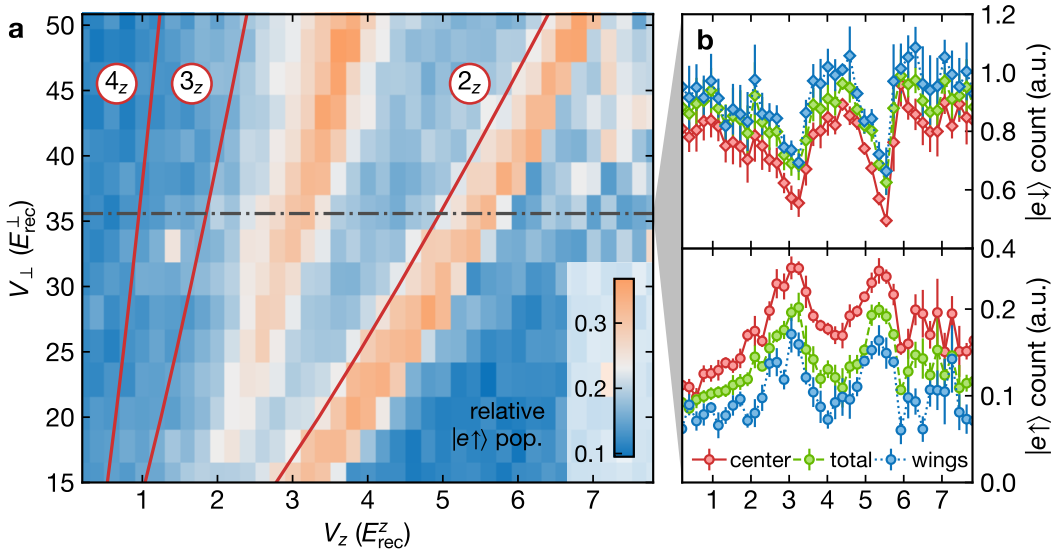

Figure 5.6 – Resonance branches in the spin-exchange rate as a function of perpendicular confinement $V_\perp$ and SDL depth V_z. Figure adapted from [172]. (a) $|e\uparrow\rangle$ fraction normalized to total $|e\rangle$ count after hold time $\tau \propto \hbar U^-/t_g^2$. The hold time is chosen such that $\tau = 12.2\,\tau_g$ for $V_z = 6\,E^z_{\rm rec}$ and $V_\perp = 30\,E^\perp_{\rm rec}$. Solid lines indicate the predicted resonance positions from the h.o. model (second, third and fourth longitudinal CM excitation from right to left). Atom numbers from trap center region. (b) Cut through the data in (a) at $V_\perp = 35.6\,E^\perp_{\rm rec}$ (dashed line) $|e\downarrow\rangle$ (diamonds) and $|e\uparrow\rangle$ (circles) atom counts, normalized to the total $|e\rangle$ population ($N_e = (0.4, 2.2, 0.2) \times 10^3$ for trap center, total cloud and wing region, as defined in Fig. 5.4) at $V_z = 8\,E^z_{\rm rec}$.

lattice potential. Still, qualitative agreement with our experimental data is found in [178] and the authors attribute the resonances to an even and odd-wave CIR.

In our model for the exchange interactions, we concentrate on the tight-binding limit where both orbitals $|g\rangle$ and $|e\rangle$ exhibit strong but different on-site confinements. We make use of the regularized Hubbard parameters derived for the mixed on-site confinement in Section 4.1.4. As as consequence of the large a^+_{eg} scattering length, ^{173}Yb features a shallow bound state $|+_b\rangle$ of the spin-singlet scattering channel with an energy U^+_b in the range of a few longitudinal CM excitation energies [see Fig. 5.7(a)]. In Chapter 4, we have verified spectroscopically that the lowest longitudinal CM excitations $|+^{(n)}_b\rangle$ can come into resonance with the weakly interacting, positive-energy trap states, leading to avoided crossings in the eigenspectrum. Similarly, we are now concerned with the lowest CM-excited bound states coming into resonance with the energy $E^{\rm os}_0$ of two non-interacting particles of different lattice sites. When this happens for certain transverse and longitudinal confinement parameters, the spin-singlet bound state $|+^{(n)}_b\rangle$ becomes available as an additional intermediate state for the spin-exchange process. Since its energy depends on the tunable optical potential depths, the overall process becomes controllable in strength and should even allow for an AFM exchange coupling (see Section 5.3.3).

Figure 5.7(b) depicts the influence of the external confinement on the spectrum of the anisotropic harmonic-oscillator Hamiltonian Eq. (4.10), describing the on-site interactions. In a first approximation, we neglect the trap anharmonicity terms, such that the rel. and CM co-

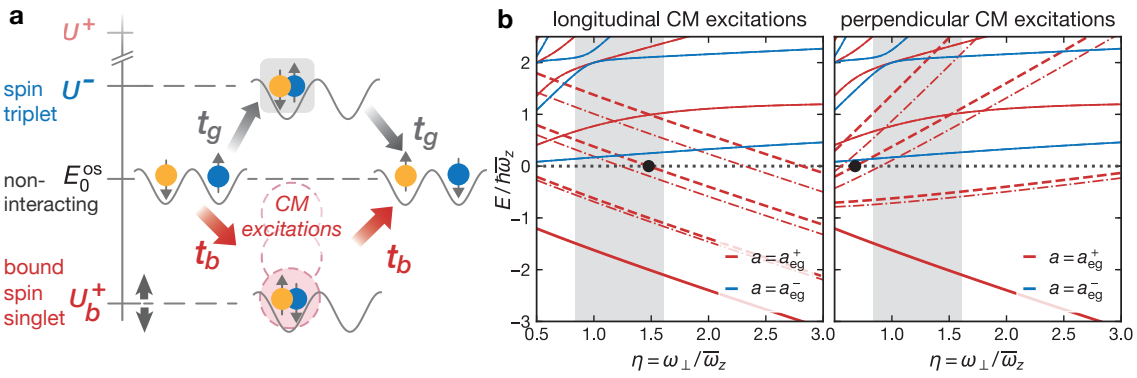

Figure 5.7 – (a) Tunable interorbital spin exchange mediated by superexchange process via near-resonant CM-excited spin-singlet bound state $|+_b\rangle$, repulsively interacting nuclear spin-singlet $|+\rangle$ (and far-detuned triplet $|-\rangle$). On-site interaction energies $U^{\pm}$ are relative to the energy E_0^{os} a pair of noninteracting atoms on separate lattice sites. (b) Tunable on-site energies in the spin-singlet (red) and triplet (blue) channel, from the h.o. model for a fixed longitudinal confinement $V_z = 6\,E_{rec}^z$ and varying on-site anisotropy $\eta = \omega_\perp/\bar{\omega}_z$. Solid lines are states without CM excitation. Longitudinal and perpendicular CM excitations (left and right plot) of $|+_b\rangle$ (dashed lines) come into resonance with E_0^{os} (dotted line). Within the accessible range of $V_\perp$ (gray area), one resonance (circle) occurs. The dash-dotted lines include the perturbative correction [Eq. (4.23)] for the excitation energies.

ordinates of the harmonic oscillator decouple. The interaction energies of the shallow bound spin-singlet $|+_b\rangle$ (red solid line) as well as its longitudinal and perpendicular CM excitations are compared to the higher-lying spin-triplet trap states (blue). At a fixed longitudinal confinement V_z, several resonances with E_0^{os} occur as a function of the on-site anisotropy η, by modifying the transverse confinement $\omega_\perp$. Note that in the experimentally accessible parameter range, only resonances with longitudinal CM excitations occur. In this figure, we also illustrate the effect of corrections to the CM excitation energies due to anharmonic terms in the SDL and perp. lattice potential, according to Eq. (4.23). The dash-dotted lines include the negative first order perturbative correction in the quartic and sextic terms.

Overlaying the extracted zero-crossing positions onto our experimental data in Fig. 5.6(a) as red lines, it is found that the resonances from the longitudinal CM excitations roughly match the functional dependence of the observed spin-exchange resonances. The validity of the h.o. model is improved with increasing SDL depth and for lower CM excitations. Indeed, for the branch with two CM excitations, also the position of the resonance is approximately reproduced.

In Fig. 5.8, we evaluate the predicted resonance positions from the h.o. model for a larger range of confinement parameters V_z and $V_\perp$. The number of longitudinal and perp. CM excitations are specified as n_z and $n_\perp$. For comparison, the experimental resonance positions are included. They are determined from a fit of two Lorentzian line shapes per $V_\perp$ to the $|e\uparrow\rangle$ fraction in Fig. 5.6. Again, it becomes clear that only coupling to longitudinal CM excitations of can explain the experimentally observed resonances. The perpendicular excitations exhibit a qualitatively different functional dependence in the confinement parameters. Significantly increasing the SDL depth at low perp. confinement could allow for access to the branch with

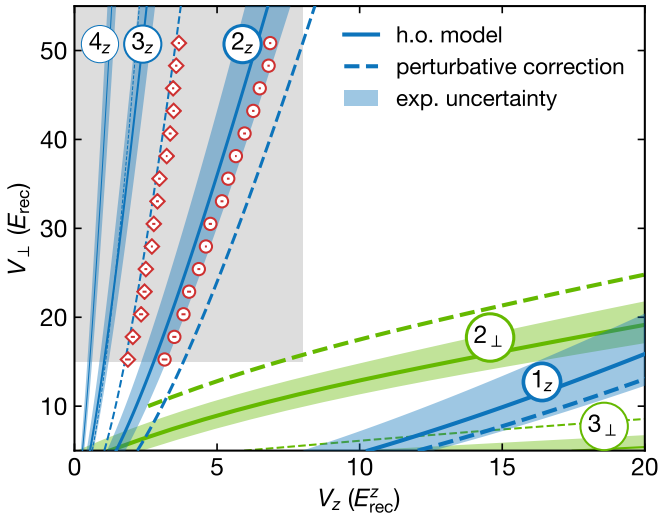

Figure 5.8 – Comparison of the anisotropic h.o. model (lines) with the experimentally determined spin-exchange resonances (red circles and diamonds): Experimental resonance positions are from a fit of two Lorentzian line shapes per $V_\perp$ to the data in Fig. 5.6; error bars are the 1σ error of the fits. Blue (green) lines indicate the crossings of $n_{z/\perp}$-th order longitudinal (perpendicular) CM excitations of the singlet bound state $|+_b\rangle$ with the energy $E_0^{\rm os}$ a pair of noninteracting atoms on separate sites. Solid lines are from pure h.o. model. The filled areas mark the systematic uncertainty from a variation of a_{eg}^+ by 10% and p by 6%. Dashed lines include the perturbative correction [Eq. (4.23)] for the excitation energies. Only long. CM excitations are experimentally accessible (gray area). The lowest $\perp$ excitation is found at low $V_z < 0.2\,E^z_{\rm rec}$ and not shown due to numerical convergence problems.

two perp. CM excitations. The "$1_\perp$" resonance branch attributed to one perp. CM excitation is not shown in Fig. 5.8 due to numerical convergence problems. However, in the displayed $V_\perp$ range, it appears only for very low $V_z < 0.2E^z_{\rm rec}$, outside of the tight-binding regime.

On a quantitative level, the anharmonicity correction of the longitudinal (perpendicular) CM excitation energies leads to a negative (positive) shift of the resonance positions in $V_\perp$ on the 10% level. This improves the agreement with the experiment data significantly for the "3_z" resonance, yet, the h.o. model is overcorrected for the "2_z" resonance. A full numerical treatment of the optical lattice Hamiltonian, analogous to the procedure in [251], could help to determine more accurate values for the effective Hubbard parameters and thereby the resonance positions. Further systematic mismatch between theory and experiment could arise from uncertainties in the polarizability ratio p of the SDL, as well as the spin-singlet scattering length a_{eg}^+. The expected variations are also indicated in Fig. 5.8.

5.3.2 Anisotropy of the perpendicular confinement

The measurements presented above have been conducted under isotropic transverse confinement. This is accomplished by choosing the same lattice depths $V_x = V_y$ for the deep transverse magic-wavelength lattices (L1 and L3). In an additional measurement using anisotropic perpendicular confinement, we have verified that, in the limit of strong confinement, the position

of the spin-exchange resonances only depends on the geometric mean $V_\perp = \sqrt{V_x V_y}$ of the individual perpendicular lattice depths. This is another strong indicator for the origin of the observed spin-exchange resonances lying in the longitudinal mixed confinement. In fact, a splitting of the CIR into two individual resonances would be expected for direct coupling to the anisotropic perp. confinement [247].

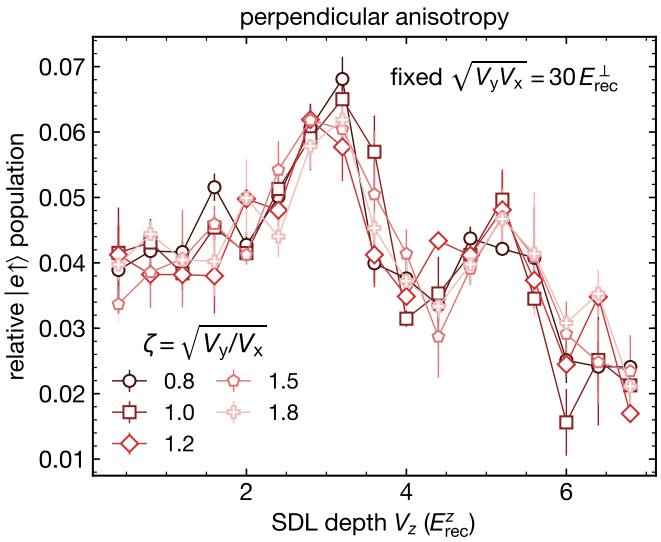

Figure 5.9 – Effect of the *perpendicular* confinement anisotropy $\zeta = \sqrt{V_y/V_x} = \omega_y/\omega_x$ on the spin-exchange rate and its resonance positions. $|e\uparrow\rangle$ population relative to the total $|e\rangle$ atom number is shown after hold time $\tau = 2\pi\,\tau_g$. No change in the resonance shapes is discernible within the SNR for a fixed geometric mean of the transverse confinement depth $\sqrt{V_y V_x} = 30\,E_{rec}^{\perp}$.

The measurement results are presented in Fig. 5.9. We fix the geometric mean of the transverse confinement to $\sqrt{V_y V_x} = 30\,E_{rec}^{\perp}$ and vary both the SDL depth and the anisotropy $\zeta = \sqrt{V_y/V_x} = \omega_y/\omega_x$ of the transverse confinement. The ζ variations are induced by varying the L3 depth between 30 and 55 $E_{rec}^{\perp}$, and L1 between 30 and 16.4 $E_{rec}^{\perp}$. The resonances in the $|e\uparrow\rangle$ fraction, populated through spin exchange during a small hold time, show no dependence on the ζ variations.

5.3.3 Tunable two-channel exchange coupling in a state-dependent double well

In the discussion above, we have used the unique confinement dependence of the Hubbard interaction energies to attribute the origin of the exchange rate resonances to coupling with CM-excited spin-singlet bound states. Yet, an effect of the singlet channel on the spin-exchange coupling requires a finite coupling for the process of a $|g\rangle$ atom tunneling to a neighboring site and forming a bound state with an $|e\rangle$ atom. We have not established a microscopic model for the two-particle scattering in the presence of the lattice potential, as e.g. in [251]. However, we presume that the shallow SDL potential experienced by the $|g\rangle$ atoms should lead

to significant next-neighbor coupling with the weakly interacting bound states. This coupling should further be enhanced through the on-site CM-rel. motion coupling, caused by the mixed confinement and anharmonicity of the SDL potential. Notably, in Chapter 4, we have spectroscopically verified the existence of a weakly bound state of spin-singlet nature (at low magnetic fields) and how its CM excitations couple to higher-lying trap states and lead to avoided crossings in the on-site two-particle spectrum.

To investigate the influence of the off-site bound state coupling, we will consider a simplified double-well model with two particles that incorporates the on-site interactions discussed above, as well as the mobility of the $|g\rangle$ atoms. The emergent Heisenberg-type spin-exchange coupling J_{ex} between localized and mobile magnetic moments results from the combined effect of all available exchange channels for a given confinement, as illustrated in Fig. 5.7(a). In particular, for configurations in which the bound singlet channel provides the largest contribution to the exchange, J_{ex} becomes widely tunable and can even switch sign between FM and AFM exchange coupling.

Controllable exchange interactions between neutral atoms in optical lattices have previously been proposed in the context of spin-dependent lattices with a single interaction channel [257]. Tilted double-well potentials have for example been used to probe time-resolved, coherent superexchange dynamics with tunable coupling [255]. In [34], Kanász-Nagy et al. derive an effective Kondo impurity model from a Hubbard-Anderson model for AEA in an orbital state-dependent lattice, taking both interorbital interaction channels into account. They find, that the anisotropy and the strength of the coupling can be tuned in the presence of static and modulated Zeeman fields.

Our double-well model system incorporates both the orbital state-dependent mobility as well as the two interorbital scattering channels, including also the coupling to the CM-excited spin-singlet bound state which enables resonant tunability. It is tailored to predict the short-time exchange dynamics after the state preparation of the mixtures of fully spin-polarized $|e\rangle$ and $|g\rangle$ atoms. We consider two particles on two lattice sites (sites L,R in a double well) of the state-dependent lattice. One particle is in $|e\rangle$ and the other one in $|g\rangle$. The $|e\rangle$ particle is localized on one of the two sites (site L) and the $|g\rangle$ particle can hop between the two sites with the lowest-band tunnel coupling t_g. Initially, the two particles are prepared in different spin states $|\uparrow\rangle$ or $|\downarrow\rangle$, non-interacting on different lattice sites, with an overall spatial wave function $|C\rangle$ and an energy E_0^{os} (we set $E_0^{\mathrm{os}}=0$ in the following).

We neglect direct next-neighbor interactions such that a spin-exchange process can only be mediated by tunneling of $|g\rangle$ atoms. The model is also simplified in that we only include a single neighboring site of the localized impurity in contrast to the full lattice treatment in [34]. If two particles tunnel onto the same site (L) while staying in the lowest lattice band (no CM excitation), they take on the on-site spatial wave function $|A\rangle$. The possible interaction channels are U^- and U^+, depending on whether they are in the spin triplet $|-\rangle=\frac{1}{2}(|ge\rangle-|eg\rangle)(|\uparrow\downarrow\rangle+|\downarrow\uparrow\rangle)|A\rangle$ or spin singlet $|+\rangle=\frac{1}{2}(|ge\rangle+|eg\rangle)(|\uparrow\downarrow\rangle-|\downarrow\uparrow\rangle)|A\rangle$ configuration. Further, the coupling of CM and rel. motion can lead to two particles on separate sites coupling into a CM-exited on-site bound state. The on-site wavefunction is then labeled by $|B\rangle$. The tunnel coupling from neighboring sites into that state is defined as t_b. The par-

ticles will then dominantly interact via a CM-excited spin-singlet bound state $|+_b\rangle$ close to the entrance energy E_0^{os}. Note that we also include the spin-triplet bound state $|-_b\rangle$ in the set of available states, as it is required for completeness of the basis. However, it is detuned by several orders of magnitude from E_0^{os} and does not contribute to the low-energy observables. The associated on-site energies, including the CM excitations, are $U_b^{\pm}$ for the states $|\pm_b\rangle = \frac{1}{2}(|ge\rangle \pm |eg\rangle)(|\uparrow\downarrow\rangle \mp |\downarrow\uparrow\rangle)|B\rangle$.

The overall Hamiltonian for the double-well system can be written as

$$\begin{aligned} H &= H_{\mathrm{int}} + H_{\mathrm{t}} \quad \text{with} \\ H_{\mathrm{int}} &= U^-|-\rangle\langle -| + U^+|+\rangle\langle +| + U_b^+|+_b\rangle\langle +_b| + U_b^-|-_b\rangle\langle -_b| \,\text{and} \\ H_{\mathrm{t}} &= \sum_\sigma \left(-t_g|g,\sigma\rangle|A\rangle\langle C|\langle g,\sigma| - t_b|g,\sigma\rangle|B\rangle\langle C|\langle g,\sigma| + \mathrm{h.c.}\right), \end{aligned} \tag{5.5}$$

with $\sigma = \uparrow, \downarrow$. The Hubbard interaction parameters in the on-site interaction part H_{int} and their confinement dependence are from the interacting, anisotropic h.o. model introduced in Chapter 4. The tunnel couplings between neighboring wells are captured in H_t.

In a first approach, we directly study the time evolution of the Hamiltonian, in order to investigate the effect of the bound-state coupling onto the spin-exchange dynamics. The computation is done in a two-particle product state basis: With internal states $|\mathrm{orbital}, \mathrm{spin}\rangle$ and the spatial wave function $|\mathrm{A/B/C}\rangle$, the relevant two-particle basis states are $|e,\uparrow\rangle|g,\downarrow\rangle|A\rangle$, $|e,\downarrow\rangle|g,\uparrow\rangle|A\rangle$, $|e,\uparrow\rangle|g,\downarrow\rangle|B\rangle$, $|e,\downarrow\rangle|g,\uparrow\rangle|B\rangle$, $|e,\uparrow\rangle|g,\downarrow\rangle|C\rangle$ and $|e,\downarrow\rangle|g,\uparrow\rangle|C\rangle$ (we omit the trivial fermionization). The last two basis states correspond to the non-interacting states $|e\uparrow\rangle_L|g\downarrow\rangle_R$ and $|e\downarrow\rangle_L|g\uparrow\rangle_R$ of particles on different sites (L,R) of the double well. Then, the Hamiltonian takes the following form:

$$H = \begin{bmatrix} \frac{U^-+U^+}{2} & \frac{U^--U^+}{2} & 0 & 0 & -t_g & 0 \\ \frac{U^--U^+}{2} & \frac{U^-+U^+}{2} & 0 & 0 & 0 & -t_g \\ 0 & 0 & \frac{U_b^-+U_b^+}{2} & \frac{U_b^--U_b^+}{2} & -t_b & 0 \\ 0 & 0 & \frac{U_b^--U_b^+}{2} & \frac{U_b^-+U_b^+}{2} & 0 & -t_b \\ -t_g & 0 & -t_b & 0 & 0 & 0 \\ 0 & -t_g & 0 & -t_b & 0 & 0 \end{bmatrix}. \tag{5.6}$$

The offsite spin-exchange process between particles on different sites corresponds to superexchange coupling between the last two basis states.

Fig. 5.10(a) depicts the coherent spin-exchange dynamics happening in the double-well model for different confinements at a finite coupling strength into the CM-excited bound state. It shows the expectation value of finding an $|e\uparrow\rangle$ atom after letting the initial state preparation $|e\downarrow\rangle_L|g\uparrow\rangle_R$ coherently evolve for a time τ. The confinement is chosen around the energetic resonance "2_z" of the bound spin-singlet state $|+_b\rangle$ with E_0^{os}. In the double-well model, the population dynamics are fully coherent and sinusoidal spin-exchange oscillations occur on variable time scales. Initially, $|e\uparrow\rangle$ is populated through spin exchange with a rate that shows a resonance structure in the confinement similar to the one observed experimentally in Fig. 5.5. The exchange rate diverges on resonance (red line). On the large-confinement

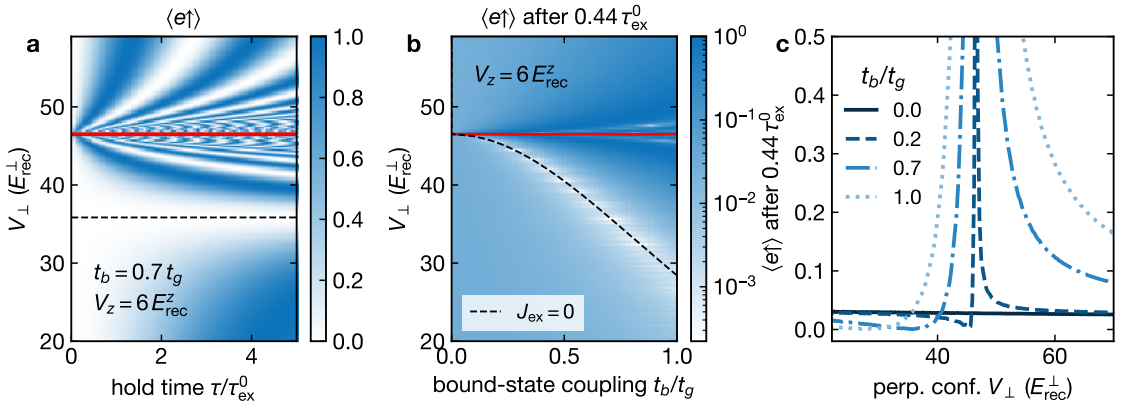

Figure 5.10 – Spin-exchange dynamics in the state-dependent double-well model (sites L, R): (a) Populated $e\uparrow$-fraction after initial state $|e\downarrow\rangle_L|g\uparrow\rangle_R$ is held for τ in units of the bare spin-exchange time $\tau^0_{\rm ex}$; for coupling strength $t_b = 0.7t_g$ to the CM-excited singlet bound state $|+^{(2)}_b\rangle$ and varying perp. confinement. Fast coherent oscillations with frequency $\sim t_b$ occur around the resonance (solid red line) of $|+^{(2)}_b\rangle$ with the energy $E^{\rm os}_0$ of two particles on different sites. Dashed lines in (a,b) indicate vanishing exchange dynamics for $J_{\rm ex} = 0$. (b-c) Dependence of the dynamics on t_b: Repopulated $|e\uparrow\rangle$-fraction after a short hold time $\tau = 0.44\,\tau^0_{\rm ex}$. (c) Asymmetric resonance shape for varying $V_\perp$ around the resonance. The resonance width depends on the coupling strength t_b into $|+_b\rangle$. Coherent oscillations from resonant coupling close to the resonance center are not shown for visual clarity.

side of the resonance, the exchange is dominated by the bare lowest-band coupling via the intermediate triplet state $|-\rangle$, and it approaches $J^0_{\rm ex} = \hbar/\tau^0_{\rm ex} \approx t_g^2/U^-$ [see Eq. (5.2)]. On the low-confinement side of the resonance, the contributions of the intermediate states $|+_b\rangle$ and $|-\rangle$ to the effective spin-exchange coupling cancel and lead to a zero in the exchange rate (dashed line, see discussion of low-energy model below).

In Fig. 5.10(b,c), the influence of the bound-state coupling strength t_b on the width of the resonance is illustrated. It shows the $|e\uparrow\rangle$ population after a short evolution time $\propto \tau^0_{\rm ex}$, matching the experimental hold time in Fig. 5.6. If the absence of coupling ($t_b = 0$, solid line), tuning of the perpendicular confinement induces only weak variations in the dynamics. In contrast, for finite $t_b > 0$, a resonance in the spin exchange occurs, caused by the intermediate state $|+_b\rangle$. The width of the resonance, determined by the distance between the $J_{\rm ex}$ resonance and the zero-crossing, becomes comparable to the one observed experimentally in Fig. 5.5(c) for $t_b \approx t_g$. Also, the asymmetry with a steep flank on the side of low $V_\perp$ is reproduced.

An effective low-energy model For our experimental confinement parameters, the lowest-band interaction parameters are large compared to the $|g\rangle$ mobility, that is $U^+ \gg U^- \gg t_g$. As shown above, this is true everywhere in the tight-binding regime for both interaction channels. Then, as long as the kinetic energy of the $|g\rangle$ atoms is limited to the lowest lattice band, it is reasonable to consider only virtual tunneling to the site of the localized magnetic moment. However, tunneling processes can become resonant around the crossings of CM-excited bound states with $E^{\rm os}_0$. The low-energy subspace around $E^{\rm os}_0$ is spanned by the last two basis states

$|c\rangle \equiv |e\uparrow\rangle_L|g\downarrow\rangle_R$ and $|o\rangle \equiv |e\downarrow\rangle_L|g\uparrow\rangle_R$ in the representation of the Hamiltonian in Eq. (5.6), and the projector into this sector is labeled $\mathbb{P}_0$.

In order to understand the low-energy physics in the presence of the bound-state coupling, we compare the numerical spectrum of H with a low-energy spin model, derived from a Schrieffer-Wolff transformation [196]. This transformation constructs an effective low-energy Hamiltonian on the order of $\mathcal{O}(t_g/U^{\pm})$, by eliminating the first order tunneling terms[7] in H, via

$$H_{\text{eff}} = \mathbb{P}_0\, e^{S}\,(H_{\text{int}} + H_{\text{t}})\, e^{-S}\,\mathbb{P}_0 \tag{5.7}$$

with the antihermitian $S = -S^{\dagger}$ obtained from

$$H_{\text{t}} = -[S, H_{\text{int}}]\,. \tag{5.8}$$

In an expansion up to second order in t_g, we obtain

$$H_{\text{eff}} = \mathbb{P}_0\,(H_{\text{int}} + [S, H_{\text{t}}]/2)\,\mathbb{P}_0 \tag{5.9}$$

which evaluates to

$$\begin{aligned} H_{\text{eff}} &= \begin{bmatrix} \alpha_{\uparrow\downarrow} & \alpha_{\pm} \\ \alpha_{\pm} & \alpha_{\uparrow\downarrow} \end{bmatrix} \quad \text{with} \\ \alpha_{\pm} &= \frac{t_g^2}{2U^{+}} + \frac{t_b^2}{2U_b^{+}} - \frac{t_g^2}{2U^{-}} \quad \text{and} \quad \alpha_{\uparrow\downarrow} = -\frac{t_g^2}{2U^{+}} - \frac{t_b^2}{2U_b^{+}} - \frac{t_g^2}{2U^{-}} \end{aligned} \tag{5.10}$$

in the basis $\{|o\rangle, |c\rangle\}$. Here, we have neglected the contribution of the far-detuned spin-triplet bound state energy U_b^{-}. The eigenenergies of the low-energy model H_{eff} are

$$E_s = -t_g^2/U^{+} - t_b/U_b^{+} \quad \text{and} \quad E_t = -t_g^2/U^{-} \tag{5.11}$$

associated to the off-site singlet and triplet states

$$\begin{aligned} |t_{\text{os}}\rangle &= (|e\uparrow\rangle_L|g\downarrow\rangle_R + |e\downarrow\rangle_L|g\uparrow\rangle_R)/\sqrt{2} \quad \text{and} \\ |s_{\text{os}}\rangle &= (|e\uparrow\rangle_L|g\downarrow\rangle_R - |e\downarrow\rangle_L|g\uparrow\rangle_R)/\sqrt{2}\,. \end{aligned} \tag{5.12}$$

In Fig. 5.11, we compare the full eigenspectrum of H (solid lines) around a bound-state resonance and the low-energy approximations $E_{s/t}$ (dashed) from the Schrieffer-Wolff transformation. Neglecting the coupling to the bound state ($t_b = 0$), the off-site triplet state $|t_{\text{os}}\rangle$ is energetically favored, with $E_t < E_s$ [compare blue dashed and red dotted lines in Fig. 5.11(b)]. This leads to FM order for all confinements and the low-energy approximation agrees with the diagonalization results. The color in the plot measures the overlap

$$\xi = |\,\langle\psi|t_{\text{os}}\rangle\,|^2 - |\,\langle\psi|s_{\text{os}}\rangle\,|^2$$

of the respective eigenstate with the off-site spin singlet ($\xi = -1$, red) and triplet ($\xi = 1$, blue).

[7] We consider the t_g and t_b to be of the same order.

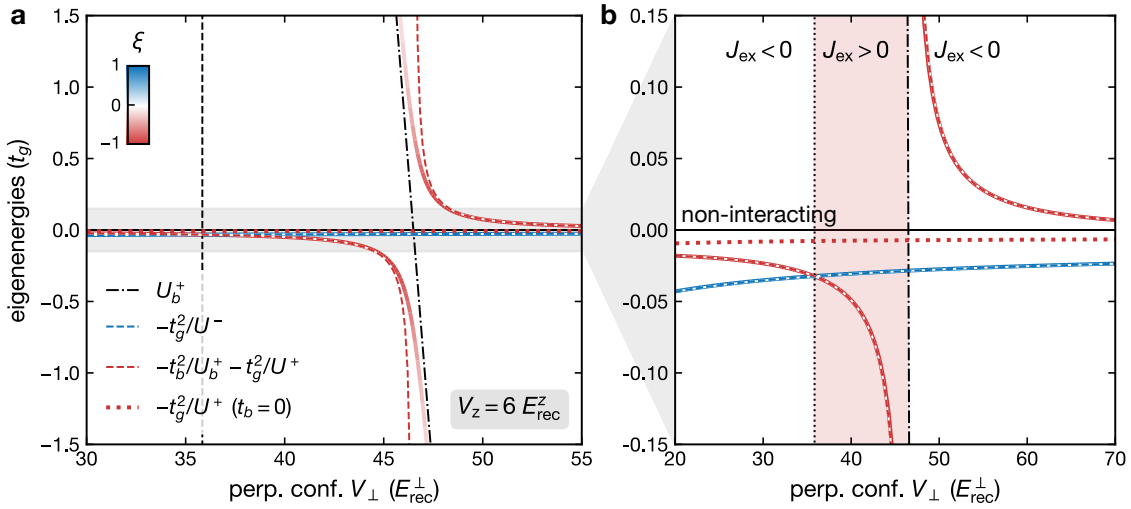

Figure 5.11 – Eigenenergies of the orbital state-dependent double-well model for varying perpendicular confinement around a resonance with a CM-excited singlet bound state $|+^{(2)}_b\rangle$ (dash-dotted); in units of $|g\rangle$ tunneling t_g and relative to the energy $E_0^{\rm os}$ of two particles on different sites: (a,b) Solid lines from numerical diagonalization for finite coupling $t_b = 0.7\,t_g$ to $|+^{(2)}_b\rangle$. The color measures the state overlap ξ with off-site spin singlet and triplet ($|s_{\rm os}\rangle$ and $|t_{\rm os}\rangle$). Dashed lines are the eigenenergies $E_{s/t}$ of the effective low-energy model for finite singlet bound state coupling t_b. Vanishing coupling $t_b = 0$ for comparison (dotted). On-site Hubbard parameters $U^\pm$ and U_b^+ are from the interacting h.o. model. (b) Low-energy part of the spectrum ($E \ll t_g$) characterizing an effective spin-model with coupling $J_{\rm ex}$. Ground state can be dominated by $|s_{\rm os}\rangle$ (red) or $|t_{\rm os}\rangle$ (blue), leading to a zero crossing of $J_{\rm ex}$ (dotted line) and another sign change around the resonance (dash-dotted).

The spin-singlet bound state energy U_b^+ crosses the energy zero at a certain confinement (dash-dotted line). Considering a finite coupling t_b opens an avoided crossing (red lines in Fig. 5.11) between this state and the bare off-site spin singlet energy $-t_g^2/U^+$. A resonant behavior of the spin-singlet energy emerges with its energetic width set by t_b. Close to the resonance, where E_s becomes of the order of $t_g \approx t_b, t_g$, the superexchange picture is increasingly invalid and the exact eigenstates gain a significant admixture of the on-site bound state $|+^{(2)}_b\rangle$ [Fig. 5.11(a)]. In contrast, for $E_s \ll t_g$, the low-energy result E_s provides an excellent approximation [Fig. 5.11(b)]. Note that due to the resonant behavior, a range of confinements $V_\perp$ emerges where the off-site spin singlet state $|s_{\rm os}\rangle$ is energetically favored which promotes AFM coupling.

Tunable Kondo coupling The Kondo impurity model is typically written in terms of a spin model with a coupling term between the localized magnetic moment and the spin of the mobile particles [4]. The effective low-energy Hamiltonian in Eq. (5.10) can be directly mapped to a spin coupling Hamiltonian

$$H_{\rm eff} = J_z\, S_z s_z + \frac{J_\perp}{2}(S_+ s_- + S_- s_+) + \text{const.} \tag{5.13}$$

expressed in terms of the spin operator $\mathbf{S} = (S_x, S_y, S_z)$ for the localized $|e\rangle$ atom, and $\mathbf{s} = (s_x, s_y, s_z)$ for the $|g\rangle$ atom on the neighboring site, respectively. We employ the standard definition of the spin rising and lowering operators $S_\pm = S_x \pm i S_y$ (and $s_\pm = s_x \pm i s_y$). The ratio of the longitudinal and perpendicular Kondo couplings J_z and $J_\perp$ determines the spin anisotropy of the model. The perpendicular coupling term induces spin flips between spins of opposite alignment and is directly related to the off diagonal elements $a_\pm$ in Eq. (5.10) via

$$J_\perp = 2a_\pm = \frac{t_g^2}{U^+} + \frac{t_b^2}{U_b^+} - \frac{t_g^2}{U^-}\,. \tag{5.14}$$

In contrast, the longitudinal term also couples neighboring spins of equal alignment. Thus, to recover the correct anisotropy of the Kondo model, we also need to include the spin-triplet states $|e\downarrow\rangle_L|g\downarrow\rangle_R$ and $|e\uparrow\rangle_L|g\uparrow\rangle_R$ into the basis set[8]. These are subject to the single-channel low-energy Hamiltonian $H_{\text{eff}} = \alpha_{\sigma\sigma} \equiv -t_g^2/U^-$. Note that $\langle S^z s_z\rangle = -1/4$ for the triplet states, and the spin-flip operators are non-zero for $\langle o|S^- s_+|c\rangle = \langle c|S^+ s_-|o\rangle = 1$. Overall, we arrive at a longitudinal coupling

$$J_z = 2(\alpha_{\sigma\sigma} - \alpha_{\uparrow\downarrow}) = J_\perp\,. \tag{5.15}$$

The SU(2) symmetry of the interactions is maintained and the Kondo coupling is fully isotropic with

$$H_{\text{eff}} = J_{\text{ex}}\,\mathbf{S}\cdot\mathbf{s} \quad \text{and} \quad J_{\text{ex}} \equiv J_z = J_\perp = E_t - E_s\,. \tag{5.16}$$

Away from the bound-state resonances, the total exchange coupling is FM ($J_{\text{ex}} < 0$). The tunability of J_{ex} is enabled by the competition of FM and AFM contributions. In Fig. 5.11, U_b^+ (and thereby E_s) is strongly dependent on the confinement and can change sign around the resonance. The ground state can then be dominated by $|s_{\text{os}}\rangle$ or $|t_{\text{os}}\rangle$, leading to a zero crossing of J_{ex} for $E_t = E_s$ and another sign change around the resonance.

5.4 Dissipative dynamics

Monitoring the overall atom count in the two electronic orbitals during a finite hold time in the SDL, it becomes clear that the spin exchange process is accompanied by atom loss on similar time scales. In particular, the enhanced spin-exchange rate on the resonance branches is reproduced in both the $|e\rangle$ and $|g\rangle$ loss rates. This is illustrated in Fig. 5.12(a,c), where we show the dynamics of the total $|e\rangle$ and $|g\rangle$ population associated to the measurement in Fig. 5.5. Clearly, both orbitals exhibit an overall atom loss which depends strongly on the external confinement. Loss rates are extracted from a linear fit to the initial dynamics and in Fig. 5.12(b,d) and we recover a resonance shape similar to the one for the spin-exchange rate in Fig. 5.5.

[8] These states were initially left out for simplicity, since they do not enter into the exchange dynamics starting from the $|e\downarrow\rangle_L|g\uparrow\rangle_R$ state.

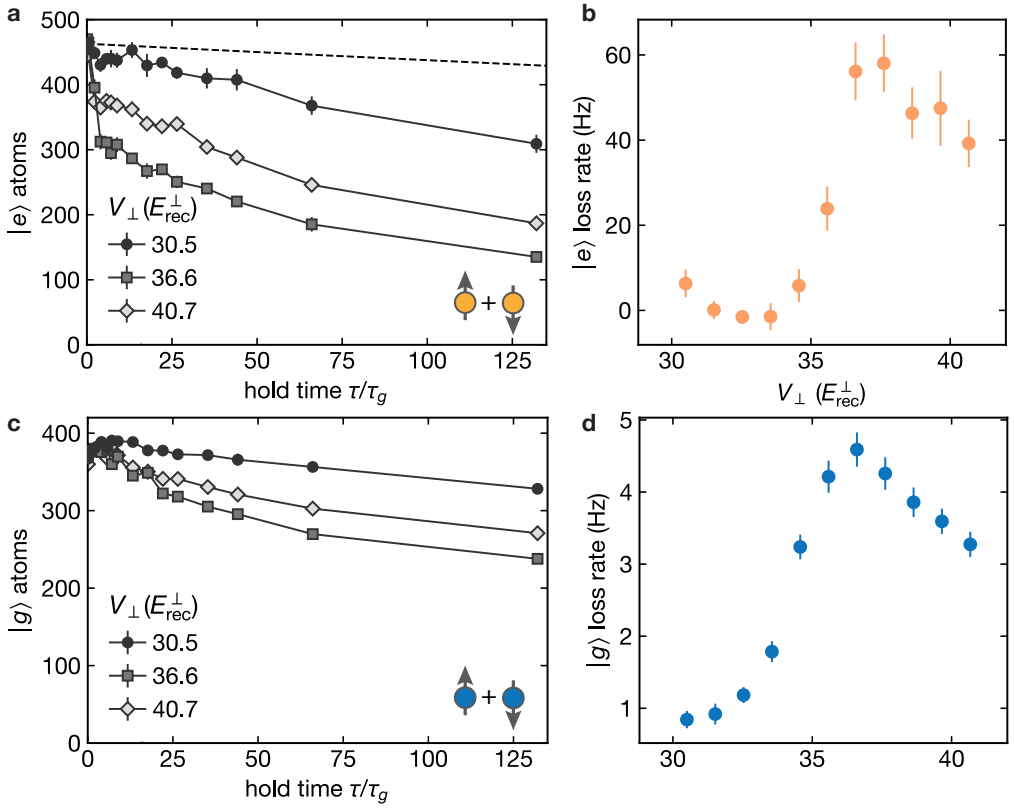

Figure 5.12 – Loss dynamics and dependence on the perpendicular confinement. (a,c) Total $|e\rangle$ ($|g\rangle$) population for varying hold time and perp. confinement. In (a), the lifetime of spin-polarized $|e\rangle$ atoms ($\tau_e = 2.0\,\mathrm{s}$, from an independent measurement in Section 2.6) is compared (dashed). (b) Loss rate of the $|e\rangle$ population normalized to the initial $|e\rangle$ atom count, from linear fit to the fast short-time dynamics (up to $\tau = 6\,\tau_g$). (d) Loss rate of the $|g\rangle$ population normalized to the initial $|g\rangle$ atom count, from linear fit to the dynamics up to $\tau = 100\,\tau_g$. Error bars indicate the 1σ uncertainties of the fits. All atom numbers from trap center region, as in Fig. 5.4. SDL depth is fixed to $V_z = 5.7\,E^z_{\mathrm{rec}}$.

The resonant structure of the loss feature implies that it is related to the coupling to CM-excited eg pairs. Then, three-body collisions with additional mobile particles could cause the relaxation of these shallow bound states into deeply bound molecular states, or to the deexcitation of the CM motion, inducing particle loss from the trap or rendering them dark for the imaging light [240, 247]. However, in contrast to what would be expected for a simple eg pair process, we observe that the $|e\rangle$ loss rate is significantly more pronounced than the $|g\rangle$ one. This indicates that the loss is not entirely caused by an $|e\rangle$-$|g\rangle$-symmetric process. We find that to be the case both on the resonances, where the short-time dynamics yields a maximum initial loss rate of 58 Hz for the $|e\rangle$-atoms and 5 Hz for the $|g\rangle$-atoms [Fig. 5.12(b,d)], as well for the off-resonant dynamics, where around 13% of the $|e\rangle$ atoms are lost after $50\,\tau_g$, compared to 7% of the $|g\rangle$ atoms [circles in Fig. 5.12(a,c)].

In the absence of interorbital collisions, the lifetime of $|e\rangle$ and $|g\rangle$ in the SDL has been characterized in Chapter 2 in independent measurements. For spin-polarized $|e\rangle$ samples, the lifetime in our experiment is limited by vacuum losses, repumping to $|g\rangle$ by the magic-

wavelength as well as state-dependent lattice light, as well as natural decay to $|g\rangle$. These single-particle processes limit the $|e\rangle$-lifetime on relatively long timescales compared to the spin-exchange rate: For the SDL confinement employed in the measurements above, we extract an overall 1/e-lifetime of $\tau_e = 2.0\,s$ (see Section 2.6). The corresponding decay dynamics are added in Fig. 5.12(a) for comparison. The bare $|g\rangle$ lifetime is even higher, with a vacuum lifetime of above 30 s in a deep 3D lattice setup.

Clearly, the observed loss cannot be explained by these single-particle processes and is dominated by collisional dynamics. Although $|e\uparrow\rangle$ is not present after the state preparation in the measurements presented here, the spin-exchange dynamics lead to its population and thereby enable an additional decay channel through $|e\downarrow\rangle$-$|e\uparrow\rangle$ collisions. In Section 2.7, we have studied the collisional loss dynamics of pure $|e\rangle$ samples for comparison: a balanced $|e\uparrow\rangle$-$|e\downarrow\rangle$-mixture with close to unit filling is held in the identical lattice configuration as used in Fig. 5.12 (black curve) ($V_z = 5.7\,E^z_{\mathrm{rec}}$, $V_\perp = 30.5\,E^\perp_{\mathrm{rec}}$). Although the $|e\rangle$ density has been higher in the $|e\uparrow\rangle$-$|e\downarrow\rangle$-mixture, the measured loss rate was in fact lower than in the eg mixture studied here[9]. A comparison of the two systems on a quantitative level is difficult, since the loss dynamics depend heavily on the density and correlations of the initial state [188].

Overall, several superexchange times remain observable before a significant fraction of the $|e\rangle$ atoms is lost through lossy ee and eg collisions. The loss is detrimental to the system stability very close to the resonances in the current lattice configurations. These areas of the confinement parameter space will probably need to be avoided for the implementation of closed many-body systems. In particular, the dissipative processes could have a strong influence on the long-time buildup dynamics of spin correlations, as studied for example in [30–32, 34, 202]. A full theoretical description would require including the loss explicitly in dissipative forms of the according Hubbard models. Furthermore, a microscopic understanding of the loss process itself could help to mitigate or avoid the issue.

Summary and outlook We have successfully engineered tunable magnetic exchange interactions between localized and mobile magnetic moments, utilizing ^{173}Yb in a state-dependent optical potential. The spin-exchange tunability mechanism relies on the confinement parameters controlled by optical potentials. This enables fast control and potentially the investigation of non-equilibrium spin dynamics [32, 33]. Our experiment has recently been upgraded to allow for controlled preparation of small $|e\rangle$ impurity fractions. This lays the groundwork for future studies of the Kondo-impurity model using AEA in optical lattices. Additional static and modulated Zeeman fields could be used to tune the anisotropy and strength of the Kondo coupling [34, 84]. Notably, the FM Kondo impurity model with easy-plane coupling ($|J_z| < |J_\perp|$) exhibits a strong renormalization group flow into the AFM strong coupling regime, leading to qualitative differences in the expected spin-relaxation dynamics [34].

[9] After 50 τ_g, only 5% of the $|e\rangle$-atoms are lost in Section 2.7, compared to 13% in the eg-mixture in Fig. 5.12.

CHAPTER 6

Mobility in hybridized lattice bands

The emergence of a heavy Fermi liquid phase is probably the most prominent consequence of the hybridization of mobile and localized lattice bands through strong anti-ferromagnetic spin-exchange interactions in the Kondo lattice model. Depending on the lattice filling and the hybridization strength, a modified effective band structure can lead to a strong mass enhancement for the itinerant electrons [4]. In the context of the KLM realized with ultracold AEA in a state-dependent optical potential [58], Foss-Feig et al. have performed a mean-field calculation predicting the hybridization of the $|g\rangle$ and $|e\rangle$ optical lattice band structure through the spin-exchange interactions [80, 81]. As an observable for the mass enhancement, they suggest probing the center-of-mass (COM) dipole oscillations induced by an external harmonic confinement.

In our setup, mobile ^{173}Yb atoms in $^1S_0$ ($|g\rangle$) can undergo spin-exchange interactions with localized $^3P_0$ ($|e\rangle$) magnetic moments in the presence of the 670 nm SDL. While this lays the groundwork for the realization of the KLM, we have not yet implemented a scheme for systematically realizing a unit-filled lattice of $|e\rangle$ atoms. Also, ^{173}Yb does not naturally feature an anti-ferromagnetic orbital spin-exchange coupling. Instead, to investigate the effect of band hybridization on the atomic mobility, we artificially induce a coupling between the $|g\rangle$ and $|e\rangle$ bands by means of adiabatic clock "light dressing". Although the coherent light coupling operates on the single particle level, the resulting band structure of the dressed states can be mapped to the quasi-particle band structure induced by the mean-field exchange coupling.

In the following, we will characterize the collective mobility in our SDL, starting with the bare ground-state mobility of fermionic ^{173}Yb and bosonic ^{174}Yb. Similar to observations in [258, 259], we find that for larger atom numbers and lattice depths, the low-energy dipole oscillations of fermionic gases are strongly suppressed by the Fermi pressure. The COM is then trapped in localized orbits of the combined lattice and harmonic oscillator potential. In order to demonstrate the effect of the optical band hybridization, we resort to BECs of ^{174}Yb, featuring a reduced spatial and momentum distribution and thereby a reduced energy dependence of the dipole oscillations.

6.1 Combined lattice and harmonic potential

Ground and excited-state atoms in the SDL do not only experience the periodic lattice potential but also an additional long-range harmonic confinement along the lattice direction ($\hat{z}$). The harmonic confinement is caused mainly by the perpendicular magic-wavelength lattice beams (L1 and L3) and is therefore state-independent, with a frequency ω_0 according to Eq. (2.3). The dynamics of non-interacting particles in a combined lattice and harmonic potential are fully described by the Hamiltonian in Eq. (2.4). Its numerical diagonalization is relatively straight-forward and gives access to to the full single-particle spectrum [260–262]. Also, analytical closed-form solutions have been obtained in the tight-binding approximation [263]. Even small harmonic potentials qualitatively change the spectrum and lead to the emergence of localized eigenstates for energies above the lowest bare lattice band.

We want to measure the COM oscillations of an atomic gas to probe the effective mass enhancement in our lattice setup. To this end, the COM is initially displaced from the harmonic oscillator minimum by a few lattice sites and then left to evolve. This problem has been studied in detail for non-interacting particles in a semiclassical approximation [259]: In the limit where the harmonic oscillator length is much larger than the lattice spacing a this approach is sufficient to describe collective in-trap dynamics. Considering only the lowest optical lattice band, the energy of a single particle is given by the sum of the quasimomentum q dependent dispersion relation $\epsilon(q)$ and the position-dependent harmonic oscillator (h.o.) energy:

$$H(q,z) = \epsilon(q) + \frac{1}{2}m\omega_0^2 z^2 \tag{6.1}$$

and the trapping frequency at an energy E can be evaluated to [259]

$$\omega(E) = \hbar\pi \left[\int_{z_i(E)}^{z_f(E)} \frac{\mathrm{d}z}{[\partial\epsilon(q)/\partial q]_{q=q(E,z)}} \right]^{-1}, \tag{6.2}$$

where $z_{i/f}(E)$ are the maximum and minimum positions reached in the trap for a given E.

For simplicity, let us consider the tight-binding regime with the lattice dispersion $\epsilon(q) = -2t\cos(qa)$ in Eq. (6.1). The resulting phase-space energy map is shown in Fig. 6.1(a). Clearly, two qualitatively different classes of isoenergetic orbits emerge, depending on the particle energy. Energies within the lowest lattice band width ($E/t < 4$) lead to "closed" orbits in phase space, whereas higher energies lead to "open" orbits which explore the entire Brillouin zone and are spatially localized. In the tight binding limit, Eq. (6.2) for the trapping frequency $\omega(E)$ can be evaluated in terms of elliptic integrals[1] and, as depicted in Fig. 6.1(b), it becomes energy-dependent. For small energies, it converges to the rescaled trapping frequency

$$\omega_0^* = \sqrt{\frac{m}{m^*}}\omega_0\,, \tag{6.3}$$

[1] Inserting the dispersion relation, Eq. (6.2) becomes $\omega(E) = \omega_0\sqrt{\frac{m}{m^*}}\pi\left[\int_{\tilde{z}_i(E)}^{\tilde{z}_f(E)} \frac{\mathrm{d}\tilde{z}}{\sqrt{1-(E/t-\tilde{z}^2)^2/4}}\right]^{-1}$ with $\tilde{z}_{i/f} = z_{i/f}\sqrt{m\omega_0^2/2t}$.

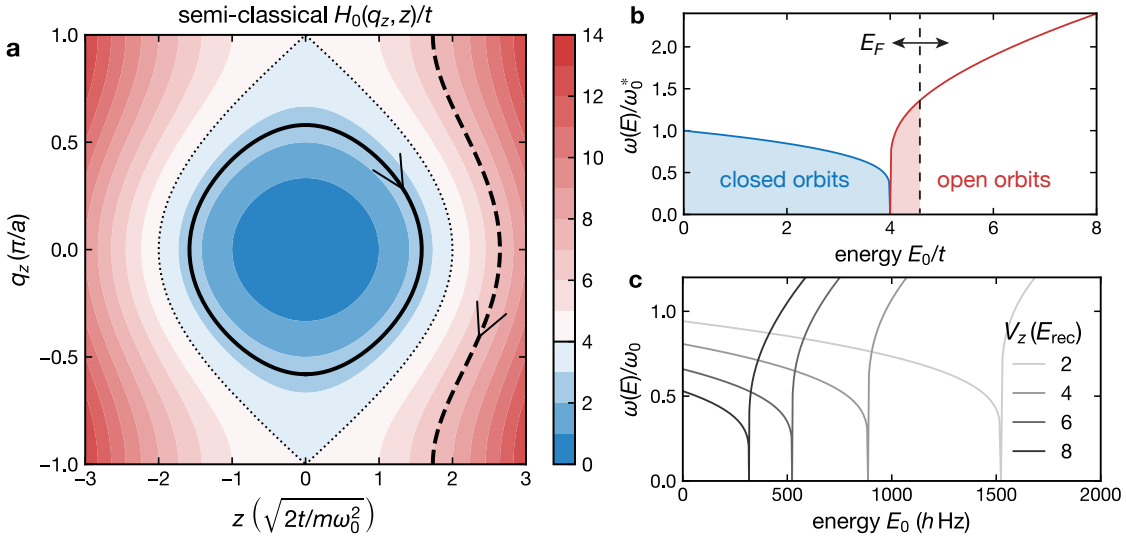

Figure 6.1 – (a) Semiclassical energy $H(q, z)$ in the phase space spanned by lattice quasimomentum q and spatial coordinate z along the lattice and an additional harmonic confinement. Dotted line indicates the upper edge $E = 4t$ of the lowest lattice band, separating closed (solid) and open (dashed) isoenergetic orbits. (b) Dispersion $\omega(E)$ of the oscillation frequencies in units of the low-energy frequency ω_0^* caused by the enhanced effective mass in the lattice. Large Fermi energies (E_F) can lead to the simultaneous population of closed (blue) and open (red) orbit states. (c) Dipole oscillation frequency in units of bare h.o. frequency ω_0 for typical experimental lattice depths V_z and energies.

slower than the bare harmonic oscillator frequency ω_0 due to the enhanced effective mass $m^* > m$ in the lattice potential[2].

In the presence of the harmonic confinement, finite energies lead to a reduction and a dispersion of the oscillation frequencies for the closed orbit states with $E/t < 4$. The open orbit states exhibit a much stronger dispersion and enhanced oscillation frequencies. This can lead to peculiar collective dynamics for multiple particles, when the mean energy associated with the excursion in the trap becomes comparable to the band width. In particular, Fermi gases quickly show insulating behavior because of the Fermi pressure [259]. For typical optical lattice setups, relatively small Fermi energies (low atom numbers) can be sufficient to create a band insulating state in the lowest lattice band. Figure 6.1(c) illustrates the dipole frequency dispersion for lattice depths used in our experiment. Fermi energies of only several 100 Hz can be enough to populate the localized orbits.

Regarding the collective COM dynamics exited by a displacement from the trap center, it is important to note that the semiclassical approximation includes the Pauli blocking as a conservation of the phase space volume. Thus, many of the low-energy closed orbits (with a trap frequency close to the effective lattice oscillation frequency ω_0^*) are fully populated and cannot exhibit conductive behavior. Because of the strong frequency dispersion, collective motion in multiple open orbits dephases faster than in closed ones and usually does not contribute to the

[2] In the tight-binding approximation, the effective mass actually scales inversely with the tunnel matrix element: $m^*(q = 0) = \hbar^2/(2a^2t)$. For weaker lattices, it can be obtained numerically from Eq. (2.6) (see Section 2.1.1).

collective oscillatory dynamics [259]. Instead, particles occupying the localized orbits cannot decay back to the trap center and lead to a long time offset of the COM after the excitation.

In contrast, a comparable number of bosons at degenerate temperatures occupies smaller phase space volumes and can be used as a more energy-selective probe of the trap mobility properties. Spin-mixtures of ^{173}Yb as well as ^{174}Yb in the electronic ground state exhibit weak s-wave scattering which has been found to preserve the conducting nature of both fermions [258] and bosons [264, 265] in low-energy orbits. Additionally, the interactions enable a decay mechanism for the localized eigenstates and a decay to the trap center on long time scales. However, increasing the interactions also leads to increased damping of the dipole oscillations.

6.2 Ground-state mobility measurements

Before using light coupling on the clock transition to hybridize the lattice bands of the SDL, we want to benchmark the mobility of the $|g\rangle$ atoms. The general experiment setup and the lattice geometry have been introduced in Chapter 3. By adiabatically loading from a crossed dipole trap, we prepare degenerate atomic samples in an array of state-independent quasi-1D tube-shaped systems. For the following measurements, the perpendicular confinement is produced by magic-wavelength lattices with a depth $V_\perp = 22\,E_{\mathrm{rec}}$ (geom. mean of $20\,E_{\mathrm{rec}}$ L1 and $25\,E_{\mathrm{rec}}$ L3). Along the tubes, a 670 nm orbital SDL is superimposed creating a lattice potential of variable depth $0 \leq V_g \leq 10\,E_{\mathrm{rec}}$ for $|g\rangle$ (see Fig. 6.2). The harmonic confinement along the SDL ($\hat{z}$) is mainly produced by transverse confinement of the Gaussian L1 and L3 lattice beams and we measure a bare dipole oscillation frequency of $\omega_0 = 2\pi \times 35\,\mathrm{Hz}$.

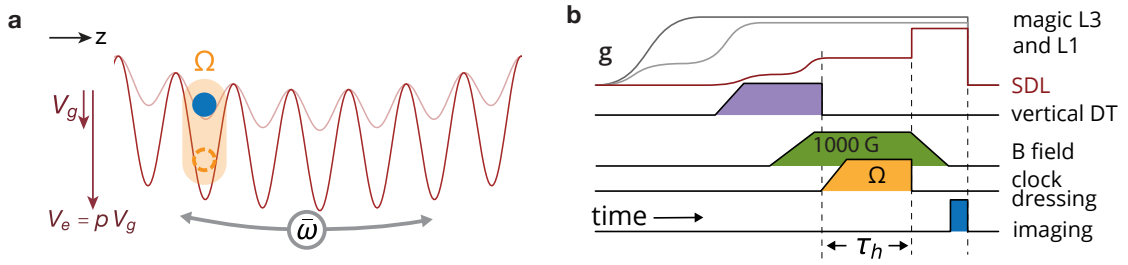

Figure 6.2 – (a) The shallow $|g\rangle$ and deep $|e\rangle$ potential (V_g and $V_e = p\,V_g$) produced by the 670 nm SDL are hybridized using adiabatic light coupling (Rabi coupling Ω) on the clock transition. The $|e\rangle$ potential is deeper by a factor $p \approx 3.3$ (see Chapter 2). The enhanced effective $|g\rangle$ mass is probed by measuring the COM dipole oscillation frequency $\bar{\omega}$. (b) Schematic of the experiment sequence to initiate COM oscillations in the bare or hybridized lattice bands. A misaligned optical dipole trap beam (vertical DT) is used to create the initial displacement from the trap center. For clock line "dressing", a strong magnetic field quenches the clock transition for the bosons and a slow up-ramp of the clock laser power ensures adiabatic coupling.

Figure 6.2(b) presents the scheme used to initiate and probe the COM motion. In order to excite a dipolar trap mode, we displace the atom cloud COM by around 2 μm (5 lattice sites) using a 1 W vertical 1064 nm dipole trap beam which is slightly misaligned from the trap center. The displacement is performed at only weak longitudinal lattice potential, such

that mobility along $\hat{z}$ is still enabled. We wish to keep the excursion in the trap as small as possible such that localized trap states are not populated. Compared to typical in-trap radii of fermionic and bosonic gases, and also considering our optical in-situ resolution of around $1.2\,\mu$m, this is a relatively small displacement. After the SDL is slowly ramped to its final depth, the displacement beam is suddenly shut off and the trap dipole mode is excited. After a variable hold time τ_h, the SDL depth is increased to its maximum in order to freeze the atoms for detection.

First, we study the oscillation dynamics of non-interacting spin-polarized fermions (^{173}Yb, $m_F = 5/2$) at different SDL depths and compare to a bosonic samples of comparable atom number ($\sim 0.4 \times 10^3$). The temperature of the spin-polarized ($m_F = 5/2$) Fermi gases before lattice loading is $T/T_F \approx 0.3$. The $1/e^2$ radius of the spin-polarized fermions in the lattice is approx. $16\,\mu$m whereas the bosons occupy a significantly smaller trap region ($10\,\mu$m).

Figure 6.3 shows the measurement results of the COM position $\langle z(t)\rangle$ with respect to the trap center for varying hold times. The dynamics of fermions (circles) for various SDL depths are compared to the bosonic case (squares). The lines are fits of an exponentially decaying oscillation $\langle z(t)\rangle = a\,\cos(\omega t)\,e^{-t/\tau} + c$, with frequency ω, amplitude a, a potential z-offset c and the damping or dephasing time τ. As expected from the discussion and Fig. 6.1(c) above, larger lattice depths lead to a reduced band width and, for a fixed number of fermions and initial displacement, an increasing population of higher-energy states. Two consequences for the collective COM dynamics arise: For deeper lattices, the collective oscillation frequency $\omega(E)$ is significantly decreased compared not only to the bare h.o. frequency ω_0, but also compared to ω^* given by the lattice effective mass [solid line in Fig. 6.3(b)]. Fitting the semiclassical theory for the oscillation frequency (Eq. (6.2)) to the measurement data in the tight-binding regime (dashed line) yields an average energy of $E = h \times 0.21\,$kHz, comparable to the tunnel matrix element for these lattice depths[3]. Moreover, as depicted in Fig. 6.3(c), the COM becomes increasingly localized at its initial displacement and the oscillation amplitude is reduced. On the probed time scales, only very small damping of the oscillations is observed for the higher lattice depths, due to dephasing of different orbits.

A qualitatively different behavior is found for the weakly interacting ^{174}Yb atoms, starting with the same initial displacement and atom number. The measurement data (squares) in Fig. 6.3(a) is for a lattice depth of $2\,E_{\mathrm{rec}}$ where the spin-polarized fermions are already strongly localized. Here, the bosons still show a conductive behavior with a trap frequency that is consistent with $\omega(E = 0) = \omega^*$ [Fig. 6.3(b)] and with symmetric oscillations around the trap center [Fig. 6.3(c)]. However, a significant damping rate ($\tau \approx 1.6/\omega = 50\,$ms) due to the interactions is measured compared to the spin-polarized fermions.

In addition to the variable SDL depth, we also analyze the dependence of the $|g\rangle$ oscillation dynamics on the total atom number in the trap. In this measurement, we compare the COM dynamics of a balanced fermionic two-spin mixture (^{173}Yb, $m_F \in \pm 5/2$) with bosonic ^{174}Yb, both weakly interacting. Figure 6.4(a-b) show the $|g\rangle$ COM oscillation dynamics in a longitudinal SDL with $V_z = 2\,E_{\mathrm{rec}}$. The same decaying cosinusoidal fit function is used as in

[3] A full numerical evaluation and integration of the dispersion relation in Eq. (6.2) would be required to extend the calculation of the oscillation frequencies to lower lattice depths.

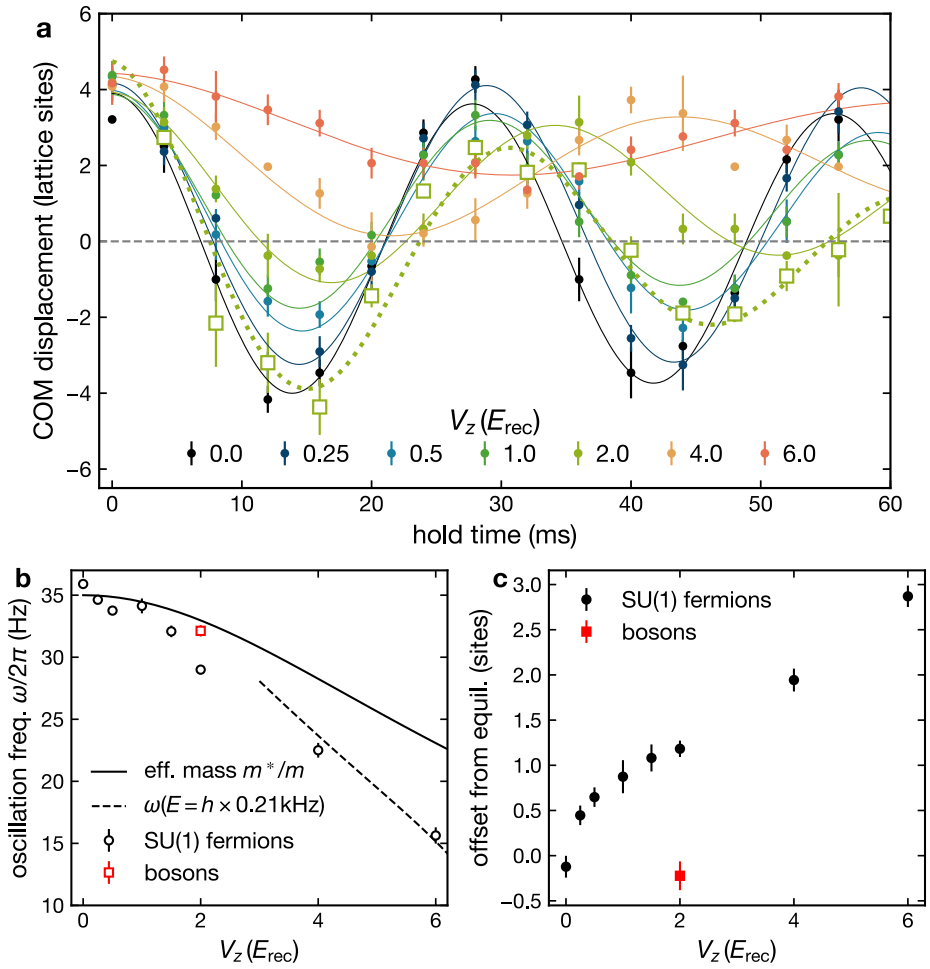

Figure 6.3 – Center-of-mass dipole oscillations $\langle z(t)\rangle$ of a spin-polarized Fermi gas (circles, solid lines) in the $|g\rangle$ band of the state-dependent lattice. Larger lattice depths V_z force more fermions into localized trap orbits. Bosonic dynamics (squares, dashed line) are shown for comparison. Lines are fits to the COM position dynamics (see main text). (b) Extracted oscillation frequency ω compared to ω^* from lattice-induced enhanced mass m^* (solid line). Energy-dependent $\omega(E)$ is from a fit of the semiclassical theory in the tight-binding limit. (c) Offset of the oscillation center from the trap equilibrium position, from fit in (a).

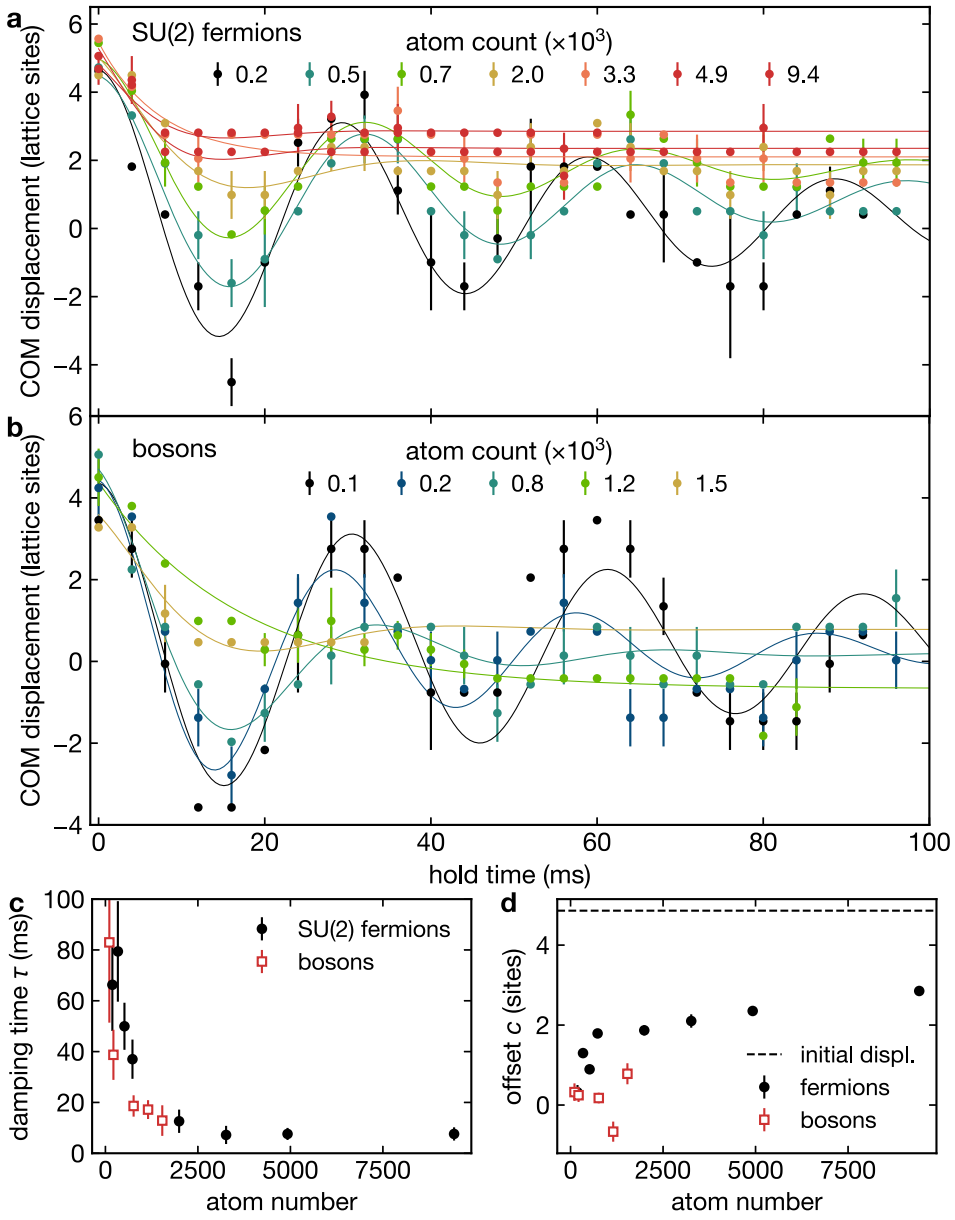

Figure 6.4 – (a) COM dipole oscillations $\langle z(t)\rangle$ of a balanced two-spin Fermi gas in the $|g\rangle$ band of the 2 E_{rec} deep SDL for various atom numbers. Lines are fits to the COM position dynamics (see main text). (b) Boson dynamics in the same trap for comparison. (c) Extracted oscillation damping time τ and (d) Offset of the oscillation center from the trap equilibrium position, from fits in (a,b).

the analysis of Fig. 6.3. Similar to [259], we find that for fermions, the effects of increased lattice depth and atom number are very similar, since they both change the ratio between band width and Fermi energy. The collective oscillation frequency decreases and the offset from the trap center increases with the atom number. Both fermions and bosons exhibit damping of the COM dynamics at large atom numbers. However, the damping time τ is significantly shorter in the bosonic case [see Fig. 6.4(c)] and no oscillations remain for atom numbers above 10^3. Interaction-driven relaxation to the trap center is also enhanced for the bosons at higher atom numbers [Fig. 6.4(d)].

Conclusions and remarks Overall, we have observed a strong energy dependence and reduced contrast of the fermionic COM oscillations already at intermediate lattice depths and small atom numbers. In the current trapping configuration, the insulating behavior induced by the trap makes them unfavorable as an observable for the heavy-fermion properties of the KLM: Atom numbers $>10^4$ would be necessary to produce a significant number of doubly occupied lattice sites in the SDL, a requirement for the realization of the KLM. Also, at the eg-polarizability of $p = 3.3$ for the 670 nm SDL, lattice depths $V_g \gtrsim 5\,E_{\mathrm{rec}}$ are needed to produce $|e\rangle$ lattice bands that are flat compared to the $|g\rangle$ band width ($t_g/t_e < 10$, see Fig. 2.8). Increasing p and lowering the lattice potential would allow us to maintain the $|e\rangle$ localization while increasing the $|g\rangle$ band width. This would decrease the relative influence of the h.o. confinement. Alternatively, one could think of lowering ω_0 directly by employing additional blue detuned dipole potentials to compensate the harmonic confinement of the perpendicular (L1 and L3) lattice beams.

6.3 Optical hybridization of lattice orbitals

The heavy-fermion properties of the KLM in higher dimensions can be explained by means of a mean-field decoupling of the spin-exchange interactions [206]. For our experiment, best described by an array of 1D systems, the mean-field treatment does not describe Luttinger liquid properties of the gas. However, it is supposed to still capture the interaction-induced mass enhancement in the paramagnetic part of the phase diagram [81]. The exchange interaction term of the KLM Hamiltonian Eq. (2.49) is then replaced by the single-particle operator:

$$V_{\mathrm{ex}} \sum_{i,\sigma,\sigma'} c^\dagger_{ig\sigma} c^\dagger_{ie\sigma'} c_{ig\sigma'} c_{ie\sigma} \rightarrow V_{\mathrm{ex}} \sum_{i,\sigma} \tilde{V}_i (c^\dagger_{ig\sigma} c_{ie\sigma} + \mathrm{h.c.}) + \mathrm{const.} \tag{6.4}$$

where $\tilde{V}_i$ is the mean-field on-site hybridization (for details, see [81]). In the translationally invariant case, the lowest-energy states are defined by the quasi-particle spectrum [80]

$$\varepsilon_\pm(q) = \frac{\epsilon_g(q) + \mu_e}{2} \pm \sqrt{V_{\mathrm{ex}}^2 \tilde{V}^2 + [\epsilon_g(q) - \mu_e]^2/4} \tag{6.5}$$

with the $|g\rangle$ dispersion $\epsilon_g(q)$ and a chemical potential μ_e fixing the unit filling of a lattice of localized $|e\rangle$ atoms. Effectively, the exchange interaction leads to a hybridization of the bare

lattice bands with a gap $2V_{\mathrm{ex}}^2\tilde{V}$ around the quasimomenta given by $\epsilon_g(q)=\mu_e$, which is illustrated in Fig. 6.5. The filling n_g of the $|g\rangle$ band (solid thick line) self-consistently determines the $|e\rangle$ chemical potential μ_e. For $n_g=1$ (where $\mu_e=0$), the Kondo insulator phase emerges, where the lower hybridized band ε_- is fully filled and separated from the upper band by a gap Δ_H. For slightly lower fillings, $n_g<1$ (where $\mu_e<0$), the conductive states at the Fermi surface probe the high-q range of ε_- where the dispersion relation is flattened, and the bare lattice effective mass m^* is enhanced by the hybridization to a value $\overline{m}>m^*$.

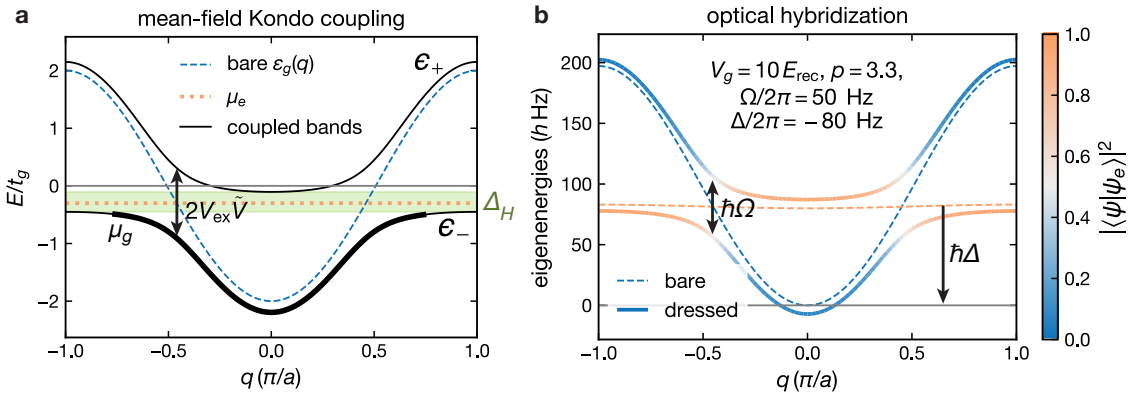

Figure 6.5 – (a) Quasi-particle spectrum of mean-field solution to KLM in the weak-coupling regime. The exchange coupling V_{ex} hybridizes the bare $|g\rangle$ (dashed) and $|e\rangle$ (dotted) dispersion relations in the SDL, opening an energy gap Δ_H (green fill) between the coupled bands $\varepsilon_\pm$ (solid). V_{ex} and $|g\rangle$-filling $n_g\leq 1$ define the $|e\rangle$ chemical potential $\mu_e\leq 0$ (dotted) for $n_e=1$. Bold line indicates a filling $n_g<1$ with strong mass enhancement at the Fermi surface. (b) Optical band hybridization via adiabatic coupling to the clock transition in the SDL. Trap and coupling (Rabi frequency Ω) are selected such that the dressed states (solid) reproduce the KLM band structure in (a). The light detuning Δ moves the bare state energies ($\Omega=0$, dashed) relatively. The color indicates the bare state admixture of the dressed states.

Optical hybridization Comparing the mean-field exchange coupling in Eq. (6.4) with the coherent two-level atom-light coupling Hamiltonian in Eq. (1.36), one finds that both carry the same mathematical structure and cause a single-particle coupling of the two electronic orbitals. The $|g\rangle$ and $|e\rangle$ band hybridization via the clock transition has first been proposed in the context of a subwavelength lattice realization for quantum information schemes with AEA [179]. Because of the perpendicular alignment of the clock laser and SDL in our setup, the quasimomentum q along the SDL is preserved. Furthermore, the use of π-polarized light ensures the coupling between identical m_F only. Then, the atom-light coupling Hamiltonian takes the form

$$H_{\mathrm{al}}(q)=\hbar\begin{bmatrix}\epsilon_g(q) & \Omega_0/2\\ \Omega_0/2 & \epsilon_e(q)-\Delta\end{bmatrix} \tag{6.6}$$

with the eigenvalues (the dressed state energies)

$$\varepsilon_\pm(q)=\frac{\epsilon_g(q)+\epsilon_e(q)-\hbar\Delta}{2}\pm\frac{1}{2}\sqrt{\Omega_0^2+[\epsilon_g(q)-\epsilon_e(q)+\hbar\Delta]^2}\,. \tag{6.7}$$

Compared to Eq. (1.36), we have inserted the dispersion relation for the ground and excited state atoms in the SDL, which are not flat compared to Rabi coupling and detuning. Ω_0 is the bare Rabi coupling and Δ the detuning from the $q = 0 \rightarrow q' = 0$ resonance. Now, for weak SDL depth and $\hbar\Omega < 4t_g$, the atom-light coupling becomes quasimomentum dependent, like the band hybridization in the Kondo coupling scenario.

Considering the case of flat $|e\rangle$ dispersion[4] $\epsilon_e = 0$, the optically dressed states can be mapped to the quasi-particle energies $\varepsilon_\pm$ in Eq. (6.5) under the replacements:

$$\begin{aligned} 2V_{\mathrm{ex}}\tilde{V} &\rightarrow \hbar\Omega_0 \\ \mu_e &\rightarrow -\hbar\Delta\,. \end{aligned} \tag{6.8}$$

The mapping is illustrated in Fig. 6.5(b) for lattice and clock light parameters that can be achieved in our experiment. In this example, we have chosen values of the Rabi coupling smaller than the $|g\rangle$ band width. This realizes the weak-coupling limit of the KLM ($-2V_{\mathrm{ex}}/t_g \ll 1$) which should feature strongly enhanced effective masses for Fermi energies around the gap opening. There, the dressed states feature a large admixture of the localized $|e\rangle$ bare state. Note that in contrast to the KLM, the position of the hybridization gap can be adjusted via the light detuning, independent of the $|g\rangle$ filling.

Probing the hybridized band structure In order to access the heavy-fermion mobility in the weak-coupling limit of the KLM via the collective dipole oscillation dynamics, as proposed in [81], $|g\rangle$ band fillings close to the hybridization gap need to be prepared. For the finite experimental eg polarizability ratio of the SDL, we require Rabi frequencies larger than the $|e\rangle$ band width such that an energy gap develops for all q. At the same time, the coupling strength needs to stay below the $|g\rangle$ band width such that the band hybridization remains momentum-dependent and leads to a strong mass enhancement. This can in principle be achieved by choosing relatively large SDL depth at a fixed p, as in Fig. 6.5(b) (with $V_g = 10\,E_{\mathrm{rec}}$ and $4t_e \ll \hbar\Omega_0 \ll 4t_g$). However, as has been discussed in the previous section, the ratio between $|g\rangle$ band width and harmonic confinement then becomes relatively small and already the non-interacting collective dynamics become strongly energy dependent. For probing the weak coupling regime, larger p and smaller harmonic confinement would therefore be favorable.

The limit of large coupling strength ($-2V_{\mathrm{ex}}/t_g \gg 1$) of the KLM is typically not realized in solid-state materials [4]. Yet, it could be accessed in optical lattice experiments with AEA where the natural orbital exchange interaction or the optically induced orbital hybridization can take large values compared to the band width. In this limit, the mean-field on-site hybridization saturates to $\tilde{V}_i = 1$ and the hybridization gap scales as $\Delta_H = 2|V_{\mathrm{ex}}|$ [80], or Ω_0 in the light coupling case. As can be seen from Eq. (6.7), the hybridized band dispersions $\varepsilon_\pm$ become equal and take on the average value of the bare lattice bands for every q. In the tight binding regime, both bands remain cosinusoidal, each with a reduced band width of $2t_e + 2t_g$. For a fully flat $|e\rangle$ band ($t_e = 0$, $V_e \rightarrow \infty$), the mass enhancement becomes maximal with $\overline{m}/m^* = 2$ (see Fig. 6.6). In the infinite exchange interaction limit, the KLM can actually be mapped to an infinite-U Hubbard model [266] and one arrives at a picture where the

[4] which is justified for lattice depths $V_g \gtrsim 5\,E_{\mathrm{rec}}$, at p=3.3 .

eg singlets are described by non-interacting spin-less fermions in an effective band of width $2t_g$ [81]. Obviously, the maximum possible mass enhancement is strongly reduced compared to the weak-coupling regime, however at the benefit of increasing the gap size between the bands and thereby reducing the temperature requirements for the stability of the HFL phase [81].

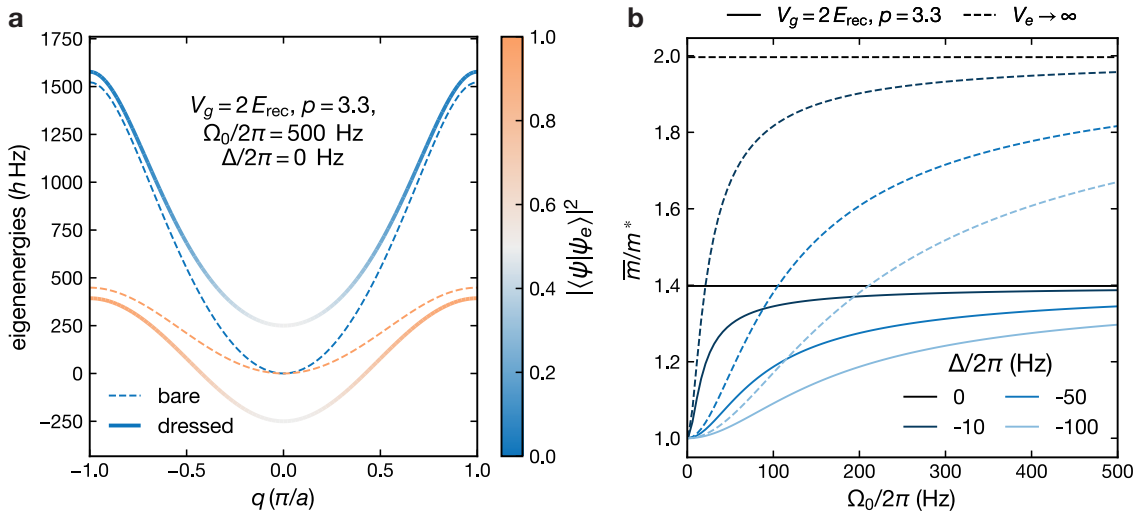

Figure 6.6 – (a) Strong optical band hybridization via in a shallow SDL with finite $|e\rangle$ band width. Rabi frequency Ω and detuning $\Delta = 0$ generate dressed states (solid) analogous to the intermediate-coupling KLM. Bare states ($\Omega = 0$, dashed) for comparison. The color indicates the bare state admixture of the dressed states. (b) Hybridization-induced enhancement of the lattice effective mass m^* to $\overline{m} > m^*$ at $q = 0$ for the experimental parameters (solid lines) and for a flat $|e\rangle$ band (dashed).

Experimentally, the strong-coupling regime is easier to probe in our current SDL configuration because of the reduced quasimomentum sensitivity and the increased gap size. As a proof-of-principle experiment for the optical band hybridization and enhanced mass, we excite a COM dipole mode of a degenerate gas of ^{174}Yb bosons in the harmonic confinement. The state preparation and detection is as described in the section above and in Fig. 6.2. In contrast to the measurement of the collective dynamics in the bare lattice bands, we now induce an optical coupling on the clock transition during the hold time in the lattice. A finite dipole coupling to the bosonic isotope is enabled through magnetic quenching of the transition at a large magnetic field of $B = 1000\,\mathrm{G}$ (see Section 1.4). The measured Rabi coupling at the given clock laser power of 2.7 mW is $\Omega = 2\pi \times 0.50\,\mathrm{kHz}$. Starting with the displaced $|g\rangle$ atoms in the final $2\,E_{\mathrm{rec}}$ SDL configuration, the light coupling is ramped on adiabatically within 4 ms, and the atoms are transferred into the dressed states. After the variable hold time, the SDL is quenched to its maximum depth and the magnetic field is reduced to zero (within 10 ms) before the $|g\rangle$ imaging pulse.

The expected hybridized band structure under the measurement conditions is shown in Fig. 6.6(a). At the given SDL depth, both bare orbitals exhibit a finite band width. The detuning is chosen resonant to the $q = 0 \to q' = 0$ transition since the low atom number sample of bosons (0.4×10^3 atoms, as in Fig. 6.3) is expected to mainly populate the bottom of the

lowest band. The clock laser intensity is not large enough to fully hybridize both lattice bands. Yet, every finite Rabi coupling $\Omega > 0$ leads to a full hybridization of the bands exactly at $q = 0$. The higher Ω, the larger the range of detunings where the bands are still hybridized. This is illustrated in Fig. 6.6(b), where the effective mass enhancement at $q = 0$ is calculated for various detunings and coupling strengths. For our SDL polarizability ratio $p = 3.3$, the maximum expected mass enhancement for resonant coupling is $\bar{m}/m^* = 1.40$. In comparison, a small detuning of 100 Hz would result in $\bar{m}/m^* = 1.30$ for the given Ω. Considering finite detunings can be relevant not only because of the finite quasimomentum distribution in the lattice, but also because of spatially inhomogeneous light shifts induced by the SDL (see Section 3.5.2).

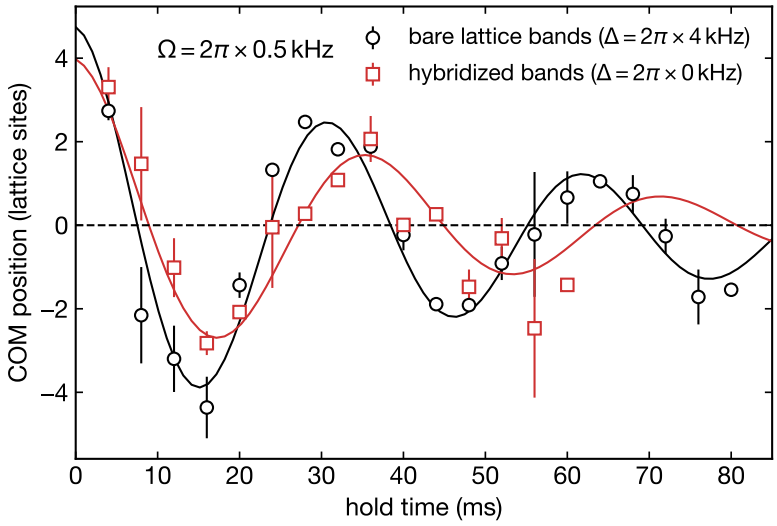

Figure 6.7 – COM dipole oscillation in the optically hybridized band structure of a 2 E_{rec} deep SDL (squares) compared to the dynamics in the uncoupled, bare lattice bands (circles, off-resonant light). Optical coupling with Rabi frequency $\Omega = 2\pi \times 0.5$ kHz at 1000 G magnetic field and detuning relative to the $q = 0 \rightarrow q' = 0$ transition; 0.4×10^3 ^{174}Yb atoms. Lines are fits to the COM position dynamics (see main text).

Figure 6.7 shows the measurement results of the COM dynamics around the trap center, comparing dipole oscillations in the bare $|g\rangle$ band and the optically hybridized bands. Both data sets have been obtained using the identical experimental sequence, except for a strong light detuning $\Delta = 2\pi \times 4$ kHz for the bare lattice case, which effectively removes the atom-light coupling. The extracted oscillation frequencies are $\omega^* = 2\pi \times 32.1(5)$ and $\overline{\omega} = 2\pi \times 27.7(10)$. This corresponds to an effective mass enhancement of $\bar{m}/m^* = (\omega^*/\overline{\omega})^2 = 1.34(10)$, consistent with the resonant hybridization scenario calculated above.

We have demonstrated that the clock transition can be used to create an artificial interorbital coupling which influences the mobility in the SDL, analogous to the Kondo coupling in the KLM leading to heavy fermion properties. The mobility in a strong coupling regime has been probed using collective dipole oscillation dynamics in the harmonic potential of the trap. In order to probe the weak-coupling regime of the KLM via collective dynamics, an enhanced eg polarizability ratio of the SDL would be required. That would allow us to maintain full $|e\rangle$ localization while increasing the $|g\rangle$ mobility relative to the harmonic oscillator strength, and

thereby prevent the occupation of localized orbits of the trapping potential. These observations concerning the probing of heavy fermion properties can be carried over to the scenario of interaction-induced Kondo coupling.

We note that the coherent light coupling between the orbitals could also be used to engineer the momentum-dependent, single-particle *s*-*d* band coupling term of the periodic Anderson model [2]. In particular, for weak optical coupling compared to the *ee* interaction strength, the limit of strong Coulomb repulsion could be realized, hosting localized magnetic states. Combining the optical band hybridization with the natural interorbital exchange coupling could allow for the realization of a Kondo model with tunable anisotropy [82].

Conclusions and outlook

In this thesis, we have presented our implementation of a two-orbital optical lattice system for ytterbium quantum gases, featuring tunable spin-exchange coupling between localized and itinerant magnetic moments. Precise optical control over the orbital and spin degree of freedom has been demonstrated in the context of state preparation and detection, turning our setup into a promising platform for the investigation of interesting many-body Hamiltonians with spin-orbital interactions. This includes the Kondo impurity and Kondo lattice model, and their potential SU(N)-symmetric generalizations.

The electronic ground state $^1S_0$ and the metastable excited clock state $^3P_0$ are employed as an orbital degree of freedom ($|g\rangle$, $|e\rangle$). The implementation of the state-dependent lattice (SDL) relies on the different dynamic polarizabilities of the electronic states, tunable with the lattice wavelength. Atoms in the metastable clock state experience a deeper lattice by a factor of 3.3(2) for the employed laser wavelength of 670 nm. The lattice potential is largely independent of the nuclear spin and should thereby preserve the SU(N) symmetry of both the intra- and interorbital interactions. We have characterized the orbital state-dependent mobility both indirectly, by spectroscopically probing the differential shift of the clock transition, and directly, by probing the band structure and collective oscillatory dynamics. Due to their similar electronic structure, our SDL implementation can be generalized to other alkaline-earth(-like) atom systems, considering a suitable choice of lattice wavelength.

We have monitored experimentally the magnetization dynamics between mobile and localized magnetic moments after a quench of the spin-exchange interactions. Starting with a unit-filled lattice of two polarized spin populations in different lattice orbitals, spin equilibration between the orbitals has been observed on a time scale of several tunneling times. We have found that the process is compatible with an effective Kondo-type exchange coupling arising from the state-dependent mobility and the interorbital on-site interactions of fermionic AEA. In our superexchange model, the overall exchange coupling emerges from a competition of the spin-singlet and triplet scattering intermediate states. Similar to the direct interorbital spin exchange observed in Ref. [59–61], its finite strength is caused by a difference in the spin-singlet and triplet scattering potentials. In particular, the exceptionally large s-wave scattering length of ^{173}Yb in the spin-singlet channel leads to the appearance of additional shallow on-site bound states which can participate in the exchange process. Their presence has been verified spectroscopically in an independent measurement and qualitative agreement is found with an on-site model for two interorbital interaction channels.

In the vicinity of resonances with these bound states, we have observed wide tunability of the spin-exchange rate with the lattice confinement. Within the framework of our model, the resulting exchange coupling can switch sign and could thereby give access to both ferro- and

antiferromagnetic Kondo models. The Kondo temperature, the critical temperature for the observation of Kondo singlet screening, is typically small compared to the band width. However, it increases exponentially with the exchange coupling strength, and near the resonances with the singlet bound states, it could be brought into an experimentally accessible range [84, 178].

Our novel tuning mechanism as well as previously proposed schemes [58, 82, 267–269] rely on optical potentials for rapidly modifying the exchange coupling. This is advantageous for the investigation of non-equilibrium spin dynamics, e.g., the formation dynamics of the Kondo singlet screening cloud or the development of magnetic correlations [32–34, 270]. Along with the enhanced spin exchange, resonant atom loss features have been detected. The loss was found to be asymmetric in the population of the two lattice orbitals. Its microscopic origin is still unclear and merits further study. Confinement parameters very close to the resonances are clearly detrimental and to be avoided for the implementation of closed many-body systems. However, motivated by our work, recent theoretical efforts incorporate the dissipative dynamics in a non-Hermitian model for the Kondo effect, predicting a phase transition between a regime of RG flow reversal and diverging imaginary Kondo coupling [83].

Heavy-fermion properties originating from the band hybridization in a Kondo lattice should manifest themselves in an enhanced effective mass [80, 81]. In a proof-of-principles experiment, we have induced a strong interorbital hybridization through adiabatic resonant light coupling to the clock transition. The expected mass enhancement has been detected through a reduced center-of-mass dipole oscillation frequency in a combined lattice and weak harmonic oscillator potential. Large atom numbers and a significant energy dependence of the dipole oscillation frequency results in a weak contrast of the collective observable. This could be mitigated by increasing the relative trap ratio for the two orbitals, e.g., by varying the lattice wavelength, which would maintain the $|e\rangle$ localization while increasing the $|g\rangle$ lattice bandwidth relative to the harmonic confinement.

Outlook

The density of the localized magnetic moments in the SDL has not been varied systematically in this work. Recent technical upgrades to our experiment allow for the controlled preparation of impurity fractions. This should give access to fundamentally different orbital many-body models and phenomena at low enough temperatures. While a unit-filled lattice of localized moments is required for the realization of the KLM, low filling fractions compared to the correlation length scales would emulate the Kondo impurity model [34, 58].

The presence of spin screening or ferromagnetic Kondo behavior in the impurity model could be detected by probing the impurity magnetization and dynamical spin susceptibility [34]. Moreover, quantum gas microscopy techniques have recently been developed for ytterbium [271, 272]. Single-site resolution and manipulation could lead to the direct in-situ observation of spin and charge correlations and their non-equilibrium dynamics [34], as well as the study of transport properties [273].

In the context of the Kondo impurity models, our confinement induced tuning mechanism could be used to vary the strength, and potentially the sign of the exchange coupling strength.

Further experimental techniques have been envisaged which are able to produce arbitrary anisotropies of the Kondo coupling. They employ direct optical coupling of the clock states or Floquet engineering of the Kondo coupling through time-dependent Zeeman shifts [34, 82]. Instead of the commonly studied antiferromagnetic Kondo model one could access the ferromagnetic coupling regime with easy-plane anisotropy, where a non-trivial renormalization group flow is predicted, leading to Kondo screening of the impurities [34]. Furthermore, in the easy-axis regime, quantum corrections to the Korringa law are expected, causing a non-linear power-law dependence of the spin-relaxation rate on temperature [201].

A clean and controllable realization of the Kondo lattice with AEA could help to improve our understanding of strongly correlated orbital physics, governed by the interplay of spin screening and magnetic ordering. The presented SDL setup, consisting of an array of one-dimensional lattices, has the potential to directly emulate the one-dimensional KLM, and is straight-forward to extend to higher dimensions. This is particularly intriguing, since until now, its phase diagram for dimensions larger than one is only known on the mean-field level or numerically in very limited system sizes [14, 203]. Ignoring possible tuning mechanisms, the natural exchange coupling of ^{173}Yb is strong and ferromagnetic. The emerging triplet correlations in the corresponding ferromagnetic KLM can lead to colossal magnetoresistive behavior [20, 21] which could be observed by probing the dynamics of spin-charge excitations in quench experiments [219].

Fermionic AEA with large nuclear spin like ^{173}Yb ($I = 5/2$) or ^{87}Sr ($I = 9/2$) allow us to work with more than two nuclear spin components, and thereby, to directly implement the Coqblin-Schrieffer model, the SU($N = 2I+1$) symmetric analog of the KLM [4, 58, 220, 221]. An exponential increase of the Kondo temperature with N is expected [4, 221], which has been previously investigated in heavy fermion systems [222] and carbon nanotube quantum dot systems [223]. Independently, the enlarged spin degeneracy should be helpful in achieving lower temperatures in the SDL after the adiabatic loading process from the crossed dipole trap [66]. Especially, the rapid scaling of the per-particle entropy with N in 1D lattice systems should allow us to reach temperatures on the superexchange energy scale [66, 151, 152, 154].

Just recently, the interorbital scattering properties of fermionic ^{171}Yb have been characterized and an antiferromagnetic exchange interaction has been extracted [88, 158]. Combined with its near-vanishing ground-state scattering length, this makes it a very promising candidate for the simulation of antiferromagnetic Kondo models. In this regard, upgrades to the atom loading stage of our experiment have now been performed which enable us to cool mixtures of isotopes and produce degenerate samples of ^{171}Yb [158].

Another wide range of non-trivial many-body systems becomes accessible when considering finite mass imbalance instead of fully localized lattice orbitals. Our SDL implementation can easily be tuned to increase the mobility of the ^{3}P$_0$ atoms by employing smaller lattice depths or larger wavelengths. Kondo impurities then transform into heavy “Kondo polarons” described by a two-channel Kondo model where the collisional recoil can suppress low-energy spin-exchange, offsetting the onset of singlet screening to higher coupling strengths [274]. Combining the orbital state-dependent mobility with the recently observed orbital Feshbach resonance in ^{173}Yb [89–91] opens the route towards strongly interacting systems with tunable

mass ratio. A rich phase diagram emerges for polaronic systems, featuring ground states that consist of trimers or FFLO-like, finite-momentum pairs [275].

In the absence of spin-exchanging interactions, the famous Anderson orthogonality catastrophe could be accessed [276]. This quantum decoherence phenomenon was first observed as a singularity in x-ray core hole spectroscopy of metals [277]. The diluteness of ultracold atomic gases compared to solid-state systems can be compensated by strong interactions in the vicinity of a Feshbach resonance. Signatures of the orthogonality catastrophe could be detected in the single-particle dephasing properties of the localized impurities, namely the non-exponential decay of their spectral function [278, 279].

In conclusion, we have demonstrated our experimental realization of an orbital state-dependent lattice, featuring extensive experimental tunability of the mobility as well as the interorbital interactions and exchange coupling. The independent and precise control over charge, spin and orbital degrees of freedoms lays a solid foundation and offers new possibilities for the exploration of strongly correlated, orbital many-body systems.

APPENDIX A

Hyperfine and Zeeman coupling in two-electron systems

Hyperfine dipole and quadrupole coefficients The dipole and quadrupole coupling constants A and B can be determined spectroscopically or by numerical CI+MBPT methods [280]. A collection of known values for experimentally relevant states in ^{173}Yb and ^{171}Yb is provided in Table A.1.

Table A.1 – Dipole and quadrupole coupling constants A and B as defined in Eq. (1.12) for low-lying $J > 0$ states in ^{173}Yb and ^{171}Yb (from [a][281], [b][103], [c][282], [d][283]).

	^{173}Yb		^{171}Yb
state	A (MHz)	B (MHz)	A (MHz)
$(6s6p)^1P_1$	57.682(29)[a]	609.065(98)[a]	−214.173(53)[a]
$(6s6p)^3P_1$	−1094.328(19)[b]	−826.635(67)[b]	3957.781(63)[b]
$(6s6p)^3P_2$	−742.71[c]	1342.3[c]	2672.27[c]
$(6s7s)^3S_1$	−1892[c]	−0.2[c]	6847.7[c]
$(6s5d)^3D_1$	562.8(5)[d]	337(2)[d]	−2040(2)[d]

Breit-Wills theory for the hyperfine cross coupling The dipole cross-coupling constants α_0, β_0, and the quadrupole coupling γ_0 of the clock state $^3P_0$ with $^3P_1$, $^1P_1$ and $^3P_2$, introduced in Section 1.2, are defined as the non-zero off-diagonal entries of the hyperfine coupling Hamiltonian H_{HFS} normalized to the respective transition frequencies ν, as in [111]:

$$\begin{aligned}
\alpha_0 &= \frac{\langle {}^3P_1, F = I | H_A | {}^3P_0^0, F = I \rangle}{\nu({}^3P_0 - {}^3P_1)} \\
\beta_0 &= \frac{\langle {}^1P_1, F = I | H_A | {}^3P_0^0, F = I \rangle}{\nu({}^3P_0 - {}^1P_1)} \\
\gamma_0 &= \frac{\langle {}^1P_1, F = I | H_B | {}^3P_0^0, F = I \rangle}{\nu({}^3P_0 - {}^3P_2^0)}
\end{aligned} \tag{A.1}$$

where H_A and H_B indicate the dipole and quadrupole components of H_{HFS}.

They can be related to experimentally measured hyperfine splittings, as demonstrated for other two-electron systems in [101, 111, 112, 122]. For the example of ^{173}Yb, we use the measured hyperfine dipole and quadrupole constants from Table A.1 and the matrix elements from [101] assuming a simple Breit-Wills model for the hyperfine interactions.

Equating the diagonal matrix elements with the known dipole constants A for the three states $^3P_1$, $^3P_2$ and $^1P_1$ is enough to infer the three unknown Breit-Wills model parameters $a_s \approx -2.66\,h\,\mathrm{GHz}$, $a_{\frac{1}{2}} \approx -0.48\,h\,\mathrm{GHz}$ and $a_{\frac{3}{2}} \approx -0.10\,h\,\mathrm{GHz}$ (we assume a relativistic correction factor $\xi = 1$ [110]). Similarly, the three quadrupole constants B give access to the Breit-Wills model parameters $b_{\frac{1}{2}} = -0.89\,h\,\mathrm{GHz}$ and $b_{\frac{3}{2}} = 1.34\,h\,\mathrm{GHz}$ and $\eta = 0.35$. The hyperfine cross-coupling constants are then evaluated as the off-diagonal dipole and quadrupole matrix elements from [101] to $\alpha_0 \approx 1.32 \times 10^{-4}$, $\beta_0 \approx -6.95 \times 10^{-6}$ and $\gamma_0 \approx -6.15 \times 10^{-6}$.

Note that this simple Breit-Wills theory for the hyperfine coupling is not expected to give quantitatively correct description for a heavy two-electron system like ytterbium. For example, it was found by Boyd et al. [111] that it overestimates the deduced clock state lifetime of ^{87}Sr. Instead, in Section 1.2 we use the measured differential Zeeman shift as well, as the clock-state lifetime from an ab initio CI+MBPT calculation [137] to infer the coupling parameters α_0 and β_0.

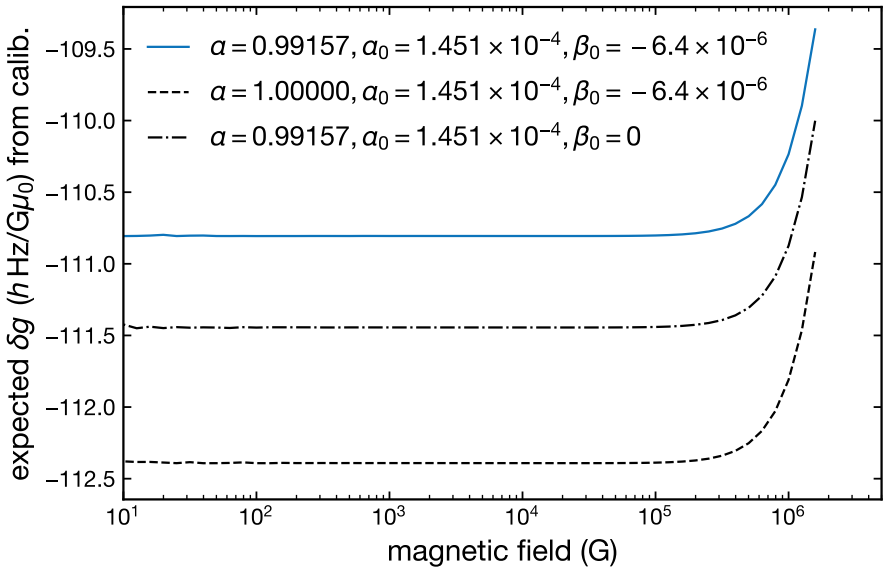

Figure A.1 – Evaluation of the validity of the differential linear Zeeman shift calibration of the clock transition in Section 3.2.2. The differential measurement scheme is simulated using the diagonalization of the hyperfine and Zeeman Hamiltonian within the ^{173}Yb (6s6p) state manifold. The extracted δ_g (mainly determined by α_0) is constant on the 1×10^{-4} level for fields up to at least 10^4 G (blue line). Black lines illustrate the influence of changes in the spin-orbit coupling (dashed, $\alpha = 1$) and in the hyperfine coupling with $^1P_1$ (dash-dotted, $\beta_0 = 0$).

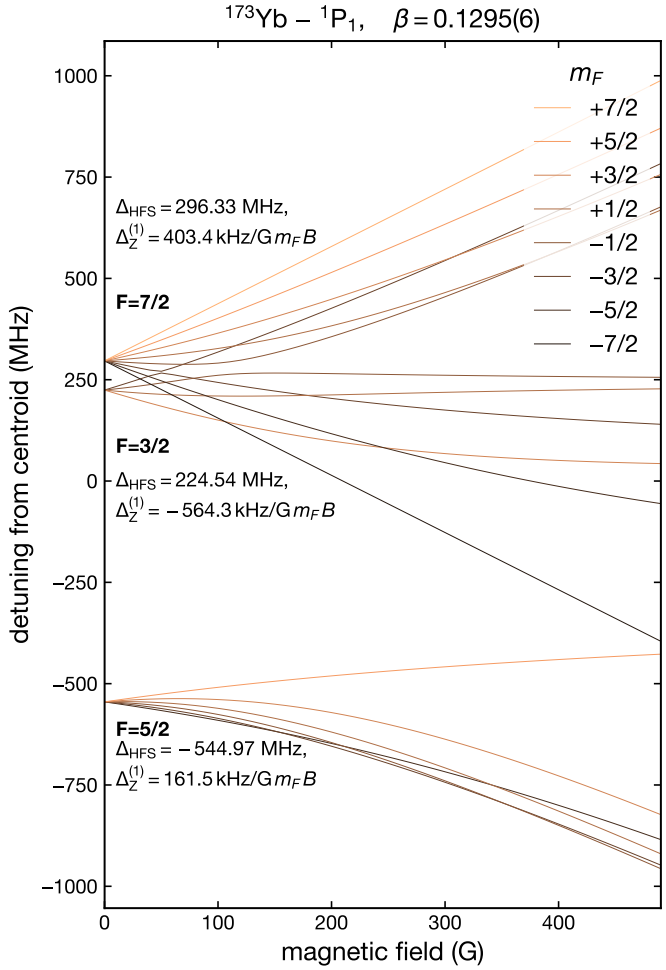

Figure A.2 – Hyperfine structure and magnetic sensitivity of ^{173}Yb (6s6p)^{1}P$_1$. All frequency shifts are relative to the $^1S_0 \rightarrow {}^1P_1$ transition centroid. Underlying hyperfine coupling constants from [281]. Eigenspectrum from diagonalization of full coupling Hamiltonian for (6s6p) manifold with an experimentally determined mixing angle $\beta = -0.1295(6)$ (see Sec. 1.2). Low-field linear Zeeman shift $\Delta_Z^{(1)}$ from Eq. (1.8).

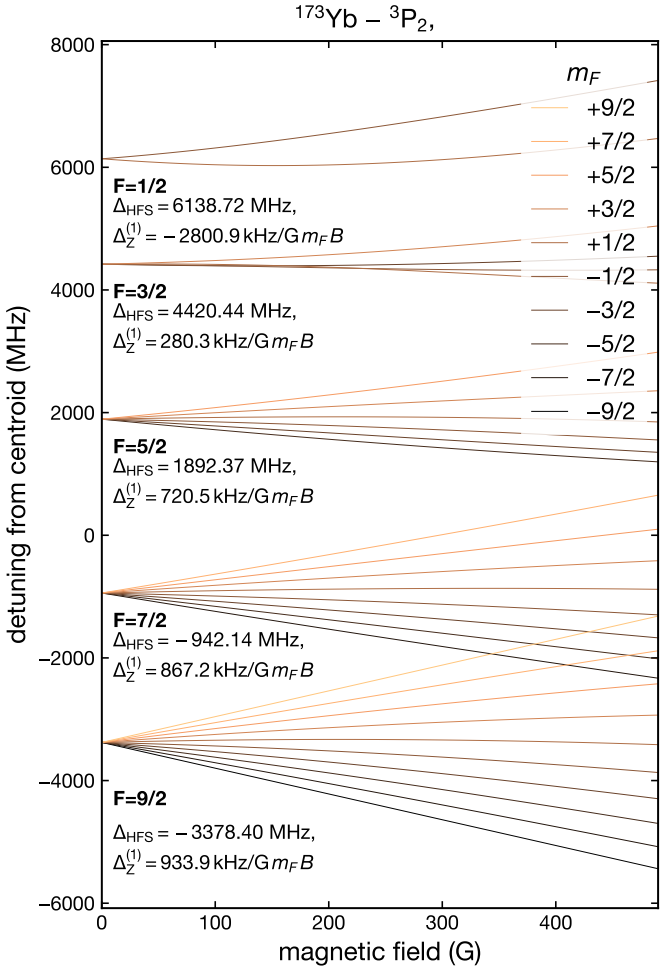

Figure A.3 – Hyperfine structure and magnetic sensitivity of ^{173}Yb (6s6p)^{3}P$_2$. All frequency shifts are relative to the ^{1}S$_0 \rightarrow {}^3$P$_2$ transition centroid. Underlying hyperfine coupling constants are from [282]. Eigenspectrum from diagonalization of full coupling Hamiltonian for (6s6p) manifold with an experimentally determined mixing angle $\beta = -0.1295(6)$ (see Sec. 1.2). Low-field linear Zeeman shift $\Delta_Z^{(1)}$ from Eq. (1.8).

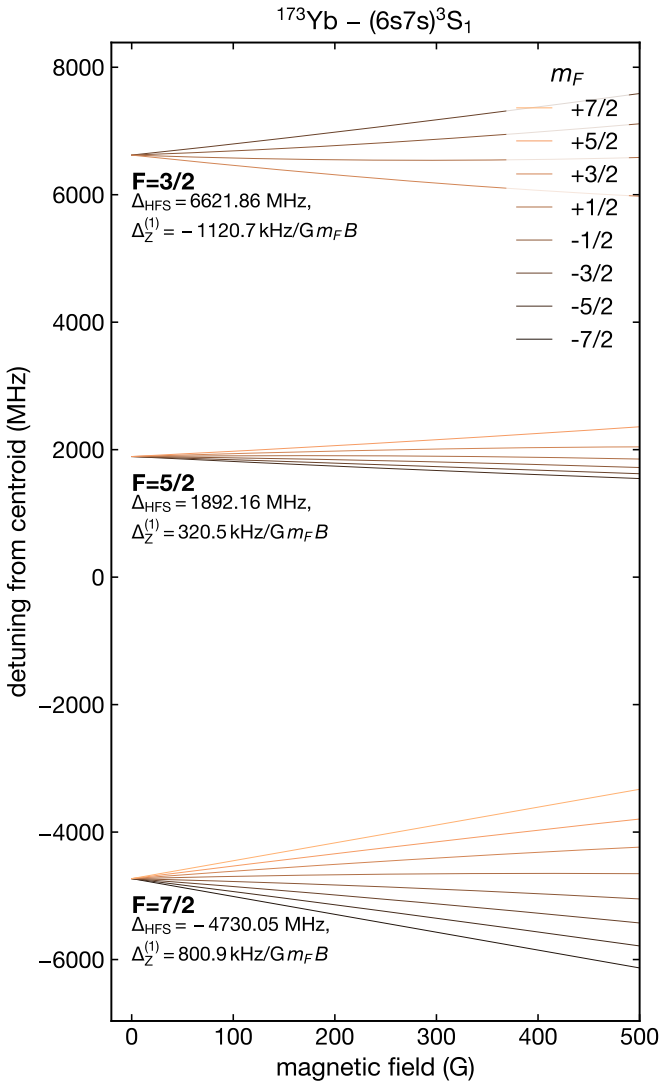

Figure A.4 – Hyperfine structure and magnetic sensitivity of ^{173}Yb (6s7s)^{3}S$_1$. All frequency shifts are relative to the ^{3}P$_0 \rightarrow {}^3$S$_1$ transition centroid. Underlying hyperfine coupling constants are from [282].

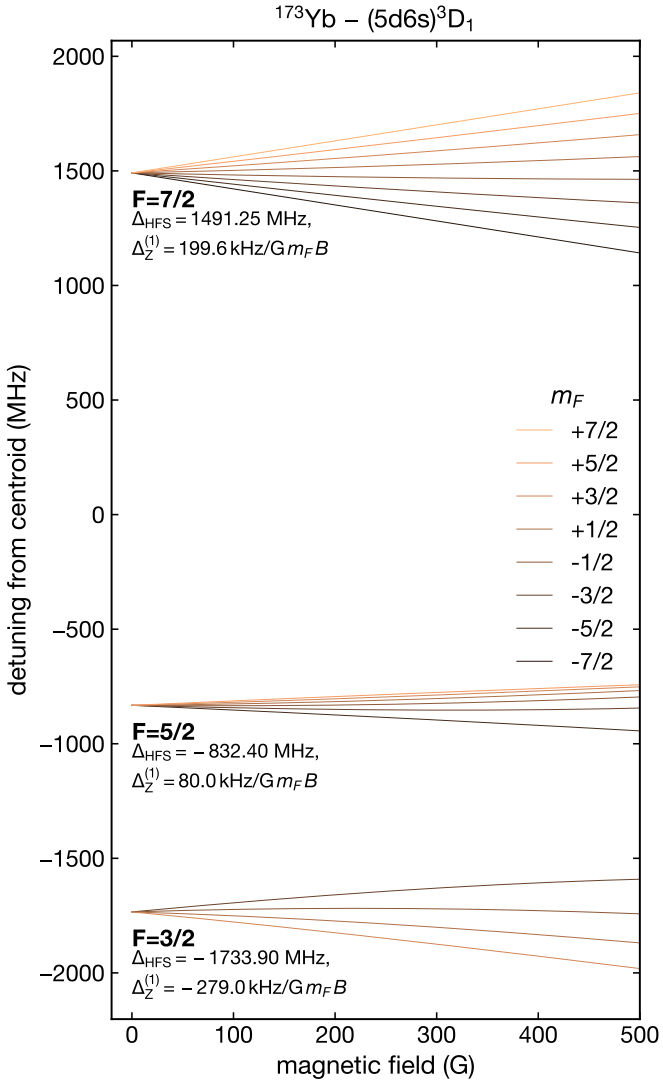

Figure A.5 – Hyperfine structure and magnetic sensitivity of the "repumper state" ^{173}Yb (5d6s)^{3}D$_1$. All frequency shifts are relative to the ^{3}P$_0 \rightarrow {}^3$D$_1$ transition centroid. Underlying hyperfine coupling constants are from [280].

APPENDIX B

Light shifts in ytterbium-173

B.1 Branching ratios in the LS coupling scheme

In Sec. 1.3.4, it was shown how the reduced dipole matrix element can be calculated from a measured transition rate between two LS coupling eigenstates. However, in many cases, only the lifetime of an excited state $|J\rangle \equiv |(l_1 l_2)LSJ\rangle$ is known experimentally and not the branching ratios into the energetically lower lying states $|J'\rangle \equiv |(l_1' l_2')L'S'J'\rangle$. The relative dipole coupling strength is given by the reduced dipole matrix element $\langle J|\mathbf{d}|J'\rangle$ between the states. Assuming the states in Table B.1 to be LS coupling eigenstates, we can decompose the fine structure reduced matrix element into a spin S part and an (unknown) orbital angular momentum L part [121]:

$$\langle J|\mathbf{d}|J'\rangle = \langle L|\mathbf{d}|L'\rangle(-1)^{J'+L+S+1}\sqrt{(2L+1)(2J'+1)}\begin{Bmatrix} L & L' & 1 \\ J' & J & S \end{Bmatrix}\delta_{S'S}(1-\delta_{\Pi'\Pi}). \tag{B.1}$$

Dipole coupling occurs only between states of different parity $\Pi = (-1)^{l_1+l_2}$ where l_1 and l_2 are the two electronic orbitals of the two-electron system.

The branching ratio from $|J\rangle$ to $|J'\rangle$ is then defined as

$$\beta(J,J') \equiv \frac{\langle J|\mathbf{d}|J'\rangle}{\sum_{J''}\langle J|\mathbf{d}|J''\rangle} \tag{B.2}$$

with a sum over all states $|J''\rangle$ lower in energy than $|J\rangle$. The orbital angular momentum part $\langle L|\mathbf{d}|L'\rangle$ cancels out in the branching ratio because of the selection rule $L' = L'' = L+1$ from the Wigner 6-j symbol.

Table B.1 – Transition properties for optical transitions starting from the clock states $^1S_0$ and $^3P_0$, as well as $^3P_1$. The associated reduced dipole matrix elements of these transitions are used to estimate the light shift for the three states in an experimentally accessible wavelength range. The transition wavelengths are taken from collections in [284–286]. The transition rates Γ are inferred from experimentally measured state lifetimes τ of the higher lying state (Blagoev-1994 [287], Takasu-2004 [104], Beloy-2012 [105], Baumann-1985 [288], Cho-2012 [107]) and theoretically estimated branching ratios β into all lower-lying states (see Appendix B.1).

Transitions from $(6s^2)^1S_0$

final state	λ (nm)	k (1/cm)	τ (ns)	β	Γ (MHz)	ref. (τ)
$(6s6p)^3P_1$	555.802	17992.01	866.1	1	1.15	Blagoev-1994
$(6s6p)^1P_1$	398.911	25068.22	5.464	1	183.02	Takasu-2004
$(7/2,5/2)_{J=1}$	346.536	28857.01	14.4	n/a	69.44	Blagoev-1994
$(6s7p)^1P_1$	246.524	40563.97	8.9	0.9964	111.96	Blagoev-1994
$(6s8p)^1P_1$	227.182	44017.60	39.1	0.9894	25.30	Blagoev-1994

Transitions from $(6s6p)^3P_0$

final state	λ (nm)	k (1/cm)	τ (ns)	β	Γ (MHz)	ref. (τ)
$(6s5d)^3D_1$	1388.761	7200.66	329.3	0.6388	1.94	Beloy-2012
$(6s7s)^3S_1$	649.087	15406.25	15.9	0.1515	9.53	Baumann-1985
$(6s6d)^3D_1$	444.044	22520.28	22.7	0.5820	25.64	Baumann-1985
$(6s8s)^3S_1$	411.073	24326.60	34.3	0.1348	3.93	Baumann-1985
$(6p6p)^3P_1$	377.117	26516.98	15	0.3764	25.09	Baumann-1985
$(6s7d)^3D_1$	370.056	27022.94	38.4	0.5707	14.86	Baumann-1985

Transitions from $(6s6p)^3P_1$

final state	λ (nm)	k (1/cm)	τ (ns)	β	Γ (MHz)	ref. (τ)
$(6s6s)^1S_0$	-555.802	-17992.01	866.1	1	1.15	Blagoyev-1994
$(6s5d)^3D_1$	1539.149	6497.10	329.3	0.3519	1.07	Beloy-2012
$(6s5d)^3D_2$	1479.303	6759.94	500	0.8785	1.76	Cho-2012
$(6s7s)^3S_1$	680.148	14702.68	15.9	0.3950	24.84	Baumann-1985
$(6s6d)^3D_1$	458.364	21816.71	22.7	0.3969	17.48	Baumann-1985
$(6s6d)^3D_2$	457.749	21846.03	24.2	0.7929	32.76	Baumann-1985
$(6s8s)^3S_1$	423.316	23623.03	34.3	0.3703	10.80	Baumann-1985
$(6s7d)^3D_1$	379.948	26319.37	38.4	0.3955	10.30	Baumann-1985
$(6s7d)^3D_2$	379.924	26321.04	66.5	0.7762	11.67	Baumann-1985

B.2 Nuclear Zeeman state-selective potentials

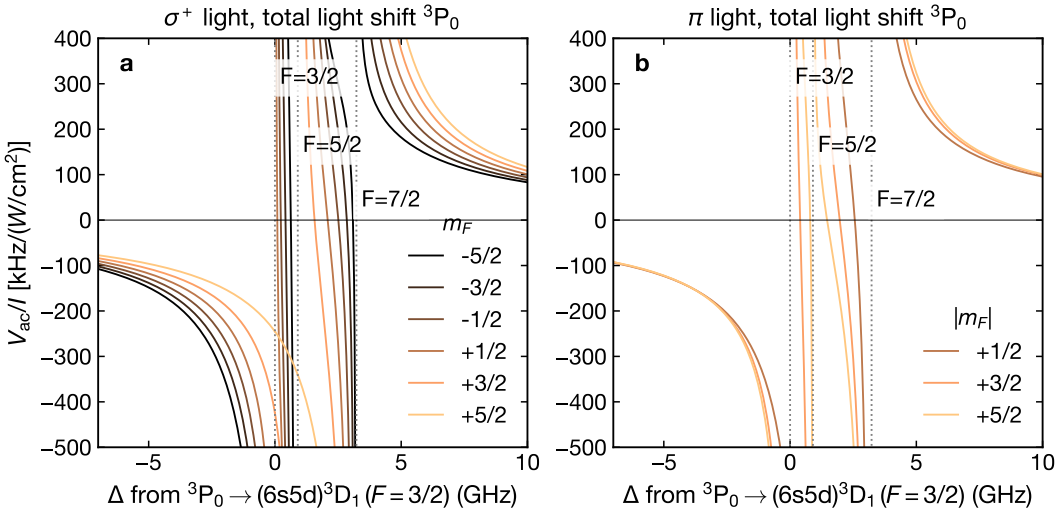

Figure B.1 – Total ac Stark shift ΔV_{ac} estimate of the $^3\mathrm{P}_0$ state induced by (a) σ^+-polarized or (b) π-polarized light of intensity I. The light detuning Δ is relative to the $^3\mathrm{P}_0 \rightarrow (5\mathrm{d}6\mathrm{s})^3\mathrm{D}_1$ (F=3/2) transition.

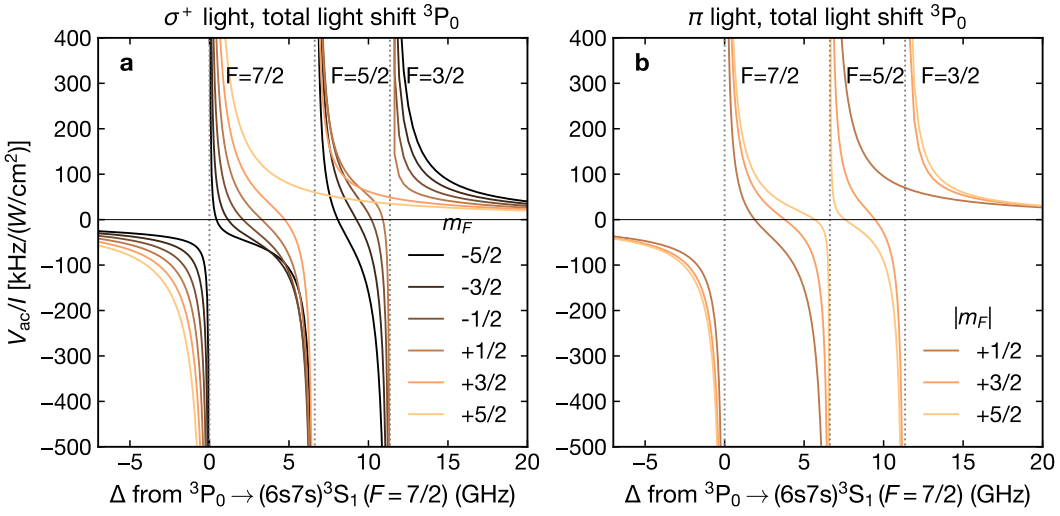

Figure B.2 – Total ac Stark shift ΔV_{ac} estimate of the $^3\mathrm{P}_0$ state induced by (a) σ^+-polarized or (b) π-polarized light of intensity I. The light detuning Δ is relative to the $^3\mathrm{P}_0 \rightarrow {}^3\mathrm{S}_1$ (F=7/2) transition.

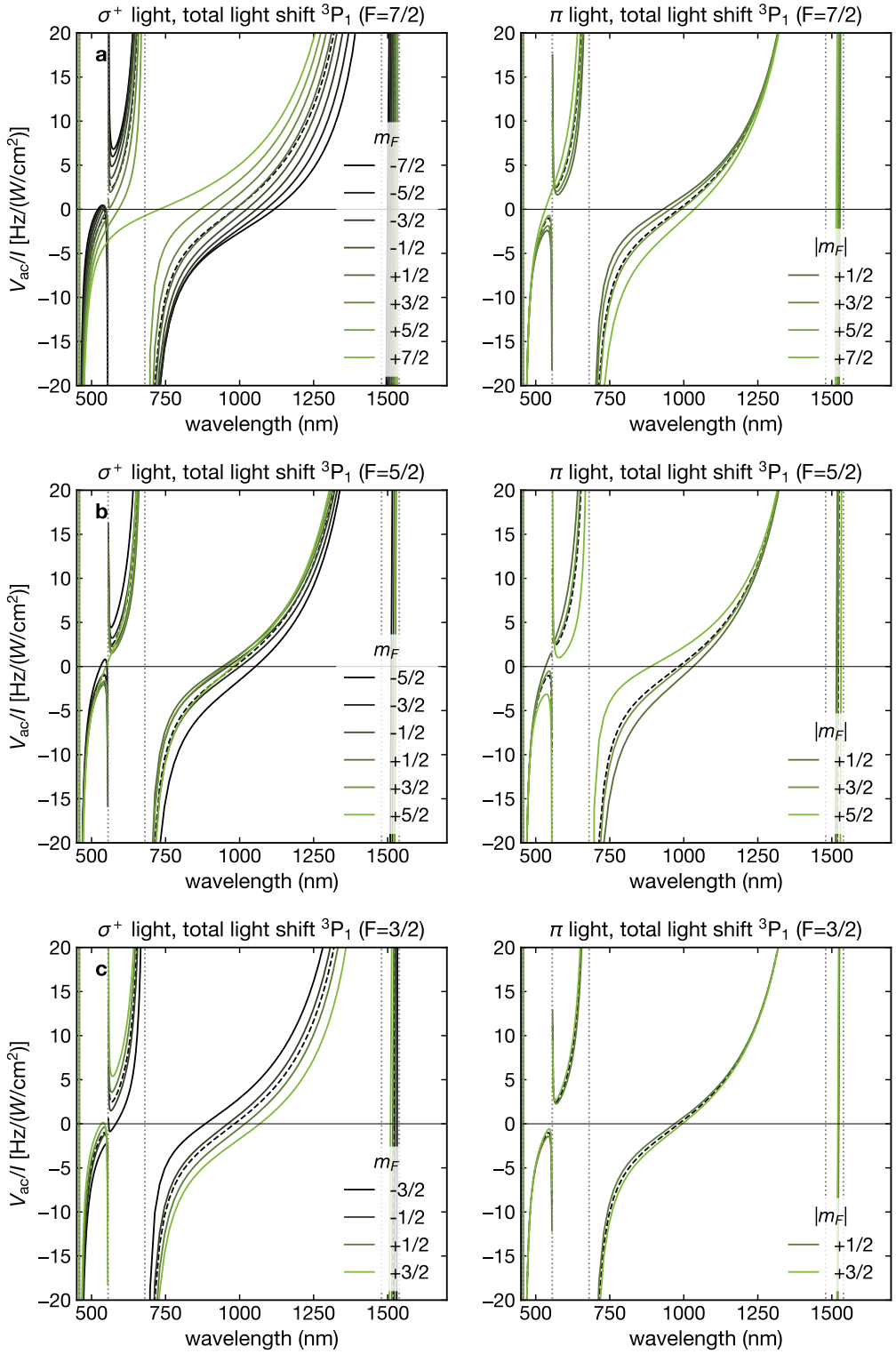

Figure B.3 – Total ac Stark shift (solid lines) for $^3P_1$ with (a) F=7/2 (b) F=5/2 (c) F=3/2 in an experimentally accessible wavelength range. Tensor and vector shift become comparable to the scalar shift (dashed) for σ (left column) and π light (right column).

APPENDIX C

Non-interacting Fermi gases in harmonic confinement

The properties of Fermi gases in our weak optical dipole traps are well described by the thermodynamics of non-interacting Fermi gases. A review of the physics of interacting and non-interacting Fermi gases in the presence of a trapping potential is provided in [41]. In particular, the thermodynamics of harmonically trapped Fermi gases in the semi-classical local density approximation are described in [289, 290]. In the following, we briefly summarize the most important results and observables that allow us to extract relevant bulk properties of our system, such as the Fermi energy, the reduced temperature or the particle number.

We consider a single particle Hamiltonian for a 3D harmonic confinement

$$H = V(\mathbf{r}) + \frac{p^2}{2m} \quad \text{with} \quad V(\mathbf{r}) = \frac{m}{2}(\omega_x^2 x^2 + \omega_y^2 y^2 + \omega_z^2 z^2) \tag{C.1}$$

where ω_r are the trapping frequencies in three spatial directions $r = x, y, z$. The density of states of a 3D anisotropic harmonic oscillator depends on the number of spin components N_σ (up to 6 in ^{173}Yb) and the energy ϵ:

$$g(\epsilon) = \frac{N_\sigma \epsilon^2}{2\hbar^3 \omega_x \omega_y \omega_z}. \tag{C.2}$$

The derivations below are independent of the dimensionality and analogous expressions can, for example, be obtained for 2D confinement using an according trapping potential and equation of state [291].

Global statistics The Fermi gas obeys the Fermi Dirac statistics $F(\epsilon, z) = \frac{1}{\frac{1}{z}\exp(\beta\epsilon)+1}$, where the temperature dependence is captured in the fugacity $z = \exp(\beta\mu)$.

Most relevant thermodynamic quantities can be obtained by carrying out integrations over powers of ϵ, $g(\epsilon)$ and $F(\epsilon, z)$, so-called Fermi-Dirac integrals. For finite T, these integrals

$$\xi_n(z) = \int_0^\infty \epsilon^n F(\epsilon, z)\, d\epsilon = -\frac{\Gamma(n+1)\,\mathrm{Li}_{n+1}(-z)}{\beta^{n+1}} \tag{C.3}$$

can be expressed in terms of the polylogarithmic function $\mathrm{Li}_n(z) = \sum_{k=1}^{\infty} \frac{z^k}{k^n}$ and the Gamma function Γ with $\Gamma(n+1) = n!$ for integer n, and $\beta = 1/k_B T$.

For example, the grand canonical potential of the Fermi gas is [292]

$$\Omega(\mu,T) = -\frac{M}{6\hbar^3\omega_x\omega_y\omega_z}\int_0^\infty \mathrm{d}\epsilon\epsilon^3 F(\epsilon,z) = \frac{M}{\hbar^3\omega_x\omega_y\omega_z}\frac{\mathrm{Li}_4(-z)}{\beta^4}. \tag{C.4}$$

The particle number in terms of $z(\mu,\beta)$ is given by

$$N(z) = \int \mathrm{d}\epsilon g(\epsilon)F(\epsilon,z) = \frac{M}{2\hbar^3\omega_x\omega_y\omega_z}\xi_2(z) = -\frac{M}{\hbar^3\omega_x\omega_y\omega_z}\frac{\mathrm{Li}_3(-z)}{\beta^3}. \tag{C.5}$$

In turn, by (numerically) inverting the equation above, one obtains the chemical potential for a fixed particle number and arbitrary temperature.

Zero-temperature properties The zero-temperature properties are straight-forward to derive (the Fermi Dirac distribution becomes a step function). The Fermi energy $E_F(N) = \mu(T = 0)$ is obtained by performing the integration $N = \int_0^{E_F}\mathrm{d}\epsilon g(\epsilon)$ for a fixed particle number N, which yields

$$E_F = \hbar(6\omega_x\omega_y\omega_z N/N_\sigma)^{\frac{1}{3}} \tag{C.6}$$

and the total particle number

$$N = \frac{N_\sigma E_F^3}{6\hbar^3\omega_x\omega_y\omega_z}. \tag{C.7}$$

The Fermi radius of the atomic distribution in the harmonic confinement along the axis $r = x,z,y$ at $T = 0$ is given by the maximum kinetic excursion of a particle, at the Fermi energy:

$$R_F = \sqrt{\frac{2E_F}{m\omega_r^2}} = \left(6N\omega_x\omega_y\omega_z/N_\sigma\right)^{1/6}\sqrt{\frac{2\hbar}{m\omega_r^2}}. \tag{C.8}$$

Low-temperature approximation For small temperatures (still in the degenerate regime $\mu \ll k_B T$), integrals of the type Eq. (C.3) can be expanded in powers of $k_B T$ using the Sommerfeld approximation [167].

In the lowest order Sommerfeld approximation, a linear relation between low energy temperatures and entropy emerges. The entropy per particle is obtained from the grand canonical potential through $S/(Nk_B) = -\partial_T\Omega(T,V,\mu)/(Nk_B)$, leading to

$$S/(Nk_B) \approx \pi^2\frac{T}{T_F}. \tag{C.9}$$

The so-called *reduced temperature* in units of the Fermi temperature $T_F = E_F/k_B$ is directly linked to the fugacity z via:

$$\frac{T}{T_F} = \left(-\frac{1}{6\mathrm{Li}_3(-z)}\right)^{1/3}. \tag{C.10}$$

Note that T/T_F (and thereby the per-particle entropy) is independent of the trap frequencies, the particle number, and the number of spin components. In practice, this makes it a well-suited fit parameter for experimental thermometry.

Local density approximation In order to describe local properties of the atom distribution in a weak harmonic trap, we employ the standard local density approximation (LDA), also known as the Thomas-Fermi approximation. The validity of the LDA is discussed in [289]. The atomic density distribution $n(\mathbf{r})$ in our xODT trapping potentials fulfills the necessary condition $n(r)l_r^3 \gg r/l_r$ over the entire Fermi radius range (with l_r the harmonic oscillator length in the direction $r = x, y, z$). Then, the trapping potential can be treated as locally homogeneous and a local chemical potential is defined as $\bar{\mu} = \mu - V(\mathbf{r})$. For large N, the particle distribution in phase space is described by the phase space density [289]:

$$w(\mathbf{r},\mathbf{p}) = \frac{N_\sigma}{(2\pi)^3}\frac{1}{\frac{1}{z}\mathrm{e}^{\beta H(\mathbf{r},\mathbf{p})}+1}\,. \tag{C.11}$$

Integrating over all momenta $\mathbf{p}$ yields the local density[1]

$$n(\mathbf{r}) = \frac{N_\sigma}{\hbar^3}\int \mathrm{d}^3\mathbf{p}\, w(\mathbf{r},\mathbf{p}) = -\frac{N_\sigma\, m^{3/2}}{(2\pi\beta)^{3/2}\hbar^3}\,\mathrm{Li}_{3/2}\left[-\bar{z}(\mathbf{r})\right] \tag{C.12}$$

with spatially varying fugacity

$$\bar{z}(\mathbf{r}) = \mathrm{e}^{\beta(\mu - V(\mathbf{r}))} = z\mathrm{e}^{-\beta V(\mathbf{r})}\,. \tag{C.13}$$

Note that the resulting in-trap density distribution $n(\mathbf{r})$ depends on the trap frequencies and is generally anisotropic, in contrast to the isotropic momentum distribution.

Expansion from the trap The expansion dynamics of the density distribution from a harmonic trap are governed by the following scaling relation for the atomic cloud widths [290]:

$$\sigma_r^2(t) = \frac{1+\omega_r^2 t^2}{\omega_r^2 m\beta}\,. \tag{C.14}$$

The density distribution behaves as (neglecting the movement of the cloud center along the direction of gravity):

$$n(x,y,z,t) = -\frac{N_\sigma}{(2\pi)^{3/2}\beta^3\hbar^3\prod_{r=x,y,z}\omega_r\sigma_r(t)}\,\mathrm{Li}_{3/2}\left[-z\,\mathrm{e}^{-\frac{x^2}{2\sigma_x^2(t)}-\frac{y^2}{2\sigma_y^2(t)}-\frac{z^2}{2\sigma_z^2(t)}}\right]. \tag{C.15}$$

For large expansion times $t \gg 1/\omega$ compared to the trap frequency, the density distribution reproduces the in-trap momentum distribution and becomes isotropic.

3D bulk column densities In order to determine the reduced temperature from an experimental absorption image, we require an equation of state for the column-integrated atomic density. We assume that the absorption image is taken along $\hat{z}$. An integration of $n(x,y,z,t)$ along that axis yields a column density

$$n_c(x,y,t) = -\frac{N_\sigma}{(2\pi)\beta^3\hbar^3\omega_z\prod_{r=x,y}\omega_r\sigma_r(t)}\,\mathrm{Li}_2\left[-z\,\mathrm{e}^{-\frac{x^2}{2\sigma_x^2(t)}-\frac{y^2}{2\sigma_y^2(t)}}\right]. \tag{C.16}$$

[1] Similarly, an integration in real space provides the momentum distribution.

Here, we have used the relation $\int_{-\infty}^{\infty} \mathrm{d}z\, \mathrm{Li}_{3/2}(B\mathrm{e}^{-\xi z^2}) = \sum_{k=1}^{\infty} \frac{B^k \sqrt{\frac{\pi}{\xi k}}}{k^{3/2}} = \sqrt{\frac{\pi}{\xi}} \mathrm{Li}_2(B)$. Details on an efficient numerical implementation of a least squares fitting routine for large absorption pictures can be found in [169].

APPENDIX D

Measurement data collection

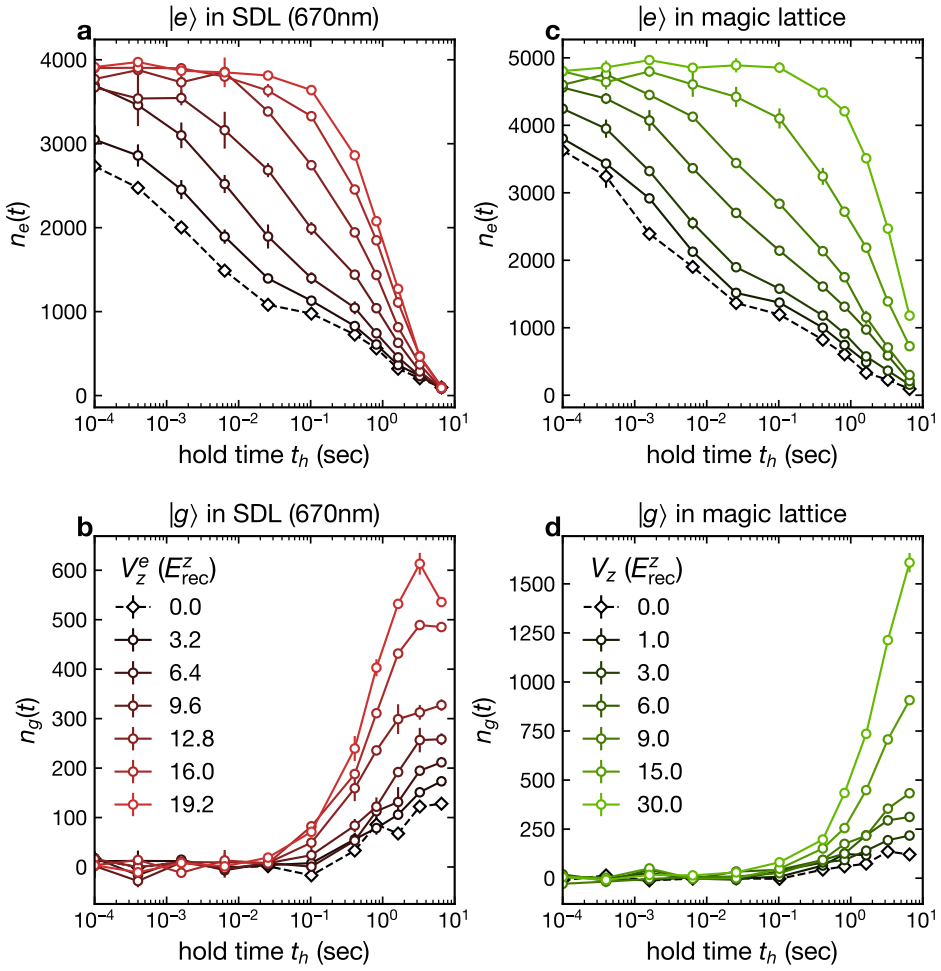

Figure D.1 – Measured excited-state loss dynamics in a two-spin $|e\rangle$ mixture. For measurement details, see Section 2.7. Dynamics of the $|e\rangle$ (a) and $|g\rangle$ (b) atom count in a longitudinal state-dependent lattice of variable depth V_z^e and fixed perpendicular magic lattice confinement $V_\perp = 30\, E_{\rm rec}^\perp$. (c–d) are the analogous measurement results for a longitudinal magic-wavelength lattice. All data are the mean of two realizations. Error bars denote the standard error of the mean.

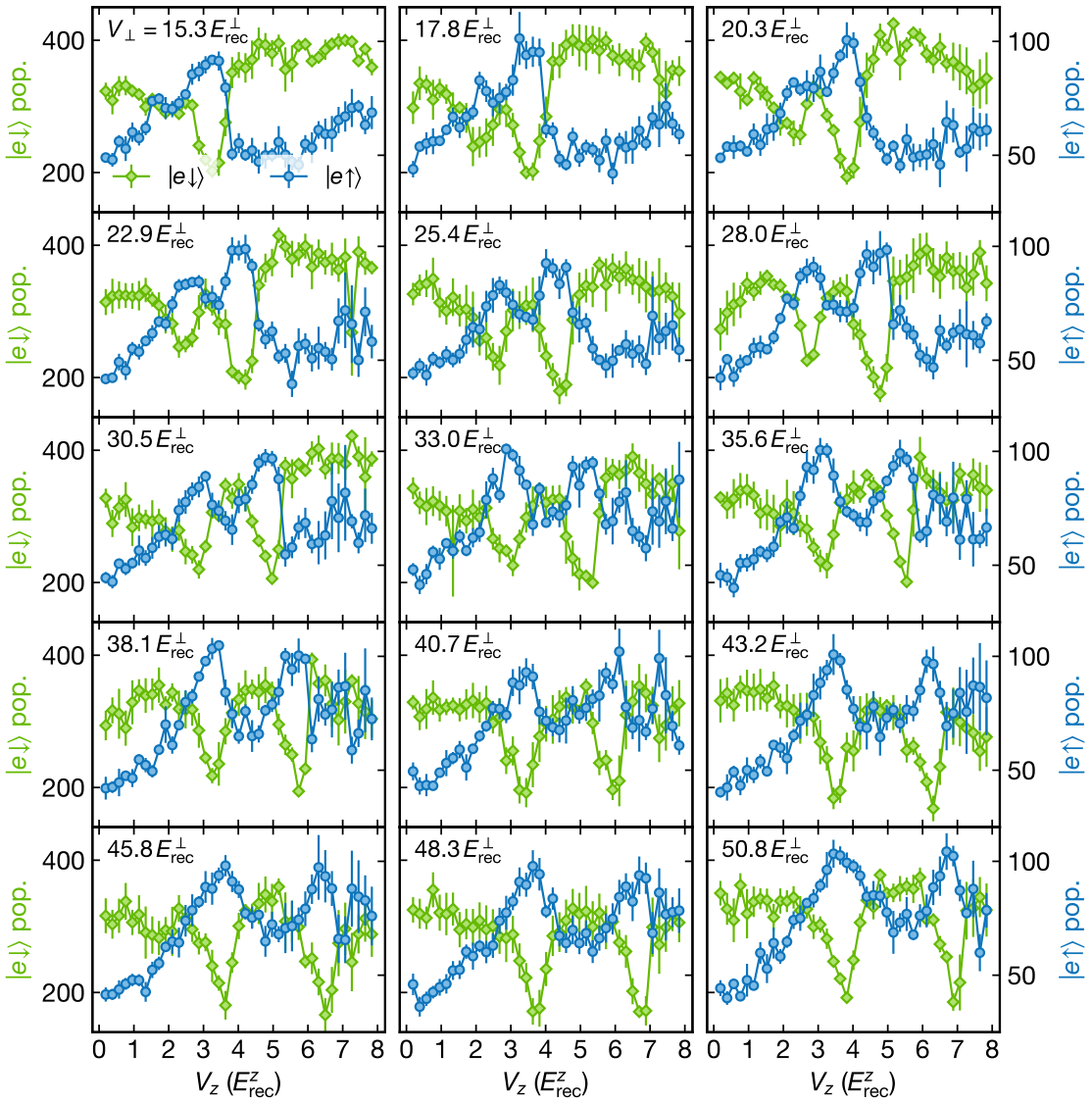

Figure D.2 – Resonances in the spin-exchange rate as a function of perpendicular confinement $V_\perp$ and SDL depth V_z. This is the non-normalized data underlying Fig. 5.6: $|e\uparrow\rangle$ atom count (circles) and $|e\downarrow\rangle$ count (diamonds) after hold time $\tau \propto \hbar U^-/t_g^2$. The hold time is chosen such that $\tau = 12.2\,\tau_g$ for $V_z = 6\,E^z_{\rm rec}$ and $V_\perp = 30\,E^\perp_{\rm rec}$. Atom numbers are from trap center region defined in Fig. 5.4.

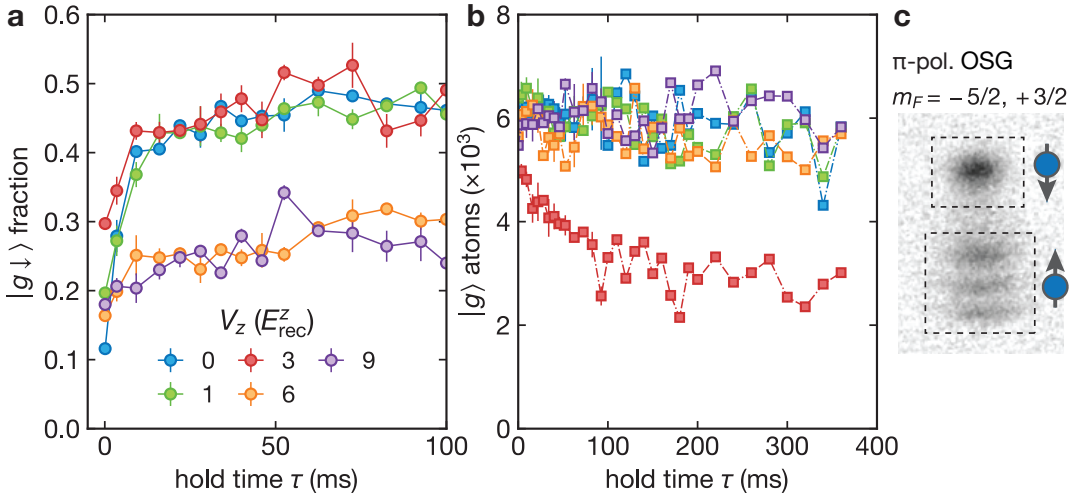

Figure D.3 – (a) Ground-state spin-exchange dynamics of a $m_F = -5/2, +3/2$ mixture after excitation of $m_F = -5/2$ to $|e\rangle$ for variable SDL depth V_z (fixed perp. confinement $V_\perp = 30\, E^\perp_{\mathrm{rec}}$). Clock excitation via 10 ms ($\pm$10 kHz) adiabatic passage at a magnetic field $B = 35$ G and hold time τ at low bias field (1 G). $|g\downarrow\rangle$ population is given relative to the total $|g\rangle$ atom count, shown in (b). Enhanced loss and exchange-dynamics are observed for $V_z = 3\, E^z_{\mathrm{rec}}$, in the vicinity of a resonance with a CM-excited bound spin-singlet state [see Section 5.3]. The initial dynamics happen during the expansion from the lattice and are not captured in this measurement. (c) $|g\rangle$ nuclear spin detection via π-polarized OSG from optical lattice (see Section 3.6.2): An absorption image after 12 ms time-of-flight from optical lattice where a short π-polarized light pulse has imparted a nuclear spin dependent momentum kick onto the atoms.

Bibliography

[1] J. Kondo. *Resistance Minimum in Dilute Magnetic Alloys*. Prog. Theor. Phys. **32**, 37–49 (1964). See pages: 1, 89

[2] P. W. Anderson. *Localized Magnetic States in Metals*. Phys. Rev. **124**, 41–53 (1961). See pages: 2, 89, 93, 177

[3] A. A. Abrikosov and A. A. Migdal. *On the theory of the Kondo effect*. J. Low Temp. Phys. **3**, 519–536 (1970). See pages: 1, 90

[4] A. C. Hewson. *The Kondo Problem to Heavy Fermions*. Cambridge Studies in Magnetism. Cambridge University Press (1993). ISBN 9780511470752. See pages: 1, 2, 87, 89, 90, 91, 93, 94, 98, 161, 165, 174, 181

[5] N. D. Mathur, F. M. Grosche, S. R. Julian, I. R. Walker, D. M. Freye, R. K. W. Haselwimmer, and G. G. Lonzarich. *Magnetically mediated superconductivity in heavy fermion compounds*. Nature **394**, 39 (1998). See pages: 1, 94

[6] C. Pfleiderer. *Superconducting phases of f-electron compounds*. Rev. Mod. Phys. **81**, 1551–1624 (2009).

[7] F. Steglich and S. Wirth. *Foundations of heavy-fermion superconductivity: lattice Kondo effect and Mott physics*. Rep. Prog. Phys. **79**, 084502 (2016). See pages: 1, 94

[8] Q. Si, J. L. Smith, and K. Ingersent. *Quantum critical behavior in Kondo systems*. Int. J. Mod. Phys. B **13**, 2331–2342 (1999). See pages: 1, 95

[9] K. Andres, J. E. Graebner, and H. R. Ott. *4f -Virtual-Bound-State Formation in Ce*Al_3 *at Low Temperatures*. Phys. Rev. Lett. **35**, 1779–1782 (1975).

[10] P. Coleman, C. Pépin, Q. Si, and R. Ramazashvili. *How do Fermi liquids get heavy and die?* J. Phys.: Condens. Matter **13**, R723 (2001).

[11] Q. Si, S. Rabello, K. Ingersent, and J. L. Smith. *Locally critical quantum phase transitions in strongly correlated metals*. Nature **413**, 804 (2001). See pages: 1, 95

[12] L. Gupta. *Theoretical and Experimental Aspects of Valence Fluctuations and Heavy Fermions*. Springer US (2012). ISBN 9781461309475. See pages: 1, 92

[13] S. Doniach. *The Kondo lattice and weak antiferromagnetism*. Physica B+C **91**, 231–234 (1977). See pages: 1, 2, 93, 94, 95

[14] P. Coleman. *Heavy Fermions: Electrons at the Edge of Magnetism*. In H. Kronmüller, S. Parkin, M. Fähnle, S. Maekawa, and I. Zutic, editors, *Handbook of Magnetism and Advanced Magnetic Materials*. John Wiley and Sons (2007). ISBN 9780470022184. See pages: 1, 2, 90, 94, 95, 181

[15] A. M. Tsvelik and M. Reizer. *Phenomenological theory of non-Fermi-liquid heavy-fermion alloys*. Phys. Rev. B **48**, 9887–9889 (1993).

[16] M. Lavagna and C. Pepin. *The Kondo Lattice Model*. Acta Phys. Pol., B **29**, 3753 (1998). See page: 1

[17] H. v. Löhneysen, A. Rosch, M. Vojta, and P. Wölfle. *Fermi-liquid instabilities at magnetic quantum phase transitions*. Rev. Mod. Phys. **79**, 1015–1075 (2007). See pages: 1, 2, 94, 95

[18] Y. Tokura. *Orbital Physics in Transition-Metal Oxides*. Science **288**, 462–468 (2000). See pages: 1, 2, 96

[19] Y. Tokura. *Colossal Magnetoresistive Oxides*. CRC Press London (2000). See page: 2

[20] E. Dagotto, S. Yunoki, A. L. Malvezzi, A. Moreo, J. Hu, S. Capponi, D. Poilblanc, and N. Furukawa. *Ferromagnetic Kondo model for manganites: Phase diagram, charge segregation, and influence of quantum localized spins*. Phys. Rev. B **58**, 6414–6427 (1998). See pages: 2, 181

[21] E. Dagotto, T. Hotta, and A. Moreo. *Colossal magnetoresistant materials: The key role of phase separation*. Phys. Rep. **344**, 1–153 (2001). See pages: 1, 2, 87, 93, 181

[22] J. Van Den Brink, G. Khaliullin, and D. Khomskii. *Orbital effects in manganites*. In *Colossal magnetoresistive manganites*, pages 263–301. Springer (2004). See pages: 1, 87, 93, 96

[23] A. Georges, G. Kotliar, W. Krauth, and M. J. Rozenberg. *Dynamical mean-field theory of strongly correlated fermion systems and the limit of infinite dimensions*. Rev. Mod. Phys. **68**, 13–125 (1996). See page: 2

[24] A. Yacoby, M. Heiblum, D. Mahalu, and H. Shtrikman. *Coherence and Phase Sensitive Measurements in a Quantum Dot*. Phys. Rev. Lett. **74**, 4047–4050 (1995). See pages: 2, 91

[25] N. Roch, S. Florens, V. Bouchiat, W. Wernsdorfer, and F. Balestro. *Quantum phase transition in a single-molecule quantum dot*. Nature **453**, 633 (2008).

[26] N. Roch, S. Florens, T. A. Costi, W. Wernsdorfer, and F. Balestro. *Observation of the Underscreened Kondo Effect in a Molecular Transistor*. Phys. Rev. Lett. **103**, 197202 (2009).

[27] C. Latta, F. Haupt, M. Hanl, A. Weichselbaum, M. Claassen, W. Wuester, P. Fallahi, S. Faelt, L. Glazman, J. von Delft, H. E. Türeci, and A. Imamoglu. *Quantum quench of Kondo correlations in optical absorption*. Nature **474**, 627 EP – (2011).

[28] H. E. Türeci, M. Hanl, M. Claassen, A. Weichselbaum, T. Hecht, B. Braunecker, A. Govorov, L. Glazman, A. Imamoglu, and J. von Delft. *Many-Body Dynamics of Exciton Creation in a Quantum Dot by Optical Absorption: A Quantum Quench towards Kondo Correlations*. Phys. Rev. Lett. **106**, 107402 (2011). See pages: 91, 92

[29] D. N. Basov, R. D. Averitt, D. van der Marel, M. Dressel, and K. Haule. *Electrodynamics of correlated electron materials*. Rev. Mod. Phys. **83**, 471–541 (2011). See pages: 2, 91

[30] D. Lobaskin and S. Kehrein. *Crossover from nonequilibrium to equilibrium behavior in the time-dependent Kondo model*. Phys. Rev. B **71**, 193303 (2005). See pages: 2, 92, 147, 164

[31] F. B. Anders and A. Schiller. *Real-Time Dynamics in Quantum-Impurity Systems: A Time-Dependent Numerical Renormalization-Group Approach*. Phys. Rev. Lett. **95**, 196801 (2005). See page: 92

[32] A. Hackl, D. Roosen, S. Kehrein, and W. Hofstetter. *Nonequilibrium Spin Dynamics in the Ferromagnetic Kondo Model*. Phys. Rev. Lett. **102**, 196601 (2009). See pages: 2, 91, 147, 164, 180

[33] M. Nuss, M. Ganahl, E. Arrigoni, W. von der Linden, and H. G. Evertz. *Nonequilibrium spatiotemporal formation of the Kondo screening cloud on a lattice*. Phys. Rev. B **91**, 085127 (2015). See pages: 91, 93, 164

[34] M. Kanász-Nagy, Y. Ashida, T. Shi, C. P. Moca, T. N. Ikeda, S. Fölling, J. I. Cirac, G. Zaránd, and E. A. Demler. *Exploring the anisotropic Kondo model in and out of equilibrium with alkaline-earth atoms*. Phys. Rev. B **97** (2018). See pages: 2, 4, 27, 37, 49, 52, 87, 89, 90, 91, 92, 93, 147, 157, 164, 180, 181

[35] J. Hubbard. *Electron correlations in narrow energy bands*. Proceedings of the Royal Society of London A: Mathematical, Physical and Engineering Sciences **276**, 238–257 (1963). See pages: 2, 61

[36] P. A. Lee, N. Nagaosa, and X.-G. Wen. *Doping a Mott insulator: Physics of high-temperature superconductivity*. Rev. Mod. Phys. **78**, 17–85 (2006). See page: 2

[37] K. I. Kugel and D. I. Khomskii. *The Jahn-Teller effect and magnetism: transition metal compounds*. Soviet Physics Uspekhi **25**, 231 (1982). See page: 2

[38] I. Bloch, J. Dalibard, and W. Zwerger. *Many-body physics with ultracold gases*. Rev. Mod. Phys. **80**, 885–964 (2008). See pages: 2, 59, 60, 61

[39] C. Gross and I. Bloch. *Quantum simulations with ultracold atoms in optical lattices*. Science **357**, 995–1001 (2017). See pages: 2, 53

[40] C. Chin, R. Grimm, P. Julienne, and E. Tiesinga. *Feshbach resonances in ultracold gases*. Rev. Mod. Phys. **82**, 1225–1286 (2010). See pages: 2, 39, 40, 42, 50, 51, 123, 129

[41] S. Giorgini, L. P. Pitaevskii, and S. Stringari. *Theory of ultracold atomic Fermi gases*. Rev. Mod. Phys. **80**, 1215–1274 (2008). See pages: 2, 108, 110, 193

[42] D. Jaksch, C. Bruder, J. I. Cirac, C. W. Gardiner, and P. Zoller. *Cold Bosonic Atoms in Optical Lattices*. Phys. Rev. Lett. **81**, 3108–3111 (1998). See pages: 2, 134

[43] D. Jaksch and P. Zoller. *The cold atom Hubbard toolbox*. Ann. Phys. **315**, 52–79 (2005). See page: 58

[44] L. Tarruell and L. Sanchez-Palencia. *Quantum simulation of the Hubbard model with ultracold fermions in optical lattices*. C. R. Phys. **6008**, 357–525 (2018). See pages: 2, 3, 45, 61

[45] U. Schneider, L. Hackermüller, S. Will, T. Best, I. Bloch, T. A. Costi, R. W. Helmes, D. Rasch, and A. Rosch. *Metallic and Insulating Phases of Repulsively Interacting Fermions in a 3D Optical Lattice*. Science **322**, 1520–1525 (2008). See page: 3

[46] R. Jördens, N. Strohmaier, K. Günter, H. Moritz, and T. Esslinger. *A Mott insulator of fermionic atoms in an optical lattice*. Nature **455**, 204 (2008). See page: 3

[47] S. Fölling, F. Gerbier, A. Widera, O. Mandel, T. Gericke, and I. Bloch. *Spatial quantum noise interferometry in expanding ultracold atom clouds*. Nature **434**, 481 (2005). See page: 3

[48] S. Fölling. *Quantum Noise Correlation Experiments with Ultracold Atoms*. In P. Törmä and K. Sengstock, editors, *Quantum Gas Experiments: Exploring Many-body States*. Imperial College Press, London (2014). See page: 3

[49] N. Gemelke, X. Zhang, C.-L. Hung, and C. Chin. *In situ observation of incompressible Mott-insulating domains in ultracold atomic gases*. Nature **460**, 995–998 (2009). See page: 3

[50] J. F. Sherson, C. Weitenberg, M. Endres, M. Cheneau, I. Bloch, and S. Kuhr. *Single-atom-resolved fluorescence imaging of an atomic Mott insulator*. Nature **467**, 68 (2010). See page: 3

[51] W. S. Bakr, A. Peng, M. E. Tai, R. Ma, J. Simon, J. I. Gillen, S. Fölling, L. Pollet, and M. Greiner. *Probing the Superfluid-to-Mott Insulator Transition at the Single-Atom Level*. Science **329**, 547–550 (2010).

[52] H. Ott. *Single atom detection in ultracold quantum gases: a review of current progress*. Rep. Prog. Phys. **79**, 054401 (2016). See page: 3

[53] G. Salomon, J. Koepsell, J. Vijayan, T. A. Hilker, J. Nespolo, L. Pollet, I. Bloch, and C. Gross. *Direct observation of incommensurate magnetism in Hubbard chains*. Nature **565**, 56–60 (2019). See page: 3

[54] M. Takamoto, F.-L. Hong, R. Higashi, and H. Katori. *An optical lattice clock*. Nature **435**, 321 (2005). See page: 3

[55] N. Hinkley, J. A. Sherman, N. B. Phillips, M. Schioppo, N. D. Lemke, K. Beloy, M. Pizzocaro, C. W. Oates, and A. D. Ludlow. *An Atomic Clock with* 10^{18} *Instability*. Science **341**, 1215–1218 (2013).

[56] S. L. Campbell, R. B. Hutson, G. E. Marti, A. Goban, N. Darkwah Oppong, R. L. McNally, L. Sonderhouse, J. M. Robinson, W. Zhang, B. J. Bloom, and J. Ye. *A Fermi-degenerate three-dimensional optical lattice clock*. Science **358**, 90–94 (2017). See page: 25

[57] A. D. Ludlow, M. M. Boyd, J. Ye, E. Peik, and P. O. Schmidt. *Optical atomic clocks*. Rev. Mod. Phys. **87**, 637–701 (2015). See pages: 3, 7, 15, 25, 72, 113, 114

[58] A. V. Gorshkov, M. Hermele, V. Gurarie, C. Xu, P. S. Julienne, J. Ye, P. Zoller, E. Demler, M. D. Lukin, and A. M. Rey. *Two-orbital SU(N) magnetism with ultracold alkaline-earth atoms*. Nat. Phys. **6**, 289–295 (2010). See pages: 3, 4, 7, 42, 43, 44, 46, 47, 48, 64, 65, 79, 87, 96, 98, 165, 180, 181

[59] F. Scazza, C. Hofrichter, M. Höfer, P. C. De Groot, I. Bloch, and S. Fölling. *Observation of two-orbital spin-exchange interactions with ultracold SU(N)-symmetric fermions*. Nat. Phys. **10**, 779–784 (2014). See pages: 3, 4, 10, 37, 41, 47, 49, 65, 70, 73, 79, 80, 88, 97, 145, 147, 150, 179

[60] G. Cappellini, M. Mancini, G. Pagano, P. Lombardi, L. Livi, M. Siciliani de Cumis, P. Cancio, M. Pizzocaro, D. Calonico, F. Levi, C. Sias, J. Catani, M. Inguscio, and L. Fallani. *Direct Observation of Coherent Interorbital Spin-Exchange Dynamics*. Phys. Rev. Lett. **113**, 120402 (2014). See pages: 4, 48, 88, 97, 145, 147, 150

[61] X. Zhang, M. Bishof, S. L. Bromley, C. V. Kraus, M. S. Safronova, P. Zoller, A. M. Rey, and J. Ye. *Spectroscopic observation of SU(N)-symmetric interactions in Sr orbital magnetism*. Science **345**, 1467–1473 (2014). See pages: 3, 4, 179

[62] M. A. Cazalilla, A. F. Ho, and M. Ueda. *Ultracold gases of ytterbium: Ferromagnetism and Mott states in an SU(6) Fermi system*. New J. Phys. **11**, 103033 (2009). See pages: 3, 45, 46

[63] M. Hermele, V. Gurarie, and A. M. Rey. *Mott Insulators of Ultracold Fermionic Alkaline Earth Atoms: Underconstrained Magnetism and Chiral Spin Liquid*. Phys. Rev. Lett. **103**, 135301 (2009).

[64] M. Hermele and V. Gurarie. *Topological liquids and valence cluster states in two-dimensional SU(N) magnets*. Phys. Rev. B **84**, 174441 (2011). See page: 3

[65] S.-K. Yip, B.-L. Huang, and J.-S. Kao. *Theory of SU(N) Fermi liquids*. Phys. Rev. A **89**, 043610 (2014). See page: 45

[66] M. A. Cazalilla and A. M. Rey. *Ultracold Fermi gases with emergent SU(N) symmetry*. Rep. Prog. Phys. **77**, 124401 (2014). See pages: 3, 4, 43, 45, 46, 181

[67] G. Pagano, M. Mancini, G. Cappellini, P. Lombardi, F. Schäfer, H. Hu, X.-J. Liu, J. Catani, C. Sias, M. Inguscio, and L. Fallani. *A one-dimensional liquid of fermions with tunable spin*. Nat. Phys. **10**, 198 EP – (2014). See pages: 3, 45

[68] S. Taie, R. Yamazaki, S. Sugawa, and Y. Takahashi. *An SU(6) Mott insulator of an atomic Fermi gas realized by large-spin Pomeranchuk cooling*. Nat. Phys. **8**, 825–830 (2012). See pages: 3, 45, 46

[69] C. Hofrichter, L. Riegger, F. Scazza, M. Höfer, D. R. Fernandes, I. Bloch, and S. Fölling. *Direct Probing of the Mott Crossover in the SU(N) Fermi-Hubbard Model*. Phys. Rev. X **6**, 021030 (2016). See pages: 3, 46, 55, 97, 118, 119, 121

[70] H. Ozawa, S. Taie, Y. Takasu, and Y. Takahashi. *Antiferromagnetic Spin Correlation of* SU($\mathcal{N}$) *Fermi Gas in an Optical Superlattice*. Phys. Rev. Lett. **121**, 225303 (2018). See page: 3

[71] A. V. Gorshkov, A. M. Rey, A. J. Daley, M. M. Boyd, J. Ye, P. Zoller, and M. D. Lukin. *Alkaline-Earth-Metal Atoms as Few-Qubit Quantum Registers*. Phys. Rev. Lett. **102**, 110503 (2009). See page: 3

[72] K. Shibata, S. Kato, A. Yamaguchi, S. Uetake, and Y. Takahashi. *A scalable quantum computer with ultranarrow optical transition of ultracold neutral atoms in an optical lattice*. Appl. Phys. B: Lasers Opt. **97**, 753–758 (2009).

[73] A. J. Daley, M. M. Boyd, J. Ye, and P. Zoller. *Quantum Computing with Alkaline-Earth-Metal Atoms*. Phys. Rev. Lett. **101** (2008). See pages: 4, 64

[74] A. J. Daley, J. Ye, and P. Zoller. *State-dependent lattices for quantum computing with alkaline-earth-metal atoms*. Eur. Phys. J. D **65**, 207–217 (2011). See pages: 4, 67

[75] G. Pagano, F. Scazza, and M. Foss-Feig. *Fast and Scalable Quantum Information Processing with Two-Electron Atoms in Optical Tweezer Arrays*. Advanced Quantum Technologies **0**, 1800067 (2019). See page: 3

[76] F. Gerbier and J. Dalibard. *Gauge fields for ultracold atoms in optical superlattices*. New J. Phys. **12**, 033007 (2010). See pages: 3, 65

[77] D. Banerjee, M. Bögli, M. Dalmonte, E. Rico, P. Stebler, U.-J. Wiese, and P. Zoller. *Atomic Quantum Simulation of U(N) and SU(N) Non-Abelian Lattice Gauge Theories*. Phys. Rev. Lett. **110**, 125303 (2013). See page: 3

[78] N. Goldman, F. Gerbier, and M. Lewenstein. *Realizing non-Abelian gauge potentials in optical square lattices: an application to atomic Chern insulators*. J. Phys. B: At., Mol. Opt. Phys. **46**, 134010 (2013). See page: 3

[79] Y. Nishida. *SU(3) Orbital Kondo Effect with Ultracold Atoms*. Phys. Rev. Lett. **111**, 135301 (2013). See page: 4

[80] M. Foss-Feig, M. Hermele, V. Gurarie, and A. M. Rey. *Heavy fermions in an optical lattice*. Phys. Rev. A **82**, 053624 (2010). See pages: 7, 94, 96, 97, 165, 172, 174, 180

[81] M. Foss-Feig, M. Hermele, and A. M. Rey. *Probing the Kondo lattice model with alkaline-earth-metal atoms*. Phys. Rev. A **81**, 051603 (2010). See pages: 4, 7, 82, 94, 95, 96, 97, 165, 172, 174, 175, 180

[82] M. Nakagawa and N. Kawakami. *Laser-Induced Kondo Effect in Ultracold Alkaline-Earth Fermions*. Phys. Rev. Lett. **115**, 165303 (2015). See pages: 177, 180, 181

[83] M. Nakagawa, N. Kawakami, and M. Ueda. *Non-Hermitian Kondo Effect in Ultracold Alkaline-Earth Atoms*. Phys. Rev. Lett. **121**, 203001 (2018). See page: 180

[84] R. Zhang, D. Zhang, Y. Cheng, W. Chen, P. Zhang, and H. Zhai. *Kondo effect in alkaline-earth-metal atomic gases with confinement-induced resonances*. Phys. Rev. A **93**, 043601 (2016). See pages: 4, 64, 91, 124, 152, 164, 180

[85] L.-M. Duan. *Controlling ultracold atoms in multi-band optical lattices for simulation of Kondo physics*. Europhys. Lett. **67**, 721 (2004). See pages: 4, 97

[86] J. Bauer, C. Salomon, and E. Demler. *Realizing a Kondo-Correlated State with Ultracold Atoms*. Phys. Rev. Lett. **111**, 215304 (2013). See page: 4

[87] B. Paredes, C. Tejedor, and J. Cirac. *Fermionic atoms in optical superlattices*. Phys. Rev. A **71**, 063608 (2005). See page: 4

[88] K. Ono, J. Kobayashi, Y. Amano, K. Sato, and Y. Takahashi. *Antiferromagnetic Interorbital Spin-Exchange Interaction of ^{171}Yb*. Preprint on arXiv:1810.00536 (2018). See pages: 4, 8, 41, 47, 88, 90, 97, 181

[89] R. Zhang, Y. Cheng, H. Zhai, and P. Zhang. *Orbital Feshbach Resonance in Alkali-Earth Atoms*. Phys. Rev. Lett. **115**, 135301 (2015). See pages: 4, 49, 50, 181

[90] M. Höfer, L. Riegger, F. Scazza, C. Hofrichter, D. R. Fernandes, M. M. Parish, J. Levinsen, I. Bloch, and S. Fölling. *Observation of an Orbital Interaction-Induced Feshbach Resonance in ^{173}*Yb. Phys. Rev. Lett. **115**, 265302 (2015). See pages: 34, 37, 47, 50, 51, 101, 107, 128, 135, 137, 138

[91] G. Pagano, M. Mancini, G. Cappellini, L. Livi, C. Sias, J. Catani, M. Inguscio, and L. Fallani. *Strongly Interacting Gas of Two-Electron Fermions at an Orbital Feshbach Resonance*. Phys. Rev. Lett. **115** (2015). See pages: 4, 34, 37, 49, 101, 181

[92] L. J. LeBlanc and J. H. Thywissen. *Species-specific optical lattices*. Phys. Rev. A **75**, 053612 (2007). See page: 4

[93] J. Bauer, E. Demler, and C. Salomon. *Employing confinement induced resonances to realize Kondo physics with ultracold atoms*. J. Phys.: Conf. Ser. **592**, 012151 (2015). See page: 4

[94] M. Anderlini, P. J. Lee, B. L. Brown, J. Sebby-Strabley, W. D. Phillips, and J. V. Porto. *Controlled exchange interaction between pairs of neutral atoms in an optical lattice*. Nature **448**, 452–456 (2007). See pages: 4, 150

[95] A. D. Ludlow, N. D. Lemke, J. A. Sherman, C. W. Oates, G. Quéméner, J. von Stecher, and A. M. Rey. *Cold-collision-shift cancellation and inelastic scattering in a Yb optical lattice clock*. Phys. Rev. A **84**, 052724 (2011). See pages: 4, 34, 79

[96] M. Bishof, Y. Lin, M. D. Swallows, A. V. Gorshkov, J. Ye, and A. M. Rey. *Resolved Atomic Interaction Sidebands in an Optical Clock Transition*. Phys. Rev. Lett. **106**, 250801 (2011). See page: 4

[97] F. Scazza. *Probing SU(N)-symmetric orbital interactions with ytterbium Fermi gases in optical lattices*. PhD thesis, Ludwig-Maximilians-Universität München (2015). See pages: 6, 35, 42, 44, 47, 63, 64, 79, 96, 99, 100, 106, 107, 108, 110, 112, 113, 140

[98] C. Hofrichter. *Probing the SU(N) Fermi-Hubbard model with ytterbium atoms in an optical lattice*. PhD thesis, Ludwig-Maximilians-Universität München (2016). See pages: 46, 55, 97, 101, 110, 112, 119

[99] M. Höfer. *A two-orbital quantum gas with tunable interactions*. PhD thesis, Ludwig-Maximilians-Universität München (2017). See pages: 6, 41, 50, 51, 99, 101, 106, 107, 128, 137, 138, 140, 141

[100] M. Kitagawa, K. Enomoto, K. Kasa, Y. Takahashi, R. Ciuryło, P. Naidon, and P. S. Julienne. *Two-color photoassociation spectroscopy of ytterbium atoms and the precise determinations of s-wave scattering lengths*. Phys. Rev. A **77**, 012719 (2008). See pages: 8, 41, 43

[101] A. Lurio, M. Mandel, and R. Novick. *Second-Order Hyperfine and Zeeman Corrections for an (sl) Configuration*. Phys. Rev. **126**, 1758–1767 (1962). See pages: 8, 11, 12, 13, 15, 16, 184

[102] C. Foot. *Atomic Physics*. Oxford University Press (2005). ISBN 9780198506959. See page: 8

[103] K. Pandey, A. K. Singh, P. V. K. Kumar, M. V. Suryanarayana, and V. Natarajan. *Isotope shifts and hyperfine structure in the 555.8-nm* $^1S_0 \rightarrow {}^3P_1$ *line of Yb*. Phys. Rev. A **80**, 022518 (2009). See pages: 9, 17, 183

[104] Y. Takasu, K. Komori, K. Honda, M. Kumakura, T. Yabuzaki, and Y. Takahashi. *Photoassociation Spectroscopy of Laser-Cooled Ytterbium Atoms*. Phys. Rev. Lett. **93**, 123202 (2004). See pages: 9, 190

[105] K. Beloy, J. A. Sherman, N. D. Lemke, N. Hinkley, C. W. Oates, and A. D. Ludlow. *Determination of the 5d6s* $^3\mathrm{D}_1$ *state lifetime and blackbody-radiation clock shift in Yb*. Phys. Rev. A **86**, 051404 (2012). See pages: 9, 116, 190

[106] S. G. Porsev and A. Derevianko. *Hyperfine quenching of the metastable* $^3P_{0,2}$ *states in divalent atoms*. Phys. Rev. A **69**, 042506 (2004). See pages: 9, 11, 35, 77

[107] J. W. Cho, H.-g. Lee, S. Lee, J. Ahn, W.-K. Lee, D.-H. Yu, S. K. Lee, and C. Y. Park. *Optical repumping of triplet-Pstates enhances magneto-optical trapping of ytterbium atoms*. Phys. Rev. A **85**, 035401 (2012). See pages: 9, 190

[108] M. Kleinert, M. E. Gold Dahl, and S. Bergeson. *Measurement of the Yb I* $^1S_0$-$^1P_1$ *transition frequency at 399 nm using an optical frequency comb*. Phys. Rev. A **94**, 052511 (2016). See page: 9

[109] G. Breit and L. A. Wills. *Hyperfine Structure in Intermediate Coupling*. Phys. Rev. **44**, 470–490 (1933). See page: 11

[110] C. Schwartz. *Theory of Hyperfine Structure*. Phys. Rev. **97**, 380–395 (1955). See pages: 11, 15, 184

[111] M. M. Boyd, T. Zelevinsky, A. D. Ludlow, S. Blatt, T. Zanon-Willette, S. M. Foreman, and J. Ye. *Nuclear spin effects in optical lattice clocks*. Phys. Rev. A **76**, 022510 (2007). See pages: 11, 12, 13, 16, 25, 34, 37, 38, 39, 43, 104, 183, 184

[112] E. Peik, G. Hollemann, and H. Walther. *Laser cooling and quantum jumps of a single indium ion*. Phys. Rev. A **49**, 402–408 (1994). See pages: 11, 16, 34, 37, 184

[113] T. Becker, J. v. Zanthier, A. Y. Nevsky, C. Schwedes, M. N. Skvortsov, H. Walther, and E. Peik. *High-resolution spectroscopy of a single* In^+ *ion: Progress towards an optical frequency standard*. Phys. Rev. A **63**, 051802 (2001). See page: 11

[114] P. J. Mohr, D. B. Newell, and B. N. Taylor. *CODATA recommended values of the fundamental physical constants: 2014*. Rev. Mod. Phys. **88**, 035009 (2016). See page: 12

[115] L. Olschewski and E. W. Otten. *Bestimmung der Kerndipolmomente von* ^{171}*Yb und* ^{173}*Yb durch optisches Pumpen*. Z. Physik **200**, 224–226 (1967). See page: 12

[116] J. Emsley. *The Elements*. Oxford chemistry guides. Clarendon Press (1998). ISBN 9780198558194. See page: 12

[117] G. H. Fuller. *Nuclear Spins and Moments*. J. Phys. Chem. Ref. Data **5**, 835–1092 (1976). See pages: 12, 105, 106

[118] L. Olschewski. *Messung der magnetischen Kerndipolmomente an freien ^{43}Ca-, ^{87}Sr-, ^{135}Ba-, ^{137}Ba-, ^{171}Yb- und ^{173}Yb-Atomen mit optischem Pumpen*. Z. Physik **249**, 205–227 (1972). See page: 12

[119] A. C. Gossard, V. Jaccarino, and J. H. Wernick. *Ytterbium NMR:*Yb^{171} *Nuclear Moment and Yb Metal Knight Shift*. Phys. Rev. **133**, A881–A884 (1964). See page: 12

[120] N. J. Stone. *Nuclear Magnetic Dipole and Electric Quadrupole Moments: Their Measurement and Tabulation as Accessible Data*. J. Phys. Chem. Ref. Data **44**, 031215 (2015). See pages: 12, 105, 106

[121] D. Steck. *Quantum and Atom Optics*. Available online at `https://steck.us/teaching/` (revision 0.10.2, 16 October 2015) (2007). See pages: 15, 18, 20, 21, 22, 24, 28, 30, 33, 115, 189

[122] R. H. Garstang. *Hyperfine Structure and Intercombination Line Intensities in the Spectra of Magnesium, Zinc, Cadmium, and Mercury*. J. Opt. Soc. Am. **52**, 845–851 (1962). See pages: 16, 184

[123] R. Grimm, M. Weidemüller, and Y. B. Ovchinnikov. *Optical Dipole Traps for Neutral Atoms*. Volume 42 of *Advances In Atomic, Molecular, and Optical Physics*, pages 95 – 170. Academic Press (2000). See pages: 17, 19, 20

[124] V. D. Ovsyannikov, V. G. Pal'chikov, H. Katori, and M. Takamoto. *Polarisation and dispersion properties of light shifts in ultrastable optical frequency standards*. Quantum Electronics **36**, 3 (2006). See pages: 21, 23

[125] V. A. Dzuba and A. Derevianko. *Dynamic polarizabilities and related properties of clock states of the ytterbium atom*. J. Phys. B: At. Mol. Opt. Phys. **43**, 074011 (2010). See pages: 24, 25, 26, 62, 63, 65, 76

[126] J. Mitroy, M. S. Safronova, and C. W. Clark. *Theory and applications of atomic and ionic polarizabilities*. J. Phys. B: At., Mol. Opt. Phys. **43**, 202001 (2010).

[127] K. Guo, G. Wang, and A. Ye. *Dipole polarizabilities and magic wavelengths for a Sr and Yb atomic optical lattice clock*. J. Phys. B: At., Mol. Opt. Phys. **43**, 135004 (2010).

[128] V. A. Dzuba, V. V. Flambaum, and S. Schiller. *Testing physics beyond the standard model through additional clock transitions in neutral ytterbium*. Phys. Rev. A **98**, 022501 (2018). See pages: 24, 25, 26, 28, 29, 34, 114

[129] Z. W. Barber, C. W. Hoyt, C. W. Oates, L. Hollberg, A. V. Taichenachev, and V. I. Yudin. *Direct Excitation of the Forbidden Clock Transition in Neutral* ^{174}Yb *Atoms Confined to an Optical Lattice*. Phys. Rev. Lett. **96**, 083002 (2006). See pages: 24, 26, 35, 39, 63, 102

[130] C. Cohen-Tannoudji, J. Dupont-Roc, and G. Grynberg. *Atom—Photon Interactions*. Wiley-VCH Verlag GmbH (1998). ISBN 978-3-527-61719-7. See page: 30

[131] H. J. Metcalf and P. van der Straten. *Laser Cooling and Trapping*. Springer, New York (1999). ISBN 9780387987286. See page: 30

[132] N. Poli, Z. W. Barber, N. D. Lemke, C. W. Oates, L. S. Ma, J. E. Stalnaker, T. M. Fortier, S. A. Diddams, L. Hollberg, J. C. Bergquist, A. Brusch, S. Jefferts, T. Heavner, and T. Parker. *Frequency evaluation of the doubly forbidden* $^1S_0 \rightarrow {}^3P_0$ *transition in bosonic* ^{174}Yb. Phys. Rev. A **77**, 050501 (2008). See pages: 34, 39, 102

[133] C. Clivati, G. Cappellini, L. F. Livi, F. Poggiali, M. S. de Cumis, M. Mancini, G. Pagano, M. Frittelli, A. Mura, G. A. Costanzo, F. Levi, D. Calonico, L. Fallani, J. Catani, and M. Inguscio. *Measuring absolute frequencies beyond the GPS limit via long-haul optical frequency dissemination*. Opt. Express **24**, 11865 (2016). See page: 34

[134] M. Pizzocaro, P. Thoumany, B. Rauf, F. Bregolin, G. Milani, C. Clivati, G. A. Costanzo, F. Levi, and D. Calonico. *Absolute frequency measurement of the* $^1S_0 \rightarrow {}^3P_0$ *transition of* ^{171}Yb. Metrologia **54**, 102–112 (2017). See page: 34

[135] A. V. Taichenachev, V. I. Yudin, C. W. Oates, C. W. Hoyt, Z. W. Barber, and L. Hollberg. *Magnetic Field-Induced Spectroscopy of Forbidden Optical Transitions with Application to Lattice-Based Optical Atomic Clocks*. Phys. Rev. Lett. **96**, 083001 (2006). See pages: 35, 39, 114

[136] N. D. Lemke. *Optical Lattice Clock with Spin-1/2 Ytterbium Atoms*. PhD thesis, University of Colorado at Boulder (2012). See page: 38

[137] S. G. Porsev, A. Derevianko, and E. N. Fortson. *Possibility of an optical clock using the* $6\,^1S_0 \rightarrow 6\,^3P_0$ *transition in* $^{171,173}Yb$ *atoms held in an optical lattice*. Phys. Rev. A **69**, 021403 (2004). See pages: 38, 104, 184

[138] K. Huang. *Statistical Mechanics*. John Wiley & Sons (1987). See pages: 40, 125

[139] T. Busch, B.-G. Englert, K. Rzażewski, and M. Wilkens. *Two Cold Atoms in a Harmonic Trap*. Found. Phys. **28**, 549–559 (1998). See pages: 40, 62, 125, 127, 128, 129

[140] W. V. Liu, F. Wilczek, and P. Zoller. *Spin-dependent Hubbard model and a quantum phase transition in cold atoms*. Phys. Rev. A **70**, 033603 (2004). See page: 40

[141] N. D. Lemke, J. von Stecher, J. A. Sherman, A. M. Rey, C. W. Oates, and A. D. Ludlow. *p-Wave Cold Collisions in an Optical Lattice Clock*. Phys. Rev. Lett. **107**, 103902 (2011). See page: 41

[142] H. T. C. Stoof, J. M. V. A. Koelman, and B. J. Verhaar. *Spin-exchange and dipole relaxation rates in atomic hydrogen: Rigorous and simplified calculations*. Phys. Rev. B **38**, 4688–4697 (1988). See page: 41

[143] J. J. García-Ripoll, S. Dürr, N. Syassen, D. M. Bauer, M. Lettner, G. Rempe, and J. I. Cirac. *Dissipation-induced hard-core boson gas in an optical lattice*. New J. Phys. **11**, 013053 (2009). See pages: 41, 80, 81

[144] D. M. Stamper-Kurn and M. Ueda. *Spinor Bose gases: Symmetries, magnetism, and quantum dynamics*. Rev. Mod. Phys. **85**, 1191–1244 (2013). See page: 42

[145] S.-K. Yip and T.-L. Ho. *Zero sound modes of dilute Fermi gases with arbitrary spin*. Phys. Rev. A **59**, 4653–4656 (1999). See page: 42

[146] J. S. Krauser, J. Heinze, N. Fläschner, S. Götze, O. Jürgensen, D.-S. Lühmann, C. Becker, and K. Sengstock. *Coherent multi-flavour spin dynamics in a fermionic quantum gas*. Nature Physics **8**, 813 EP – (2012). See page: 42

[147] U. Ebling, J. S. Krauser, N. Fläschner, K. Sengstock, C. Becker, M. Lewenstein, and A. Eckardt. *Relaxation Dynamics of an Isolated Large-Spin Fermi Gas Far from Equilibrium*. Phys. Rev. X **4**, 021011 (2014).

[148] J. S. Krauser, U. Ebling, N. Fläschner, J. Heinze, K. Sengstock, M. Lewenstein, A. Eckardt, and C. Becker. *Giant Spin Oscillations in an Ultracold Fermi Sea*. Science **343**, 157–160 (2014).

[149] U. Ebling and A. Eckardt. *Spin Relaxation in a One-Dimensional Large-Spin Degenerate Fermi Gas*. Preprint on arXiv:1612.02618 (2016). See page: 42

[150] R. W. Cherng, G. Refael, and E. Demler. *Superfluidity and Magnetism in Multicomponent Ultracold Fermions*. Phys. Rev. Lett. **99**, 130406 (2007). See page: 45

[151] L. Bonnes, K. R. A. Hazzard, S. R. Manmana, A. M. Rey, and S. Wessel. *Adiabatic Loading of One-Dimensional SU(N) Alkaline-Earth-Atom Fermions in Optical Lattices*. Phys. Rev. Lett. **109**, 205305 (2012). See pages: 45, 181

[152] K. R. A. Hazzard, V. Gurarie, M. Hermele, and A. M. Rey. *High-temperature properties of fermionic alkaline-earth-metal atoms in optical lattices*. Phys. Rev. A **85**, 041604 (2012). See page: 181

[153] E. V. Gorelik and N. Blümer. *Mott transitions in ternary flavor mixtures of ultracold fermions on optical lattices*. Phys. Rev. A **80**, 051602 (2009). See page: 45

[154] S. R. Manmana, K. R. A. Hazzard, G. Chen, A. E. Feiguin, and A. M. Rey. *SU(N) magnetism in chains of ultracold alkaline-earth-metal atoms: Mott transitions and quantum correlations*. Phys. Rev. A **84**, 043601 (2011). See pages: 46, 181

[155] H. Song and M. Hermele. *Mott insulators of ultracold fermionic alkaline earth atoms in three dimensions*. Phys. Rev. B **87**, 144423 (2013). See page: 46

[156] C. Honerkamp and W. Hofstetter. *Ultracold Fermions and the SU(N) Hubbard Model*. Phys. Rev. Lett. **92**, 170403 (2004). See page: 46

[157] F. F. Assaad. *Phase diagram of the half-filled two-dimensional* SU(N) *Hubbard-Heisenberg model: A quantum Monte Carlo study*. Phys. Rev. B **71**, 075103 (2005). See page: 46

[158] G. Pasqualetti. *Isotopic mixtures of ytterbium for quantum simulation of Kondo physics*. Master's thesis, Ludwig-Maximilians-Universität München (2018). See pages: 47, 88, 106, 181

[159] S. G. Porsev, M. S. Safronova, A. Derevianko, and C. W. Clark. *Long-range interaction coefficients for ytterbium dimers*. Phys. Rev. A **89**, 012711 (2014). See page: 51

[160] V. V. Flambaum, G. F. Gribakin, and C. Harabati. *Analytical calculation of cold-atom scattering*. Phys. Rev. A **59**, 1998–2005 (1999). See page: 51

[161] C. A. Regal, M. Greiner, and D. S. Jin. *Lifetime of Molecule-Atom Mixtures near a Feshbach Resonance in* ^{40}K. Phys. Rev. Lett. **92**, 083201 (2004). See page: 51

[162] J. Xu, R. Zhang, Y. Cheng, P. Zhang, R. Qi, and H. Zhai. *Reaching a Fermi-superfluid state near an orbital Feshbach resonance*. Phys. Rev. A **94**, 033609 (2016). See page: 51

[163] J.-G. Chen, T.-S. Deng, W. Yi, and W. Zhang. *Polarons and molecules in a Fermi gas with orbital Feshbach resonance*. Phys. Rev. A **94**, 053627 (2016). See page: 51

[164] J.-G. Chen, Y.-R. Shi, X. Zhang, and W. Zhang. *Polarons in alkaline-earth-like atoms with multiple background Fermi surfaces*. Front. Phys. **13**, 136702 (2018).

[165] T.-S. Deng, Z.-C. Lu, Y.-R. Shi, J.-G. Chen, W. Zhang, and W. Yi. *Repulsive polarons in alkaline-earth-metal-like atoms across an orbital Feshbach resonance*. Phys. Rev. A **97**, 013635 (2018). See page: 51

[166] I. Bloch, J. Dalibard, and S. Nascimbène. *Quantum simulations with ultracold quantum gases*. Nat. Phys. **8**, 267–276 (2012). See page: 53

[167] N. Ashcroft and N. Mermin. *Solid State Physics*. HRW international editions. Holt, Rinehart and Winston (1976). ISBN 9780030839931. See pages: 55, 194

[168] C. Kittel, P. McEuen, and P. McEuen. *Introduction to solid state physics*. Wiley New York, 7 edition (1996). See page: 55

[169] U. Schneider. *Interacting Fermionic Atoms in Optical Lattices - A Quantum Simulator for Condensed Matter Physics*. PhD thesis, Mainz (2010). See pages: 56, 196

[170] O. Morsch and M. Oberthaler. *Dynamics of Bose-Einstein condensates in optical lattices*. Rev. Mod. Phys. **78**, 179–215 (2006). See page: 57

[171] W. Kohn. *Analytic Properties of Bloch Waves and Wannier Functions*. Phys. Rev. **115**, 809–821 (1959). See page: 59

[172] L. Riegger, N. Darkwah Oppong, M. Höfer, D. R. Fernandes, I. Bloch, and S. Fölling. *Localized Magnetic Moments with Tunable Spin Exchange in a Gas of Ultracold Fermions*. Phys. Rev. Lett. **120**, 143601 (2018). See pages: 61, 91, 92, 123, 145, 146, 152, 153

[173] Z. Barber, J. Stalnaker, N. Lemke, N. Poli, C. Oates, T. Fortier, S. Diddams, L. Hollberg, C. Hoyt, A. Taichenachev, and V. Yudin. *Optical Lattice Induced Light Shifts in an Yb Atomic Clock*. Phys. Rev. Lett. **100**, 103002 (2008). See page: 63

[174] N. Lemke, A. Ludlow, Z. Barber, T. Fortier, S. Diddams, Y. Jiang, S. Jefferts, T. Heavner, T. Parker, and C. Oates. *Spin-1/2 Optical Lattice Clock*. Phys. Rev. Lett. **103**, 063001 (2009). See page: 63

[175] G. Cappellini. *Two-Orbital Quantum Physics in Yb Fermi Gases Exploiting the* $^1S_0 \rightarrow {}^3P_0$ *Clock Transition*. PhD thesis, Universita degli Studi Firenze (2015). See page: 64

[176] C. Schweizer. *A Bi-Chromatic Optical Lattice Setup for Kondo-Lattice Physics with Ultracold Ytterbium Atoms*. Master's thesis, Ludwig-Maximilians-Universität München (2013). See page: 64

[177] Y. Cheng, R. Zhang, P. Zhang, and H. Zhai. *Enhancing Kondo coupling in alkaline-earth-metal atomic gases with confinement-induced resonances in mixed dimensions*. Phys. Rev. A **96**, 063605 (2017). See pages: 64, 124

[178] R. Zhang and P. Zhang. *Control of spin-exchange interaction between alkali-earth-metal atoms via confinement-induced resonances in a quasi-(1+0)-dimensional system*. Phys. Rev. A **98**, 043627 (2018). See pages: 64, 124, 152, 153, 180

[179] W. Yi, A. J. Daley, G. Pupillo, and P. Zoller. *State-dependent, addressable subwavelength lattices with cold atoms*. New J. Phys. **10**, 073015 (2008). See pages: 65, 173

[180] O. Mandel, M. Greiner, A. Widera, T. Rom, T. W. Hänsch, and I. Bloch. *Coherent Transport of Neutral Atoms in Spin-Dependent Optical Lattice Potentials*. Phys. Rev. Lett. **91**, 010407 (2003). See page: 67

[181] M. Karski, L. Forster, J.-M. Choi, A. Steffen, W. Alt, D. Meschede, and A. Widera. *Quantum Walk in Position Space with Single Optically Trapped Atoms*. Science **325**, 174–177 (2009).

[182] B. Gadway, D. Pertot, R. Reimann, and D. Schneble. *Superfluidity of Interacting Bosonic Mixtures in Optical Lattices*. Phys. Rev. Lett. **105**, 045303 (2010). See page: 67

[183] G. Jotzu, M. Messer, F. Görg, D. Greif, R. Desbuquois, and T. Esslinger. *Creating State-Dependent Lattices for Ultracold Fermions by Magnetic Gradient Modulation*. Phys. Rev. Lett. **115**, 073002 (2015). See page: 67

[184] A. Ludlow. *The Strontium Optical Lattice Clock: Optical Spectroscopy with Sub-Hertz Accuracy*. PhD thesis, Graduate School of the University of Colorado (2008). See page: 70

[185] S. Blatt. *Ultracold Collisions and Fundamental Physics with Strontium*. PhD thesis, Graduate School of the University of Colorado (2011). See page: 70

[186] R. Jáuregui, N. Poli, G. Roati, and G. Modugno. *Anharmonic parametric excitation in optical lattices*. Phys. Rev. A **64**, 033403 (2001). See page: 71

[187] D. Leibfried, R. Blatt, C. Monroe, and D. Wineland. *Quantum dynamics of single trapped ions*. Rev. Mod. Phys. **75**, 281–324 (2003). See page: 72

[188] K. Sponselee, L. Freystatzky, B. Abeln, M. Diem, B. Hundt, A. Kochanke, T. Ponath, B. Santra, L. Mathey, K. Sengstock, and C. Becker. *Dynamics of Ultracold Quantum Gases in the Dissipative Fermi-Hubbard Model*. ArXiv e-prints (2018). See pages: 79, 80, 81, 82, 84, 85, 164

[189] B. Yan, S. A. Moses, B. Gadway, J. P. Covey, K. R. A. Hazzard, A. M. Rey, D. S. Jin, and J. Ye. *Observation of dipolar spin-exchange interactions with lattice-confined polar molecules*. Nature **501** (2013). See page: 81

[190] B. Zhu, B. Gadway, M. Foss-Feig, J. Schachenmayer, M. L. Wall, K. R. A. Hazzard, B. Yan, S. A. Moses, J. P. Covey, D. S. Jin, J. Ye, M. Holland, and A. M. Rey. *Suppressing the Loss of Ultracold Molecules Via the Continuous Quantum Zeno Effect*. Phys. Rev. Lett. **112**, 070404 (2014). See pages: 81, 85

[191] S. K. Baur and E. J. Mueller. *Two-body recombination in a quantum-mechanical lattice gas: Entropy generation and probing of short-range magnetic correlations*. Phys. Rev. A **82**, 023626 (2010). See page: 81

[192] S. Dürr, J. J. García-Ripoll, N. Syassen, D. M. Bauer, M. Lettner, J. I. Cirac, and G. Rempe. *Lieb-Liniger model of a dissipation-induced Tonks-Girardeau gas*. Phys. Rev. A **79**, 023614 (2009). See page: 85

[193] A. Sotnikov, A. Cichy, and J. Kuneš. *Suppression and revival of long-range ferromagnetic order in the multiorbital Fermi-Hubbard model*. Phys. Rev. B **97**, 235157 (2018). See pages: 86, 88

[194] A. Cichy and A. Sotnikov. *Orbital magnetism of ultracold fermionic gases in a lattice: Dynamical mean-field approach*. Phys. Rev. A **93**, 053624 (2016). See page: 88

[195] P. Nozières. *A Fermi-liquid description of the Kondo problem at low temperatures*. J. Low Temp. Phys. **17**, 31–42 (1974). See page: 89

[196] J. R. Schrieffer and P. A. Wolff. *Relation between the Anderson and Kondo Hamiltonians*. Phys. Rev. **149**, 491–492 (1966). See pages: 89, 93, 160

[197] W. Koller, A. C. Hewson, and D. Meyer. *Singular dynamics of underscreened magnetic impurity models*. Phys. Rev. B **72**, 045117 (2005). See page: 90

[198] P. W. Anderson. *A poor man's derivation of scaling laws for the Kondo problem*. J. Phys. C: Solid State Phys. **3**, 2436–2441 (1970). See pages: 90, 91

[199] Y. Ashida, T. Shi, M. C. Bañuls, J. I. Cirac, and E. Demler. *Solving Quantum Impurity Problems in and out of Equilibrium with the Variational Approach*. Phys. Rev. Lett. **121**, 026805 (2018). See page: 92

[200] J. Korringa. *Nuclear magnetic relaxation and resonnance line shift in metals*. Physica **16**, 601–610 (1950). See page: 92

[201] W. Zwerger. *Dynamics of a dissipative two level system*. Z. Physik B **53**, 53–62 (1983). See pages: 92, 181

[202] F. B. Anders and A. Schiller. *Spin precession and real-time dynamics in the Kondo model: Time-dependent numerical renormalization-group study*. Phys. Rev. B **74**, 245113 (2006). See pages: 92, 147, 164

[203] H. Tsunetsugu, M. Sigrist, and K. Ueda. *The ground-state phase diagram of the one-dimensional Kondo lattice model*. Rev. Mod. Phys. **69**, 809–864 (1997). See pages: 93, 94, 95, 96, 181

[204] P. Sinjukow and W. Nolting. *Exact mapping of periodic Anderson model to Kondo lattice model*. Phys. Rev. B **65**, 212303 (2002). See page: 93

[205] P. Gegenwart, Q. Si, and F. Steglich. *Quantum criticality in heavy-fermion metals*. Nature Physics **4**, 186 (2008). See pages: 94, 95

[206] C. Lacroix and M. Cyrot. *Phase diagram of the Kondo lattice*. Phys. Rev. B **20**, 1969–1976 (1979). See pages: 94, 95, 172

[207] J. Kienert and W. Nolting. *Magnetic phase diagram of the Kondo lattice model with quantum localized spins*. Phys. Rev. B **73**, 224405 (2006). See pages: 94, 95, 96

[208] S. Yunoki, J. Hu, A. L. Malvezzi, A. Moreo, N. Furukawa, and E. Dagotto. *Phase Separation in Electronic Models for Manganites*. Phys. Rev. Lett. **80**, 845–848 (1998). See page: 95

[209] D. J. Garcia, K. Hallberg, B. Alascio, and M. Avignon. *Spin Order in One-Dimensional Kondo and Hund Lattices*. Phys. Rev. Lett. **93**, 177204 (2004). See pages: 94, 95, 96

[210] M. A. Ruderman and C. Kittel. *Indirect Exchange Coupling of Nuclear Magnetic Moments by Conduction Electrons*. Phys. Rev. **96**, 99–102 (1954). See page: 94

[211] T. Kasuya. *A Theory of Metallic Ferro- and Antiferromagnetism on Zener's Model*. Prog. Theor. Phys. **16**, 45–57 (1956).

[212] K. Yosida. *Magnetic Properties of Cu-Mn Alloys*. Phys. Rev. **106**, 893–898 (1957). See page: 94

[213] A. P. Ramirez. *Colossal magnetoresistance*. J. Phys.: Condens. Matter **9**, 8171 (1997). See page: 96

[214] Y. A. Izyumov and Y. N. Skryabin. *Double exchange model and the unique properties of the manganites*. Physics-Uspekhi **44**, 109 (2001). See page: 96

[215] M. Feldbacher, C. Jurecka, F. F. Assaad, and W. Brenig. *Single-hole dynamics in the half-filled two-dimensional Kondo-Hubbard model*. Phys. Rev. B **66**, 045103 (2002). See page: 97

[216] T. Yanagisawa and Y. Shimoi. *Ground State of the Kondo-Hubbard Model at Half Filling*. Phys. Rev. Lett. **74**, 4939–4942 (1995). See page: 97

[217] J. Silva-Valencia and A. M. C. Souza. *Entanglement of alkaline-earth-metal fermionic atoms confined in optical lattices*. Phys. Rev. A **85**, 033612 (2012). See page: 97

[218] J. Silva-Valencia and A. M. C. Souza. *Ground state of alkaline-earth fermionic atoms in one-dimensional optical lattices*. Eur. Phys. J. B **85**, 5 (2012). See page: 97

[219] L. Isaev, J. Schachenmayer, and A. M. Rey. *Spin-Orbit-Coupled Correlated Metal Phase in Kondo Lattices: An Implementation with Alkaline-Earth Atoms*. Phys. Rev. Lett. **117**, 135302 (2016). See pages: 98, 181

[220] B. Coqblin and J. R. Schrieffer. *Exchange Interaction in Alloys with Cerium Impurities*. Phys. Rev. **185**, 847–853 (1969). See pages: 98, 181

[221] I. Kuzmenko, T. Kuzmenko, Y. Avishai, and G.-B. Jo. *Coqblin-Schrieffer model for an ultracold gas of ytterbium atoms with metastable state*. Phys. Rev. B **93**, 115143 (2016). See pages: 98, 181

[222] C. Pepin and P. Coleman. *Breakdown of the Fermi liquid theory in heavy fermion compounds*. Preprint on arXiv:cond-mat/0211284 (2002). See pages: 98, 181

[223] I. Kuzmenko and Y. Avishai. *SU(12) Kondo effect in a carbon nanotube quantum dot*. Phys. Rev. B **89**, 195110 (2014). See pages: 98, 181

[224] G. M. Bruun and K. Burnett. *Interacting Fermi gas in a harmonic trap*. Phys. Rev. A **58**, 2427–2434 (1998). See page: 110

[225] M. Köhl. *Thermometry of fermionic atoms in an optical lattice*. Phys. Rev. A **73**, 031601 (2006). See page: 112

[226] P. Ketterer. *A stable laser setup for the 578 nm clock transition of Ytterbium*. Master's thesis, Johannes Gutenberg Universität Mainz (2012). See page: 113

[227] B. Hundt. *Optical Potentials for the Realization of Dissipative Fermi-Hubbard Models with Ultracold Ytterbium Atoms*. PhD thesis, Universität Hamburg, Hamburg (2016). See pages: 115, 116

[228] N. V. Vitanov, T. Halfmann, B. W. Shore, and K. Bergmann. *Laser-induced population transfer by adiabatic passage techniques*. Ann. Rev. Phys. Chem. **52**, 763–809 (2001). See page: 115

[229] G. Pasqualetti. *Report 1389nm Ytterbium Repumper*. Technical report, Ludwig-Maximilians-Universität München (2017). See page: 116

[230] C.-L. Hung and C. Chin. *In Situ Imaging of Atomic Quantum Gases*. In P. Törmä and K. Sengstock, editors, *Quantum Gas Experiments: Exploring Many-body States*, Cold Atoms, Chapter *6*. Imperial College Press, London (2014). See pages: 120, 121

[231] G. Reinaudi, T. Lahaye, Z. Wang, and D. Guéry-Odelin. *Strong saturation absorption imaging of dense clouds of ultracold atoms*. Opt. Lett. **32**, 3143 (2007). See pages: 120, 121

[232] K. Hueck, N. Luick, L. Sobirey, J. Siegl, T. Lompe, H. Moritz, L. W. Clark, and C. Chin. *Calibrating high intensity absorption imaging of ultracold atoms*. Opt. Express **25**, 8670–8679 (2017). See page: 121

[233] T. Sleator, T. Pfau, V. Balykin, O. Carnal, and J. Mlynek. *Experimental demonstration of the optical Stern-Gerlach effect*. Phys. Rev. Lett. **68**, 1996–1999 (1992). See page: 121

[234] S. Taie, Y. Takasu, S. Sugawa, R. Yamazaki, T. Tsujimoto, R. Murakami, and Y. Takahashi. *Realization of a* SU(2) × SU(6) *System of Fermions in a Cold Atomic Gas*. Phys. Rev. Lett. **105**, 190401 (2010). See page: 121

[235] Z. Idziaszek and T. Calarco. *Two atoms in an anisotropic harmonic trap*. Phys. Rev. A **71**, 050701 (2005). See pages: 123, 127, 128, 130, 137

[236] Y. Nishida and S. Tan. *Universal Fermi Gases in Mixed Dimensions*. Phys. Rev. Lett. **101**, 170401 (2008). See page: 124

[237] P. Massignan and Y. Castin. *Three-dimensional strong localization of matter waves by scattering from atoms in a lattice with a confinement-induced resonance*. Phys. Rev. A **74**, 013616 (2006).

[238] G. Lamporesi, J. Catani, G. Barontini, Y. Nishida, M. Inguscio, and F. Minardi. *Scattering in Mixed Dimensions with Ultracold Gases*. Phys. Rev. Lett. **104**, 153202 (2010). See page: 124

[239] F. Deuretzbacher, K. Plassmeier, D. Pfannkuche, F. Werner, C. Ospelkaus, S. Ospelkaus, K. Sengstock, and K. Bongs. *Heteronuclear molecules in an optical lattice: Theory and experiment*. Phys. Rev. A **77**, 032726 (2008). See pages: 127, 131, 133

[240] S. Sala and A. Saenz. *Theory of inelastic confinement-induced resonances due to the coupling of center-of-mass and relative motion*. Phys. Rev. A **94**, 022713 (2016). See pages: 130, 131, 132, 133, 144, 163

[241] M. Olshanii. *Atomic Scattering in the Presence of an External Confinement and a Gas of Impenetrable Bosons*. Phys. Rev. Lett. **81**, 938–941 (1998). See pages: 130, 131, 132

[242] T. Bergeman, M. G. Moore, and M. Olshanii. *Atom-Atom Scattering under Cylindrical Harmonic Confinement: Numerical and Analytic Studies of the Confinement Induced Resonance*. Phys. Rev. Lett. **91**, 163201 (2003). See pages: 130, 132

[243] D. S. Petrov and G. V. Shlyapnikov. *Interatomic collisions in a tightly confined Bose gas*. Phys. Rev. A **64**, 012706 (2001). See page: 130

[244] S. Sala, G. Zürn, T. Lompe, A. N. Wenz, S. Murmann, F. Serwane, S. Jochim, and A. Saenz. *Coherent Molecule Formation in Anharmonic Potentials Near Confinement-Induced Resonances*. Phys. Rev. Lett. **110**, 203202 (2013). See pages: 131, 132

[245] C. Ospelkaus, S. Ospelkaus, L. Humbert, P. Ernst, K. Sengstock, and K. Bongs. *Ultracold Heteronuclear Molecules in a 3D Optical Lattice*. Phys. Rev. Lett. **97**, 120402 (2006). See page: 131

[246] S. Sala, P.-I. Schneider, and A. Saenz. *Inelastic Confinement-Induced Resonances in Low-Dimensional Quantum Systems*. Phys. Rev. Lett. **109**, 073201 (2012). See page: 131

[247] E. Haller, M. J. Mark, R. Hart, J. G. Danzl, L. Reichsöllner, V. Melezhik, P. Schmelcher, and H.-C. Nägerl. *Confinement-Induced Resonances in Low-Dimensional Quantum Systems*. Phys. Rev. Lett. **104**, 153203 (2010). See pages: 132, 156, 163

[248] S. Grishkevich, S. Sala, and A. Saenz. *Theoretical description of two ultracold atoms in finite three-dimensional optical lattices using realistic interatomic interaction potentials*. Phys. Rev. A **84**, 062710 (2011). See page: 133

[249] J. Mentink and S. Kokkelmans. *Two interacting atoms in an optical lattice site with anharmonic terms*. Phys. Rev. A **79**, 032709 (2009). See page: 133

[250] F. Werner, O. Parcollet, A. Georges, and S. R. Hassan. *Interaction-Induced Adiabatic Cooling and Antiferromagnetism of Cold Fermions in Optical Lattices*. Phys. Rev. Lett. **95**, 056401 (2005). See page: 134

[251] H. P. Büchler. *Microscopic Derivation of Hubbard Parameters for Cold Atomic Gases*. Phys. Rev. Lett. **104**, 090402 (2010). See pages: 134, 155, 156

[252] Private communication with M. M. Parish and J. Levinsen, Monash University (2017). See page: 137

[253] E. L. Bolda, E. Tiesinga, and P. S. Julienne. *Effective-scattering-length model of ultracold atomic collisions and Feshbach resonances in tight harmonic traps*. Phys. Rev. A **66** (2002). See page: 137

[254] J. Walraven. *Quantum Gases - Statistics and Interactions*. (2014). See pages: 137, 138

[255] S. Trotzky, P. Cheinet, S. Folling, M. Feld, U. Schnorrberger, A. M. Rey, A. Polkovnikov, E. A. Demler, M. D. Lukin, and I. Bloch. *Time-Resolved Observation and Control of Superexchange Interactions with Ultracold Atoms in Optical Lattices*. Science **319**, 295–299 (2008). See pages: 150, 157

[256] Y. Cheng, R. Zhang, P. Zhang, and H. Zhai. *Enhancing Kondo Coupling in Alkaline-Earth Atomic Gases with Confinement-Induced Resonances in Mixed Dimensions*. arXiv:1705.06878 [cond-mat] (2017). See page: 152

[257] L.-M. Duan, E. Demler, and M. D. Lukin. *Controlling Spin Exchange Interactions of Ultracold Atoms in Optical Lattices*. Phys. Rev. Lett. **91**, 090402 (2003). See page: 157

[258] N. Strohmaier, Y. Takasu, K. Günter, R. Jördens, M. Köhl, H. Moritz, and T. Esslinger. *Interaction-Controlled Transport of an Ultracold Fermi Gas*. Phys. Rev. Lett. **99**, 220601 (2007). See pages: 165, 168

[259] L. Pezzè, L. Pitaevskii, A. Smerzi, S. Stringari, G. Modugno, E. de Mirandes, F. Ferlaino, H. Ott, G. Roati, and M. Inguscio. *Insulating Behavior of a Trapped Ideal Fermi Gas*. Phys. Rev. Lett. **93**, 120401 (2004). See pages: 165, 166, 167, 168, 172

[260] M. Rigol and A. Muramatsu. *Confinement control by optical lattices*. Phys. Rev. A **70**, 043627 (2004). See page: 166

[261] C. Hooley and J. Quintanilla. *Single-Atom Density of States of an Optical Lattice*. Phys. Rev. Lett. **93**, 080404 (2004).

[262] P. B. Blakie, A. Bezett, and P. Buonsante. *Degenerate Fermi gas in a combined harmonic-lattice potential*. Phys. Rev. A **75**, 063609 (2007). See page: 166

[263] A. M. Rey, G. Pupillo, C. W. Clark, and C. J. Williams. *Ultracold atoms confined in an optical lattice plus parabolic potential: A closed-form approach*. Phys. Rev. A **72**, 033616 (2005). See page: 166

[264] M. Krämer, C. Menotti, L. Pitaevskii, and S. Stringari. *Bose-Einstein condensates in 1D optical lattices*. Eur. Phys. J. D **27**, 247–261 (2003). See page: 168

[265] H. Ott, E. de Mirandes, F. Ferlaino, G. Roati, G. Modugno, and M. Inguscio. *Collisionally Induced Transport in Periodic Potentials*. Phys. Rev. Lett. **92**, 160601 (2004). See page: 168

[266] C. Lacroix. *Some exact results for the Kondo lattice with infinite exchange interaction*. Solid State Commun. **54**, 991 – 994 (1985). See page: 174

[267] Y. Zhong, Y. Liu, and H.-G. Luo. *Simulating heavy fermion physics in optical lattice: Periodic Anderson model with harmonic trapping potential*. Front. Phys. **12** (2017). See page: 180

[268] F. Görg, M. Messer, K. Sandholzer, G. Jotzu, R. Desbuquois, and T. Esslinger. *Enhancement and sign change of magnetic correlations in a driven quantum many-body system*. Nature **553** (2018).

[269] I. Kuzmenko, T. Kuzmenko, and Y. Avishai. *Optical Control of Exchange Interaction and Kondo Temperature in Cold Atom Gas*. arXiv:1801.00482 [cond-mat, physics:physics] (2018). See page: 180

[270] L. Kouwenhoven and L. Glazman. *Revival of the Kondo effect*. Phys. World **14**, 33–38 (2001). See page: 180

[271] M. Miranda, R. Inoue, Y. Okuyama, A. Nakamoto, and M. Kozuma. *Site-resolved imaging of ytterbium atoms in a two-dimensional optical lattice*. Phys. Rev. A **91**, 063414 (2015). See page: 180

[272] R. Yamamoto, J. Kobayashi, T. Kuno, K. Kato, and Y. Takahashi. *An ytterbium quantum gas microscope with narrow-line laser cooling*. New J. Phys. **18**, 023016 (2016). See page: 180

[273] M. A. Nichols, L. W. Cheuk, M. Okan, T. R. Hartke, E. Mendez, T. Senthil, E. Khatami, H. Zhang, and M. W. Zwierlein. *Spin transport in a Mott insulator of ultracold fermions*. Science (2018). See page: 180

[274] A. Lamacraft. *Kondo Polarons in a One-Dimensional Fermi Gas*. Phys. Rev. Lett. **101**, 225301 (2008). See page: 181

[275] M. M. Parish and J. Levinsen. *Highly polarized Fermi gases in two dimensions*. Phys. Rev. A **87**, 033616 (2013). See page: 182

[276] P. W. Anderson. *Infrared Catastrophe in Fermi Gases with Local Scattering Potentials*. Phys. Rev. Lett. **18**, 1049–1051 (1967). See page: 182

[277] P. Nozières and C. T. De Dominicis. *Singularities in the X-Ray Absorption and Emission of Metals. III. One-Body Theory Exact Solution*. Phys. Rev. **178**, 1097–1107 (1969). See page: 182

[278] J. Goold, T. Fogarty, N. Lo Gullo, M. Paternostro, and T. Busch. *Orthogonality catastrophe as a consequence of qubit embedding in an ultracold Fermi gas*. Phys. Rev. A **84**, 063632 (2011). See page: 182

[279] M. Knap, A. Shashi, Y. Nishida, A. Imambekov, D. A. Abanin, and E. Demler. *Time-Dependent Impurity in Ultracold Fermions: Orthogonality Catastrophe and Beyond*. Phys. Rev. X **2**, 041020 (2012). See page: 182

[280] S. G. Porsev, Y. G. Rakhlina, and M. G. Kozlov. *Calculation of hyperfine structure constants for ytterbium*. J. Phys. B: At. Mol. Opt. Phys. **32**, 1113–1120 (1999). See pages: 183, 188

[281] D. Das, S. Barthwal, A. Banerjee, and V. Natarajan. *Absolute frequency measurements in Yb with 0.08ppb uncertainty: Isotope shifts and hyperfine structure in the 399-nm* $^1S_0 \rightarrow ^1P_1$ *line*. Phys. Rev. A **72**, 032506 (2005). See pages: 183, 185

[282] A. Yamaguchi. *Metastable State of Ultracold and Quantum Degenerate Ytterbium Atoms: High-resolution Spectroscopy and Cold Collisions*. PhD thesis (2008). See pages: 183, 186, 187

[283] C. J. Bowers, D. Budker, S. J. Freedman, G. Gwinner, J. E. Stalnaker, and D. DeMille. *Experimental investigation of the $6s^2\,{}^1S_0 \rightarrow 5d6s\,{}^3D_{1,2}$ forbidden transitions in atomic ytterbium*. Phys. Rev. A **59**, 3513–3526 (1999). See page: 183

[284] W. Meggers and J. Tech. *1st Spectrum of Ytterbium (Yb I)*. J. Res. Natl. Inst. Stan. **83**, 13–70 (1978). See page: 190

[285] C. J. Bowers, D. Budker, E. D. Commins, D. DeMille, S. J. Freedman, A.-T. Nguyen, S.-Q. Shang, and M. Zolotorev. *Experimental investigation of excited-state lifetimes in atomic ytterbium*. Phys. Rev. A **53**, 3103–3109 (1996).

[286] A. Kramida, Y. Ralchenko, J. Reader, and NIST ASD Team. *NIST Atomic Spectra Database (ver. 5.5.6)*. [Online]. Available: https://physics.nist.gov/asd [2017, April 9]. National Institute of Standards and Technology, Gaithersburg, MD. (2018). See page: 190

[287] K. Blagoev and V. Komarovskii. *Lifetimes of Levels of Neutral and Singly Ionized Lanthanide Atoms*. Atomic Data and Nuclear Data Tables **56**, 1 – 40 (1994). See page: 190

[288] M. Baumann, M. Braun, A. Gaiser, and H. Liening. *Radiative lifetimes and g_J factors of low-lying even-parity levels in the Yb I spectrum*. J. Phys. B: At. Mol. Phys. **18**, L601 (1985). See page: 190

[289] D. A. Butts and D. S. Rokhsar. *Trapped Fermi gases*. Phys. Rev. A **55**, 4346–4350 (1997). See pages: 193, 195

[290] G. M. Bruun and C. W. Clark. *Ideal gases in time-dependent traps*. Phys. Rev. A **61**, 061601 (2000). See pages: 193, 195

[291] J. R. Engelbrecht, M. Randeria, and L. Zhang. *Landau f function for the dilute Fermi gas in two dimensions*. Phys. Rev. B **45**, 10135–10138 (1992). See page: 193

[292] L. D. Carr, G. V. Shlyapnikov, and Y. Castin. *Achieving a BCS Transition in an Atomic Fermi Gas*. Phys. Rev. Lett. **92**, 150404 (2004). See page: 194

Danksagung

Zum Ende dieser Doktorarbeit möchte ich zunächst meinem Doktorvater Prof. Immanuel Bloch danken, der mir die Gelegenheit gegeben hat, Teil einer großartigen Arbeitsgruppe und einer motivierenden wissenschaftlichen Umgebung zu sein. Ebenfalls danke ich meinem Gruppenleiter Simon Fölling für die gute Betreuung unserer Arbeit am Ytterbiumexperiment. Von seinem beinahe unerschöpflichen Wissensreichtum in physikalischen und technischen Dingen habe ich über die Jahre viel gelernt. Und ohne seine geduldigen Ratschläge, physikalische Intuition und Erfahrung wären wir bestimmt nicht so weit gekommen.

Ein großes Dankeschön möchte ich meinen Mitdoktoranden und Teamkollegen, insbesondere Francesco Scazza, Christian Hofrichter, Moritz Höfer, Nelson Darkwah Oppong, Oscar Bettermann, Giulio Pasqualetti und Diogo Rio Fernandes schenken, die mit mir den Alltag im Labor geteilt haben und mit denen ich eine aufregende, produktive und schöne Zeit verbracht habe.

Vielen Dank an die ganze Bloch Gruppe für die tolle Zusammenarbeit und viele schöne Momente, insbesondere auch an Ildiko Kecskesi und Kristina Schuldt, die immer für einen reibungslosen Ablauf und ein gutes Miteinander gesorgt haben.

Nicht zuletzt möchte ich mich auch für die gute und intensive Zusammenarbeit mit Meera Parish und Jesper Levinsen bedanken, sowie für viele hilfreiche und inspirierende Diskussionen mit Agnieszka Cichy, Andrii Sotnikov, Hui Zhai, Peng Zhang, Eugene Demler, Marton Kanász-Nagy, Richard Schmidt, Jan von Delft, Seung-Sup Lee, Frank Deuretzbacher, Vladimir Dzuba und vielen anderen.